Linear viscoelastic characterization of bituminous mixtures from dynamic tests back analysis

Jean-Claude Carret

N°d'ordre NNT: 2018LYSET012

DOCTORAL THESIS OF THE UNIVERSITY OF LYON
prepared at
Ecole Nationale des Travaux Publics de l'Etat

Ecole Doctorale N° 162
Mécanique, Energétique, Génie Civil et Acoustique (MEGA)

Specialty: **Civil Engineering**

Publicly defended the 11th of December 2018 by:
Jean-Claude Carret

Linear viscoelastic characterization of bituminous mixtures from dynamic tests back analysis

---

Before the committee composed of:

TOUSSAINT, Evelyne	Prof., Clermont Auvergne University	President
BHASIN, Amit	Ass. Prof., University of Texas	Reviewer
RYDEN, Nils	Ass. Prof., Lund University	Reviewer
WISTUBA, Michael	Prof., University of Braunschweig	Examiner
DI BENEDETTO, Hervé	Prof., University of Lyon	Advisor
SAUZEAT Cédric	Prof., University of Lyon	Co-advisor
GUDMARSSON, Anders	Dr., PEAB asfalt	Invited

N°d'ordre NNT : 2018LYSET012

THESE de DOCTORAT DE L'UNIVERSITE DE LYON
opérée au sein de
L'Ecole Nationale des Travaux Publics de l'Etat

Ecole Doctorale N° 162
Mécanique, Energétique, Génie Civil et Acoustique (MEGA)

Spécialité/ discipline de doctorat : **Génie Civil**

Soutenue publiquement le 11/12/2018, par :
Jean-Claude Carret

Caractérisation viscoélastique linéaire des enrobés bitumineux par analyse inverse d'essais dynamiques

---

Devant le jury composé de :

TOUSSAINT, Evelyne	Prof., Clermont Auvergne Université	Présidente
BHASIN, Amit	Prof. Ass., Université du Texas	Rapporteur
RYDEN, Nils	Prof. Ass., Université de Lund	Rapporteur
WISTUBA, Michael	Prof., Université de Braunschweig	Examinateur
DI BENEDETTO, Hervé	Prof., Université de Lyon	Directeur de thèse
SAUZEAT Cédric	Prof., Université de Lyon	Co-directeur
GUDMARSSON, Anders	Dr., PEAB asphalte	Invité

TABLE OF CONTENTS

ACKNOWLEDGEMENTS

The preparation of a PhD thesis is a long process that requires many ingredients to be successful. I sincerely think that it is very difficult if not impossible to go through it alone. Also, I want to spend some words to thank and express all my gratitude to all the people that helped me in many different ways to accomplish this thesis.

Firstly, I want to express my sincere gratitude and profound respect to my PhD advisor, Professor Hervé Di Benedetto. I have discovered the research field thanks to him when I was a second year student at ENTPE. Since then, I have learned so much working with him. His scientific rigorousness always pushed me further and all the great discussions and meetings we had together were very helpful and interesting. I strongly hope that we'll keep working together in the future, I'm certain that there are many more things I can learn from him. I would also like to warmly thank Professor Cédric Sauzéat who co-directed this work. He always encouraged me and his advices were very precious in many occasions. I am confident we'll remain in touch for many more years and I'm convinced he will be a wonderful PhD advisor for the future PhD students of the team after Hervé Di Benedetto retires.

I would also like to kindly thank the PhD reviewers, Professors Amit Bhasin and Nils Ryden, who worked really hard to perform a very through and well-documented evaluation of my PhD dissertation. I am grateful that you accepted to review my work and your comments are very valuable to me. I also want to thank the other members of my committee, Professors Evelyne Toussaint and Michael Wistuba. I am honored for your participation to my defense and I thank you for your comments on my work. I also would like to deeply thank Doctor Anders Gudmarsson who accepted the invitation in my committee. His help at the beginning of my PhD thesis was very helpful and I've learned so many things from him. It has always been a great pleasure working with him and it surely helped developing our friendship.

I want to thank all my fellow PhD students, and especially the members of the "bitumen team" for all the good moments we shared and all the very nice memories I have with them. I am grateful to have met them during my PhD thesis and I feel privileged to have great friends like them. I strongly hope that our friendship will last long after I leave ENTPE and that most of you will visit us in Montréal.

I wish to thank a lot my parents, my sister and my two brothers. I love them so much and their support and encouragements have been a tremendous help. I'm blessed to have such a lovely family and I wish them only the best. Finally, I want to express all my love to my wife, Margot. Her presence, her unconditional support and all her love were my strongest source of motivation. I am so delighted to share my life with her and very excited about our future with the birth of our first baby and our move to Montréal. **I dedicate this thesis to you Margot and to our first child** and I love both of you more than anything.

ABSTRACT

Characterizing the behaviour of bituminous materials is essential for the design of pavement structures and to predict their service life more accurately. Indeed, these materials are subjected to complex phenomenon, mechanical, thermal, physical and chemical that are often coupled. Due to the complexity of the phenomenon observed and with the development of new materials and new fabrication process, advanced laboratories studies and rheological modelling are necessary.

With the existing test methods, it is possible to characterize bituminous materials in laboratory using expensive devices such as hydraulic presses. These conventional tests consist in applying cyclic loading to determine the complex modulus and complex Poisson's ratio of the tested materials. However, complicated experimental procedures are necessary to accurately perform the time-consuming preparation of the test set-up and tested samples must be either fabricated in laboratories or cored from road infrastructures.

In this thesis, the possibility of using dynamic tests to characterize accurately the linear viscoelastic (LVE) behaviour of bituminous mixtures is studied. Dynamic tests are economic nondestructive tests, simple to perform and could be adapted for in situ measurements. The experimental methodology developed to measure the frequency response functions (FRFs) from dynamic impact loadings is first presented. Then, different inverse methods to determine the LVE properties from FRFs measurements are proposed and their accuracy is evaluated using numerical experimentation. Finally, the performed experimental campaigns and associated results are presented. In these experimental campaigns, dynamic tests and conventional cyclic tension-compression tests were performed on a wide variety of bituminous mixtures including 5 different materials and 28 specimens. The repeatability of the dynamic tests was studied and the LVE properties determined from both tests were compared.

The numerical experimentation showed that three of the proposed methods of inverse analysis are accurate to characterize the LVE behaviour from FRFs. Two of these methods only give access to the complex modulus and one gives access to both the complex modulus and complex Poisson's ratio. In addition, one method is very interesting because of its simplified approach that considerably facilitates the optimization process and reduces the computational time.

Results from the experimental campaigns showed the good repeatability of dynamic tests, even when using different geometries (cylinders, discs and straight beams) and modes of vibration (longitudinal and flexural). In addition, results from dynamic tests and from conventional cyclic complex modulus tests are in good agreement, especially for the low temperatures (or high frequencies). The norm of the complex modulus determined from dynamic tests is little higher (about 15% higher on average at 15°C and 10 Hz), which can be

explained, at least for a part by the nonlinear behaviour of bituminous mixtures with the strain amplitude (strain amplitude is about 500 times lower in dynamic tests). Dynamic tests also have interesting potential to determine the complex Poisson's ratio even if some differences exist between the results from dynamic and cyclic tests.

The results of this research suggest that dynamic tests are a great alternative to conventional cyclic tests and they can be used to characterize accurately the LVE behaviour of bituminous mixtures.

RESUME

La caractérisation du comportement des matériaux bitumineux est primordiale pour pouvoir dimensionner les structures de chaussées, mais aussi pour prédire de manière plus précise leur durée de vie. En effet, ces matériaux sont soumis à des phénomènes complexes, mécaniques, thermiques, physiques et chimiques qui apparaissent souvent de manière couplée. Devant la complexité des problèmes observés et avec le développement de nouveaux matériaux et de nouveaux procédés de fabrication, des études avancées de laboratoire et des modélisations rhéologiques sont nécessaires.

Les méthodes existantes permettent de caractériser avec les matériaux en laboratoire grâce à l'utilisation de presses hydrauliques très couteuses. Ces essais consistent à appliquer des chargements cycliques pour déterminer le module complexe et le coefficient de Poisson complexe des matériaux testés. Cependant, les procédures expérimentales pour préparer le montage de ces essais avec la précision nécessaire sont complexes et longues à mettre en œuvre. De plus, les échantillons testés doivent être fabriqués en laboratoire ou prélevés sur la chaussée.

Dans cette thèse, la possibilité d'utiliser des essais dynamiques pour caractériser le comportement viscoélastique linéaire (VEL) des enrobés bitumineux est étudiée. Il s'agit d'essais non destructif, simples à appliquer et qui peuvent s'adapter pour des mesures in-situ. La procédure expérimentale développée pour mesurer les fonctions de réponse fréquentielle (FRFs) à partir d'essais dynamiques est d'abord présentée. Puis différentes méthodes d'analyse inverse permettant d'obtenir les propriétés VEL à partir de FRFs mesurées sont proposées et leur précision est évalué grâce à des simulations numériques. Enfin, les campagnes expérimentales et les résultats associés sont présentés. Dans ces campagnes expérimentales, des essais dynamiques et des essais cycliques conventionnels de traction-compression ont été réalisés sur une large gamme d'enrobés incluant 5 matériaux différents et 28 échantillons. La répétabilité des essais dynamiques a été étudiée et les propriétés VEL déterminées par les deux types d'essais ont été comparées.

Les simulations numériques ont permis d'identifier trois méthodes d'analyse inverse qui permettent de caractériser le comportement VEL avec précision à partir de FRFs. Deux de ces méthodes permettent seulement de déterminer le module complexe et une permet également de déterminer le coefficient de Poisson complexe. De plus, l'une des méthodes est particulièrement intéressante car son approche simplifiée permet de faciliter grandement le procédé d'optimisation et de réduire le temps de calcul.

Les résultats des campagnes expérimentales ont montré la bonne répétabilité des essais dynamiques, même en utilisant différentes géométries (cylindres, disques, poutres droites) et modes de vibration (longitudinal et flexion). De plus, les résultats des essais dynamiques et des essais cycliques de module complexe présentent une bonne concordance, particulièrement pour

les basses températures (ou hautes fréquences). La norme du module complexe déterminée avec les essais dynamiques est légèrement plus élevée (environ 15% plus élevée en moyenne à 15°c et 10 Hz), ce qui peut s'expliquer, au moins en partie, par le comportement non linéaire des enrobés bitumineux par rapport à l'amplitude de déformation (l'amplitude de déformation est environ 500 fois plus faible dans les essais dynamiques). Les essais dynamiques sont également intéressants pour déterminer le coefficient de Poisson complexe, bien que des différences existent entre les résultats des essais dynamiques et cycliques.

Les résultats de ce travail de recherche suggèrent que les essais dynamiques sont une vraie alternative aux essais cycliques et ils peuvent être utilisés pour caractériser le comportement VEL des enrobés bitumineux avec précision.

LIST OF TABLES

LIST OF FIGURES

MAIN SYMBOLS

All sections

E^*, G^*, ν^*	Complex modulus, complex shear modulus and complex Poisson's ratio
$\|E^*\|$, $\|G^*\|$, $\|\nu^*\|$	Norm of a given complex property
φ_{E^*}, φ_{G^*}, φ_{ν^*}	Phase angle of a given complex property
σ	Stress
ε	Strain
ρ	Bulk density
f	Frequency
ω	Angular frequency or pulsation ($\omega=2\pi f$)
T	Temperature
T_{ref}	Reference temperature
τ_E, τ_ν	Characteristic time of the complex modulus, complex Poisson's ratio
a_T	Shift factor from time-temperature superposition principle
C_1, C_2	Complex modulus

Section 3

$H(f)$	Frequency response function
$CF(f)$	Coherence function
$S_{xy}(f)$	Cross-power spectrum
$S_{xx}(f)$	Auto-power spectrum of the loading force
$S_{yy}(f)$	Auto power spectrum of the acceleration response
$X(f)$	Measured loading force in frequency domain
$X^*(f)$	Complex conjugate of the loading
$Y(f)$	Measured acceleration response in frequency domain
$Y^*(f)$	Complex conjugate of the response

Sections 4 and 5

E^*_{BCp}	Complex modulus back-calculated in the first step of method P (p=1, 2, 3, 4 or 5)
E^*_{Dynp}	Complex modulus of the 2S2P1D model simulating the global LVE behaviour of the material determined in the second step of method P (p=1, 2, 3, 4 or 5)
ν_{BC5}	Real Poisson's ratio back-calculated in the first step of method V
ν^*_{Dyn5}	Complex Poisson's ratio of the 2S2P1D model simulating the global LVE behaviour of the material determined in the second step of method V

Section 4

E^*_{Ref}	Complex modulus of the reference LVE material
ν^*_{Ref}	Complex Poisson's ratio of the reference LVE material

Section 5

E^*_{ExpTC}	Experimental complex modulus data from tension-compression tests
E^*_{TC}	Complex modulus of the 2S2P1D model simulating the global LVE behaviour of the material determined from tension-compression tests
ν^*_{ExpTC}	Experimental complex Poisson's ratio data from tension-compression tests
ν^*_{TC}	Complex Poisson's ratio of the 2S2P1D model simulating the global LVE behaviour of the material determined from tension-compression tests

LIST OF ABBREVIATIONS

LVE	Linear viscoelastic
TTSP	Time-temperature superposition principle
WLF	William-Landel-Ferry
2S2P1D	2 Springs, 2 parabolic elements, 1 dashpot
HN	Havriliak-Negami
SD	Standard deviation
RSD	Relative standard deviation
FFT	Fast Fourier transformation
FRF(s)	Frequency response function(s)
FEM	Finite element method
RAP	Reclaimed asphalt pavement

1 INTRODUCTION

Roads are major infrastructures that greatly contribute to the economic development of a country. Most of the medium and heavy traffic pavement infrastructures are constructed with bituminous materials. For example, in France, the length of the paved road network exceed one million kilometers (Commissariat général au développement durable, 2018). These structures are conceived for a certain lifetime determined from design methods. Traditionally, empirical considerations have been used in French design methods to determine material properties suitable for specific climate and traffic conditions. Therefore, the applicability of this type of approach is limited and it has not helped understanding the fundamental mechanical behaviour of pavements. Nowadays, the road construction industry increasingly looks to use mechanical design methods to optimize the costs and the lifecycles of pavement infrastructures. In the meantime, new materials (e.g. mixtures with increasing reclaimed asphalt pavement (RAP) content, polymer modified bitumen, etc.) and new fabrication process (e.g. cold or warm coating) are developing, within a sustainable development approach. In this context, accurate characterization of the mechanical properties of bituminous materials is necessary.

In conventional test methods, cyclic loadings are applied to determine the linear viscoelastic (LVE) properties of bituminous mixtures (Corté & Di Benedetto, 2005). However, this type of test requires the use of expensive experimental devices such as hydraulic presses. In addition, complicated experimental procedures are necessary to accurately perform the time-consuming preparation of the test set-up and tested samples must be either fabricated in laboratories or cored from road infrastructures.

Dynamic tests, which are based on wave propagation, are a great alternative to conventional cyclic tests. They are nondestructive tests, economic and simple to perform. They also can possibly be adapted for in-situ measurements on pavement structures. Impulse techniques using impact loadings (ASTM-C215-02, 2002; Halvorsen & Brown, 1977) are known to provide accurate characterization of material properties in the case of elastic materials (Migliori & Sarrao, 1997). For these tests, the elastic modulus is generally derived from the measurement of the fundamental resonance frequency using simplified analytical formulas. For bituminous mixtures, the complex modulus has an elastic component but also a viscous component that accounts for the viscous damping of bitumen. Various authors (Whitmoyer & Kim, 1994; Kweon & Kim, 2006; Lacroix, Kim, Sadat, & Far, 2009) used the same methodology that in the elastic case to determine the complex modulus of bituminous mixtures, adding correction factors to take into account the damping and using the half-power bandwidth method to determine the phase angle. However, it is not possible to describe accurately the frequency dependency of the behaviour over a wide frequency range with this type of analysis. The same limitations have been found for tests using measurements of wave propagation time on bituminous mixtures (Di Benedetto, Sauzéat, & Sohm, 2009; Mounier, Di Benedetto, & Sauzéat, 2012; Norembuena-Contreras, Castro-Fresno, Vega-Zamanillo, Celaya, & Lombillo-

Vozmediano, 2010). More recently, measurement of frequency response functions (FRFs) have been successfully used to characterize various LVE materials over a wide frequency range such as metal polymer sandwich beams (Ren, Atalla, & Ghinet, 2011) or highly damped acoustical porous materials (Guo, 2000; Renault, Jaouen, & Sgard, 2011; Rupitsch, Ilg, Sutor, Lerch, & Döllinger, 2011). FRFs measurements have also been performed on a limited variety of bituminous mixtures (Gudmarsson, Ryden, & Birgisson, 2012; Gudmarsson, et al., 2014; Gudmarsson, Ryden, Di Benedetto, & Sauzéat, 2015; Carret, Pedraza, Di Benedetto, & Sauzéat, 2018) and they reveal to be a very promising approach to characterize accurately the LVE behaviour of bituminous mixtures over a wide frequency range.

In this thesis, the possibility of using FRFs measurements to characterize accurately the global LVE behaviour of bituminous mixtures has been rigorously studied. More specifically, the principle objectives of this research are:

- To develop an accurate and repeatable methodology to perform FRFs measurements on bituminous mixture specimens at different temperatures and for different modes of vibration (longitudinal, flexural and torsional).
- To propose accurate back-analysis (or inverse) methods to determine the LVE properties of bituminous mixtures from FRFs measurements.
- To demonstrate the good accuracy of dynamic tests for different types of bituminous mixtures using comparisons of the LVE properties determined from dynamic tests and with more conventional cyclic tension-compression complex modulus tests.

The dissertation is organized in seven sections. After this introduction presenting the context and the objectives of the study, generalities about the linear viscoelastic behaviour of bituminous materials are presented together with an introduction to wave propagation in elastic and viscoelastic materials. Then, the experimental methodology developed to perform dynamic tests on bituminous mixtures is introduced. Afterwards, numerical simulations of the dynamic tests are performed to develop different inverse analysis methods to derive the LVE properties from FRFs measurements. In this section, the accuracy of all proposed inverse methods is evaluated. In the next section, the different performed experimental campaigns are presented. The materials and the tests performed are described and the results and analyses procedures are reported. The papers published in or submitted to scientific journals during this thesis are gathered in the sixth section. Finally, the general conclusions of the study and perspectives for future research are presented.

2 ISOTROPIC LINEAR VISCOELASTIC (LVE) BEHAVIOUR

2.1 General considerations

2.1.1 Definition of an isotropic linear viscoelastic behaviour

A material is defined isotropic when its rheological properties are identical in all directions. Bituminous mixtures are generally considered as isotropic materials. Nevertheless, the behavior of bituminous mixtures is not perfectly isotropic in practice (Motola & Uzan, 2007; Di Benedetto, Sauzéat, & Clec'h, 2016).

When subjected to small amplitude strain, bituminous mixtures express a linear viscoelastic behavior. Viscoelasticity is a time-dependent behaviour, characterizing materials showing both an elastic and a viscous behaviour when a deformation is imposed. To be defined as viscoelastic, a material must show a complete stress recovery at an infinite time (the residual stress σ_∞ at $t \rightarrow \infty$ is equal to 0) when subjected to a "cancellation test" (Salençon, 2009). This test illustrated in Figure 2.1 consists in applying a constant strain for a given time before returning to zero and to monitor the resulting stress. This principle is valid only for non-aging materials whose properties remain unaltered when the material is undisturbed.

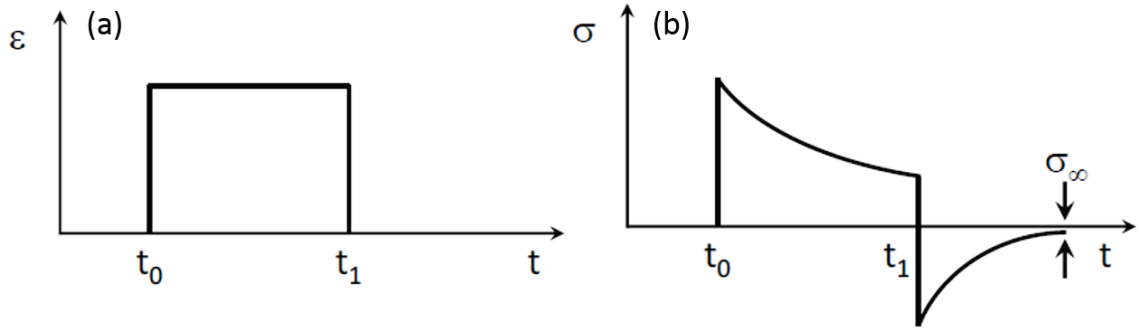

Figure 2.1. "Cancellation test": (a) strain history; (b) resulting stress.

The linearity of the behaviour is valid if it verifies Boltzmann superposition principle (Boltzmann, 1874). It means that the response to the superposition of different loads is equal to the superposition of the individual responses to each load. The LVE behaviour can be characterized in time domain or in frequency domain with material properties similar to elastic properties such as the Young's modulus E or the Poisson's ratio ν. However, in the case of LVE materials, the mechanical properties are complex numbers which depend on time and frequency.

2.1.2 Time domain properties

Creep and relaxation are two classical quasi-static tests used to characterize the LVE behaviour in time domain. In the creep test (Figure 2.2), a stress σ_0 is applied to the material initially at rest and kept constant over time. It is observed that the resulting strain signal ε increases with time. This corresponds to a material flow called the creep phenomenon. The creep function D, defined as the ratio between the variable strain and the constant stress is obtained from this test:

$$D(t) = \frac{\varepsilon(t)}{\sigma_0} \tag{2-1}$$

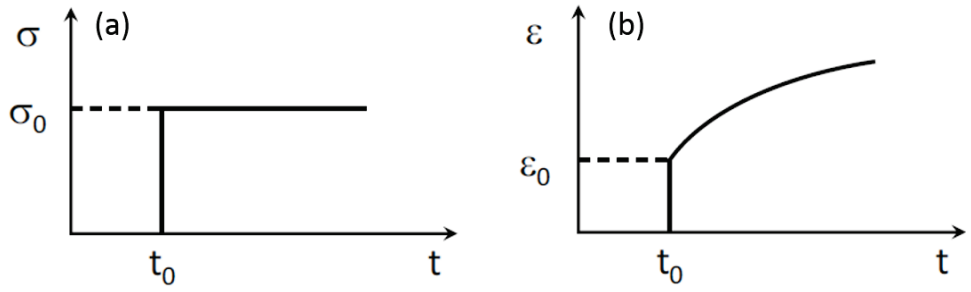

Figure 2.2. Creep test for a LVE material: (a) imposed stress; (b) resulting stain.

In the relaxation test (Figure 2.3), an instant strain ε_0 is applied to the material initially at rest and kept constant over time. It is observed that the resulting strain signal σ decreases with time. This is called the relaxation phenomenon. The relaxation function J, defined as the ratio between the variable stress and the constant strain is obtained from this test:

$$J(t) = \frac{\sigma(t)}{\varepsilon_0} \tag{2-2}$$

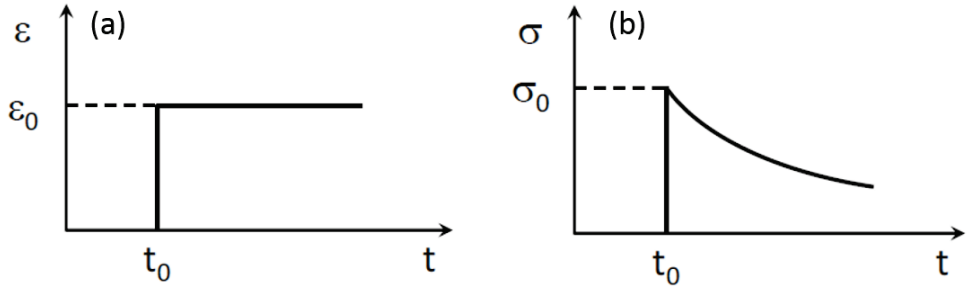

Figure 2.3. Relaxation test for a LVE material: (a) imposed strain; (b) resulting stress.

It is possible to extend equations (2-1) and (2-2) in the case of strain or stress varying with time from the application of Boltzmann superposition principle. Relations obtained between the strain signal response ε to the applied stress history σ and between the stress response σ to the applied strain history ε are presented in equations (2-3) and (2-4) when strain and stress are differentiable:

$$\varepsilon(t) = \int_0^t D(t-\tau)\dot{\sigma}(\tau)d\tau \tag{2-3}$$

$$\sigma(t) = \int_0^t J(t-\tau)\dot{\varepsilon}(\tau)d\tau \tag{2-4}$$

where τ is a time-variable used in the integration, D is the creep function and J is the relaxation function. These convolution integrals are difficult to apply. Therefore, the Laplace-Carson transform is introduced to turn these integrals into algebraic equations and to ease calculations (Corté & Di Benedetto, 2005). The Laplace-Carson transform of a time-dependent function f is defined as:

$$\tilde{f}(p) = p\int_0^\infty f(t)e^{-pt}dt \tag{2-5}$$

where p is a complex variable corresponding to time in the transform domain. After application of the Laplace-Carson transform, equations (2-3) and (2-4) become:

$$\tilde{\varepsilon}(p) = \tilde{D}(p)\tilde{\sigma}(p) \tag{2-6}$$

$$\tilde{\sigma}(p) = \tilde{J}(p)\tilde{\varepsilon}(p) \tag{2-7}$$

where $\tilde{\varepsilon}$, $\tilde{\sigma}$, $\tilde{D}$ and $\tilde{J}$ are the Laplace-Carson transforms of strain, stress, creep function and relaxation function. It should be noted that equations (2-6) and (2-7) are very similar to fundamental relations of elasticity. These equations can be used to obtain the LVE solution to a given boundary value problem from the elastic solution for the same problem, according to the elastic-viscoelastic correspondence principle (Biot, 1959). Moreover, the existing reciprocity between the Young's modulus and the relaxation modulus in the elastic theory is preserved:

$$\tilde{D}(p)\tilde{J}(p) = 1 \tag{2-8}$$

2.1.3 Frequency domain properties: complex modulus and complex Poisson's ratio

If a LVE material is subjected to an axial sinusoidal stress $\sigma(t) = \sigma_0 \sin(\omega t)$ where $\omega=2\pi f$ is the pulsation and f is the frequency, the steady state resulting axial strain $\varepsilon_1(t) = \varepsilon_{01}\sin(\omega t - \varphi)$ is also sinusoidal at the same frequency and with a phase lag ϕ called the phase angle. Considering the complex notation ($i^2=-1$), the stress and strain can be written:

$$\sigma^*(t) = \sigma_0 e^{i\omega t} \tag{2-9}$$

$$\varepsilon_1^*(t) = \varepsilon_{01}e^{i(\omega t-\varphi)} \tag{2-10}$$

The complex modulus E* is defined as the ratio between the sinusoidal stress and the sinusoidal strain:

$$E^* = \frac{\sigma^*}{\varepsilon_1^*} = \frac{\sigma_0 e^{i\omega t}}{\varepsilon_{01} e^{i(\omega t-\varphi)}} = \frac{\sigma_0}{\varepsilon_{01}} e^{i\varphi} = \left|E^*\right| e^{i\varphi} \tag{2-11}$$

where |E*| is the norm of the complex modulus defined as the ratio between the stress and strain amplitudes. Note that the complex modulus E* corresponds to the Laplace-Carson transform of the relaxation function calculated in p=iω. The complex modulus can also be expressed as:

$$E^* = E_1 + iE_2 \tag{2-12}$$

where E_1 is the storage or elasticity modulus that accounts for the recoverable part of the energy stored by the material during loading and E_2 is the loss modulus that accounts for the energy lost during loading due to the irreversible viscous component of the behaviour. If the phase angle ϕ=0°, the behaviour is purely linear elastic while if ϕ=90°, the behaviour is purely viscous. Between these two extreme case, when 0<ϕ<90, the behaviour is considered LVE.

In addition to the axial response, a radial response is also observed due to Poisson's ratio effect. During simple compression loading on isotropic LVE material, when a contraction is observed in the axial direction, an extension is observed in the radial direction. Therefore, the axial strain and the radial strain are in phase opposition but the radial strain may also present a phase lag with respect to the axial strain so that the radial strain is expressed in complex notation as:

$$\varepsilon_2^*(t) = \varepsilon_{02} e^{i(\omega t-\varphi+\pi+\varphi_\nu)} = -\varepsilon_{02} e^{i(\omega t-\varphi+\varphi_\nu)} \tag{2-13}$$

where π represents the phase opposition between the axial and radial strains and ϕ_ν is the phase angle of Poisson's ratio. The complex Poisson's ratio is then defined as the opposite of the ratio between the radial strain and the axial strain:

$$\nu^* = -\frac{\varepsilon_2^*}{\varepsilon_1^*} = \frac{\varepsilon_{02} e^{i(\omega t-\varphi+\pi+\varphi_\nu)}}{\varepsilon_{01} e^{i(\omega t-\varphi)}} = \frac{\varepsilon_{02}}{\varepsilon_{01}} e^{i\varphi_\nu} = \left|\nu^*\right| e^{i\varphi_\nu} \tag{2-14}$$

Instead of an axial sinusoidal loading test, a shear sinusoidal loading test may also be used. In this case, the complex shear modulus is obtained:

$$G^* = \frac{\tau^*}{\gamma^*} = \frac{\tau_0 e^{i\omega t}}{\gamma_0 e^{i(\omega t-\varphi_G)}} = \frac{\tau_0}{\gamma_0} e^{i\varphi_G} = \left|G^*\right| e^{i\varphi_G} \tag{2-15}$$

where γ is the shear strain applied to the material, τ is the resulting shear stress and ϕ_G is the phase angle of the complex shear modulus. For an isotropic behavior, E*, ν* and G* are linked similarly as in the elastic case:

$$G^* = \frac{E^*}{2(1+\nu^*)} \tag{2-16}$$

The complex modulus and complex Poisson's ratio can be represented with different graphs that highlight their frequency and temperature dependency. The isotherms (respectively the isochrones) present the norm or the phase of the complex modulus or complex Poisson's ratio as a function of the loading frequency (respectively the tested temperature). These curves show at a fixed temperature (respectively frequency) the effect of the loading frequency (respectively the temperature) as seen in Figure 2.4. Another graphical representation is the Cole-Cole plot (Figure 2.4 (a)) where the imaginary part of the complex modulus or complex Poisson's ratio is plotted against the real part. This representation is well adapted for the low temperatures or high frequencies that are particularly visible. In the Black space (Figure 2.4 (b)), the phase angle of the complex modulus is plotted against the norm. This representation suits well the high temperatures or low frequencies. Cole-Cole and Black representations are particularly interesting because the curves obtained are independent of the temperature and frequency if the time temperature superposition principle is respected.

2.1.4 Time-Temperature Superposition Principle

The complex modulus generally depends on temperature and frequency for LVE materials. Observations on several LVE materials raised by different authors (Gross, 1968; Ferry, 1980) showed that the complex modulus values tend to form a unique curve in the Cole-Cole or Black representations, independently of loading frequency or test temperature as shown in Figure 2.4 (a) and (b). Materials presenting this behaviour are called "thermo-rheologically simple" (Corté & Di Benedetto, 2005) and their frequency and temperature dependency can be reduced to one single parameter. Therefore, values of the complex modulus obtained at different pairs of temperature and frequency might be equal and an equivalency exists between the effects of temperature and frequency. This equivalency is called the Time-Temperature Superposition Principle (TTSP).

The main consequence of the TTSP is that one single variable can be used to describe the variations of the complex modulus. Therefore, it is possible to generate unique curves describing the variations of the norm or the phase of the complex modulus as a function of frequency at any chosen reference temperature T_{ref}. This type of curves, called master curves, are obtained by shifting the isothermal curves along the frequency axis. The frequencies of each isotherm are multiplied by a shift factor a_T, which depends only on the temperature T of the isotherm and the reference temperature T_{ref} (cf Figure 2.4). The frequencies multiplied by the shift factors are called reduced frequencies and the following equation links the complex modulus at a frequency f and a temperature T to the modulus at the corresponding reduced frequency $f.a_T$ and temperature T_{ref}:

$$E^*(f,T) = E^*(f.a_T(T), T_{ref}) \tag{2-17}$$

The shift factors are commonly fitted to temperature using the Williams-Landel-Ferry (WLF) equation (Williams, Landel, & Ferry, 1955):

$$\log(a_T) = \frac{-C_1(T - T_{ref})}{C_2 + T - T_{ref}} \tag{2-18}$$

where C_1 and C_2 are material constants varying with the reference temperature T_{ref}. The WLF equation can be applied over the entire range of temperature tested. It is therefore possible to generate master curves at any desired reference temperature. Consequently, application of the TTSP is very interesting because it gives access to values of the complex modulus at frequencies and temperatures not accessible experimentally. Note that the TTSP is also applicable to generate master curves for the complex Poisson's ratio. For bituminous Materials the same values of the shift factor are obtained for the complex modulus and complex Poisson's ratio. (Nguyen Q. T., Di Benedetto, Sauzéat, & Tapsoba, 2013).

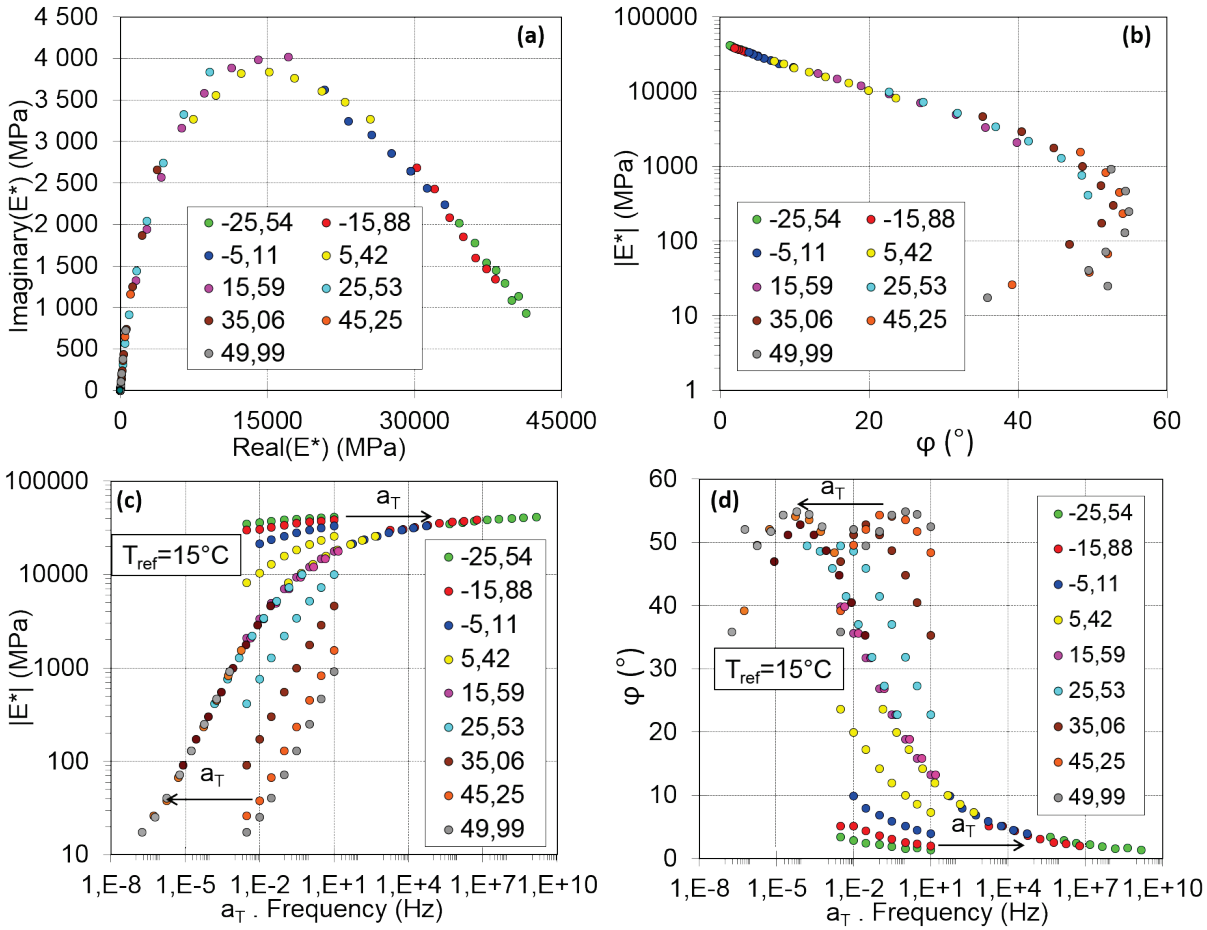

Figure 2.4. Example of graphical representation for the complex modulus: (a) Cole-Cole representation; (b) Black space representation; (c) master curve of the norm of the complex modulus at 15°C; (d) master curve of the norm of the complex modulus at 15°C.

2.2 Complex modulus test developed at ENTPE

Different test geometries may be used with homogeneous or non-homogeneous test to characterize the complex modulus of bituminous mixtures. At ENTPE, tension-compression tests on cylindrical specimen are used, which is a homogeneous test, allowing to obtain the rheological behaviour without assumptions. In this type of tests, a hydraulic press is used in strain controlled mode to apply a homogeneous axial loading to a cylindrical sample while the material response is measured. The samples have approximately a 75 mm diameter and a 150 mm length. They are glued to the upper and lower aluminum caps prior to the test. The upper cap is fixed to the press actuator which generates tension or compression in the specimen while the lower cap is attached to the fixed axis of the press.

The experimental set-up used in this thesis is presented in Figure 2.5. The targeted axial strain amplitude was about 50 µm/m. The behaviour is considered LVE for this imposed strain level. The axial strain was measured with three extensometers placed at 120° from each other. Each extensometer has a total span of 72.5 mm with a measuring range of ±1 mm and a 0.5 µm accuracy. The axial load was measured with a Dynacell® load cell having a ±25kN capacity and a 25N accuracy. The radial strain was deduced from measurements of two non-contact transducers (Micro-Epsilon eddy current sensors with 0-500 µm range and a resolution of 0.05 µm) placed diametrically opposed. Tests were performed inside a thermal chamber operating between -40°C and 150°C. A PT100 temperature probe with a 0.1°C accuracy was used to measure the temperature at the surface of the specimen. The tension-compression tests were performed at 8 different loading frequencies from 0.003Hz to 10Hz and 9 different temperatures from -25°C to 55°C in steps of 10°C.

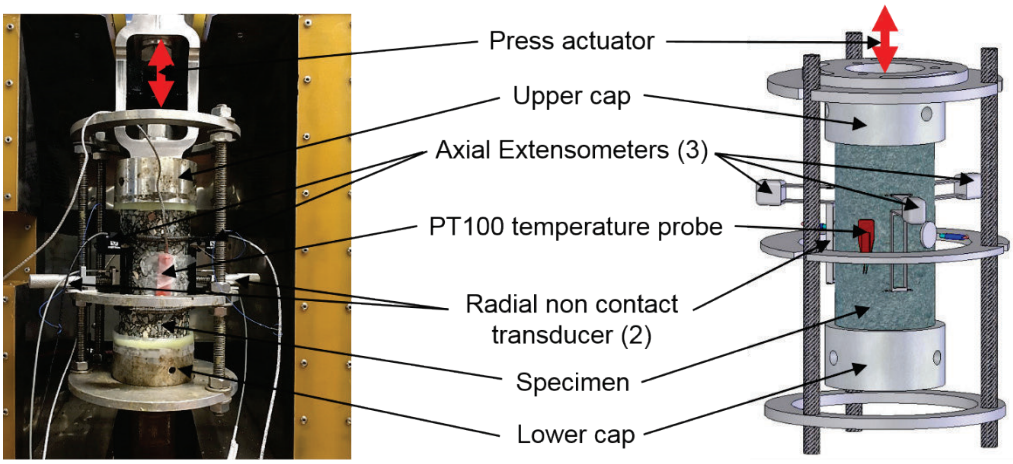

Figure 2.5. Test set-up for the cyclic tension-compression tests (ENTPE laboratory) and detailed scheme of the sample and measurement sensors.

The complex modulus and complex Poisson's ratio values are then deduced from the measurements of the sensors and according to equations (2-11) and (2-14). An example of the experimental signals recorded by the sensors during a tension-compression test is given in Figure 2.6. for two loading cycles. Further information about cyclic tension-compression tests can be found in literature (Gayte, Di Benedetto, Sauzéat, & Nguyen, 2015; Perraton, et al., 2016; Graziani, et al., 2017).

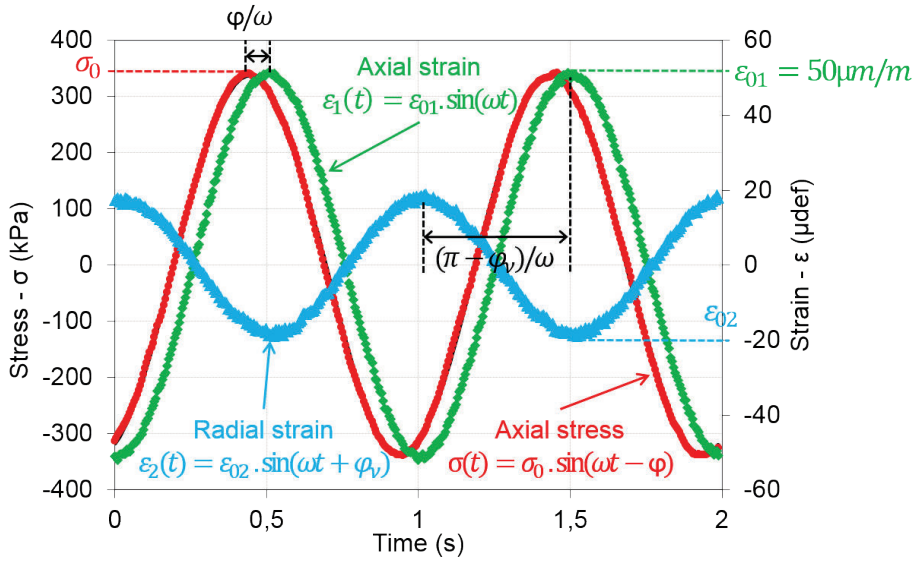

Figure 2.6. Example of experimental signals recorded during a tension-compression test for two loading cycles at 15°C and 1 Hz: axial stress σ, axial strain ε_1 and radial strain ε_2.

2.3 Waves propagation in isotropic linear elastic and LVE materials

When a deformable solid is subjected to an external force, a deformation is induced in the solid. This deformation generates a disturbance of the matter around its equilibrium state. As particles of the medium are deformed, the disturbance also called wave progresses through the medium, carrying energy inside the medium through motions of particles and without any mass transport. This is called a mechanical wave. The study of the propagation of this type of waves in solids is very well documented in literature (Mandel, 1966; Graff, 1975; Ingard, 1988; Bedford & Drumheller, 1994). The aim of this section is to describe the case of waves propagating in isotropic linear elastic and LVE materials.

2.3.1 Types of body waves

Body waves are waves propagating inside a solid. Two types of particle motion are observed for the body waves, resulting in two different types of body waves:

- The primary waves or pressure waves called P-waves. They are associated to relatively small particle displacements and are polarized in the same direction of propagation. P-waves are the fastest body waves and their mode of propagation is always longitudinal. An illustration of the particle motions corresponding to P-waves is given in Figure 2.7.
- The secondary waves or shear waves called S-waves. They are polarized in the transverse direction of propagation. S-waves are slower than P-waves and their mode of propagation is always transverse. An illustration of the particle motions corresponding to S-waves is given in Figure 2.7.

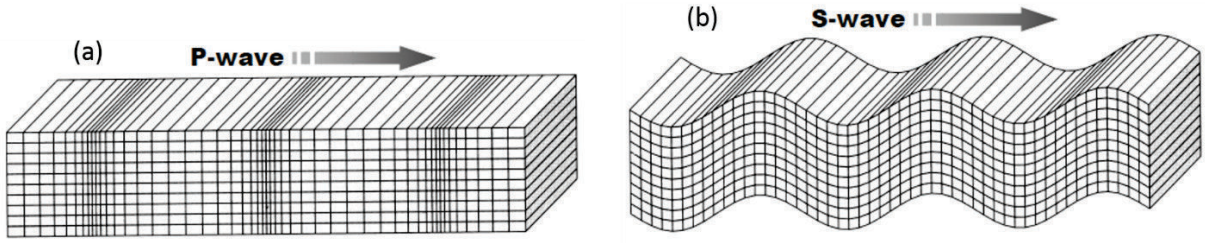

Figure 2.7. Particle motions characteristic of body waves propagation: (a) P-waves; (b) S-waves (Shearer, 1999).

2.3.2 Wave equation and resonance phenomenon

Newton's second law states that sum of force applied to a solid are equal to mass times acceleration, which could be written in continuous mechanics without bulk forces:

$$\mathrm{div}(\sigma) = \rho \frac{\partial^2 u}{\partial t^2} \tag{2-19}$$

where div is the divergence tensor operator, σ is the stress tensor, ρ is the density, u is the displacement vector and t is the time. If the material is isotropic and linear elastic, Hooke's law is valid:

$$\sigma = \lambda \mathrm{div}(u) + 2\mu \mathrm{tr}(\varepsilon) \tag{2-20}$$

where div is the divergence vector operator, λ and μ are Lamé's elastic constants of the material and ε is the strain tensor. In the small strain domain, the strain tensor is linked to the displacements as follow:

$$\varepsilon = \frac{1}{2}\left(\mathrm{grad}(u) + {}^{T}\mathrm{grad}(u)\right) \tag{2-21}$$

where grad is the gradient vector operator. By using equations (2-21) and (2-20), it is possible to substitute displacements to stress in equation (2-19):

$$(\lambda + \mu)\mathrm{grad}(\mathrm{div}(u)) + \mu \Delta u = \rho \frac{\partial^2 u}{\partial t^2} \tag{2-22}$$

where Δ is the Laplace vector operator, div is the divergence vector operator and grad is the gradient vector operator. Equation (2-22) is called the displacement equation of motion or wave equation. This equation admits only two solutions that are plane-waves propagating in the same direction x and polarized in the direction of propagation or in the transverse direction (Mandel, 1966). These two solutions correspond to the two types of body waves introduced in the previous section. The displacement fields are expressed:

$$U_P(x,t) = U_{P0} e^{i\omega\left(t - \frac{x}{V_P}\right)} \tag{2-23}$$

$$U_S(x,t) = U_{S0} e^{i\omega\left(t - \frac{x}{V_S}\right)} \tag{2-24}$$

where U_p and U_s are the displacement fields of the P-wave and of the S-wave, U_{p0} and U_{s0} are the amplitudes of the displacement of the P-wave and of the S-wave, x is the position, ω is the pulsation or angular frequency and V_p and V_s are the velocities of the P-wave and of the S-wave that can be expressed:

$$V_P = \sqrt{\frac{\lambda + 2\mu}{\rho}} = \sqrt{\frac{E(1-\nu)}{\rho(1+\nu)(1-2\nu)}} \tag{2-25}$$

$$V_S = \sqrt{\frac{\mu}{\rho}} = \sqrt{\frac{E}{2\rho(1+\nu)}} \tag{2-26}$$

In the case of LVE materials, the frequency dependency of the complex modulus and complex Poisson's ratio has to be taken into account. The Hooke's law of elasticity is therefore modified as follow:

$$\sigma^* = \lambda^* \mathrm{div}(u^*) + 2\mu^* \mathrm{tr}(\varepsilon^*) \tag{2-27}$$

where σ^*, ε^*, u^*, λ^* and μ^* are the complex versions of the stress tensor, the strain tensor, the displacement vector and Lamé's constants whose values vary with frequency. In harmonic regime at pulsation ω, the stress tensor and the displacement vector are expressed:

$$\sigma^* = \sigma_0 e^{i\omega t} \tag{2-28}$$

$$u^* = u_0 e^{i\omega t} \tag{2-29}$$

where σ_0 and u_0 are not depending on the frequency but only on space-variables. By application of the Boltzmann superposition principle (Boltzmann, 1874), the wave equation in elasticity (equation (2-22) is also valid for the LVE behaviour in the Laplace-Carson transform domain under the form:

$$(\lambda^* + \mu^*)\mathrm{grad}(\mathrm{div}(u^*)) + \mu^* \Delta u^* + \rho\omega^2 u_0 = 0 \tag{2-30}$$

This equation is very similar to the one obtain for elastic materials. If the Poisson's ratio is considered as a real number depending on the frequency, the same type of solutions than in the elastic case are obtained. However, an attenuation term ϕ depending on the frequency appears due to the viscous component of the behaviour. The displacement fields of the P-waves and S-waves are depending on the frequency (Mandel, 1966) and are expressed:

$$U_P(x,t) = U_{P0} e^{i\omega\left(t - \frac{x}{V_P(\omega)}\right)} e^{-\omega \frac{x \tan(\varphi(\omega)/2)}{V_P(\omega)}} \tag{2-31}$$

$$U_S(x,t) = U_{S0} e^{i\omega\left(t-\frac{x}{V_S(\omega)}\right)} e^{-\omega\frac{x\tan(\varphi(\omega)/2)}{V_S(\omega)}} \tag{2-32}$$

where the velocities V_p and V_s of the P-waves and of the S-waves are also depending on the frequency. For a fixed frequency, they are expressed:

$$V_P = \frac{1}{\cos(\frac{\varphi}{2})}\sqrt{\frac{|E^*|(1-\nu)}{\rho(1+\nu)(1-2\nu)}} \tag{2-33}$$

$$V_S = \frac{1}{\cos(\frac{\varphi}{2})}\sqrt{\frac{|E^*|}{2\rho(1+\nu)}} \tag{2-34}$$

where $|E^*|$ and ϕ are the norm and phase angle of the complex modulus at the considered frequency and ν is the real value of the Poisson's ratio at the same frequency. The velocities of the body waves are directly linked to the material properties. Therefore, measuring the travel time of a wave over a known distance enables an estimation of the modulus. This approach has already been used on bituminous mixtures (Nazarian, Tandon, & Yuan, 2005; Di Benedetto, Sauzéat, & Sohm, 2009; Norembuena-Contreras, Castro-Fresno, Vega-Zamanillo, Celaya, & Lombillo-Vozmediano, 2010; Mounier, Di Benedetto, & Sauzéat, 2012). However, this method is limited to the very high frequencies and is accurate only if the plane-waves approximation is verified.

An interesting alternative to record the flying time of body waves is to exploit the resonance phenomenon. Resonance occurs when the loading frequency of a material is equal to one of its natural frequencies. This is traduced by oscillations of the structure at greater amplitudes for these natural frequencies also called resonance frequencies. These resonance frequencies are a function of the geometry, of the density and of the material properties (e.g. Young's modulus and Poisson's ratio for elastic materials; complex modulus and complex Poisson's ratio for LVE materials). Moreover, measurements of resonance frequencies do not rely on the plane-waves approximation since they account for the complex vibrations of the material. Therefore, measurements of the resonance frequencies have been widely used to derive the elastic constants of different materials with methods called resonant ultrasonic spectroscopy (RUS) (Maynard, 1996; Leisure & Willis, 1997; Migliori & Sarrao, 1997) or resonant acoustic spectroscopy (RAS) (Ostrovsky, et al., 2001). RAS has also been applied to LVE materials (Ryden, 2011; Gudmarsson, Ryden, & Birgisson, 2012). In addition to RAS, other methods based on the same principle but using only the first resonance frequency have been used on LVE materials by various authors (Whitmoyer & Kim, 1994; Kweon & Kim, 2006; Lacroix, Kim, Sadat, & Far, 2009).

2.3.3 Strain amplitude corresponding to wave propagation

Measuring the resonance frequencies of a structure requires to excite the material over a wide frequency range. This can be achieved using contact excitation with an impact hammer

for example or through non-contact excitation with a speaker for example. This type of solicitation corresponds to a certain level of strain that can be determined from the vibratory response of the material. For a material excited in harmonic regime at the pulsation ω, the following equation links the amplitudes of the displacement and acceleration:

$$A(\omega) = \omega^2 U(\omega) \tag{2-35}$$

where A is the amplitude of the acceleration and U is the amplitude of the displacement. For a wave propagating in a beam of length L in the main direction x, different wavelengths corresponding to different resonant frequencies coexist. They are represented in Figure 2.8. If r is the number of the mode of vibrations, for each resonance frequencies $f_r=\omega_r/2\pi$, displacements inside the material can be expressed:

$$U_r(x,t) = U_r(x)\sin(\omega_r t) \tag{2-36}$$

where U_r is function of the position x equal to:

$$U_r(x) = U_r \sin(\frac{2\pi x}{\lambda_r}) \tag{2-37}$$

where U_r is the maximum amplitude of the displacement at the resonance frequency f_r and λ_r is the corresponding wavelength. It's possible to express equation (2-37) in function of the amplitude of the acceleration using equation (2-35). Then, derivation of equation (2-37) and injecting in equation (2-36) gives:

$$\varepsilon_r(x,t) = \frac{dU_0}{dx}(x)\sin(\omega_r t) = \frac{2\pi A_r}{\lambda_r \omega_r^2}\cos(\frac{2\pi x}{\lambda_r})\sin(\omega_r t) \tag{2-38}$$

where ε_r and A_r are the strain and the maximum amplitude of the acceleration at the resonance frequency f_r. In the case of a P-wave propagating in the x direction and polarized in the same direction, A_r corresponds to the term ε_{xx} of the strain tensor. In the case of a S-wave propagating in the x direction and polarized in the transverse direction y, A_r corresponds to the term ε_{xy} of the strain tensor. A rapid study of equation (2-38) shows that the maximum strain is obtained when x is a multiple of $\lambda_r/2$ and when $\sin(\omega_r t)=1$. The maximum strain for the resonance f_r frequency is therefore:

$$\varepsilon_{max,r} = \frac{2\pi A_r}{\lambda_r \omega_r^2} = \frac{A_r}{2\pi \lambda_r f_r^2} \tag{2-39}$$

It should be noted that the frequency and the wavelength are linked to the wave velocity. It has been established that the maximum strain regarding all the resonance frequencies is obtained for the first or fundamental resonance frequency f_1 corresponding to the wavelength $\lambda_1=2L$ (TenCate, et al., 2004; Pasqualini, 2006):

$$\varepsilon_{max} = \frac{A_1}{4\pi L f_1^2} \tag{2-40}$$

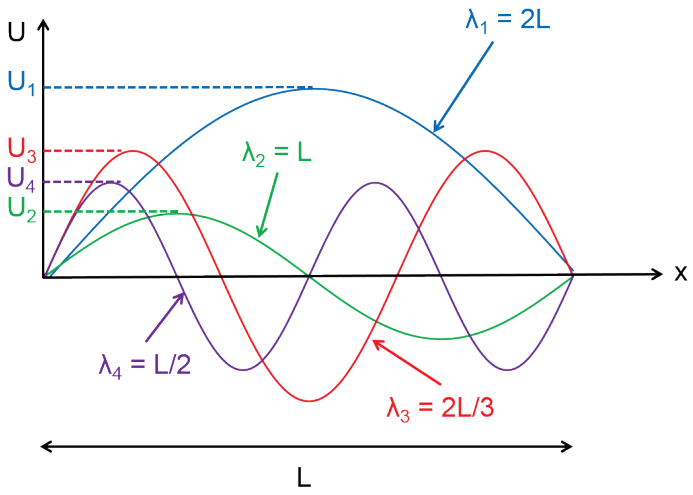

Figure 2.8. Example of wavelengths corresponding to resonance frequencies for a wave in a beam of length L in the main direction x.

Equation (2-40) is valid for an elastic behaviour. In the case of a LVE behaviour, the only difference is the appearance of an attenuation term due to the viscous component of the behaviour. However, this attenuation term, which has a limited impact on the strain, can only reduce the maximum strain. Therefore, as a first approximation, the maximum strain corresponding to a wave propagating in a LVE material can be considered equal to the maximum strain occurring in the case of an elastic behaviour.

2.4 LVE Continuous spectrum models for bituminous materials

Many rheological LVE models exist and have the purpose of providing a mathematical approximation of real material behaviour. Some of these models have an analogical representation which is a combination of springs, dashpots and parabolic elements. The springs are purely elastic elements, the dashpots are purely viscous elements and parabolic elements are viscous elements with a parabolic creep function. LVE models can have a discrete relaxation spectrum or a continuous relaxation spectrum:

- models with a discrete relaxation spectrum can be represented by the association of a finite number of Maxwell elements (a spring and a dashpot associated in series) or Kelvin-Voigt elements (a spring and a dashpot associated in parallel).
- models with a continuous relaxation spectrum can be represented by the association of an infinite number of Maxwell and Kelvin-Voigt elements

In this section, focus is given on two continuous spectrum models used in this work.

2.4.1 2S2P1D model

The 2S2P1D model is the association in series of two springs, two parabolic elements and one dashpot (Olard & Di Benedetto, 2003; Di Benedetto, Olard, Sauzéat, & Delaporte, 2004). This model is an extension of the Huet-Sayegh model (Sayegh, 1965) to adequately describe the low frequencies or high temperatures behaviour of bitumen. The Huet-Sayegh model is itself an improvement of the Huet model (Huet, 1963) to fit the behaviour of bituminous

mixtures at high temperatures or low frequencies. An analogical scheme of the 2S2P1D model is presented in Figure 2.9.

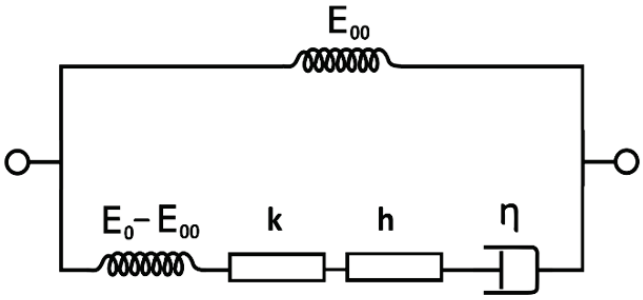

Figure 2.9. Analogical representation of the 2S2P1D model.

The 2S2P1D model has an expression for the complex modulus that depends on seven constants:

$$E^*(\omega) = E_{00} + \frac{E_0 - E_{00}}{1 + \delta(i\omega\tau)^{-k} + (i\omega\tau)^{-h} + (i\omega\beta\tau)^{-1}} \qquad (2\text{-}41)$$

where ω is the pulsation (ω=2πf where f is the frequency), E_{00} is the static modulus when ω→0, E_0 is the glassy modulus when ω→+∞, k and h are dimensionless constants of the two parabolic elements such as 0<k<h<1, δ is dimensionless constant, β is a dimensionless constant related to Newtonian viscosity η of the dashpot (η=(E_0-E_{00})βτ) and τ is a characteristic time depending on the temperature. For bituminous materials, the TTSP is valid and the WLF equation can be used to model the evolution of the characteristic time as a function of the temperature (see section 2.1.4). This adds two more constants C_1 and C_2 to describe the temperature susceptibility of the material. The 2S2P1D model can successfully fit the LVE behaviour of bituminous mixtures (Olard & Di Benedetto, 2003; Di Benedetto, Olard, Sauzéat, & Delaporte, 2004; Delaporte, Di Benedetto, Chaverot, & Gauthier, 2007) and more generally of bituminous materials (Di Benedetto, Olard, Sauzéat, & Delaporte, 2004). Figure 2.10 shows the influence of the 2S2P1D model constants on the Cole-Cole plot.

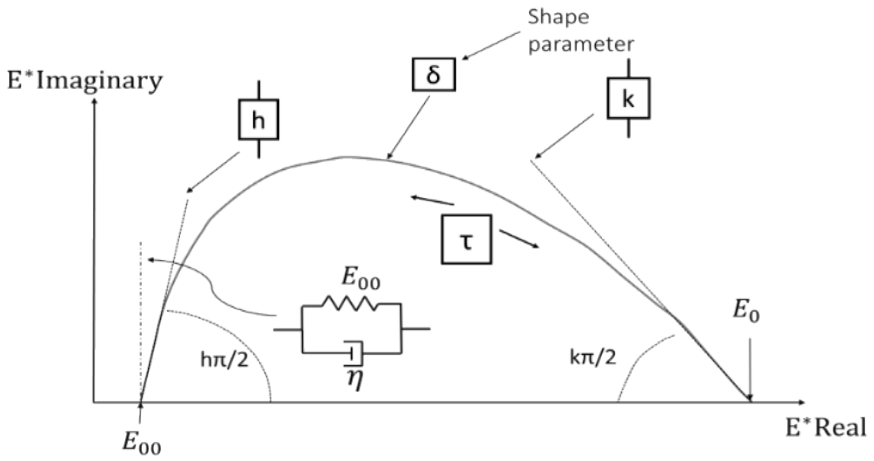

Figure 2.10. Influence of the 2S2P1D model constants on the Cole-Cole plot.

In the 3-dimensions case (Di Benedetto, Delaporte, & Sauzéat, 2007), the model also has an expression for the complex Poisson's ratio:

$$\nu^*(\omega) = \nu_{00} + \frac{\nu_0 - \nu_{00}}{1 + \delta(i\omega\tau_\nu)^{-k} + (i\omega\tau_\nu)^{-h} + (i\omega\beta\tau_\nu)^{-1}} \tag{2-42}$$

where ν_0 and ν_{00} are the glassy and static Poisson's ratios and τ_ν is the characteristic time of the Poisson's ratio directly linked to the characteristic time of the complex modulus ($\tau_\nu=\tau/\gamma$ where γ is a dimensionless constant). Therefore, a total of twelve constants (seven for the complex modulus, three for the complex Poisson's ratio and two for the WLF equation) are needed to fully characterize the isotropic LVE behaviour over the whole frequency and temperature domains.

2.4.2 Havriliak-Negami (HN) model

The Havriliak-Negami (HN) model is a rheological model initially used to describe the dielectric relaxation of polymers (Havriliak & Negami, 1966). The HN model was formulated to model both the complex modulus and complex Poisson's ratio (Gudmarsson A. , 2014; Gudmarsson, et al., 2014; Gudmarsson, Ryden, Di Benedetto, & Sauzéat, 2015):

$$E^*(\omega) = E_0 + \frac{E_{00} - E_0}{\left(1 + (i\omega\tau)^\alpha\right)^\beta} \tag{2-43}$$

$$\nu^*(\omega) = \nu_0 + \frac{\nu_{00} - \nu_0}{\left(1 + (i\omega\tau_\nu)^\alpha\right)^\beta} \tag{2-44}$$

where E_0, E_{00}, ν_0, ν_{00}, τ and τ_ν have the same signification than for the 2S2P1D model and α and β are dimensionless constants. The evolution of the characteristic times of the complex modulus and Poisson's ratio can also be described with the WLF equation. HN model is known to accurately model the LVE behaviour of polymers (Havriliak & Negami, 1967; Hartmann, Lee, & Lee, 1994; Madigosky, Lee, & Niemiec, 2006; Zhao, Liu, Bai, & Tan, 2013). A total of ten constants (five for the complex modulus, three for the complex Poisson's ratio and two for the WLF equation) are necessary to fully characterize the LVE behaviour on the whole frequency and temperature range. Figure 2.11 shows the influence of the HN model constants on the Cole-Cole plot.

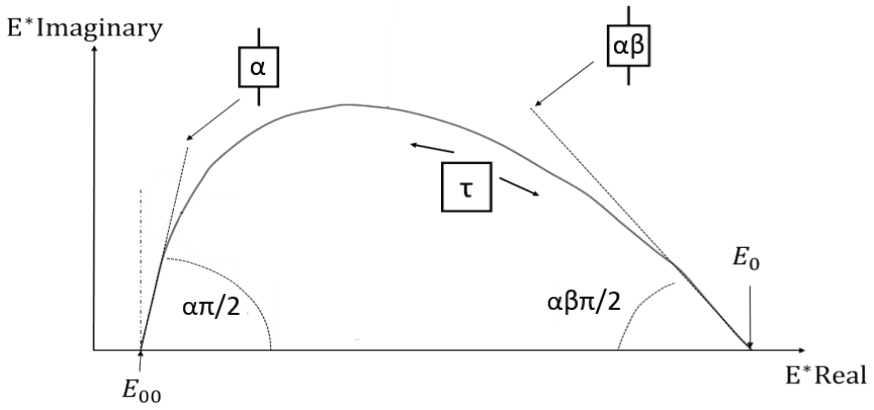

Figure 2.11. Influence of the HN model constants on the Cole-Cole plot.

2.4.3 Comparison of the two models

The two rheological models introduced in the previous sections present some differences. The number of constants needed to fully characterize the LVE behaviour is the first difference. The 2S2P1D model has two extra constants compared to the HN model. The consequences are that the 2S2P1D model, contrarily to the HN model, has one shape constant (δ) to adjust the shape of the loss modulus peak and one constant to account for the Newtonian viscosity (β). Figure 2.10 and Figure 2.11 show the asymptotic behaviours of the two models. It is seen that to obtain the same asymptotic behaviours with the 2S2P1D model and HN model, relations exist between the constants k and h of the 2S2P1D model and α and β of the HN model:

$$\begin{aligned} \alpha &= h \\ \alpha\beta = k \rightarrow \beta &= \frac{k}{h} \end{aligned} \tag{2-45}$$

Relations (2-45) must be verified or the two models will exhibit different asymptotic behaviours. In addition, the glassy and static complex modulus and complex Poisson's ratio should be the same for the two models since they are material mechanical properties. Therefore, all constants of the HN model at the exception of the characteristic time can be obtained from the constants of the 2S2P1D model. This highlights an important drawback of the HN model: once the constants are fixed to fit the low and high frequencies behaviours, it is not possible to adjust the loss modulus peak. Constants of the 2S2P1D model representing an average LVE material (Carret, Di Benedetto, & Sauzéat, 2018) were chosen to illustrate this difference. The static modulus was set to 100 MPa, the glassy modulus was set to 35 GPa, k was fixed at 0.17 and h at 0.55. Consequently, by applying relations (2-45), α must be equal to 0.55 and β to 0.31. The two models are compared in the Cole-Cole plot in Figure 2.12. It is seen that the different values used for constant δ can change significantly the shape of the curve of the 2S2P1D model while it is not possible to adjust the shape with the HN model. Note also that the best fit between the two models is obtained when δ is equal to 0.9 while δ is closer than 2 for most of the bituminous mixtures. This indicates that differences will appear between the two models: either the symptotic behaviours or the loss modulus peak will not match.

In addition, the same analysis was performed for constant β of the 2S2P1D model. The value of constant δ was fixed at 0.9, the values that gives the best fit in the Cole-Cole plot. The two models are compared in the Black space representation in Figure 2.13. It is seen that constant β of the 2S2P1D model has an influence on the shape of the curve of the 2S2P1D model. The influence is less important than the influence of constant δ and it mostly affects the high temperatures or low frequencies that correspond to the lower portion of the curve.

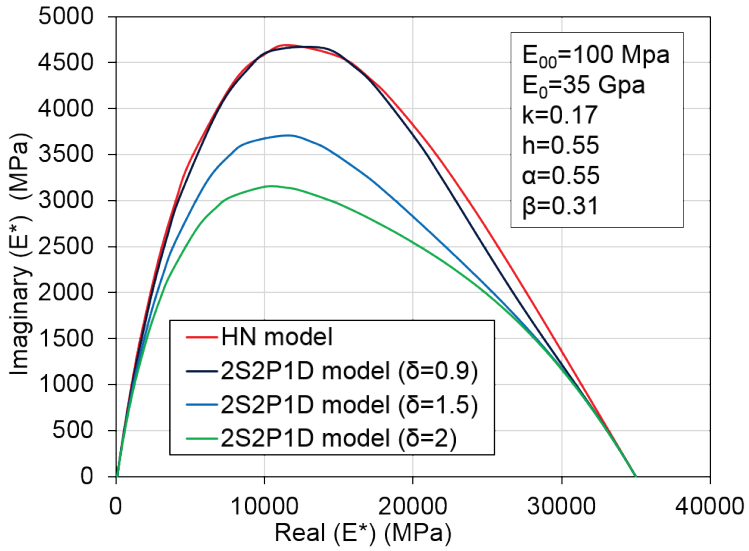

Figure 2.12. Comparison of the HN model and 2S2P1D model with different values of constant δ of the 2S2P1D model in the Cole-Cole representation.

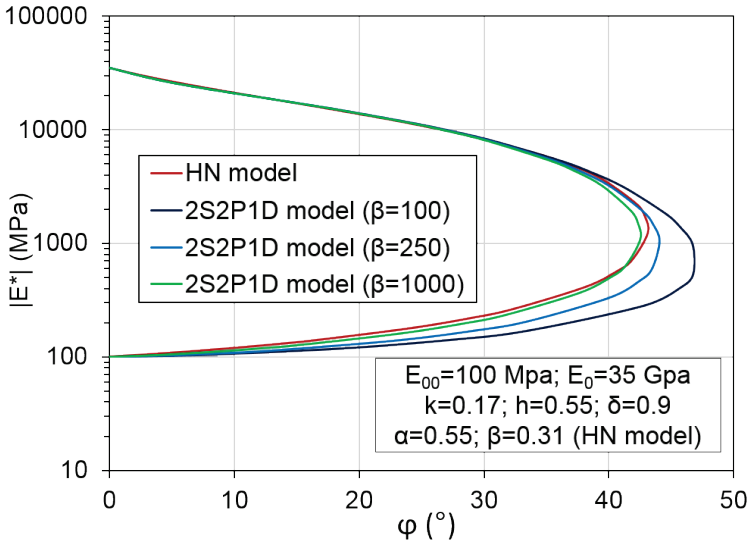

Figure 2.13. Comparison of the HN model and 2S2P1D model with different values of constant β of the 2S2P1D model in the Black space representation.

Differences between the HN and 2S2P1D models have been highlighted. It is clearly established that if the constants of the HN model are set to match the low and high frequencies behaviours of the 2S2P1D model, a mismatch will be observed between the two models unless the values of constants δ and β of the 2S2P1D model are adjusted adequately. Therefore, the 2S2P1D model offers more flexibility to model material behaviour because of its two extra constants. Moreover, given that the 2S2P1D model is specifically designed to model the LVE behaviour of bituminous mixtures, it is recommended to use this model instead of the HN model. In addition, the 2S2P1D model is also adapted for bitumen and mastics. A procedure to obtain the LVE properties of bituminous materials from the properties of the binder is also proposed. It includes the geometrical transformation SHStS (Di Benedetto, Olard, Sauzéat, & Delaporte, 2004; Pouget, Sauzéat, Di Benedetto, & Olard, 2010).

3 DEVELOPED DYNAMIC TEST

3.1 Presentation of the dynamic test

3.1.1 General considerations

The dynamic test developed in this thesis is dedicated to measure the frequency response functions (FRFs) of a bituminous mixture specimen with free boundary conditions. FRFs are very interesting because they give the possibility to identify not only the resonance frequencies but also the damping properties (linked to the amplitudes of the peaks) of a material. Therefore, analyzing FRFs measurements is a good possibility to derive material properties. FRFs measurements have been successfully used to characterize different LVE materials over a wide frequency range such as metal polymer sandwich beams (Ren, Atalla, & Ghinet, 2011) or highly damped acoustical porous materials (Guo, 2000; Renault, Jaouen, & Sgard, 2011; Rupitsch, Ilg, Sutor, Lerch, & Döllinger, 2011). FRFs measurements have also been performed on a limited variety of bituminous mixtures (Gudmarsson, Ryden, & Birgisson, 2012; Gudmarsson, et al., 2014; Gudmarsson, Ryden, Di Benedetto, & Sauzéat, 2015).

FRFs are frequency domain signals defined as the ratio between an output Y (displacement or acceleration for example) and an input X (force for example). To reduce noise when determining FRFs signals, the cross power spectrum S_{xy} and the input auto power spectrum S_{xx} are used in practice (Halvorsen & Brown, 1977) and FRFs are defined as:

$$H(f) = \frac{S_{xy}(f)}{S_{xx}(f)} \tag{3-1}$$

where H is the FRF, f is the frequency and the cross power spectrum S_{xy} and the input auto power spectrum S_{xx} are defined as follow:

$$S_{xy}(f) = X^{*}(f).Y(f) \tag{3-2}$$

$$S_{xx}(f) = X^{*}(f).X(f) \tag{3-3}$$

where X and X^{*} are the input in the frequency domain and its complex conjugate and Y is the output in the frequency domain. FRFs are complex numbers which contain both an amplitude and a phase but only the amplitude is necessary for material characterization. Consequently, the phase of the FRFs is not used in this thesis. A great advantage of using FRFs is that the amplitude of the FRFs is not depending on the input. Therefore, FRFs account only for the reaction of the material and can very easily be compared at different temperatures to highlight changes of material properties.

The coherence function is an indicator often associated to FRFs measurement that is used to evaluate the quality of the measurements (Halvorsen & Brown, 1977). More precisely, the coherence function evaluates the correlation between the input and output signals at each frequency. The coherence is a real function that ranges between zero and one. A value of one indicates that the output is fully explained by the input while decreasing values mean there is noise in the system that has disrupted the test. The coherence function is calculated as follow:

$$CF(f) = \frac{S_{xy}^2}{S_{xx}.S_{yy}} \tag{3-4}$$

where CF is the coherence function, S_{xy} and S_{xx} correspond to the cross power spectrum and input auto power spectrum defined in equations (3-2) and (3-3) and S_{yy} corresponds to the output auto power spectrum:

$$S_{yy}(f) = Y^*(f).Y(f) \tag{3-5}$$

where Y and Y^* are the output in the frequency domain and its complex conjugate.

3.1.2 Experimental devices and procedures

To achieve free boundary conditions during physical tests, the specimen is placed on soft foam. The excitation is generated with an automated impact hammer equipped with a load cell (PCB model 086E80) to record the impulse signal. The vibrations of the specimen are measured with a piezoelectric accelerometer (PCB model 353B15) screwed on a mounting base glued to the specimen. The technical specifications and the calibration certificates of the sensors will be found in APPENDIX A. Figure 3.1 shows the automated impact hammer with a scheme of principle and the accelerometer.

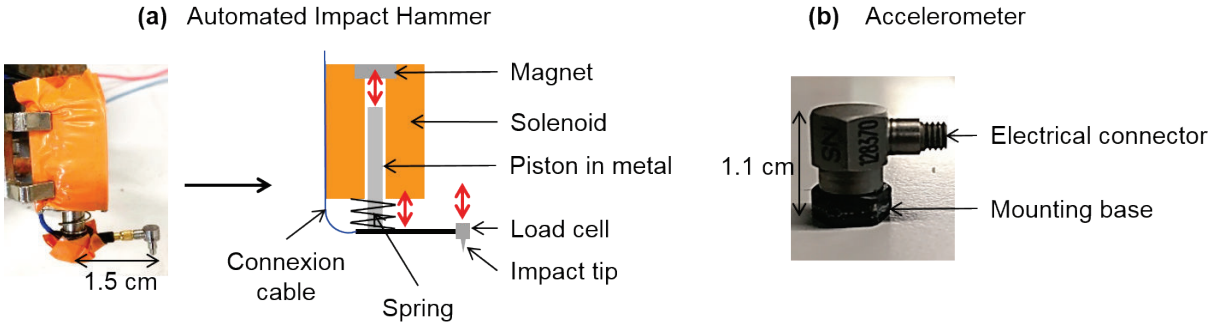

Figure 3.1 Sensors used for the dynamic tests: (a) automated impact hammer and scheme of principle; (b) accelerometer

Both the impact hammer and the accelerometer are connected to a signal conditioner (PCB model 482C15) that conditions the signals for analog to digital conversion. The technical specifications and the calibration certificate of the signal conditioner can be found in APPENDIX A. The signal conditioner is connected to a data acquisition device (NI model USB-6356) which converts the signals from analog signals to digital signals. The data acquisition device has a simultaneous sampling rate of 1.25 MHz which allows a sampling rate of 1 MHz on each channel (one data point acquired every 10^{-6} second). The length of the

recorded signals is chosen to record the entire vibratory response. Due to the damping properties that changes with temperature, the record length varies with the test temperature, which is measured with a PT 100 surface probe. The data acquisition device is connected to a computer through a USB cable and the data acquisition is managed by a Matlab application specially developed for this test. Figure 2.1 illustrates the test set-up for the measurements of the longitudinal mode of vibrations of a cylinder. Note that three different modes of vibration (longitudinal, flexural and torsional) were considered depending on the geometry and on the positions of the impact and of the accelerometer. An example for each mode of vibrations is shown in Figure 3.3.

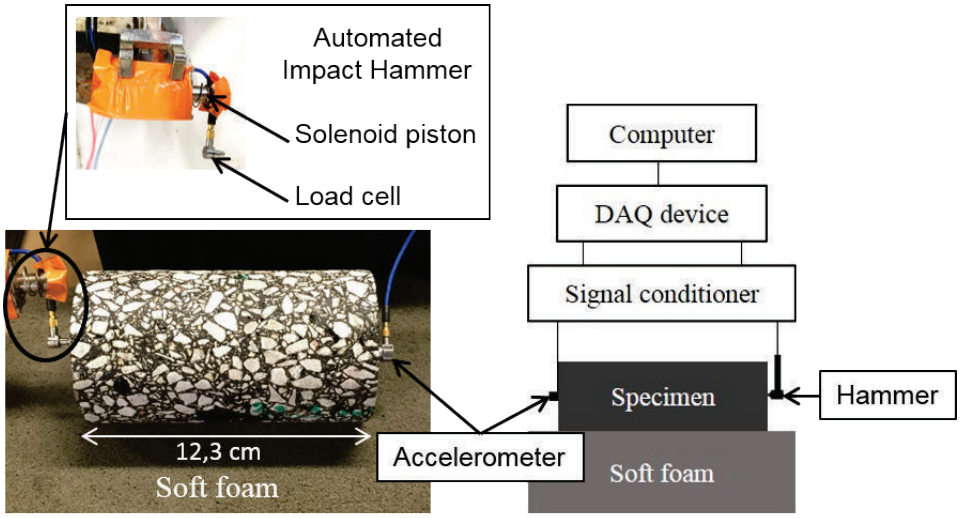

Figure 3.2. Dynamic test set-up for the measurements of the FRFs of the longitudinal mode of vibrations (ENTPE laboratory).

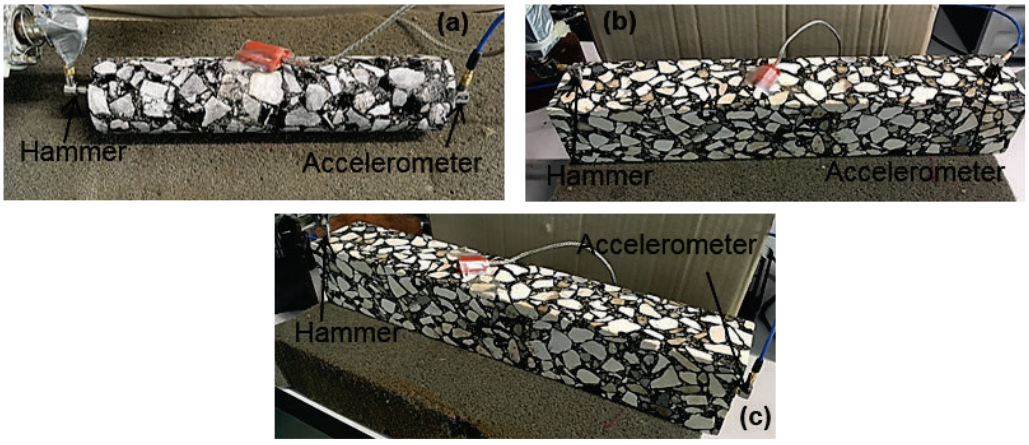

Figure 3.3. Example of dynamic test set-up for three different modes of vibrations: (a) longitudinal mode of a cylinder; (b) flexural mode of a straight beam; (c) torsional mode of a straight beam

The signals measured are in time domain. They must be transformed into frequency domain signals to calculate the FRFs. The fast Fourier transform (FFT) is used for that purpose and signals have a 1 Hz resolution in the frequency domain. In addition, it is common practice to perform different measurements of the FRFs to ensure a reliable estimation. Therefore, FRFs

are averaged from the signals recorded on five repetitions of the test that correspond to five impact with the automated impact hammer. Equations (3-1) and (3-4) are transformed to:

$$H(f) = \frac{\overline{S_{xy}(f)}}{\overline{S_{xx}(f)}} \tag{3-6}$$

$$CF(f) = \frac{\overline{S_{xy}^2}}{\overline{S_{xx}}.\overline{S_{yy}}} \tag{3-7}$$

where the bar above the cross-power spectrum S_{xy}, the input auto power spectrum S_{xx} and the output auto power spectrum S_{yy} corresponds to the arithmetic average on the five impacts.

The test and procedures described above are derived from the work of Gudmarsson (Gudmarsson A. , 2014). However, two important improvements have been developed in this thesis and must be highlighted. The first improvement is a doubled sampling rate for the data acquisition. This is possible because the data acquisition device used has a higher maximum sampling rate. It guarantees a finer description of the recorded signals in time domain and therefore a better accuracy of the measurements. The second improvement is the development of an automated impact hammer (Figure 3.1 (a)) inspired from existing impact devices (Norman, Jung, Ratcliffe, Crane, & Davis, 2012; Brüggemann, Biermann, & Zabel, 2015). The developed automated impact hammer is suitable for many different geometries (cylinders, discs, beams, etc.) as shown in Figure 3.3. The device is connected to a microcontroller (Arduino Uno R3) and can be programmed with the Arduino interface. Details about the electronic circuit of the automated impact hammer and the Arduino microcontroller are given in APPENDIX A

The use of an automated impact system improves significantly the quality of the impacts and their repeatability (see Figure 3.5 and Figure 3.6). It is quite interesting because the duration and the position of the impacts are two essential parameters to determine the usable frequency range. Indeed, an impact excitation provides energy to the specimen over a certain frequency range that is directly dependent on the contact time between the hammer and the specimen. The contact time should be as short as possible to obtain a wider usable frequency range. For example, hitting the binder instead of a stone result in a longer contact time and a reduced usable frequency range. A good programming of the automated impact hammer coupled to a careful positioning guarantees to obtain the widest possible usable frequency range. Another great advantage of using an automated device is the possibility to use it inside a thermal chamber without opening the door. Since bituminous mixtures are highly thermosensitive materials, it is essential to perform FRFs measurements at different temperatures. Without having an automated impact hammer, an operator must open the thermal chamber to perform the measurements at each temperature. This complicates the test procedure and may introduce experimental errors. By synchronizing the programming of the automated impact hammer and the thermal chamber, it is possible to run measurements at all desired temperatures faster and with more accuracy without any intervention from an operator. The improvements of the methodology to measure FRFs are therefore very useful for practical experimentation and to come up with a standardization of the test in the future.

3.1.3 Example of dynamic test results

All the results presented in this section correspond to measurements performed on the same cylinder of material GB5 (see section 5.3). An example of the signals in time domain and in frequency domain corresponding to five impact is given in Figure 3.4. The FFT being a complex number, only the amplitude of the signals is presented for the frequency domain.

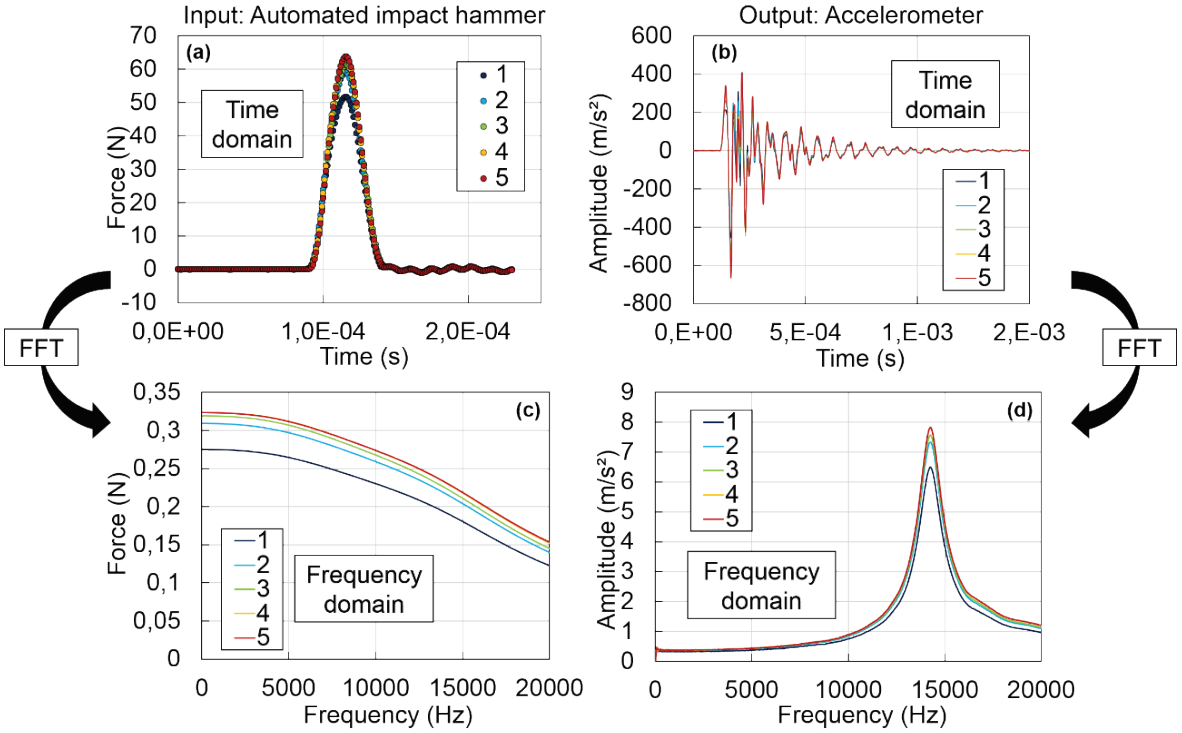

Figure 3.4. Example of signals recorded during a dynamic test for five impacts: (a) force in time domain; (b) acceleration in time domain; (c) amplitude of the force in frequency domain; (d) amplitude of the acceleration in frequency domain.

Figure 3.4 (c) shows that the level of force decreases with frequency. When the value of force is close to zero, the signals are not useable. In practice, frequency range from 0 up to 30 kHz at most can be used depending on the quality of the impacts. The FRFs corresponding to the five individual impacts displayed in Figure 3.4 and the corresponding averaged FRF are given in Figure 3.5 (a). It is seen in Figure 3.5 (a) that the curves corresponding to the six FRFs are almost perfectly overlaid. This proves the excellent repeatability of the test from one impact to another due to the use of an automated impact hammer. The averaged FRFs obtained at five different temperatures for the same specimen are plotted in Figure 3.5 (b). It shows the influence of temperature on the FRFs. The resonance frequencies and amplitudes decrease with temperature, which corresponds to material properties changes: the norm of the complex modulus decreases and the phase angle increases. The coherence functions corresponding to the five individual impacts displayed in Figure 3.4 and the corresponding averaged coherence function are plotted in Figure 3.6 (a). The same observation than for the FRFs is made on Figure 3.6 (a) for the coherence function. This confirms the good quality of the measurements. The averaged coherence functions obtained at five different temperatures for the same specimen are displayed in Figure 3.6 (b). A zone of interferences is observed for frequencies lower than approximately 3 000 Hz. Therefore, it is recommended to not use frequencies below 3 000 Hz

for which there is some noise in the system. For higher frequencies, value of the coherence function is very close to one for all temperatures.

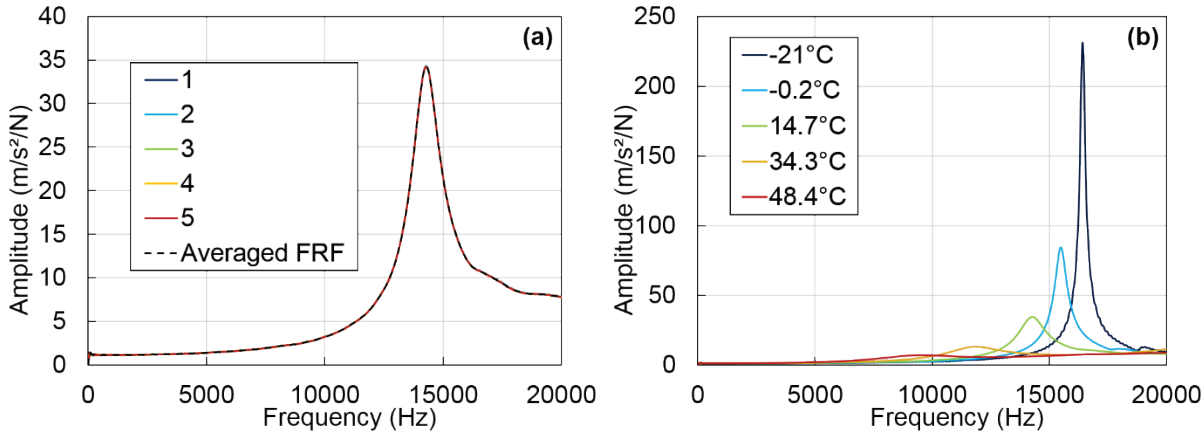

Figure 3.5. (a) Example of FRFs for five individual impacts and the corresponding averaged FRF. (b) Example of FRFs at five different temperatures for the same specimen.

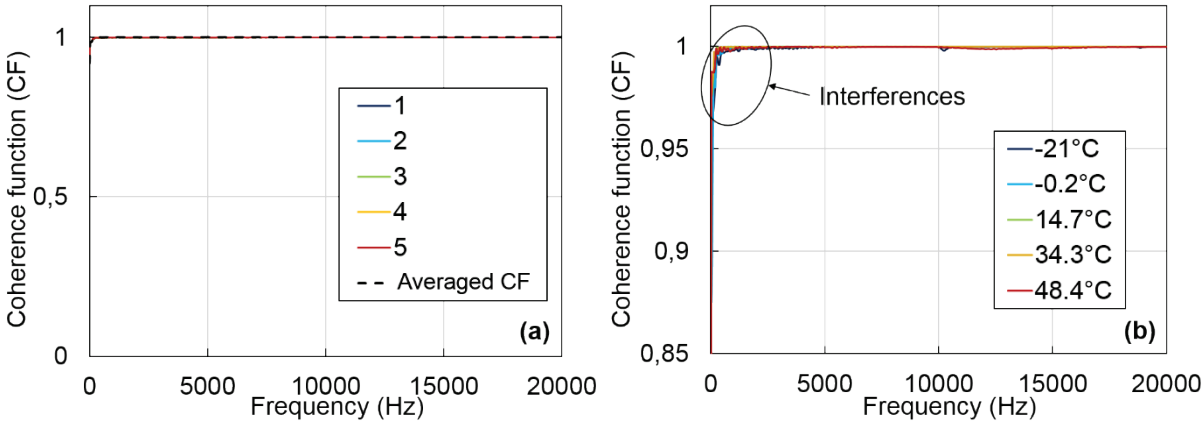

Figure 3.6. (a) Example of coherence functions for five individual impacts and the corresponding averaged coherence function. (b) (b) Example of coherence functions at five different temperatures for the same specimen.

3.2 Differences with cyclic tension-compression tests

The resonance frequencies obtained from FRFs measurements are approximately between 5 kHz and 30 kHz depending on the geometry and density of the specimen and also the testing temperature. FRFs can be measured from approximately -20°C to 50°C depending on the damping properties of the material. Therefore, FRFs measurements are only high frequency measurements and cannot give access to the entire master curves of LVE materials. Traditional complex modulus cyclic tension-compression tests are performed at much smaller frequencies (from 0.003 Hz to 10 Hz) and in a similar temperature range (from -25°C to 55°C). Cyclic tension-compression tests cover a larger portion of the master curves but are limited to lower frequencies than the dynamic tests. This difference should be considered when comparing the LVE properties of bituminous mixtures determined with the two tests. The two tests are expected to match best on the frequency range that contains experimental results for both tests. Figure 3.7 shows the frequency range accessible in function of the reference temperature for the cyclic tension-compression tests and the dynamic tests. Figure 3.7 confirms the previous

comments. Figure 3.7 was obtained by creating master curves with experimental data from tension-compression tests and then from dynamic tests at different reference temperatures. The same constants of the WLF equation at the reference temperature of 15°C were considered for both tests (C_1=30 and C_2=210). At each reference temperature, the minimum and the maximum reduced frequencies of the experimental data were saved for both tests. The frequency ranges obtained for the GB5 cylinder considered in section 3.1.3 are reported at the corresponding reference temperature in Figure 3.7. Note that Figure 3.7 only gives an order of magnitude of the frequency ranges and variations may exist from one material to another. Note also that the value of the modulus at 15°C and 10 Hz, which is used for pavement design in the French standards is accessible with both tests.

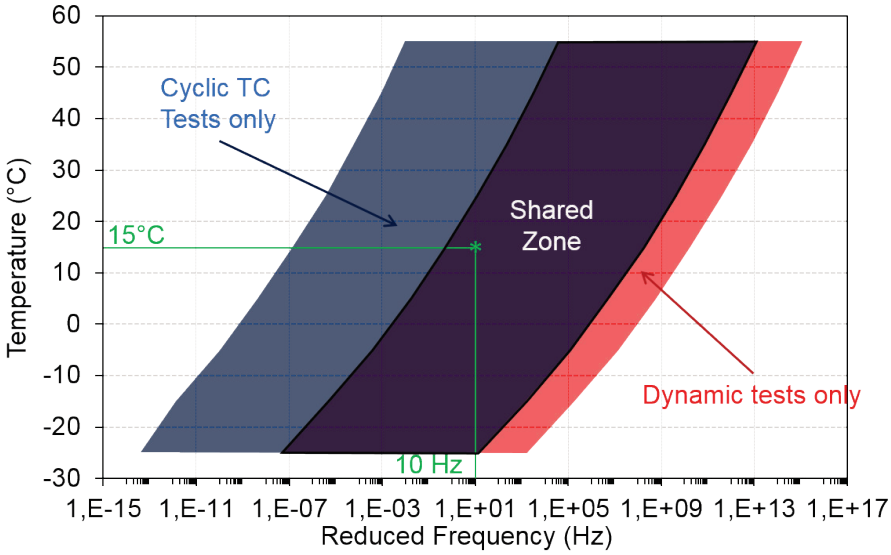

Figure 3.7. Frequency range containing experimental data in function of the reference temperature for the cyclic tension-compression tests and for the dynamic tests. Example for a GB5 cylinder. The frequency ranges may vary from one material to another.

Another important difference between the two tests is the level of strain applied to the material. Cyclic-tension compression tests are performed with a strain of about 50 µm/m. The maximum level of strain for a dynamic test can be approximated from the first resonance frequency and the corresponding amplitude of the acceleration using equation (2-40).The maximum strain level estimated for seven specimens of bituminous mixtures tested in this work (see sections 5.1, 5.3 and 5.4) are presented in Figure 3.8. The maximum strain level is between 0.01 µm/m and 0.25 µm/m with most of the values being less than 0.1 µm/m. Also, the maximum strain level increases with the frequency. This indicates that the strain level of the dynamic tests varies with temperature, and the lower strain levels corresponds to the highest temperatures. Therefore, strains occurring during dynamic tests are approximately a thousand times lower than the level of strain applied in the cyclic tension-compression tests. The properties of bituminous mixtures being dependent of the magnitude of the applied strain (Nguyen, Di Benedetto, & Sauzéat, 2015; Airey & Rahimzadeh, 2004; Mangiafico, Babadopoulos, Sauzéat, & Di Benedetto, 2018), non-linearity's effects should be accounted for when comparing material properties estimated from FRF measurements and from cyclic tension-compression tests.

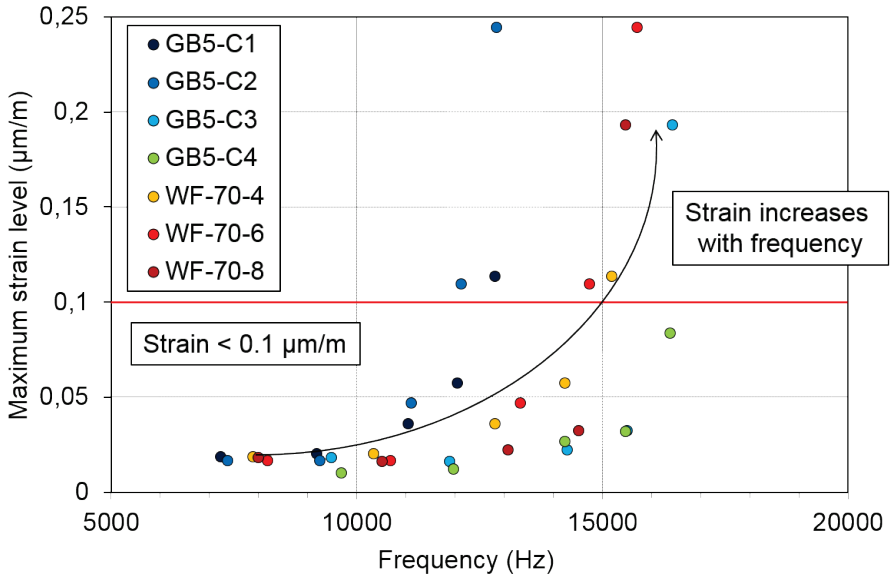

Figure 3.8. Maximum strain level for the dynamic tests estimated at the first resonance frequency of the longitudinal mode of vibrations for seven specimens (see sections 5.1, 5.3 and 5.4).

3.3 Experimental verifications

3.3.1 Repeatability of the test

FRFs are determined from the average of five individual impacts. This should guarantee the repeatability and the reliability of the test. To verify these assumptions, dynamic measurements of the longitudinal mode of vibration have been repeated three times on the same GB5 specimen than in the previous sections. The repeated measurements were performed at five temperatures (-20°C, 0°C, 15°C, 35°C, 50°C) without opening the door of the thermal chamber and without any modification of the experimental set-up. The first and second resonance frequencies and amplitudes are given in Table 3.1. The average values for the three tests, the standard deviation (SD) and the relative standard deviation (RSD) are also listed in Table 3.1. The values of the RSD of the resonance frequencies are excellent with less than 1% at most and values really close to 0. The values of the RSD of the amplitudes are also very satisfying with a maximum of 3.9%. Figure 3.9 presents the evolution of the values of the RSD with temperature. It can be seen that the RSD of the amplitudes is a little bit higher than the RSD of the resonance frequencies. This indicates that the measurement of the amplitude is a little bit more sensitive than the measurement of the resonance frequencies. This repeatability study demonstrates the excellent overall repeatability of the dynamic tests.

Table 3.1. Results obtained for the three dynamic tests performed on the same GB5 specimen at five different temperatures (longitudinal mode of vibration). Measurements were repeated without any modification of the experimental set-up.

T (°C)	Test nr.	1	2	3	Average	SD	RSD (%)
-20°C	**1st frequency (Hz)**	13 188	13 208	13 214	13 203	13.6	**0.1**
	1st amplitude (m/s²/N)	179.6	173.2	180.3	177.7	3.9	**2.2**
	2nd frequency (Hz)	25 454	25 470	25 488	25 471	17.0	**0.1**
	2nd amplitude (m/s²/N)	261.0	241.4	251.0	251.1	9.8	**3.9**
0°C	**1st frequency (Hz)**	12 429	12 474	12 473	12 459	25.7	**0.2**
	1st amplitude (m/s²/N)	64.9	66.3	64.2	65.1	1.1	**1.6**
	2nd frequency (Hz)	24 088	24 137	24 145	24 123	30.9	**0.1**
	2nd amplitude (m/s²/N)	86.8	87.3	87.3	87.1	0.3	**0.3**
15°C	**1st frequency (Hz)**	11 477	11 514	11 500	11 497	18.7	**0.2**
	1st amplitude (m/s²/N)	27.7	28.2	27.3	27.7	0.5	**1.6**
	2nd frequency (Hz)	22 391	22 447	22 410	22 410	28.5	**0.1**
	2nd amplitude (m/s²/N)	36.9	36.4	36.7	36.7	0.3	**0.7**
35°C	**1st frequency (Hz)**	9 593	9 551	9 541	9 562	27.6	**0.3**
	1st amplitude (m/s²/N)	10.8	10.6	10.5	10.6	0.2	**1.4**
	2nd frequency (Hz)	18 905	18 714	18 776	18 798	97.4	**0.5**
	2nd amplitude (m/s²/N)	14.0	13.0	13.8	13.6	0.5	**3.9**
50°C	**1st frequency (Hz)**	7 623	7 654	7 575	7 617	39.8	**0.5**
	1st amplitude (m/s²/N)	5.3	5.4	5.4	5.4	0.1	**1.1**
	2nd frequency (Hz)	15 174	15 207	15 429	15 270	138.7	**0.9**
	2nd amplitude (m/s²/N)	6.0	6.2	6.3	6.2	0.2	**2.4**

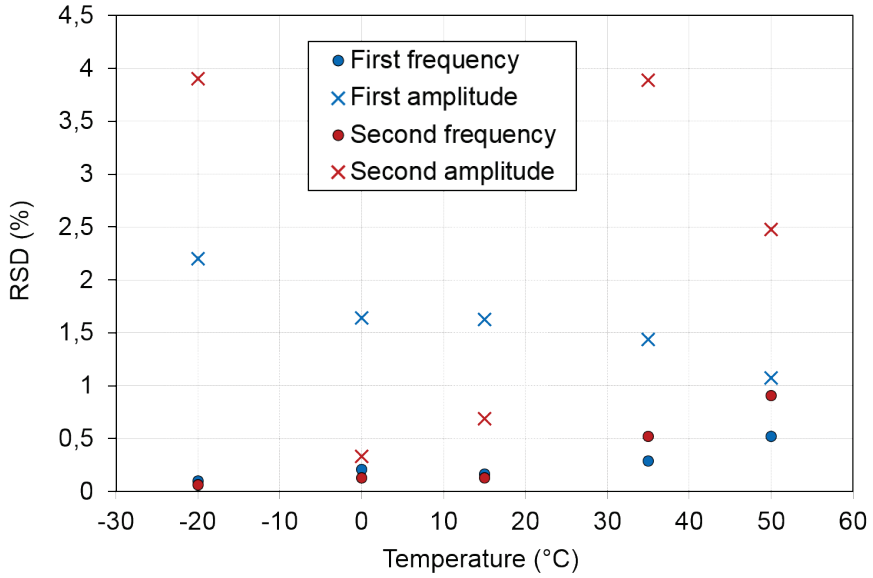

Figure 3.9. Relative standard deviation for the three dynamic tests performed on the same specimen at five different temperatures (longitudinal mode of vibrations).

3.3.2 Sensitivity of the sensors

A cylindrical sample of duralumin has been used to investigate the sensitivity of the sensors. This material was chosen because its behaviour is not dependent on the frequency and is very little sensitive to temperature changes. Indeed, the Young's modulus of duralumin is about 70 GPa at 0°C and it decreases linearly of approximately 0.04 GPa (≈0.06 %) per degree (Young's Modulus of Elasticity for Metals and Alloys, 2004). FRFs corresponding to the longitudinal mode of vibrations of the duralumin specimen have been measured at fifteen different temperatures from -20°C to 50°C in steps of 5°C. This temperature range corresponds to the range on which FRFs can be measured on bituminous mixtures and therefore to the range of use of the sensors in this thesis. The Young's modulus of duralumin was evaluated using the first resonance frequency according to the ASTM C215-02 standard (ASTM-C215-02, 2002). The evolution of the evaluated Young's modulus in function of temperature is plotted in Figure 3.10 along with the curve found in literature (Young's Modulus of Elasticity for Metals and Alloys, 2004). A very nice agreement is seen between the curves plotted in Figure 3.10. In addition, the value of the Young's modulus is 70.7 GPa at 0°C which is also in very good agreement with values found in literature. The Young's modulus decreases linearly (correlation coefficient R^2=0.9997) from 71.4 GPa at -20°C to 68.8 GPa at 50°C. This corresponds to a loss of 0.036 GPa per degree, in the same order of magnitude than the thermal sensitivity of duralumin. Therefore, the Young's modulus variation is mainly due to the material and the thermal sensitivity of the sensors is negligible for the evaluation of the resonance frequencies.

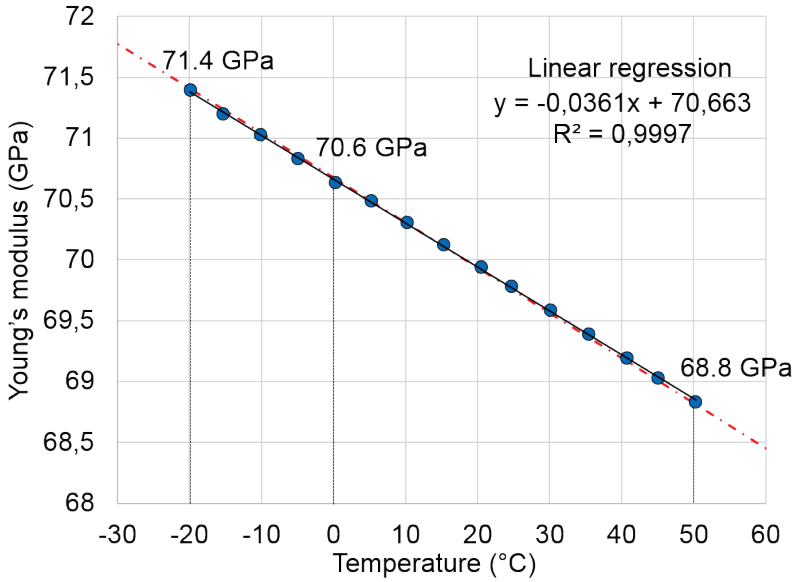

Figure 3.10. Young's modulus of duralumin specimen evaluated from dynamic tests. The red dotted line represents the decreasing of the Young's modulus of duralumin with temperature found in literature (Young's Modulus of Elasticity for Metals and Alloys, 2004).

The amplitude measured at the first resonance frequency was also studied. The amplitude is linked to the damping properties and it is possible to determine the damping ratio ζ at the first resonance frequency with the half-power bandwidth method (Bachmann, 1991):

$$\xi = \frac{\Delta f}{2f} \tag{3-8}$$

where f is the first resonance frequency and Δf is the width of the FRFs at 0.707 of the amplitude at the first resonance. The damping ratio is then used to determine the phase angle ϕ of the material according to the following relationship (Clough & Penzien, 1993):

$$\varphi = \arctan(2\xi) \tag{3-9}$$

The phase angles calculated for the duralumin specimen are displayed in Figure 3.11. It can be seen that the values of the phase angle are extremely low with a maximum of 0.027°. This was expected because duralumin is considered as a purely elastic material. Also, variations of the phase angle do not follow a clear trend and the difference between the maximum and the minimum values of the phase angle is less than 0.01°, which proves the very good repeatability of the measurements. However, the amplitudes measured for the duralumin specimen are at least ten times higher than the amplitudes measured for bituminous mixtures. Therefore, it is not possible to conclude about the sensitivity of the sensors regarding the measured amplitudes. According to the calibration certificates provided with the sensors (cf. APPENDIX A), the sensors are not impacted by temperature or frequency on the range used in this work.

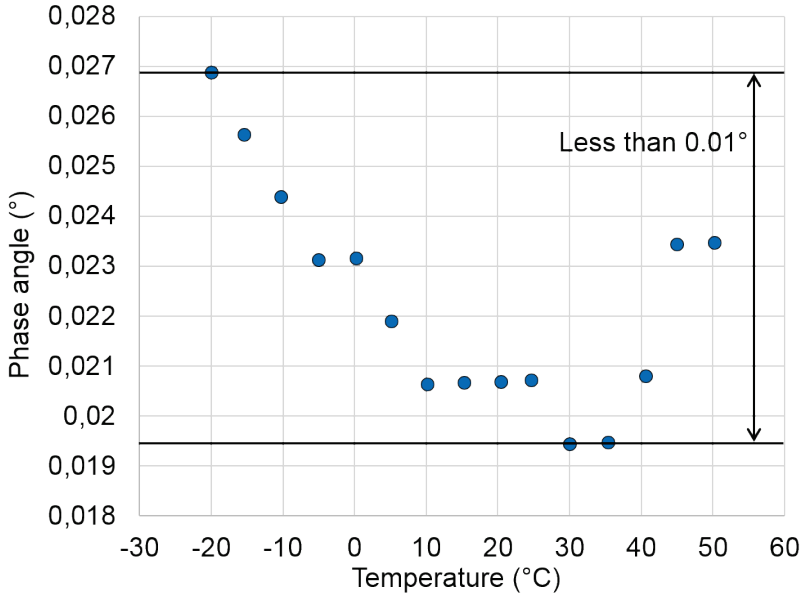

Figure 3.11. Phase angle of duralumin specimen evaluated from dynamic tests.

3.3.3 Effect of the frequency resolution on the fast Fourier transformation (FFT)

FRFs are calculated from the frequency domain signals of the impact hammer and accelerometer. FFT is used to transform these signals recorded in time domain to frequency domain with a frequency resolution chosen equal to 1 Hz. Care must be taken during this operation because in general, to return a correct FFT amplitude, FFT has to be normalized by the number of input time samples. In the Fourier theory, the frequency resolution is directly linked to the number of time samples acquired and the sampling frequency:

$$\Delta f = \frac{F_s}{N} \tag{3-10}$$

where Δf is the frequency resolution of the FFT, F_s is the sampling frequency and N is the number of samples acquired. The number of samples is defined by the length of the oscillatory

part of the accelerometer signal to observe the vibrations of the material on the right window of time. The number of samples must be the same for the impact hammer or the amplitude of the FRF cannot be estimated correctly. Equation (3-10) indicates that it is necessary to record a number of samples equal to the sampling frequency to obtain a frequency resolution of 1 Hz. The used sampling frequency is 1 MHz so a million of samples are needed to have a frequency resolution of 1 Hz. Figure 3.4 (b) and Figure 3.12 show examples of time domain signals from the accelerometer. Oscillations only last a few milliseconds. Therefore, the number of samples recorded limit the frequency resolution between 1 500 Hz and 150 Hz at best depending on the temperature.

Fortunately, it is possible to increase the frequency resolution. Since the signals recorded are transient non-periodic signals, it is possible to extend them numerically. This process consists in adding virtual samples equal to zero at the end of the signals. To reach a frequency resolution of 1 Hz, virtual samples must be added so that the total number of samples is one million to equal the sampling frequency. Figure 3.12 shows an example of time signals measured and the corresponding extended signals. Logarithmic scale has been used for clarity.

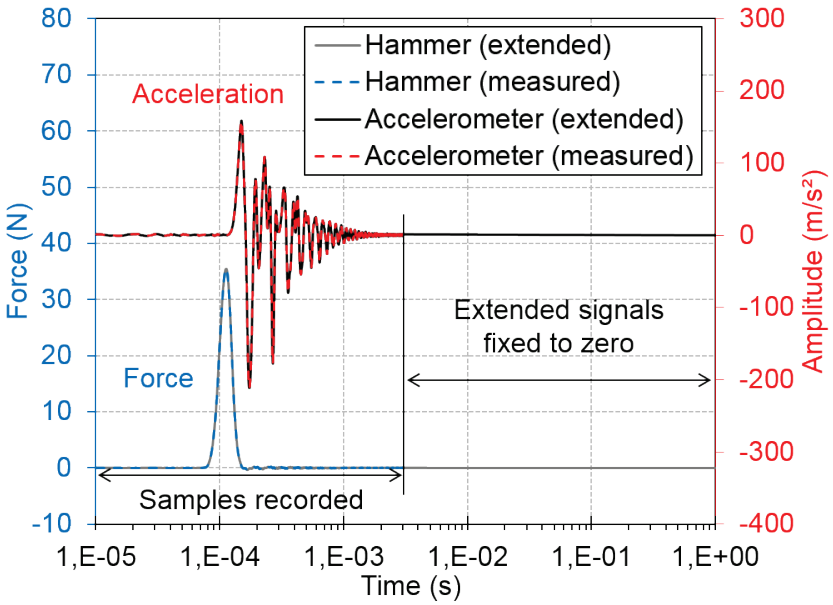

Figure 3.12. Example of measured and extended signals of the impact hammer and accelerometer in time domain.

Using a larger number of samples is very useful to improve the frequency resolution. However, in this case, the amplitude of the FFT must be normalized by the number of samples recorded in the oscillatory part of the accelerometer signal and not by the total number of samples in the extended signals. In the contrary case, amplitudes of the FFT of the impact hammer and accelerometer are not estimated correctly. The FRF is not sensitive to this effect because it is defined as the ratio between the cross power and auto power spectrum (equation (3-1)). The amplitudes of the FFT of the impact hammer and accelerometer calculated from the extended signal and the corresponding FRF are plotted in Figure 3.13. The same curves are also plotted for the measured time signals. Figure 3.13 confirms that the proposed methodology does not affect the amplitude of the FFT and of the FRF and that the frequency resolution is increased for the extended signals.

Finally, according to the Nyquist sampling theorem (Nyquist, 1928), the highest frequency that a time signal can represent is half of the sampling frequency. With a sampling frequency of 1 MHz, it is possible to reach frequency up to 500 000 Hz. FRFs are calculated for frequencies up to 30 kHz at most in this work which is largely below 500 000 Hz.

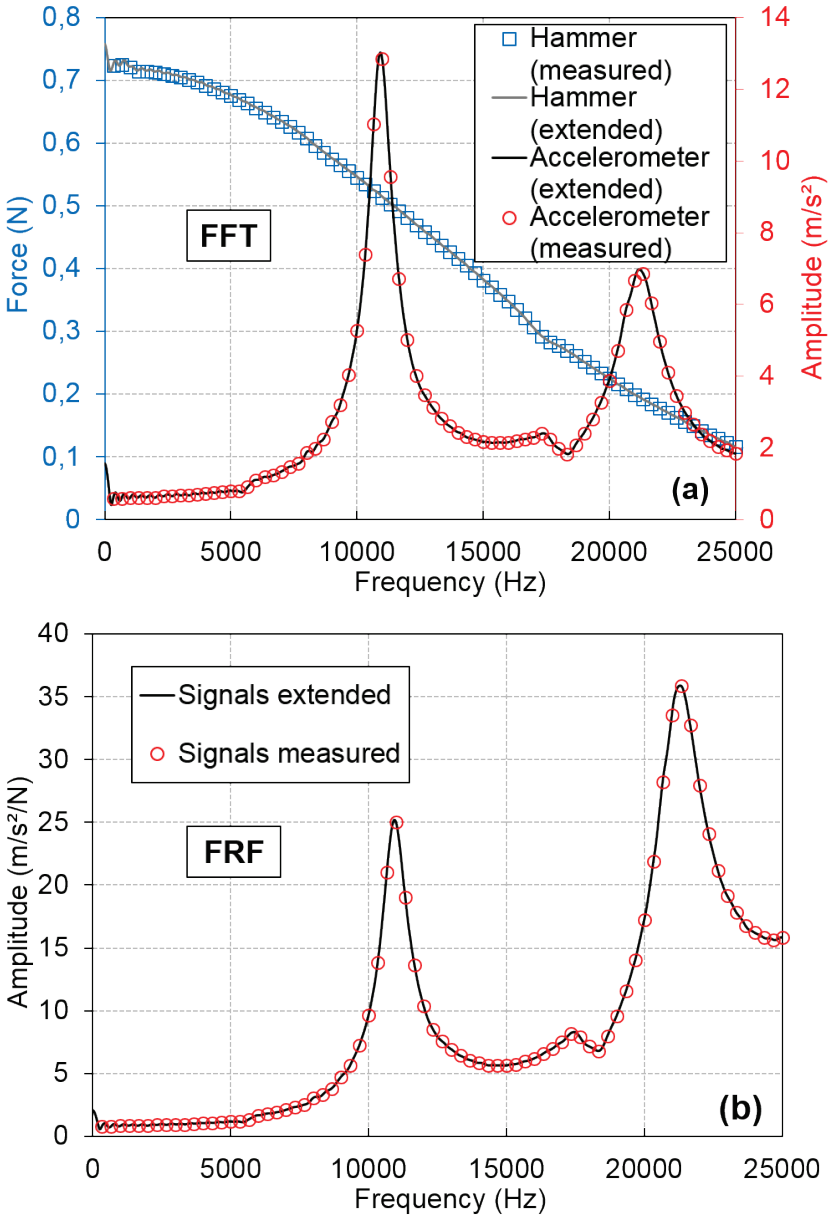

Figure 3.13. FFT (a) and FRF (b) calculated from the measured and extended signals of the impact hammer and accelerometer.

4 NUMERICAL SIMULATIONS OF THE DYNAMIC TESTS ON REFERENCE ISOTROPIC LVE BITUMINOUS MIXTURE

Characterizing the LVE properties of bituminous mixtures from dynamic tests is a complicated process. It requires to use an inverse analysis method to determine the LVE properties from the FRFs measurements. The developments made during this thesis bring us to propose different inverse analysis methods, all based on finite element method (FEM) (section 4.3). Therefore, as a first step, it was necessary to develop numerical calculation tools to perform the FEM calculations (section 4.1.1). Then, a numerical model corresponding to a reference isotropic LVE bituminous mixtures with averaged LVE properties was built up (section 4.1.2). The reference LVE material was developed to test and evaluate the accuracy of the different inverse analysis methods (section 4.3). This procedure based on numerical experimentation eliminates any potential divergence due to experimental measurement errors or to material behaviour that is not perfectly isotropic and LVE in practice. This step is essential to validate or not the proposed inverse analysis scenario. In addition, reducing the number of LVE properties or model constants to be identified in the inverse analysis process is needed to limit the computational time and the risk of finding non valid local solutions. For this purpose, a parametric analysis was performed to evaluate the influence of the LVE properties on the FRFs (section 4.2). The results of the parametric analysis were used to fit the different inverse analysis methods.

4.1 Numerical calculation tools

4.1.1 Finite element method (FEM) calculation

A FEM model was developed with the COMSOL software. The first step when building a FEM model is to define the geometry. Three geometries were studied: cylinders (C), straight beams (B) and discs (D). The dimensions considered for each geometry correspond to the dimensions of bituminous mixtures specimen commonly used for laboratory testing: the cylinder used in the parametric analysis has a 15cm length and a 7.5cm diameter, the cylinder used in the inverse analysis has a 16cm length and a 6.5cm diameter, the straight beam has a 30cm length and a 5cm width and height and the disc has a 3cm height and a 10cm diameter. In a second step, the mesh is created. It consists in tetrahedral elements with a maximum element size of 2cm that was determined through mesh size convergence studies for each geometry.

Different material behaviours corresponding to different modulus and Poisson's ratio were used:

- Isotropic linear elastic behaviour (used in inverse analysis method I in section 4.3.1.1)
- LVE behaviour with a constant complex modulus value and a constant real Poisson's ratio value (used in inverse analysis method IV in section 4.3.1.4)
- LVE behaviour with constant complex modulus and complex Poisson's ratio values (used in the first parametric analysis in section 4.2.1)
- LVE behaviour with a complex modulus frequency and temperature dependent modelled with the 2S2P1D model (cf. equations (2-41)) and a constant real value of the Poisson's ratio (used in inverse analysis method V in section 4.3.2)
- LVE behaviour with a complex modulus and a complex Poisson's ratio frequency and temperature dependents modelled with the 3-dim version of the 2S2P1D (cf. equations (2-41) and (2-42)) (used in the second parametric analysis in section 4.2.2 and in all inverse methods except the first one).

After the material behaviour, the boundary conditions are entered. They were set to be in accordance with physical experimentations in which the material placed on soft foam is excited with an impact hammer and the resulting acceleration is recorded with an accelerometer. Therefore, free boundary conditions are assumed everywhere except at the position corresponding to the impact where a cyclic load $e^{i\omega t}$ is applied in the direction of the impact. The last step before launching the calculation is to define the parameters of the frequency study. The frequencies for which the calculation is performed were chosen to match the frequency range accessible with physical tests: from 100 Hz to 30 kHz. The frequency resolution was set to 20 Hz to limit the computational time but it can be adjusted if needed. Finally, for the LVE behaviour temperature dependents, the temperature range accessible in physical tests, between -20°C and 50°C, was considered.

Once the geometry, the mesh, the material behaviour, the boundary conditions and the parameters of the study are introduced, the following three-dimensional equation of motion is solved for each specified frequency:

$$-\rho\omega^2 u - \nabla.\sigma = 0 \tag{4-1}$$

where ρ is the bulk density of the material, ω is the angular frequency, u is the displacement vector, ∇ is the gradient tensor operator and σ is the Cauchy stress tensor. This equation corresponds to the wave equation applicable for elastic material (2-22) or LVE material(2-30). The results of the calculation are processed to obtain the amplitude of the acceleration at the position and in the direction of vibration of the accelerometer during physical test. Since the cyclic load applied in the model is unitary, this value directly corresponds to the value of the FRF. Note that depending on the geometry and on the positions of the impact and of the accelerometer, different modes of vibration can be obtained. In the next sections, the longitudinal (L), flexural (F) and torsional (T) modes of vibration are studied. A total of seven different configurations are considered for the parametric analysis(section 4.2) and the inverse analysis (section 4.3). Table 4.1 lists the configurations used in each case. Table 4.2 gives the

position of the sensors, the direction of the impact and the direction of vibration of the accelerometer for the different combinations considered. The longitudinal mode for cylinders is particularly interesting because it is the only axisymmetric configuration. Therefore, two-dimensions calculations are possible instead of three-dimensions calculations for all the other configurations. This is a great advantage that makes calculations approximately ten times faster.

Table 4.1. Configurations studied in the parametric analysis (section 4.2) and inverse analysis (section 4.3). C, B and D correspond to the geometry (cylinders, straight beams or discs) and L, F and T correspond to the mode of vibration (longitudinal, flexural or torsional).

Configuration	C-L	C-F	C-T	C-L+F	B-L	B-T	D-F
Direct analysis (section 4.2)	x	-	-	-	-	x	x
Inverse analysis: method 1 for the complex modulus (section 4.3.1.1)	x	x	x	-	-	-	-
Inverse analysis: method 2 for the complex modulus (section 4.3.1.2)	x	-	-	x	x	-	x
Inverse analysis: method 3 for the complex modulus (section 4.3.1.3)	x	-	-	x	x	-	x
Inverse analysis: method 4 for the complex modulus (section 4.3.1.4)	x	-	-	x	x	-	x
Inverse analysis: method 5 for the complex modulus and complex Poisson's ratio (section 4.3.2)	x	-	-	-	x	-	-

Table 4.2. Position of the sensors, direction of the impact and direction of vibration of the accelerometer for the different considered combinations of geometry and mode of vibration.

	Cylinders (C)	Straight beams (B)	Discs (D)
Longitudinal mode of vibration (L)	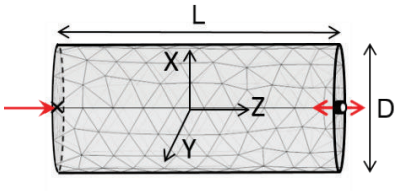	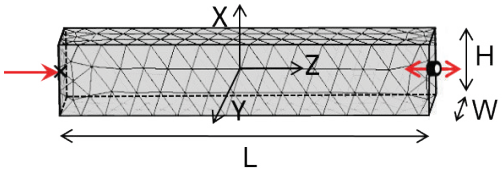	X
Flexural mode of vibration (F)	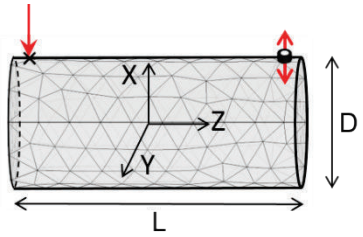	X	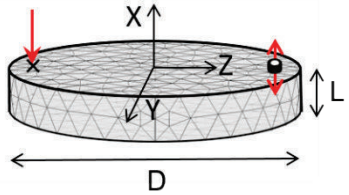
Torsional mode of vibration (T)	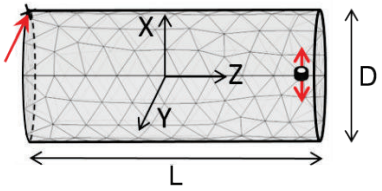	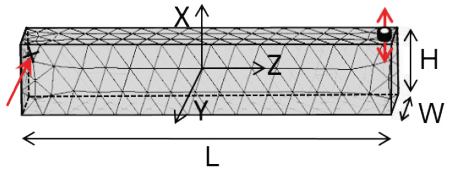	X
Longitudinal and flexural modes of vibration (L+F)	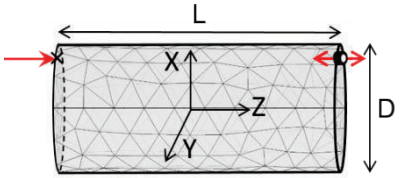	X	X

4.1.2 Reference LVE material with averaged LVE properties

A reference isotropic LVE bituminous mixture is considered in this section. It consists in a numerical simulation material with averaged LVE properties called reference LVE material. This reference LVE material was used in section 4.3 to study different inverse methods to obtain the LVE properties of bituminous mixtures from FRF measurements and to evaluate their accuracy. The behaviour of the reference LVE material is described with the 2S2P1D model (cf. equations (2-41) and (2-42)) and the WLF equation (cf. equation (2-18)). The constants of the 2S2P1D model and the WLF equation were fixed following the procedure presented in the next paragraph. The bulk density of the reference LVE material was fixed to 2 400 kg/m^3.

Cyclic tension-compression tests were previously performed on a total of 54 specimens of bituminous mixtures covering 32 different bituminous materials. These tests were performed during 4 different PhD thesis carried out at the University of Lyon / ENTPE, LTDS laboratory (Mangiafico, 2014; Pham N. H., 2014; Phan, 2016; Pedraza, 2018)and are presented in different publications (Mangiafico, et al., 2013; Nguyen Q. T., Di Benedetto, Sauzéat, & Tapsoba, 2013; Mangiafico, et al., 2015; Pham N. H., et al., 2015; Pham N. H., et al., 2015; Phan, et al., 2017). For each test, the 2S2P1D model and the WLF equation constants were calibrated to fit the experimental data. The resulting 54 sets of 2S2P1D model and WLF equation constants are given in APPENDIX B. They constitute a data base that was used to determine the 2S2P1D model and WLF equation constants of the reference LVE material. Each constant is taken in the vicinity of the average value of the corresponding constant of the 54 sets. The data base was also used to determine a realistic range of variations for each constant. The procedure to determine the 2S2P1D model and WLF constants of the reference LVE material is explained in Figure 4.1 and the values of the obtained constants are listed in Table 4.3. The minimum, maximum and average values and the standard deviation (SD) are also listed in Table 4.3for each constants.

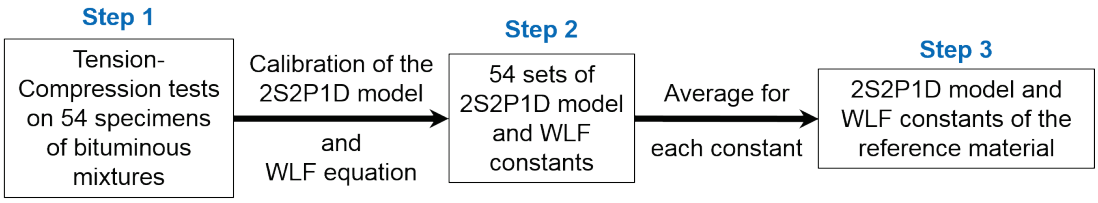

Figure 4.1. Procedure to determine the 2S2P1D model and WLF equation constants of the reference LVE material with averaged LVE properties.

Table 4.3. 2S2P1D model and WLF equation constants of the reference LVE material. The minimum, maximum and average values of the 2S2P1D model and WLF equation constants of the data base and the standard deviation (SD) are also indicated.

	2S2P1D model										WLF Equation at 15°C	
	E_{00} (MPa)	E_0 (MPa)	ν_0	ν_{00}	δ	k	h	β	$\tau_{E15°C}$ (s)	$\tau_{\nu15°C}$ (s)	C_1	C_2
Reference LVE material	**100**	**35 000**	**0.19**	**0.45**	**2.15**	**0.17**	**0.53**	**250**	**0.1**	**3.16**	**30**	**210**
Minimum	9	30 900	0.10	0.24	1.79	0.14	0.45	95	0.002	0.1	18	133
Maximum	180	42 000	0.47	0.63	2.63	0.23	0.57	$9E^3$	16.5	333.1	59	376
Average	35	36 500	0.19	0.43	2.12	0.17	0.53	630	0.71	51.8	31	209
SD	27	2 850	0.07	0.09	0.18	0.01	0.03	$1E^3$	2.3	72.9	5	28

4.2 Parametric analysis

The parametric analysis consists in calculating FRFs for different LVE properties obtained with different complex modulus and complex Poisson's ratio values or different 2S2P1D model and WLF constants, chosen in a realistic range of variations (see Table 4.3). It allowed to identify the constants that have a negligible influence and that can be fixed for the inverse analysis.

Three different configurations were studied for the parametric analysis: the longitudinal mode of a cylinder (D=7.5cm and L=15cm), the torsional mode of a straight beam (L=30cm, H=5cm and W=5cm) and the flexural mode of a disc (D=10cm and L=3cm). Two parametric analyses corresponding to two different modeling of the LVE behaviour were performed. First, the complex modulus and complex Poisson's ratio were considered independent of the frequency and of the temperature and the influence of the norm and phase angle of the complex modulus and complex Poisson's ratio were studied. Then, the complex modulus and complex Poisson's ratio were considered temperature and frequency dependents and were modelled with the 3-dim version of the 2S2P1D model. In this parametric analysis, the influence of the 2S2P1D model constants were studied.

4.2.1 Influence of the norm and of the phase angle of the complex modulus and complex Poisson's ratio

The complex modulus and the complex Poisson's ratio are considered as complex numbers independent of frequency:

$$E^* = E.e^{i\varphi_E} \tag{4-2}$$

$$\nu^* = \nu.e^{i\varphi_\nu} \tag{4-3}$$

where E and ϕ_E (respectively ν and ϕ_ν) are the norm and the phase angle of the complex modulus (respectively complex Poisson's ratio). The ranges of variations of these four LVE properties were defined to match those accessible with dynamic tests. For each LVE property, one median

value and four additional values were chosen in the corresponding range of variation. These values are listed in Table 4.4. To evaluate the influence of each LVE property, five FRFs corresponding to the five selected values were calculated while the three other LVE properties are set to their median values. Therefore, a total of twenty FRFs were calculated for each configuration studied. The FRFs showing the influence of E, ϕ_E, ν and ϕ_ν for the longitudinal mode of the cylinder are displayed in Figure 4.2.

Table 4.4. Values of the norm and of the phase angle of the complex modulus and complex Poisson's ratio considered for the parametric analysis. When one LVE property varies, the rest of the properties are set to their median values.

LVE property	Median value	Values chosen for the parametric analysis			
E (MPa)	25 000	10 000	17 500	32 500	40 000
φ_E (°)	6	0.5	2	12	25
ν	0.300	0.150	0.225	0.375	0.450
φ_ν (°)	-3	-1	-2	-4	-5

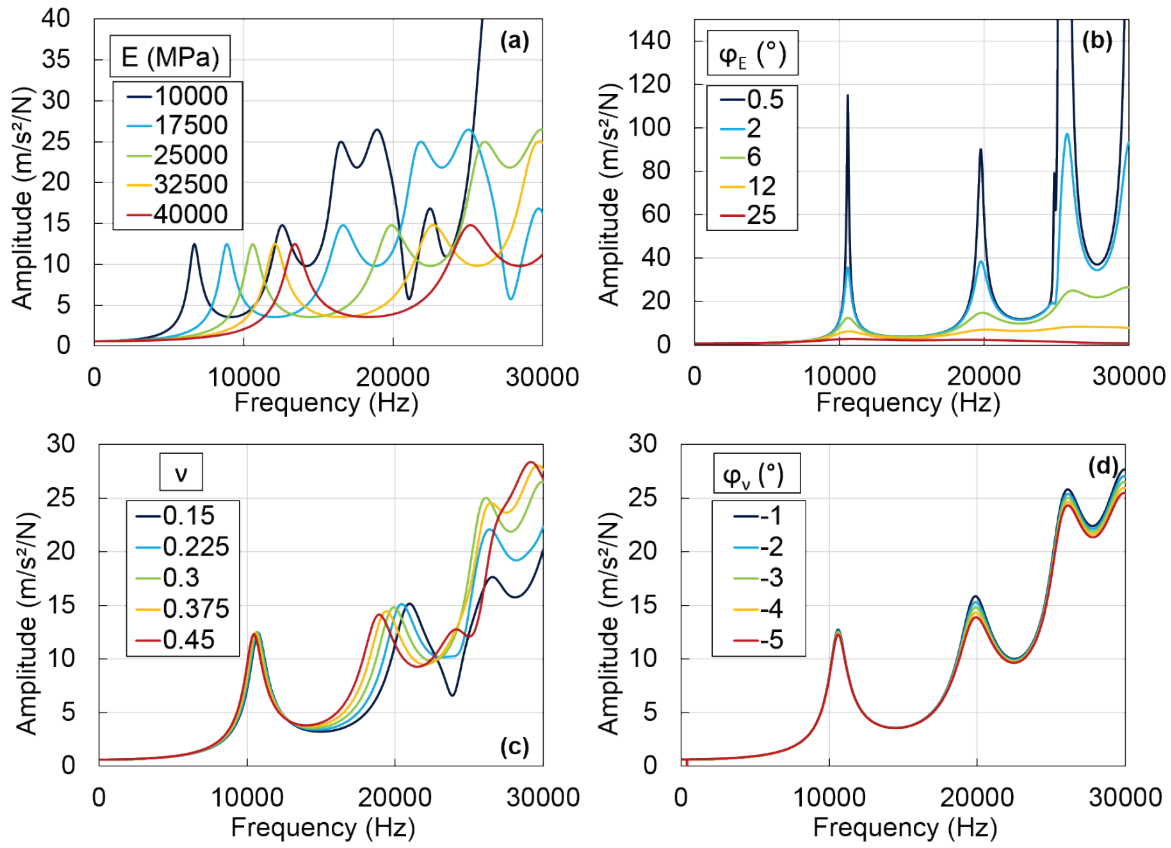

Figure 4.2. Influence of the LVE properties on the FRFs of the longitudinal mode of the cylinder: (a) norm of the complex modulus; (b) phase angle of the complex modulus; (c) norm of the complex Poisson's ratio; (d) phase angle of the complex Poisson's ratio. The constants not listed in each figure have the median value given in Table 4.4.

The relative standard deviation (RSD) for the two to three first resonance frequencies and amplitudes was calculated for each LVE property. The RSD is a good indicator of the sensitivity of the FRFs to one LVE property and it is very efficient to compare the influence of the different

LVE properties. Values of the RSD for this configuration and for each LVE property are listed in Table 4.5 for the two first resonance frequencies and amplitudes.

Table 4.5. Values of the RSD for the two first resonance frequencies and amplitudes for the longitudinal mode of the cylinder. The LVE property indicated in the left column varies while the other properties are set to their median values indicated in Table 4.4

LVE property	RSD 1st frequency (%)	RSD 1st amplitude (%)	RSD 2nd frequency (%)	RSD 2nd amplitude (%)
E	25.5	0.0	25.6	0.0
φ_E	0.9	135.9	2.3	118.1
ν	1.1	0.6	4.1	3.0
φ_ν	0.0	1.5	0.1	5.3

Figure 4.2 and Table 4.5 show that in the considered frequency domain, the norm of the complex modulus has an important influence on the resonance frequencies but almost no effect on the amplitudes. It is the contrary for the phase angle of the complex modulus that has an important influence on the amplitudes and a very limited effect on the resonance frequencies. The complex Poisson's ratio has a far lower influence than the complex modulus on the FRFs. More interestingly, the influence of the complex Poisson's ratio on the first resonance is almost negligible. The norm of the complex Poisson's ratio has a small influence on the second resonance frequency and amplitude while the phase angle of the complex Poisson's ratio only has a very limited influence on the amplitude.

Results of the direct analysis for the two other studied configurations are given in APPENDIX C. The influence of the complex modulus is very similar for all the configurations. The complex Poisson's ratio also has a far lower influence than the complex modulus for all the configurations. However, the longitudinal mode of the cylinder is the only configuration for which the effect of the Poisson's ratio is almost negligible for the first resonance (the RSD for ν for the first resonance frequency is 3.9% for the flexural mode of the disc and 4.6% for the torsional mode of the straight beam). This is an interesting observation that proves that the complex modulus can be identified independently of the complex Poisson's ratio using the first resonance of the longitudinal mode. For the other modes of vibration, the effect of the complex Poisson's ratio can be neglected as a first approximation. It allows to limit the number of unknowns values to be determined in the inverse analysis.

4.2.2 Influence of the 2S2P1D model constants

For this analysis, the complex modulus and complex Poisson's ratio are modelled with the 3-dim version of the 2S2P1D model (equations (2-41) and (2-42)). The influence of the ten constants of the 2S2P1D model was evaluated at five temperatures (-20°C, 0°C, 15°C, 35°C; 50°C). The range of variations of each constant of the model was defined from the data base of the constants values (see section 4.1.2). Following the same approach than in the previous section, one median value and four additional values were chosen for each constant in the corresponding range of variations. The values used for each constant of the model are listed in Table 4.6. For the ten constants of the model, five FRFs corresponding to the five selected values were calculated while the nine other constants are fixed to their median values. It represents a total of fifty FRFs that were calculated for each temperature and configuration.

Note that the temperature dependency of the characteristic times $\tau_{E15°C}$ and $\tau_{v15°C}$ was modelled with the WLF equation with C_1=30 and C_2=210 at the reference temperature of 15°C.

Table 4.6. Values of the 2S2P1D model constants considered for the parametric analysis. When one constant varies, the rest of the constants are set to their median values.

2S2P1D model constant	Median value	Values chosen for the parametric analysis			
E_{00} (MPa)	100	10	50	150	200
E_0 (MPa)	35 000	30 000	32 500	37 500	40 000
k	0.17	0.13	0.15	0.19	0.21
h	0.53	0.47	0.50	0.56	0.59
δ	2.15	1.75	1.95	2.35	2.55
β	250	10	100	500	1000
$\tau_{E15°C}$ (s)	0.1	0.01	0.05	0.5	1
ν_{00}	0.4	0.3	0.35	0.45	0.5
ν_0	0.2	0.1	0.15	0.25	0.3
$\tau_{v15°C}$ (s)	100	10 000	1 000	10	1

Evolution of the RSD with temperature for the two first resonance frequencies and amplitudes is plotted for all the constants in the case of the longitudinal mode of the cylinder in Figure 4.3.

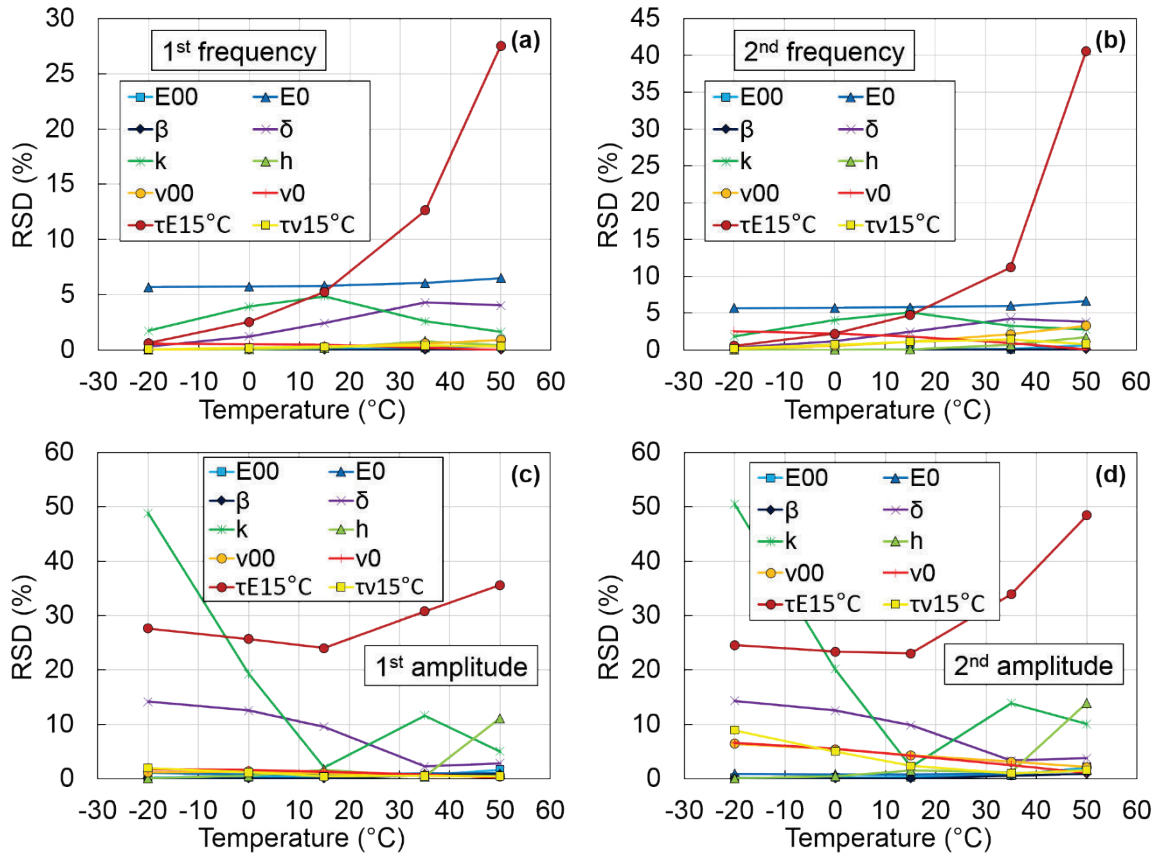

Figure 4.3. RSD in function of temperature for each of the ten constants of the 2S2P1D model for the longitudinal mode of the cylinder: (a) 1st resonance frequency; (b) 2nd resonance frequency; (c) 1st resonance amplitude; (d) 2nd resonance amplitude.

From this figure, four constants can be identified as the constants having the main influence on the FRFs: the constant E_0 has an important influence on the resonance frequencies while constants $\tau_{E15°C}$, k and δ have an influence on both the resonance frequencies and amplitudes. For each of these four constants, the FRFs calculated when the considered constant varies (the nine other constants are fixed to their median values) are plotted at 15°C for the longitudinal mode of the cylinder in Figure 4.4. It shows an example of how these four constants influence the FRFs. Figure 4.3 also shows that the constants ν_{00}, ν_0 and $\tau_{\nu 15°C}$ governing the value of the complex Poisson's ratio have almost a negligible influence on the first resonance and a small influence on the second resonance. This observation is very similar to the observation raised from the study of the influence of the complex Poisson's ratio on the longitudinal mode of the cylinder in section 4.2.1. The rest of the constants of the 2S2P1D model (E_{00}, β and h) have a negligible influence on the FRFs, which is logical because they influence the low frequencies behaviour of the model and FRFs are calculated at very high frequencies.

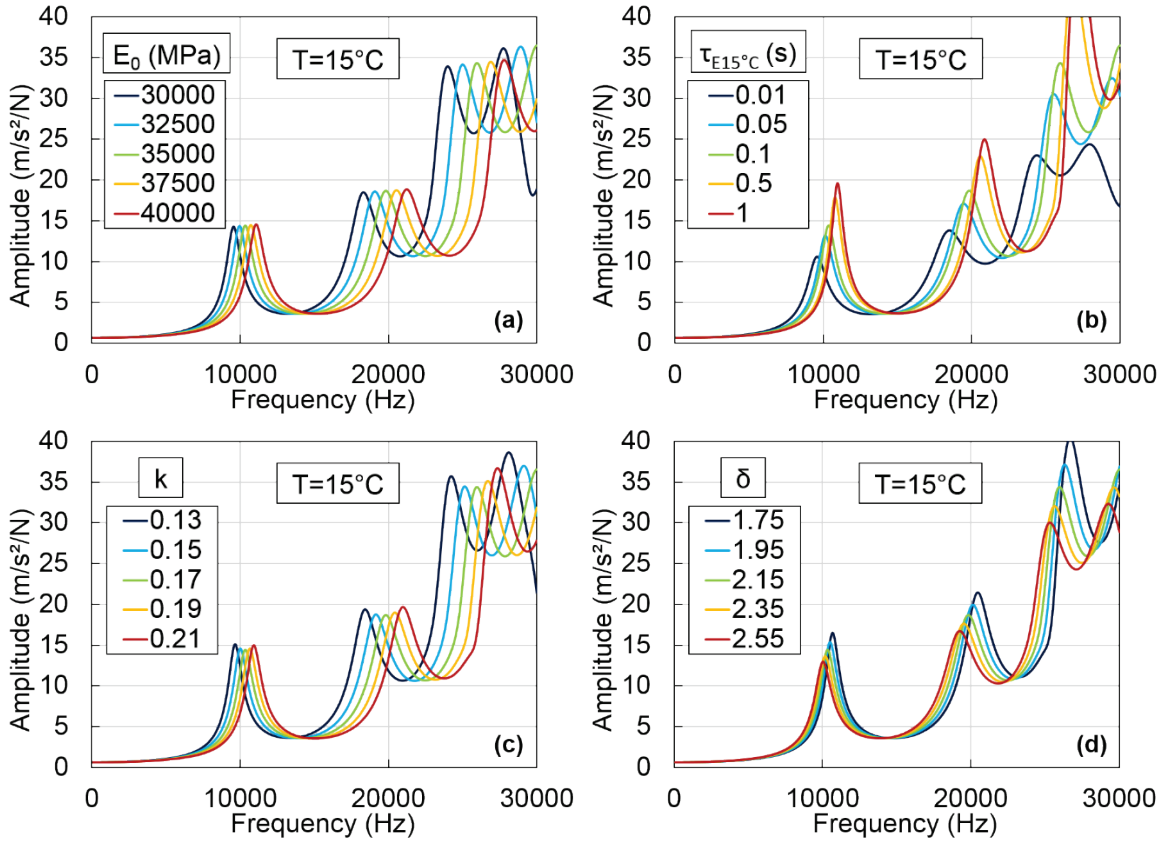

Figure 4.4. Influence of four constants of the 2S2P1D model on the FRFs of the longitudinal mode of the cylinder at 15°C: (a) E0; (b) τE15°C; (c) k; (d) δ. The constants not listed in each figure have the median value given in Table 4.6.

The results for the two other configurations are given in APPENDIX D. Similarly, to what was observed for the influence of the complex modulus and complex Poisson's ratio, the constants of the 2S2P1D model have comparable effects on all the configurations studied. In addition, the longitudinal mode is again the only configuration for which the first resonance is almost not impacted by the values of constants ν_{00}, ν_0 and $\tau_{\nu 15°C}$ governing the value of the complex Poisson's ratio. Therefore, the longitudinal mode of vibration seems to be the more suitable for practical application since the number of constants to identify in the inverse analysis can be reduced to four, at least when studying the first resonance only.

4.3 Inverse analysis

The inverse analysis consists in determining the LVE properties of a material from FRFs measurements. In this thesis, different inverse methods based on FEM calculations were developed to do so. The five proposed methods were applied to the reference LVE material described in section 4.1.2 to evaluate their accuracy. This approach presents the great advantage to eliminate any potential divergence due to experimental measurements errors or to the material behaviour that is not perfectly isotropic and LVE in practice. Therefore, only the accuracy of the different inverse analysis methods is evaluated. This step is essential to verify that the inverse methods selected for practical application on bituminous mixtures specimens introduce no bias for the characterization of the LVE properties.

First, four methods that give only access to the complex modulus are presented. Then, another method for which it is possible to determine the complex Poisson's ratio is introduced. For the five methods, different FRFs are compared after applying the method to the reference LVE material:

- The FRFs calculated with the LVE properties or the constants of the 2S2P1D model determined at each temperature in the first step of the methods. They are called FRFs after optimization and are noted FRF A.O.
- The FRFs calculated with the constants of the 2S2P1D model and WLF equation simulating the global LVE behaviour of the material determined in the second steps of the methods. They are called global LVE FRFs and are noted G.LVE.FRF.
- The FRFs of the reference LVE material calculated with the constants of the 2S2P1D model and WLF equation of the reference LVE material (cf. Table 4.3).

Similarly, different complex modulus values are also compared:

- The complex modulus back-calculated in the first step of the methods, noted E^*_{BCp} (norm $|E^*_{BCp}|$ and phase angle φ_{E^*BCp}) where p is the index of the considered method (p=1, 2, 3, 4 or 5).
- The complex modulus of the 2S2P1D model simulating the global LVE behaviour of the material determined in the second step of the methods, noted E^*_{Dynp} (norm $|E^*_{Dynp}|$ and phase angle φ_{E^*Dynp}) where p is the index of the considered method (p=1, 2, 3, 4 or 5).
- The complex modulus of the reference LVE material, noted E^*_{Ref} (norm $|E^*_{Ref}|$ and phase angle φ_{E^*Ref}).

4.3.1.1 Method I: simplified back analysis method

All the details about this method and the results obtained are presented in Paper I and Paper II. In this section, only a summary of the method and of the main results is given.

4.3.1.1.1 Principle of the method

This method is the simplest method proposed in this thesis. It is divided in two distinct steps. The first step consists to back analyze the FRFs obtained at each temperature to determine

one value of the complex modulus at the first resonance frequency. The second step consists to fit the 2S2P1D model and the WLF equation simulating the global LVE behaviour of the material using the results of the first step.

The first step of the method gives access to one value of the complex modulus at the first resonance frequency for each temperature. This value is obtained following a process divided into two stages described in Figure 4.5:

- First, the norm of the complex modulus ($|E^*_{BC1}|$) is determined from the first resonance frequency f. The material behaviour is considered elastic and the modulus is back-calculated using the FEM so that the first resonance frequency of the elastic calculation matches the first resonance frequency of the FRF to back-analyze or input FRF. For the longitudinal and flexural modes of vibration, it is necessary to fix the value of the Poisson's ratio to perform the elastic back-calculation of the modulus. The torsional mode of vibration is independent of the value of the Poisson's ratio.
- Then, the frequency bandwidth at -3dB, Δf, is determined with the half-power bandwidth method applied to the first resonance peak of the input FRF. The phase angle of the complex modulus is calculated from the frequency bandwidth Δf and the first resonance frequency f according to the following relationship (Clough & Penzien, 1993):

$$\varphi_{E^*BC1} = \arctan\left(\frac{\Delta f}{f}\right) \tag{4-4}$$

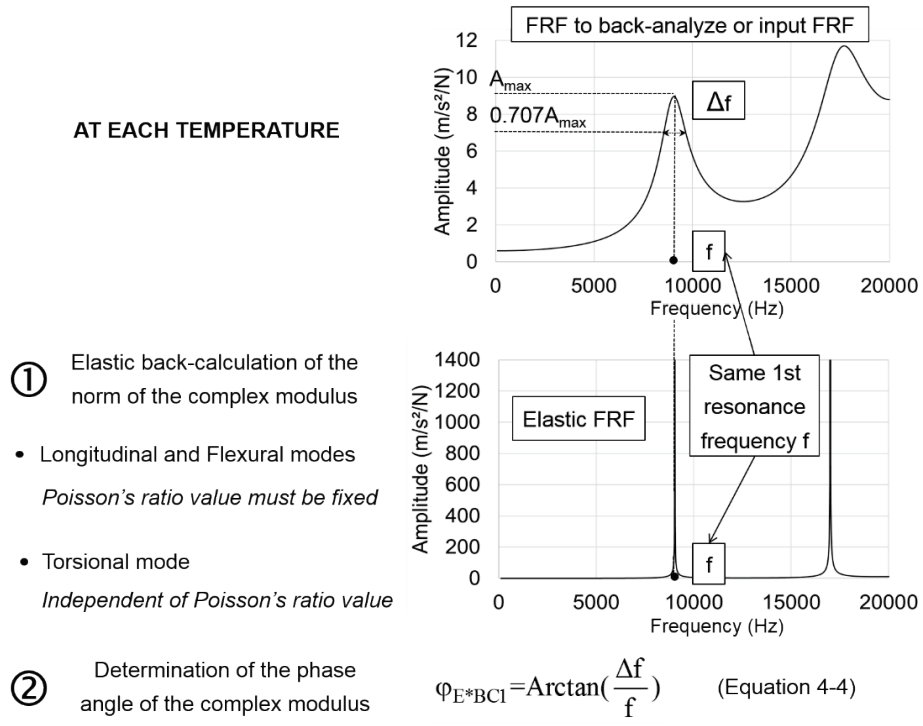

Figure 4.5. Principle of the two-stages process to determine the value of the complex modulus at the first resonance frequency for each temperature in the first step of method I.

In the second step of the method, the complex modulus simulating the global LVE behaviour of the material (E^*_{Dyn1}) is determined. To do so, the values of the complex modulus back-calculated at each temperature in the first step (one value at each temperature) are used as data points to fit a unique 2S2P1D model and to find the WLF equation of the material. This is done in three stages explained in Figure 4.6 for an example in which five temperatures are considered:

- The first stage consists in adjusting manually the values of the 2S2P1D model constants until the fit in the cole-cole plan between the 2S2P1D model and the data points is satisfying. Only the values of constants E_0, k, δ and h of the 2S2P1D model can be found considering the range of values of the data points. Constants E_{00} and β are fixed to the values of the reference LVE material listed in Table 4.3. or to values determined from other tests. Constants $\tau_{E15°C}$ of the 2S2P1D model and C_1 and C_2 of the WLF equation are not considered in this stage because the Cole-Cole representation of the 2S2P1D model is independent of the frequency and temperature.
- In the second stage, the experimental characteristic times τ_{exp} are determined at each temperature. To do so, the constants of the 2S2P1D model obtained in the first stage are used to calculate the values of the complex modulus at the same frequencies than the data points. The experimental characteristic times τ_{exp} are optimized at each temperature separately to minimize the relative difference between the norm of the complex modulus calculated as described above and the norm of the complex modulus of the data points (i.e. the norm of the back-calculated complex modulus, E^*_{BC1}).
- Finally, the characteristic time at the reference temperature $\tau_{E15°C}$ and the constants C_1 and C_2 of the WLF equation at 15°C are found in the third stage using the excel solver with characteristic times τ_{exp} found in the second stage.

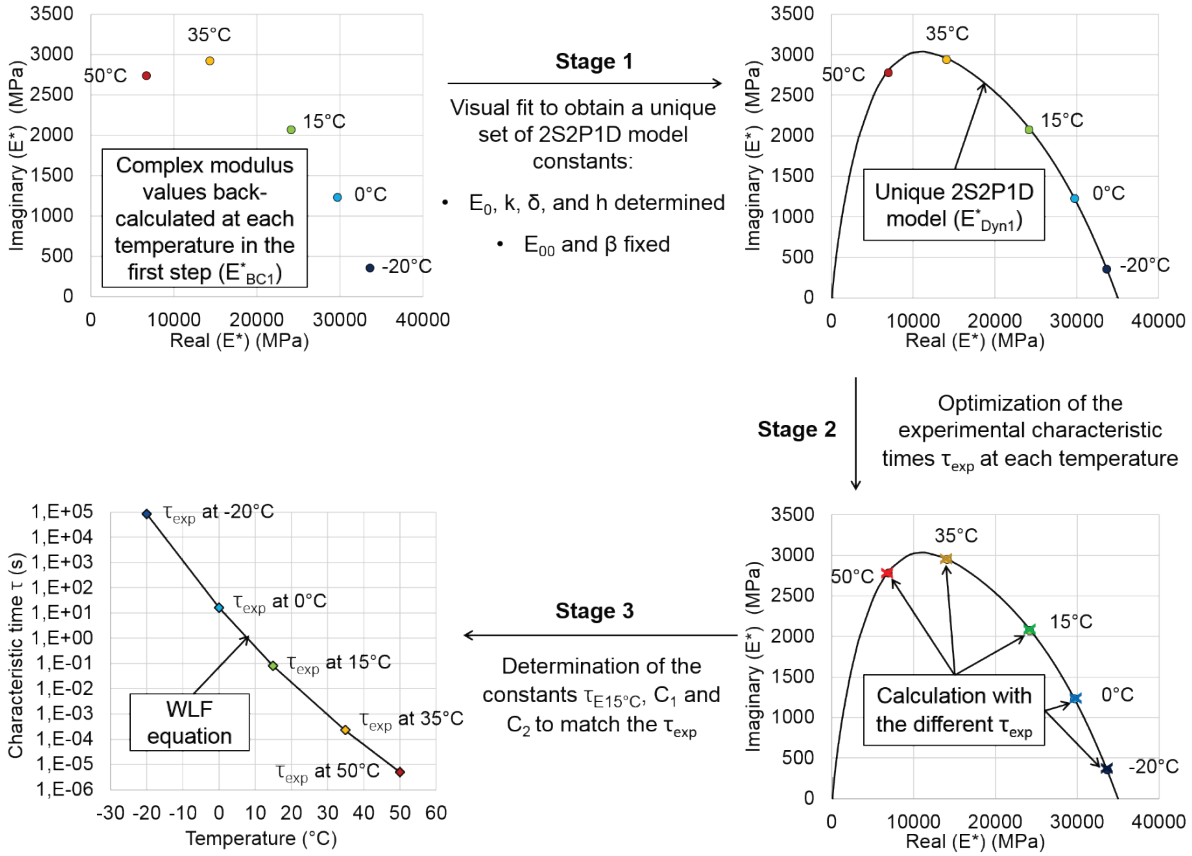

Figure 4.6. Three-stages process to determine the values of constants E_0, $\tau_{E15°C}$, k, δ, h, C_1 and C_2 of the 2S2P1D model and WLF equation simulating the global LVE behaviour of the material that are identified in the second step of method I. Example in which five temperatures are considered.

4.3.1.1.2 Results for the reference LVE material

The method described in the previous section was applied to a cylinder (L=15cm, D=7.5cm) of the reference LVE material and three modes of vibration (longitudinal, flexural and torsional) were studied. Values of the constants of the 2S2P1D model of the reference LVE material considered in this section are slightly different than those listed in Table 4.3and the reference temperature is 10°C instead of 15°C (cf. Paper I and Paper II). The effect of the temperature was also studied and ten temperatures between -40°C and 50°C were used. For the longitudinal and flexural modes of vibration, the influence of the fixed value of the Poisson's ratio for the elastic back-calculation in the first step was studied. To do this, three back-calculations of the norm of the complex modulus corresponding to three different values of the Poisson's ratio were performed: ν_1=0.2, ν_2 equal to the value of the norm of the Poisson's ratio of the reference LVE material at the first resonance frequency for the considered mode of vibration ($\nu_2 = |\nu^*_{Ref\text{-}L}|$ for the longitudinal mode and $\nu_2 = |\nu^*_{Ref\text{-}F}|$ for the flexural mode) and ν_3=0.45. Consequently, three values of the complex modulus were obtained for the longitudinal and flexural modes while only one value the complex shear modulus was obtained for the torsional mode. The notations corresponding to the complex modulus back-calculated in the first step and to the complex modulus of the reference LVE material are summarized in Table 4.7 for the three studied modes of vibration..

Table 4.7. Notations used for the complex modulus back-calculated in the first step of method I and for the complex modulus of the reference LVE material for the three studied modes of vibration. (Suffixes L, F and T corresponds respectively to the longitudinal, flexural and torsional modes).

Mode of Vibration	Poisson's ratio	Complex modulus from the back analysis at the 1st resonance frequency	Complex modulus of the reference LVE material at the 1st resonance frequency
Longitudinal	ν_1=0.2	$E^*_{BC1-L1} = \left\|E^*_{BC1-L1}\right\|.e^{i\varphi^*_{BC1-L}}$	$E^*_{Ref-L} = \left\|E^*_{Ref-L}\right\|.e^{i\varphi^*_{Ref-L}}$
	$\nu_2 = \left\|\nu^*_{Ref-L}\right\|$	$E^*_{BC1-L2} = \left\|E^*_{BC1-L2}\right\|.e^{i\varphi^*_{BC1-L}}$	
	ν_3=0.45	$E^*_{BC1-L3} = \left\|E^*_{BC1-L3}\right\|.e^{i\varphi^*_{BC1-L}}$	
Flexural	ν_1=0.2	$E^*_{BC1-F1} = \left\|E^*_{BC1-F1}\right\|.e^{i\varphi^*_{BC1-F}}$	$E^*_{Ref-F} = \left\|E^*_{Ref-F}\right\|.e^{i\varphi^*_{Ref-F}}$
	$\nu_2 = \left\|\nu^*_{Ref-F}\right\|$	$E^*_{BC1-F2} = \left\|E^*_{BC1-F2}\right\|.e^{i\varphi^*_{BC1-F}}$	
	ν_3=0.45	$E^*_{BC1-F3} = \left\|E^*_{BC1-F3}\right\|.e^{i\varphi^*_{BC1-F}}$	
Torsional	Independent of ν	$G^*_{BC1-T} = \left\|G^*_{BC1-T}\right\|.e^{i\varphi^*_{BC1-T}}$	$G^*_{Ref-T} = \left\|G^*_{Ref-T}\right\|.e^{i\varphi^*_{Ref-T}}$

The relative difference (respectively the difference) between the norm (respectively the phase angle) of the complex modulus evaluated in the first step of method I and the norm (respectively the phase angle) of the complex modulus of the reference LVE material calculated at the same frequencies is presented in Figure 4.7. A good agreement is seen for both the norm and phase angle of the complex modulus for the low temperatures. Figure 4.7 (a) also shows that the Poisson's ratio has a limited impact (less than 5%) on the calculation of the norm of the complex modulus. For temperatures higher than 10°C, differences increase, especially for the phase angle. For temperatures higher than 30°C, it is seen on Figure 4.7 (b) that the phase angle cannot be evaluated with the back analysis method for the longitudinal and torsional modes. These observations highlight the limits of the half-power bandwidth method for the evaluation of the phase angle when there is too much damping in the material. Because of the previous observations, it is expected that the global LVE behaviour determined in the second step of the method will not be in good agreement with the behaviour of the reference LVE material.

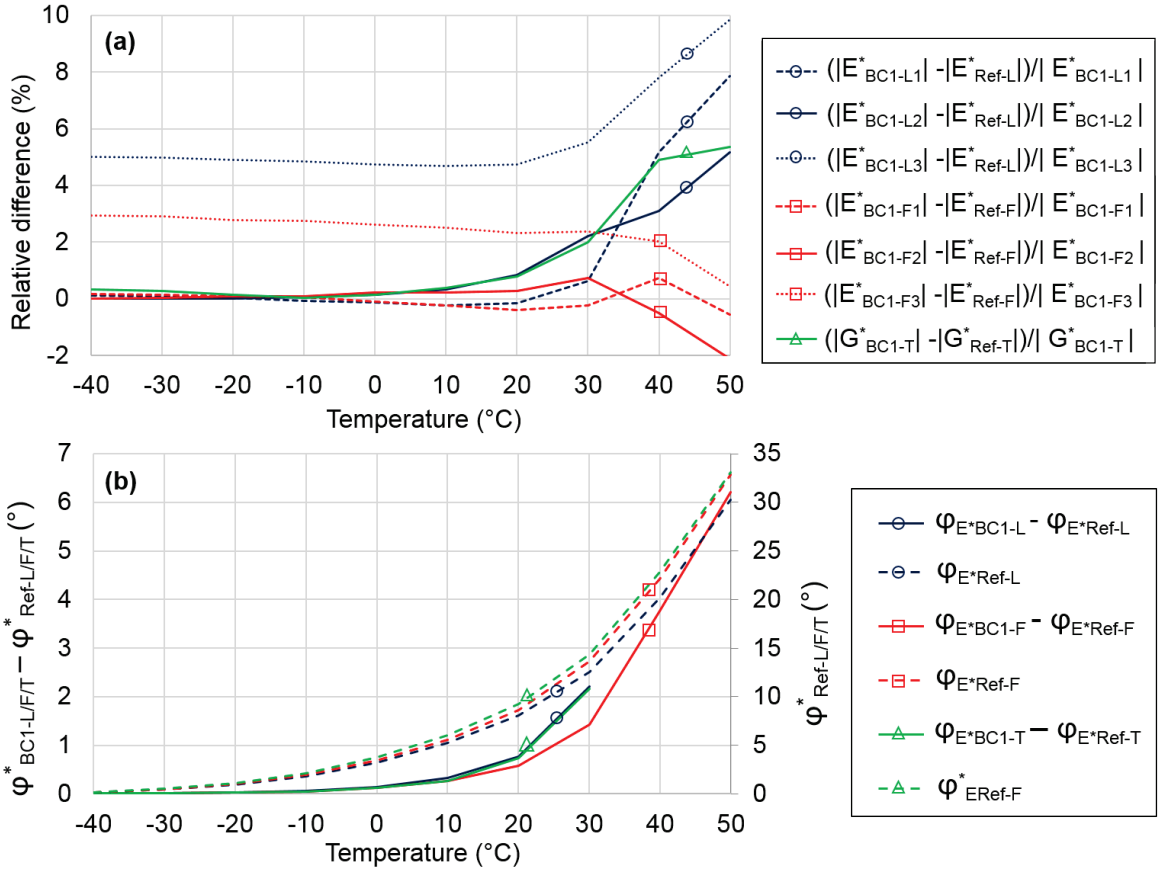

Figure 4.7. a) Relative difference between the norm of the complex modulus determine in the first step of method I ($E^*_{BC1\text{-}L/F/T}$) and the norm of the complex modulus of the reference LVE material ($E^*_{Ref\text{-}L/F/T}$); (b) difference between the phase angle of the complex modulus determined in the first step of method I ($\varphi^*_{BC1\text{-}L/F/T}$) and the phase angle of the complex modulus of the reference LVE material ($\varphi^*_{Ref\text{-}L/F/T}$). Suffixes L, F and T corresponds respectively to the longitudinal, flexural and torsional modes.

The values of the constants of the 2S2P1D model and WLF equation determined in the second step of the method are listed in Table 4.8 for the three studied modes of vibration. Values listed in Table 4.8were obtained by using as input data points for the second step:

- For the longitudinal and flexural modes, the values of the complex modulus back calculated in the first step that are in best agreement with the values of E^*_{Ref} ($E^*_{BC1\text{-}L2}$ for the longitudinal mode and $E^*_{BC1\text{-}F2}$ for the flexural mode)
- For the torsional mode, the values of $G^*_{BC1\text{-}T}$ transformed to complex modulus values using equation (2-16).

Table 4.8. Values of the seven constants E_0, $\tau_{E10°C}$, k, δ, h, C_1 and C_2 of the 2S2P1D model and WLF equation simulating the global LVE behaviour of the material determined in the second step of method I for the three studied modes of vibration.

	2S2P1D model					WLF equation at 10°C	
Mode of vibration	**E_0 (MPa)**	**$\tau_{E10°C}$ (s)**	**k**	**δ**	**h**	**C_1**	**C_2**
Longitudinal	34 900	0.013	0.162	1.35	0.49	17.2	132.8
Flexural	34 900	0.065	0.182	2.10	0.62	27.2	197.5
Torsional	35 000	0.023	0.185	1.90	0.58	24.2	186.9

The master curves at 10°C of the relative difference (respectively the difference) between the norm (respectively the phase angle) of E^*_{Dyn1} and E^*_{Ref} are plotted in Figure 4.8. As expected, Figure 4.8 confirms the observations raised from Figure 4.7. For all modes of vibration, method I is very accurate for temperatures lower than 10°C (or reduced frequencies higher than 10^5 Hz) with less than 2% of error for the norm of the complex modulus and 0.5° for the phase angle. However, for temperatures higher than 10°C (or reduced frequencies lower than 10^5 Hz), the error increases and the norm of the complex modulus is underestimated up to 30% while the phase angle is overestimated up to 10°

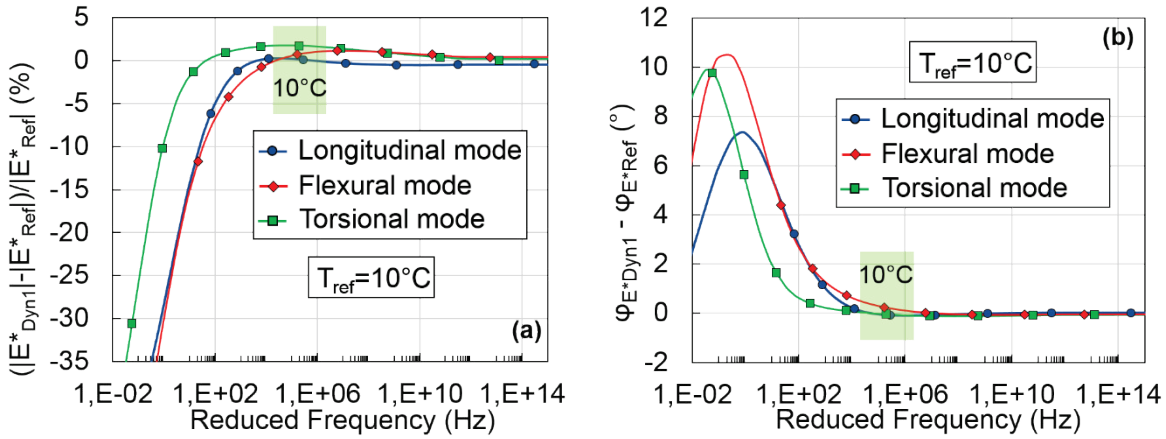

Figure 4.8. Master curve at 10°C of: (a) the relative difference between the norm of the complex modulus determined with method I ($|E^*_{Dyn1}|$) and of the reference LVE material ($|E^*_{Ref}|$) ;(b) the difference between the phase angle of the complex modulus determined with method I (φ_{E^*Dyn1}) and of the reference LVE material (φ_{E^*Ref}). Results for three studied modes of vibrations.

To conclude, method I is very interesting to evaluate quickly and accurately the high frequencies or low temperatures behaviour of bituminous mixtures. However, it is not recommended to use this method for characterizing bituminous mixtures properties on a wider frequency and temperature range.

4.3.1.2 Method II: determination of the complex modulus simulating the global LVE behaviour of the material in one step

4.3.1.2.1 Principle of the method

In this method, the behaviour of the material is modelled with the 3-dim version of the 2S2P1D model and the temperature dependency is described with the WLF equation. The constants of the 2S2P1D model and of the WLF equation simulating the global LVE behaviour of the material are directly determined from one single optimization of all the input FRFs of the material for a given mode of vibration. The optimization consists in optimizing FRFs calculated with the FEM (cf. section 4.1.1) to match the input FRFs. This is done with an optimization algorithm that adjusts iteratively the values of the constants of the 2S2P1D model and WLF equation until the fit with the input FRFs is good enough.

The direct analysis showed that constants E_{00}, β, h, ν_{00}, ν_0 and $\tau_{\nu 15°C}$ of the 2S2P1D model have a negligible influence on the FRFs calculation, at least as a first approximation (see section 4.2.2). Therefore, these six constants can be fixed and are not identified during the optimization.

Consequently, the complex Poisson's ratio is not determined with this method. In this thesis, the values chosen for the six fixed constants of the 2S2P1D model were set to the values of the constants of the reference LVE material (cf. Table 4.3) or to values determined from other tests. Note that constant $\tau_{\nu 15°C}$ is not fixed to a constant value but is continuously adjusted so that the ratio $\gamma_{E\nu}$ between $\tau_{E15°C}$ and $\tau_{\nu 15°C}$ is constant (equal to the value of the reference LVE material unless the value is known from other tests):

$$\gamma_{E\nu} = \frac{\tau_{E15°C}}{\tau_{\nu 15°C}} = \text{Constant} \tag{4-5}$$

The four remaining constants E_0, $\tau_{E15°C}$, k and δ of the 2S2P1D model are determined with this method. In addition, if the temperature dependency of the characteristic time $\tau_{E15°C}$ is not known, constants C_1 and C_2 of the WLF equation must also be determined in the optimization process. In the contrary case, they can be fixed to their known values during the optimization.

The frequencies used as input in the optimization are chosen around the resonance frequencies seen on the input FRFs according to previous studies that showed their meaningful importance (Gudmarsson, Ryden, & Birgisson, 2012; Gudmarsson, et al., 2014; Gudmarsson, Ryden, Di Benedetto, & Sauzéat, 2015). At each temperature, a total of 10 frequencies are selected along each resonance peak and the error function to minimize is defined as follow:

$$\text{Error} = \sum_{T=1}^{5} E_T \tag{4-6}$$

where T is the index of the temperatures and E_T is the error at temperature T defined as:

$$E_T = \sum_{i=1}^{NpeakT} \sum_{j=1}^{10} \left(\left| \frac{\left|H_{InpT_{ij}}\right| - \left|H_{OptT_{ij}}\right|}{\left|H_{InpT_{ij}}\right|} \right| \right) \tag{4-7}$$

where H_{InpT} is the input FRF at temperature T, H_{OptT} is the FRF calculated during the optimization process at temperature T, N_{peakT} is the number of resonance peaks at temperature T, i is the index of the peaks and j is the index of the frequencies. The starting values of the constants to be optimized can be adjusted manually before launching the optimization to reduce the initial error. The optimization is performed in MATLAB with the "fminsearch" algorithm and the optimization is stopped when the error and the parameter tolerance of 1% is reached (e.g. when the variation of the error and of all the values of the constants to be optimized is less than 1% between two iterations of the algorithm). The principle of the method is explained in Figure 4.9 in the cases for which constants C_1 and C_2 of the WLF equation are fixed.

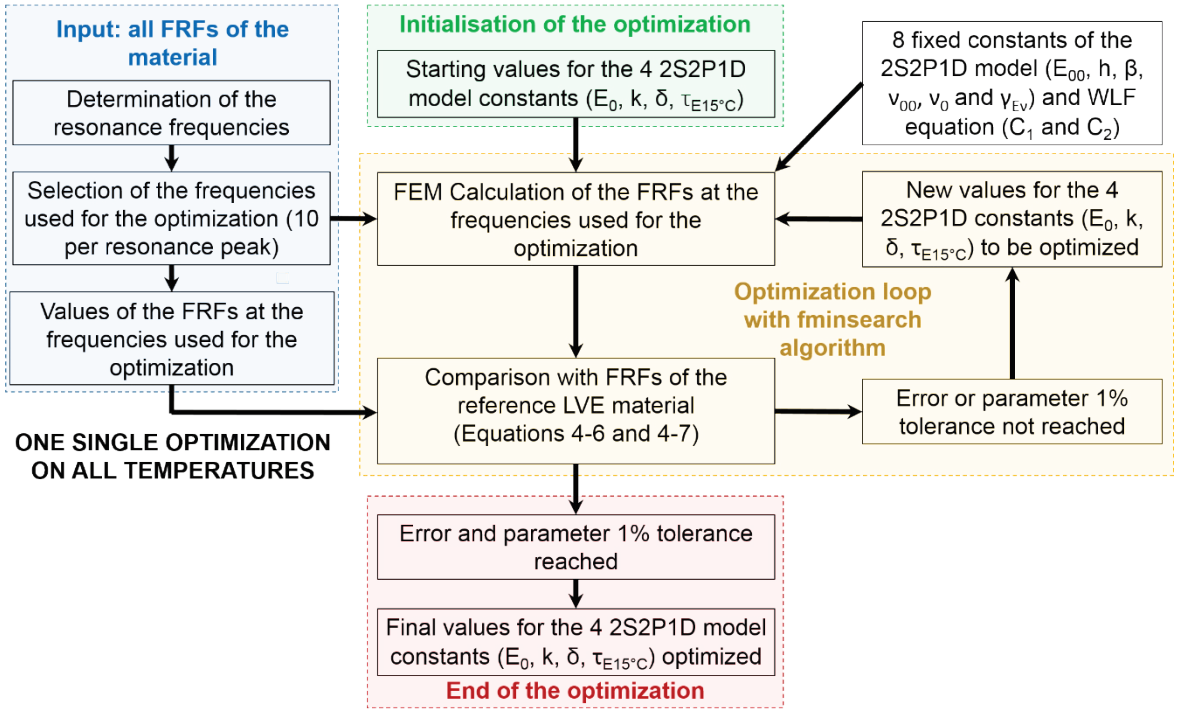

Figure 4.9. Principle of the optimization process for method II in the cases for which constants C_1 and C_2 of the WLF equation are fixed. In the other cases, constants C_1 and C_2 are optimized along with constants E_0, $\tau_{E15°C}$, k and δ of the 2S2P1D model.

This method is based on a unique optimization of all the input FRFs for a given mode of vibration. Potential measurement errors at some temperatures in physical tests may not be detected with this global approach. A good alternative is to use a two steps process including a local approach in the first step, as for method I (cf. 4.3.1.1.1). The methods that are introduced in the next sections are all based on this same principle.

4.3.1.2.2 Results for the reference LVE material

The method described in the previous section was tested on the reference LVE material. Four configurations were studied: the longitudinal mode of a cylinder (L=16cm, D=6.5cm) and of a straight beam (L=30cm, H=W=5cm), the longitudinal and flexural modes of the same cylinder and the flexural mode of a disc (L=3cm, D=10cm). For each configuration, the FRFs of the reference LVE material (reference FRFs) were calculated at five temperatures (-20°C, 0°C, 15°C, 35°C and 50°C) for frequencies between 100 Hz and 20 kHz in steps of 20 Hz.

The values of the four constants E_0, $\tau_{E15°C}$, k and δ of the 2S2P1D model determined with this method are given in Table 4.9 for the four studied configurations. To obtain these values, the values of the six constants of the 2S2P1D model (E_{00}, β, h, ν_{00}, ν_0 and $\tau_{\nu 15°C}$) that are not optimized were fixed to the values of the constants of the reference LVE material listed in Table 4.3 except for $\tau_{\nu 15°C}$ which was continuously adjusted so that the ratio γ_{Ev} between $\tau_{E15°C}$ and $\tau_{\nu 15°C}$ is constant and equal to the ratio of the reference LVE material:

$$\gamma_{Ev} = \frac{\tau_{E15°C}}{\tau_{\nu 15°C}} = \frac{0.1}{3.16} = 0.0316 \qquad (4\text{-}8)$$

The temperature dependency of the characteristic time $\tau_{E15°C}$ was supposed known and constants C_1 and C_2 of the WLF equation were also fixed the values of the reference LVE material. The starting values of the four 2S2P1D model constants to be optimized were chosen randomly by taking values in a range of +/- 15% around the values of the reference LVE material listed in Table 4.3.

Table 4.9. Values of the four constants E_0, $\tau_{E15°C}$, k and δ of the 2S2P1D model simulating the global LVE behaviour of the material determined with method II for the four studied configurations.

Configuration	E_0 (MPa)	$\tau_{E15°C}$ (s)	k	δ
C-L	34 150	0.117	0.188	2.34
C-P+F	35 351	0.088	0.165	2.00
B-L	35 059	0.086	0.167	2.03
D-F	35 099	0.072	0.164	1.89

Table 4.9 shows that the final values of the four identified constants are slightly different than the constants of the reference LVE material. Though, the global LVE FRFs are in very good agreement with the reference FRFs as seen in Figure 4.10 for the longitudinal mode of the cylinder. The figures corresponding to the three other studied configurations can be found in APPENDIX E. They confirm observations raised from Figure 4.10. It shows that the optimization process works correctly for all the studied configurations

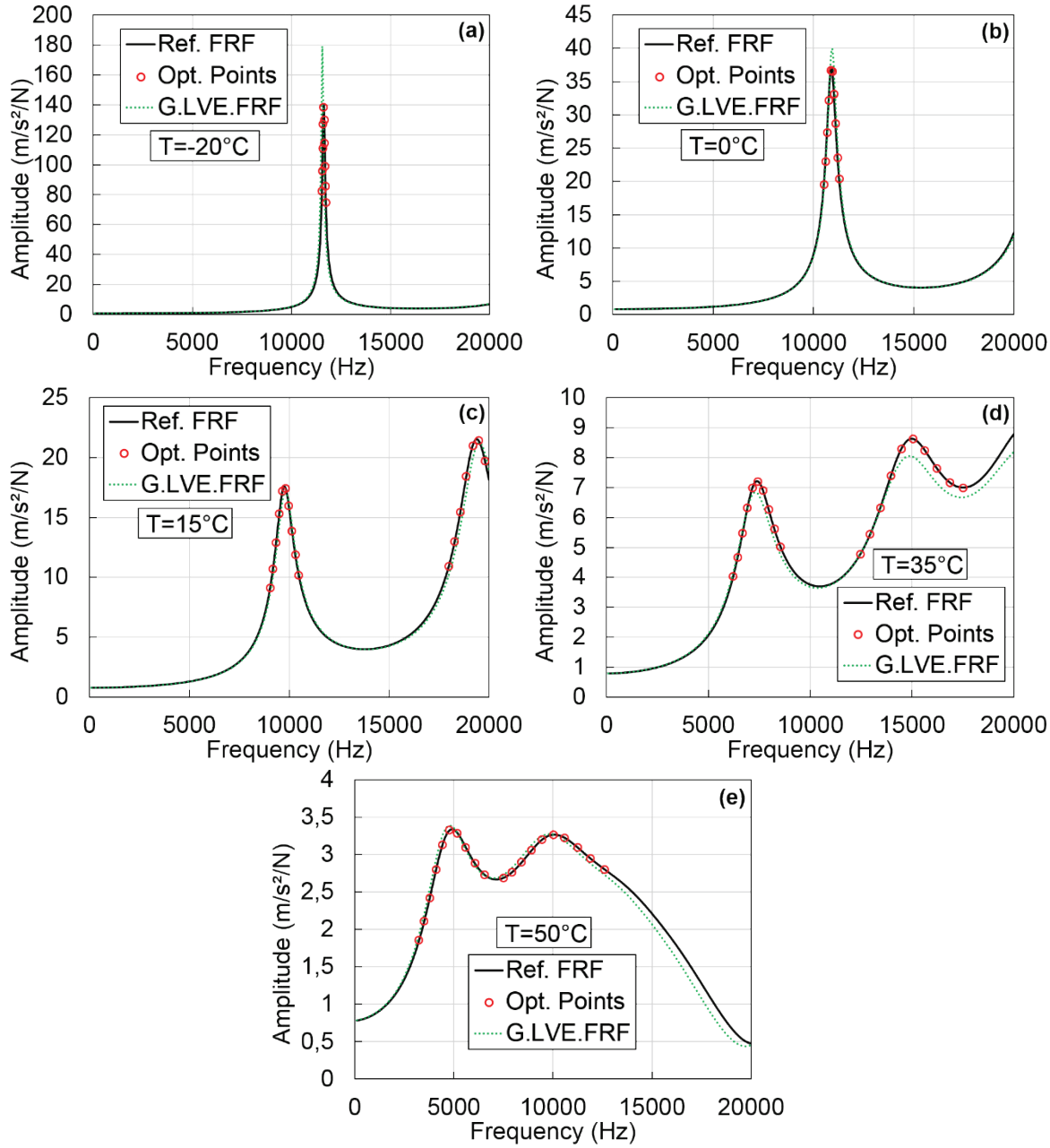

Figure 4.10. Comparison of the reference FRFs (noted Ref. FRF) with the global LVE FRFs (noted G.LVE.FRF) for method II. Values of the reference FRFs at the frequencies where the optimization is performed (noted Opt. Points) are also plotted. Example for the longitudinal mode of the cylinder at: (a) -20°C; (b) 0°C; (c) 15°C; (d) 35°C; (e) 50°C.

Then, the values of E^*_{Dyn2} (i.e. the values of the complex modulus calculated with the 2S2P1D model simulating the global LVE behaviour which constants values are listed in Table 4.9) were compared with the values of $E^*_{Ref.}$ The comparison was performed for six frequencies selected at each temperature in a narrow domain including all the resonance frequencies (cf. Figure 4.11). The frequencies corresponding to each configuration studied are given in APPENDIX E The principle of the comparison is illustrated in Figure 4.11.

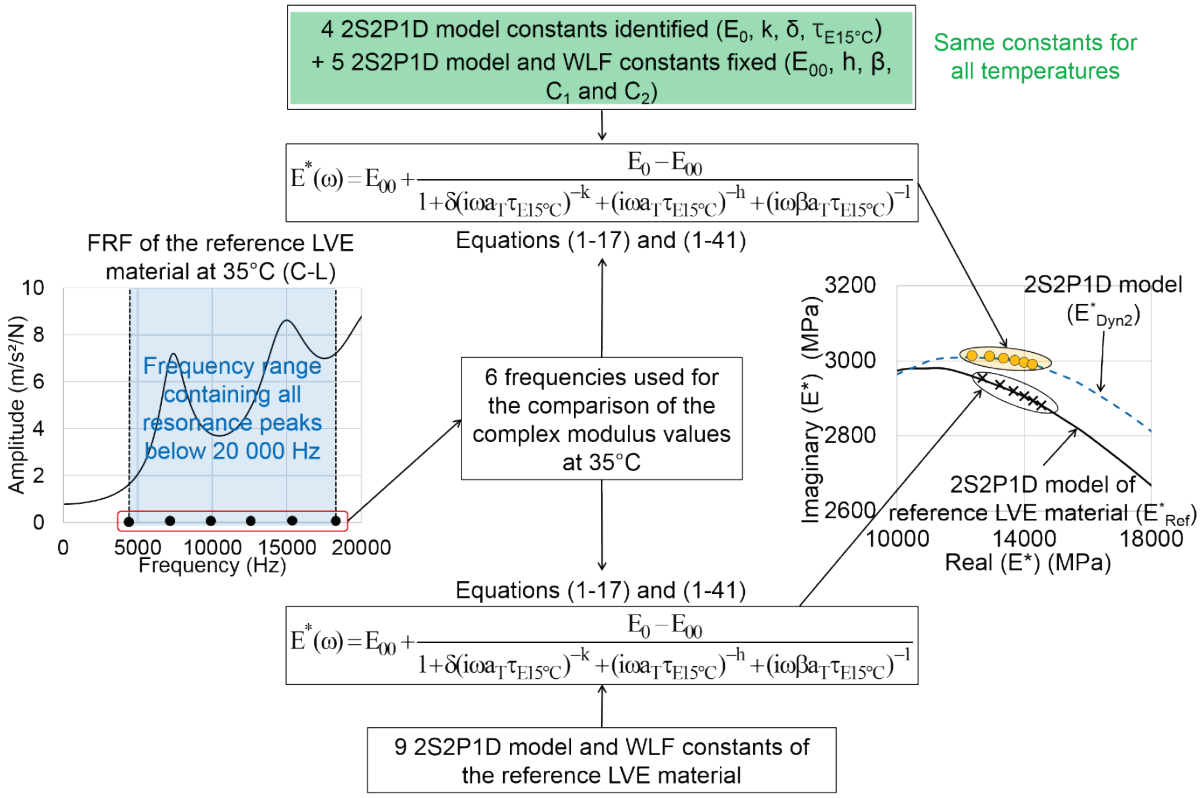

Figure 4.11. Principle of the comparison of the values of the complex modulus of the reference LVE material (E^*_{Ref}) with the values of the complex modulus determined in the second inverse method (E^*_{Dyn2}). Example for the longitudinal mode of the cylinder at 35°C.

Figure 4.12 shows the Cole-Cole plot and the master curves at 15°C of the norm and phase angle of the different complex modulus (E^*_{Dyn2} and E^*_{Ref}) for the longitudinal mode of the cylinder. A very good fit is seen between the values of E^*_{Dyn2} and E^*_{Ref}. This observation is confirmed in Figure 4.13 where master curves at 15°C of the relative difference (respectively the difference) between the norm (respectively the phase angle) of E^*_{Dyn2} and E^*_{Ref} is presented. It is seen in Figure 4.13 that the maximum relative difference is about 5% for the norm of the complex modulus and the maximum difference is less than 1° for the phase angle except for the longitudinal mode of the straight beam for which the difference reaches 2° at 50°C. The overall agreement between the values of E^*_{Dyn2} and E^*_{Ref} is very satisfying. It demonstrates the good accuracy of the method. However, it should be remembered that the shift factors were supposed known before the optimization, which is generally not the case in physical experimentation.

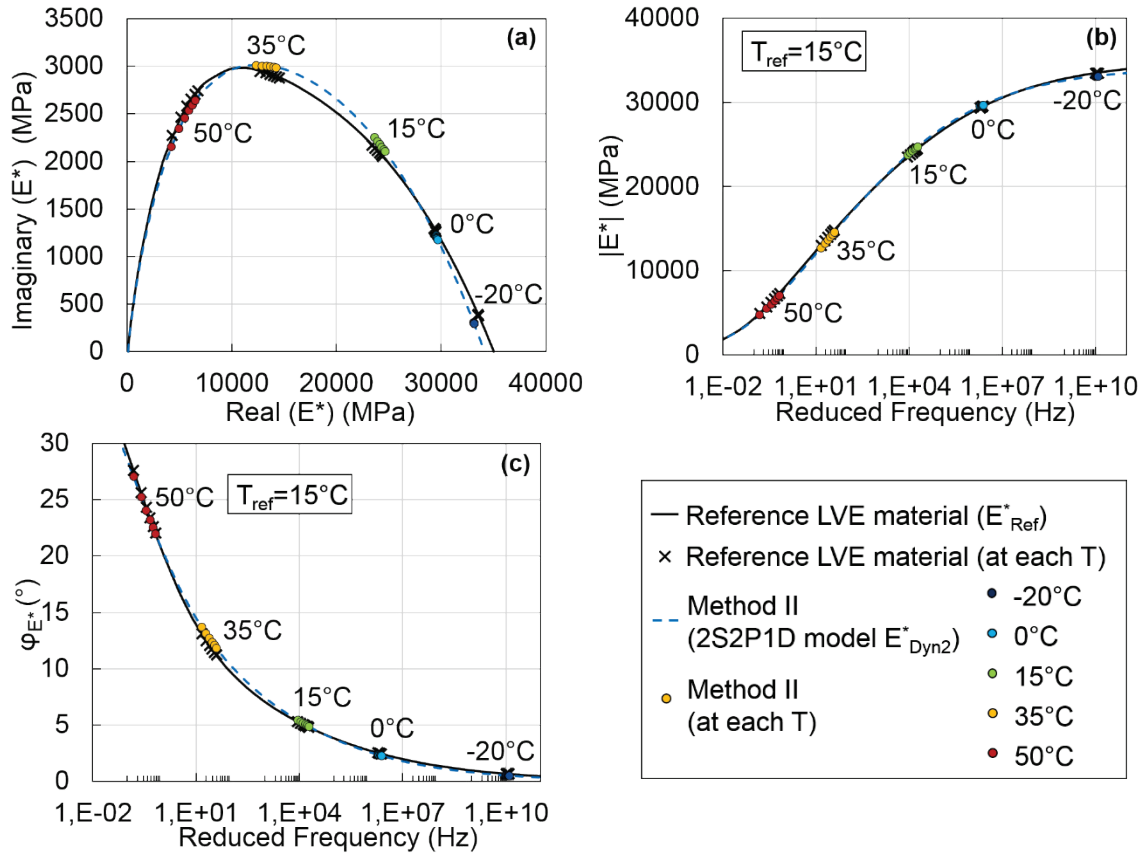

Figure 4.12. Comparison of the values of the complex modulus determined with method II (E^*_{Dyn2}) with the values of the complex modulus of the reference LVE material (E^*_{Ref}). (a) Cole-Cole plot; (b) and (c) master curves of the norm and of the phase angle of the complex modulus at 15°C. Results for the longitudinal mode of the cylinder.

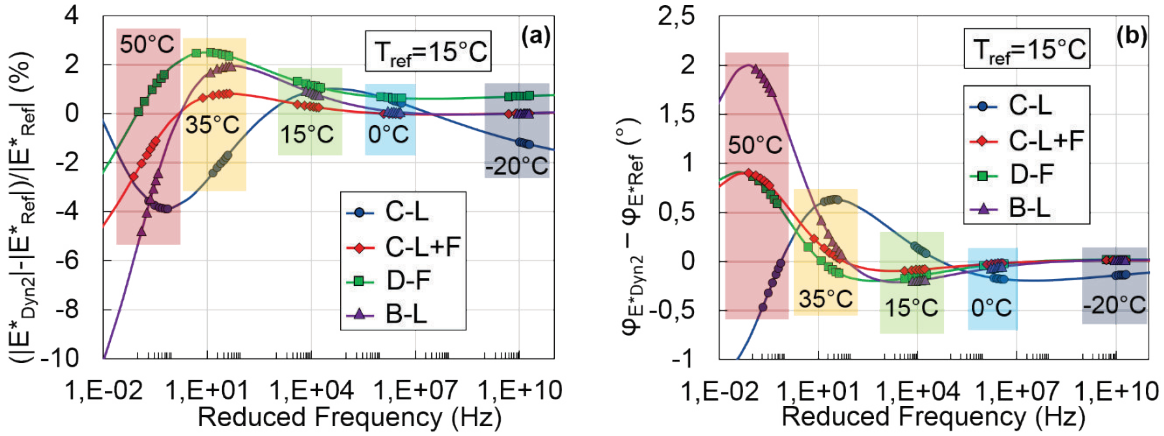

Figure 4.13. Master curve at 15°C of: (a) the relative difference between the norm of the complex modulus determined with method II ($|E^*_{Dyn2}|$) and of the reference LVE material ($|E^*_{Ref}|$) ;(b) the difference between the phase angle of the complex modulus determined with method II (φ_{E^*Dyn2}) and of the reference LVE material (φ_{E^*Ref}). Results for the four studied configurations.

4.3.1.3 Method III: determination of the complex modulus simulating the global LVE behaviour of the material in two steps

4.3.1.3.1 Principle of the method

This method is described in details in Paper IV. In this method, the constants of the 2S2P1D model and of the WLF equation simulating the global LVE behaviour of the material are determined in two distinct steps.

In the first step, the optimization process used in method II is applied at each temperature separately (i.e. only the FRF corresponding to the considered temperature is taken as input for the optimization). Therefore, the number of optimizations performed corresponds to the number of temperatures tested. The error function to minimize at each temperature is defined in equation (4-7). One set of the four 2S2P1D model constants optimized (E_0, $\tau_{E15°C}$, k and δ) is obtained at each temperature. The principle of the optimization process at each temperature is illustrated in Figure 4.14

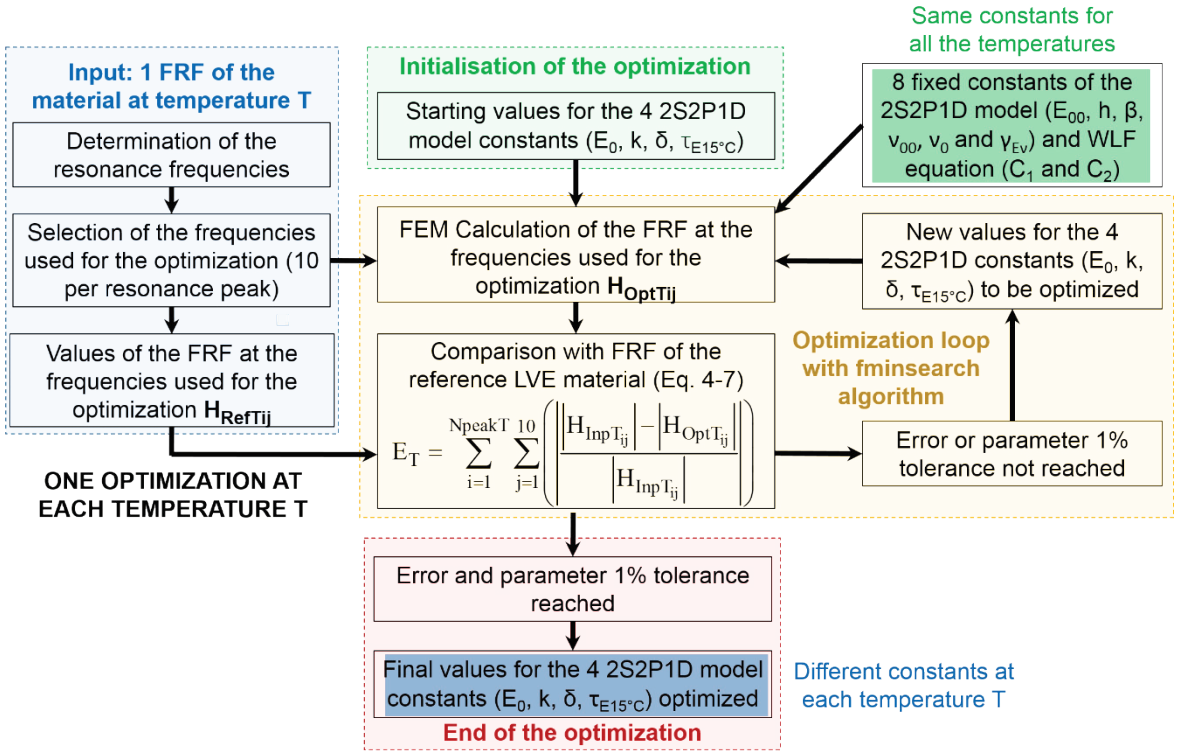

Figure 4.14. Principle of the optimization process repeated at each temperature in the first step of method III.

At each temperature, values of the complex modulus are back-calculated using the four 2S2P1D model constants (E_0, $\tau_{E15°C}$, k and δ) determined at the corresponding temperature. The six remaining constants of the 2S2P1D model (E_{00}, β, h, v_{00}, v_0 and γ_{Ev}) are fixed to the values of the constants of the reference LVE material (cf. Table 4.3) or to values determined from other tests. Six values of the complex modulus are back-calculated (E^*_{BC3}) at frequencies selected in a frequency range including all the resonance frequencies following the procedure illustrated in Figure 4.11:. This back-calculation process is explained in Figure 4.15.

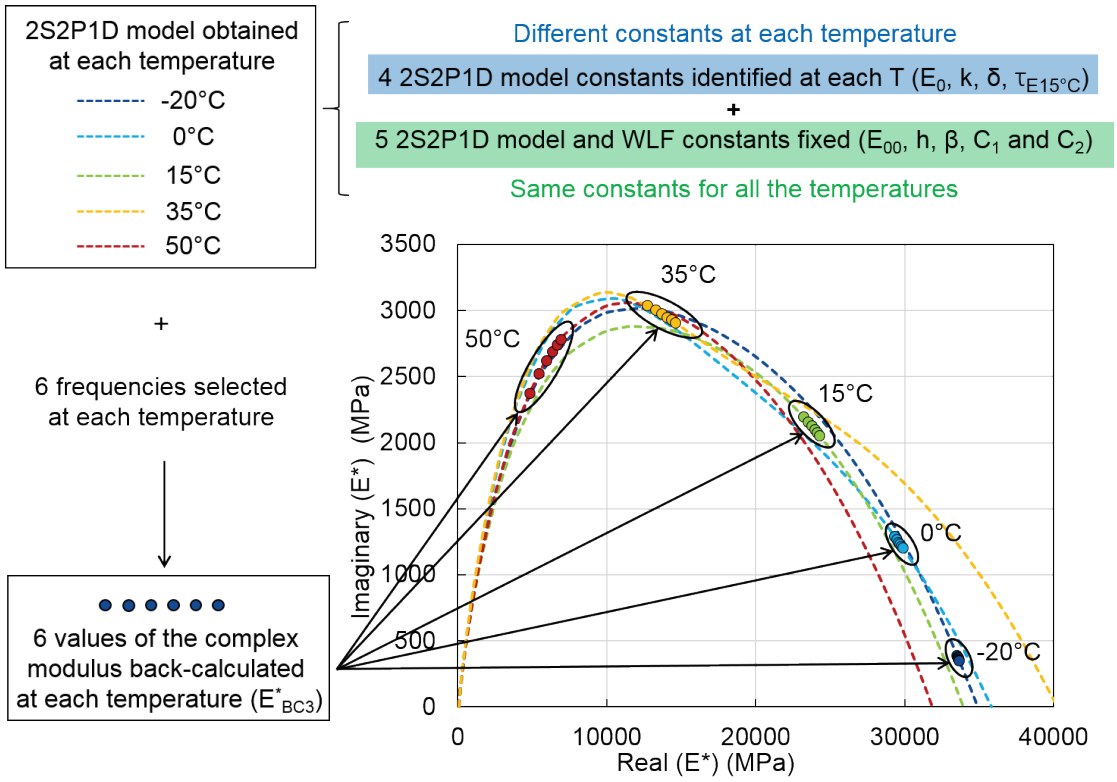

Figure 4.15. Principle of the back-calculation of the values of the complex modulus (E^*_{BC3}) at each temperature in the first step of method III.

In the second step of the method, the global LVE behaviour of the material is determined following the same process than in the second step of method I (cf. section 4.3.1.1.1). The only difference is that six values of the complex modulus are used at each temperature to fit the 2S2P1D model and WLF equation instead of only one value.

4.3.1.3.2 Results for the reference LVE material

Method III was tested on the reference LVE material using the same configurations, temperatures and hypothesis to calculate the reference FRFs than for method II (cf. section 4.3.1.2.2).

The values of the four constants E_0, $\tau_{E15°C}$, k and δ obtained at each temperature (in the first step) for the longitudinal mode of the cylinder are listed in Table 4.10. The values of the constants for the other configurations are given in APPENDIX F.

Table 4.10. Values of the four constants E_0, $\tau_{E15°C}$, k and δ of the 2S2P1D model determined at each temperature in the first step of method III for the longitudinal mode of the cylinder.

Temperature (°C)	E_0 (MPa)	$\tau_{E15°C}$ (s)	k	δ
-20	34 903	0.050	0.181	2.28
0	35 820	0.096	0.152	1.90
15	33 934	0.165	0.183	2.42
35	40 251	0.045	0.139	2.11
50	31 832	0.138	0.193	2.03

During the optimization at each temperature, the values of the six constants of the 2S2P1D model (E_{00}, β, h, ν_{00}, ν_0 and γ_{Ev}) that are not optimized were fixed to the values of the constants of the reference LVE material (cf. Table 4.3 and equation (4-8)) The constants listed in Table 4.10 are different at each temperature and are also different than those of the reference LVE material. It shows that they should only be used to calculate values of the complex modulus at the corresponding temperature and frequency range.

The values of the seven constants of the 2S2P1D model and WLF equation simulating the global LVE behaviour of the material determined in the second step of the method (E_0, $\tau_{E15°C}$, k, δ, h, C_1 and C_2) are given in Table 4.11.

Table 4.11. Values of the seven constants E_0, $\tau_{E15°C}$, k, δ, h, C_1 and C_2 of the 2S2P1D model and WLF equation simulating the global LVE behaviour of the material determined in the second step of method III for the four studied configurations.

	2S2P1D model					**WLF equation at 15°C**	
Configuration	**E_0 (MPa)**	**$\tau_{E15°C}$ (s)**	**k**	**δ**	**h**	**C_1**	**C_2**
C-L	35 300	0.076	0.169	2.01	0.50	28.0	198.1
C-P+F	35 000	0.117	0.172	2.27	0.54	34.6	244.8
B-L	35 100	0.102	0.169	2.20	0.52	30.0	211.2
D-F	35 000	0.088	0.170	2.10	0.51	29.5	207.4

The two remaining constants of the 2S2P1D model governing the value of the complex modulus (E_{00} and β) that are not optimized were fixed to the values of the constants of the reference LVE material (cf. Table 4.3). The FRFs after optimization and the global LVE FRFs are compared to the reference FRFs in Figure 4.16 for the longitudinal mode of the cylinder. The same comparisons will be found in APPENDIX F for the other configurations. The fit between the reference FRFs and both the FRFs after optimization and the global LVE FRFs is excellent. It is not as good for the flexural mode of the disc but the fit remains very satisfying. The best results are obtained when studying the longitudinal mode of the cylinder or of the straight beam.

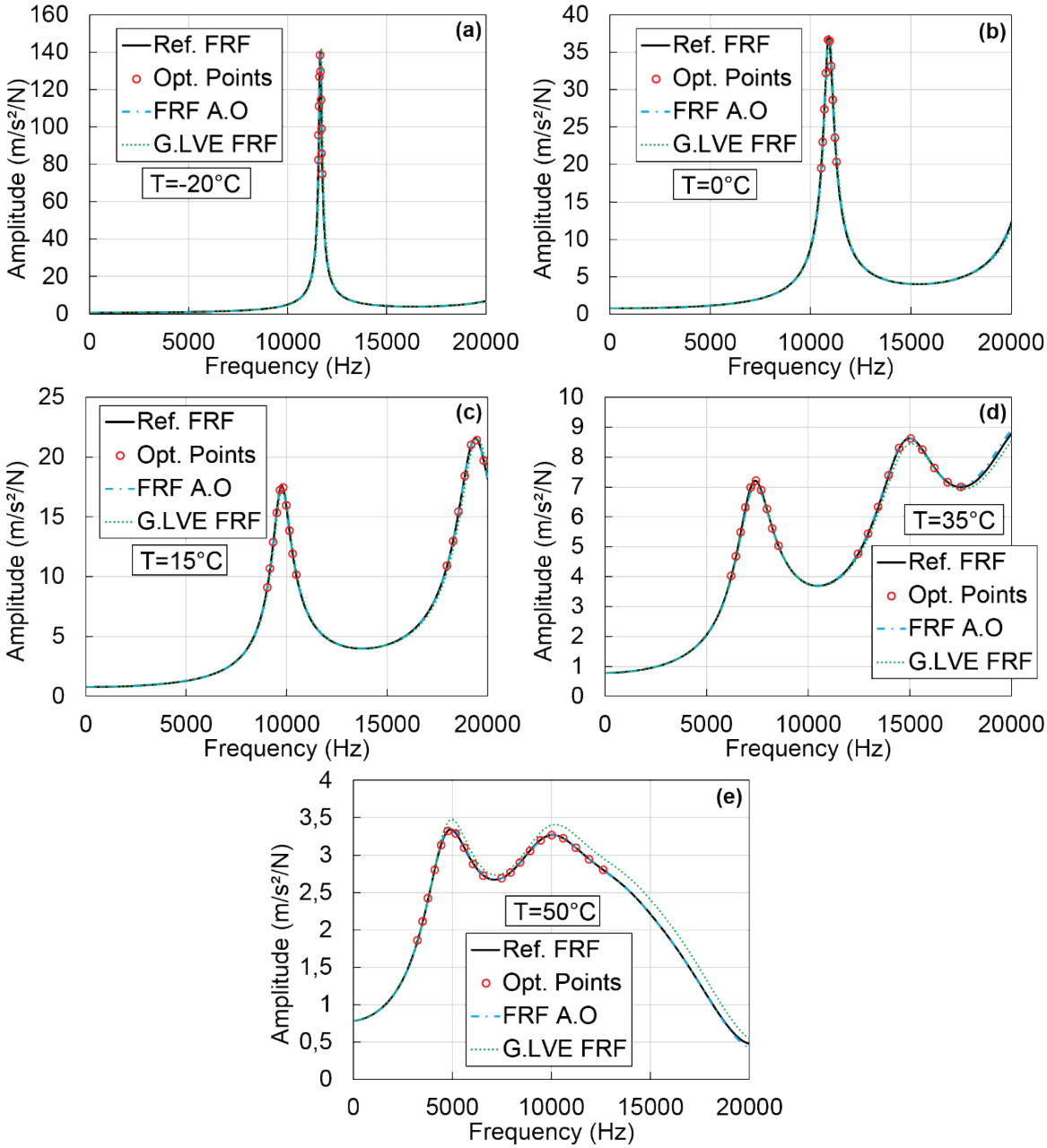

Figure 4.16. Comparison of the reference FRFs (noted Ref. FRF) with the FRFs after optimization (noted FRF A.O) and the global LVE FRFs (noted G.LVE FRF) for method III. Values of the reference FRFs at the frequencies where the optimization is performed (noted Opt. Points) are also plotted. Example for the longitudinal mode of the cylinder at: (a) -20°C; (b) 0°C; (c) 15°C; (d) 35°C; (e) 50°C.

Then, the values of E^*_{BC3} back-calculated in the first step (cf. Figure 4.15) and the values of E^*_{Dyn3} determined in the second step (cf. Figure 4.6) were compared with the values of $E^*_{Ref.}$ The Cole-Cole plot and the master curves at 15°C of the norm and phase angle of the complex modulus for the longitudinal mode of the cylinder are plotted in Figure 4.17. A very good agreement is seen between the values of E^*_{BC3} and E^*_{Dyn3} which demonstrates the good efficiency of the second step of the method. In addition, the values of E^*_{Dyn3} and E^*_{Ref} are also in good agreement, which shows the high accuracy of method III.

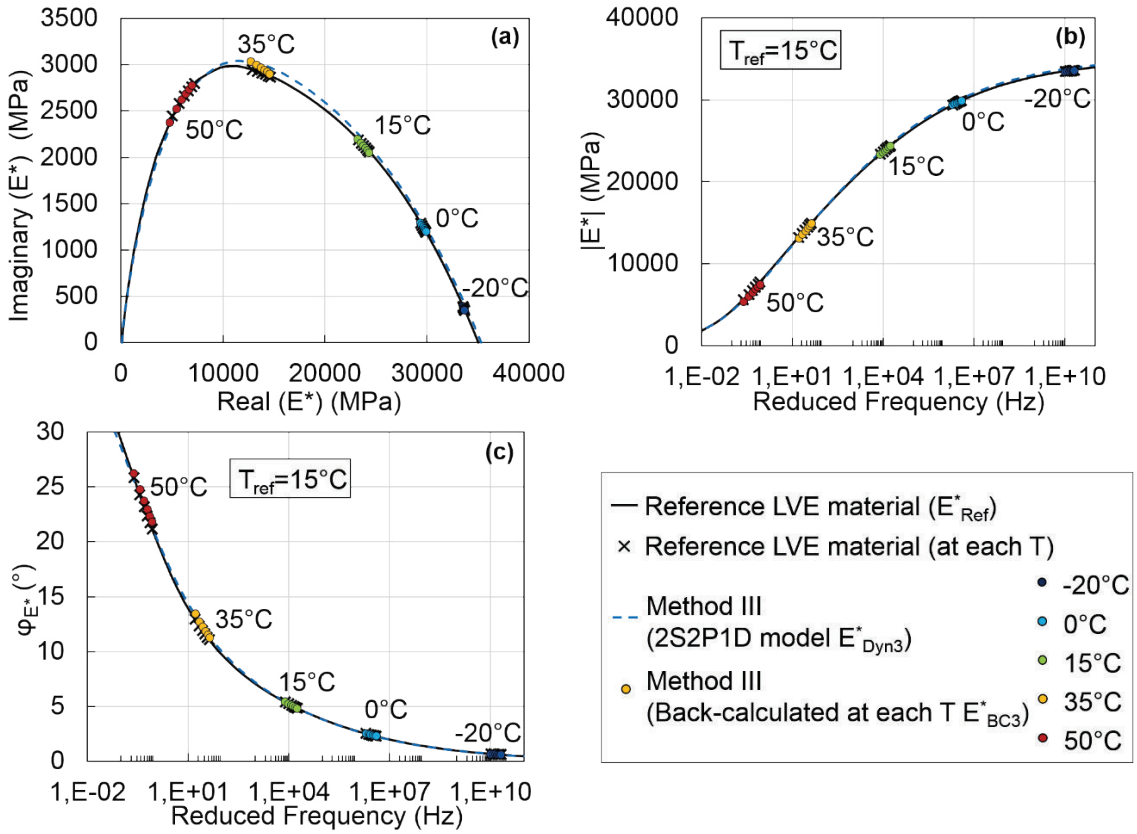

Figure 4.17. Comparison of the values of the complex modulus determined with method III (E^*_{BC3} and E^*_{Dyn3}) with the values of the complex modulus of the reference LVE material (E^*_{Ref}). (a) Cole-Cole plot; (b) and (c) master curves of the norm and of the phase angle of the complex modulus at 15°C. Results for the longitudinal mode of the cylinder.

Observations raised from Figure 4.17 are confirmed in Figure 4.18 in which the relative difference (respectively the difference) between the norm (respectively the phase angle) of E^*_{Dyn3} and E^*_{Ref} are plotted at 15°C for all studied configurations. The maximum difference is about 2% for the norm of the complex modulus and less than 1° for the phase angle.

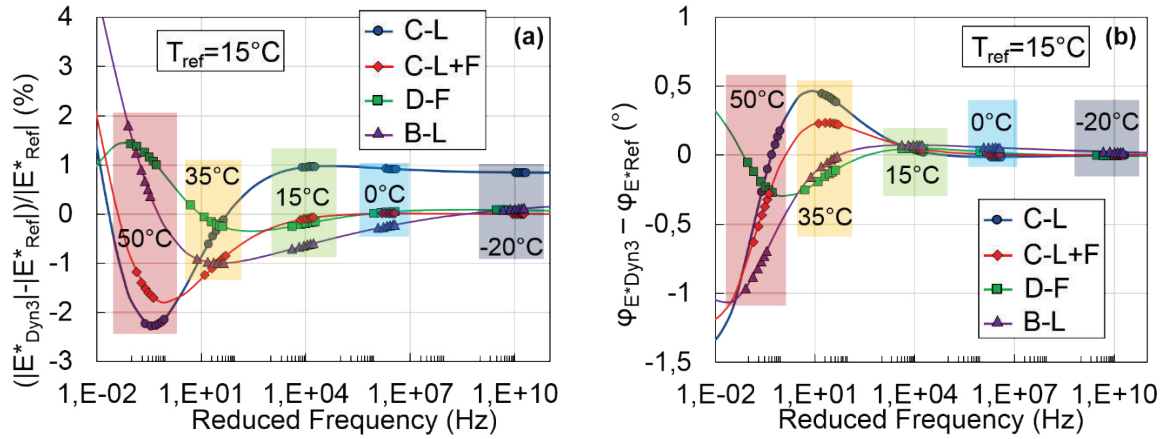

Figure 4.18. Master curve at 15°C of: (a) the relative difference between the norm of the complex modulus determined with method III ($|E^*_{Dyn3}|$) and of the reference LVE material ($|E^*_{Ref}|$) ;(b) the difference between the phase angle of the complex modulus determined with method III (φ_{E^*Dyn3}) and of the reference LVE material (φ_{E^*Ref}). Results for the four studied configurations.

In addition, the shift factors obtained in the second step of the method are compared to the shift factors of the reference LVE material in Figure 4.19 for all studied configurations. The different curves plotted in Figure 4.19 almost perfectly overlap and cannot be distinguished. The observations raised from Figure 4.18 and Figure 4.19 confirm that method III is very accurate. Moreover, the shift factors and the WLF equation of the material are determined with this method, which is a great advantage compared to method II.

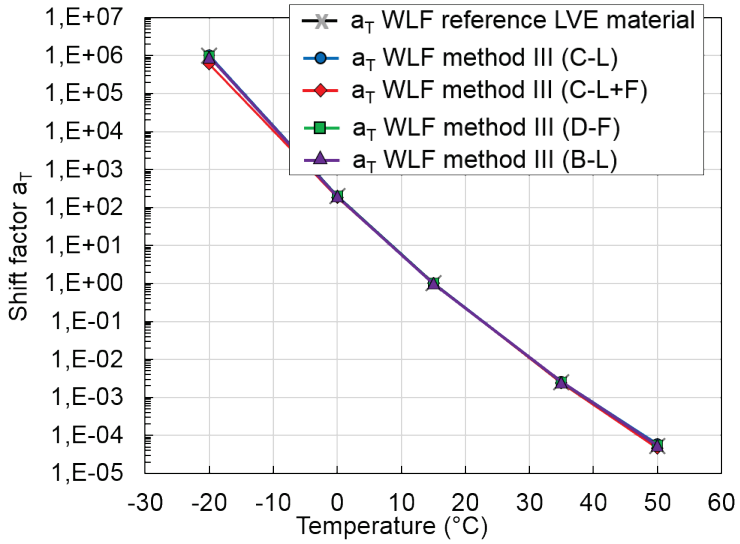

Figure 4.19. Comparison of the shift factors of the reference LVE material with the shift factors of the WLF equation determined with method III for the four studied configurations.

4.3.1.4 Method IV: determination of the complex modulus simulating the global LVE behaviour of the material in two steps using a simplified approach in the first step

4.3.1.4.1 Principle of the method

This method is based on the same principle than method III. However, in the first step of the method, a simplified approach that does not require a rheological model taking into account the frequency and temperature dependency of the behaviour is used. The behaviour of the material is simply modelled with a constant complex modulus value and a constant real Poisson's ratio fixed at 0.3. The Poisson's ratio is fixed at 0.3 because the parametric analysis of the LVE properties (cf. section 4.2.1) showed the small influence of the complex Poisson's ratio, and particularly of its phase angle, comparing to the influence of the complex modulus.

At each temperature, the norm and the phase angle of the complex modulus are determined at the first resonance frequency. Because the norm and phase angle of the complex modulus have separated effects on the FRFs calculation (cf. section 4.2.1), it is possible to back-calculate their values using two distinct dichotomy calculations repeated iteratively until the error on the amplitude at the first resonance frequency is less than 0.1% (cf. Figure 4.20):

- First, the norm of the complex modulus is determined by dichotomy so that the first resonance frequency f of the input FRF matches the first resonance frequency of the FRF calculated.

- Then, the phase angle of the complex modulus is determined by dichotomy so that the amplitude A at the first resonance frequency of the input FRF matches the amplitude at the first resonance frequency of the FRF calculated.

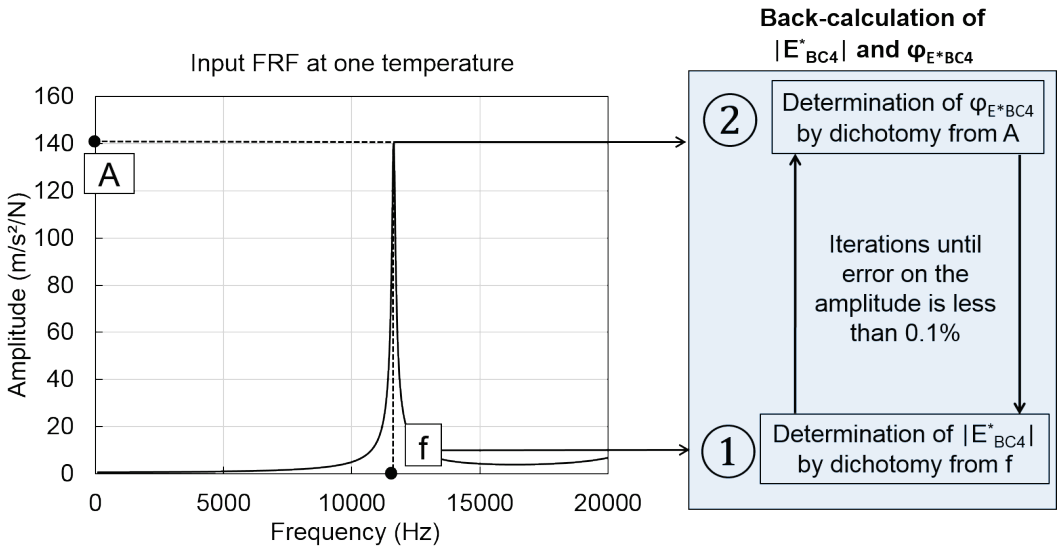

Figure 4.20. Principle of the back-calculation of the norm ($|E^*_{BC4}|$) and phase angle (φ_{E^*BC4}) of the complex modulus at each temperature from the first resonance frequency in the first step of method IV.

In the second step of the method, the same procedure than in methods I and III is applied (see Figure 4.6) to determine the global LVE behaviour of the material.

4.3.1.4.2 Results for the reference LVE material

The method described in the previous section was tested on the reference LVE material. The same configurations, temperatures and hypothesis to calculate the reference FRFs than for the methods II and III (cf. sections 4.3.1.2.2 and 4.3.1.3.2) were used for this method.

The values of the first resonance frequencies and of $|E^*_{BC4}|$ and φ_{E^*BC4} determined in the first step of the method at each temperature are given in APPENDIX G. The relative difference (respectively the difference) between the norm (respectively the phase angle) of $|E^*_{BC4}|$ and ($|E^*_{Ref}|$) is plotted against the temperature in Figure 4.21 for all studied configurations. It is seen in Figure 4.21 that differences appear for the flexural mode of the cylinder (up to 15% for the norm and 2.5° for the phase angle) and for the flexural mode of the disc (up to 8% for the norm and 1° for the phase angle) while there are almost no differences for the longitudinal mode of the cylinder and of the straight beam (less than 1% for the norm and 0.2° for the phase angle). This is probably an effect of the modelling of the Poisson's ratio with a constant real value. Indeed the Poisson's ratio has a limited influence for all modes of vibration, but its influence is negligible only for the first resonance of the longitudinal mode (cf. section 4.2.1). Consequently, the first step used in method IV is accurate only for the longitudinal mode and should not be used with other modes of vibration.

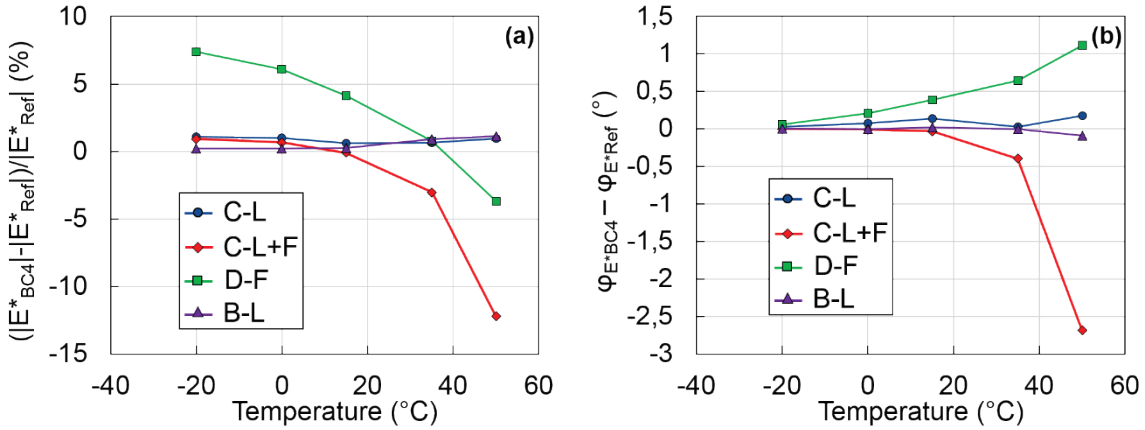

Figure 4.21. (a) Relative difference between the norm of the complex modulus determined in the first step of method IV ($|E^*_{BC3}|$) and of the reference LVE material ($|E^*_{Ref}|$) ;(b) difference between the phase angle of the complex modulus determined in the first step of method IV (φ_{E^*BC4}) and of the reference LVE material (φ_{E^*Ref}). Results for the four studied configurations.

In accordance with the results of the first step, only the longitudinal mode of the cylinder and of the straight beam were considered in the second step of the method. The values of E^*_{BC4} are in very good agreement with the values of E^*_{BC3} as seen in Figure 4.23. Consequently, the seven constants of the 2S2P1D model and WLF equation (E_0, $\tau_{E15°C}$, k, δ, h, C_1 and C_2) simulating the global LVE behaviour determined in the second step of method IV are the same than those determined in the second step of method III (cf. Table 4.11).

Using a simplified approach with a constant real value for the Poisson's ratio has an impact on the FRFs calculation that can be seen in Figure 4.22. The fit between the FRFs after optimization, the global LVE FRFs and the reference FRF is very good for frequencies below the first resonance frequency while slight deviations are seen for higher frequencies. These deviations from the reference FRFs are mostly due to the value of the Poisson's ratio that is fixed to 0.3 instead of being modelled with the 2S2P1D model. Moreover, deviations are more important for the FRFs after optimization than for the global LVE FRFs because the FRFs after optimization are calculated with a constant complex modulus independent of the frequency (E^*_{BC4}) contrarily to the global LVE FRFs calculated with the complex modulus of the 2S2P1D model which constants are determined in the second step (E^*_{Dyn4}) The same observations can be made for all the configurations (cf. APPENDIX G).

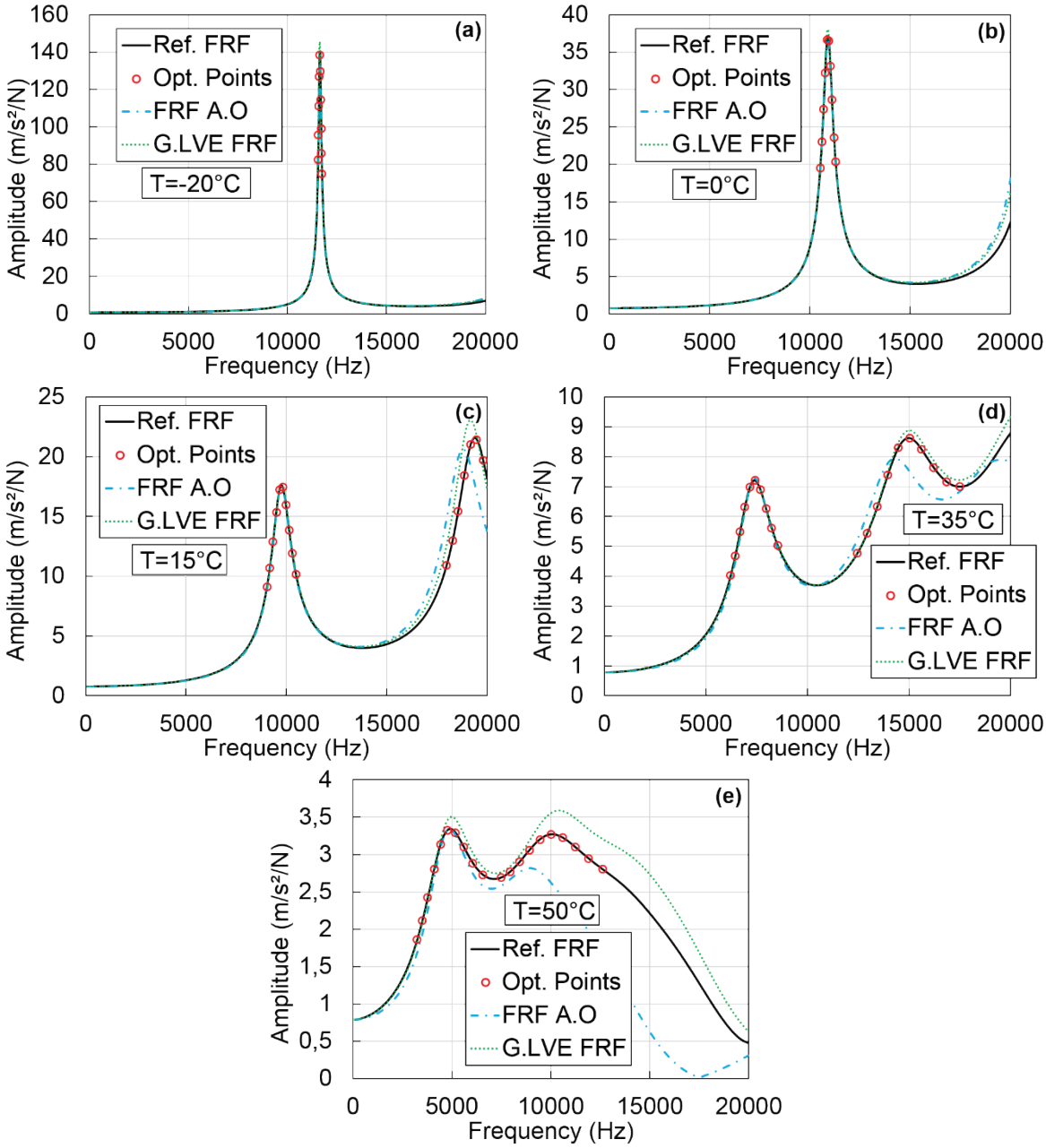

Figure 4.22. Comparison of the reference FRFs (noted Ref. FRF) with the FRFs after optimization (noted FRF A.O) and the global LVE FRFs (noted G.LVE FRF) for method IV. Values of the reference FRFs at the frequencies where the optimization is performed (noted Opt. Points) are also plotted. Example for the longitudinal mode of the cylinder at: (a) -20°C; (b) 0°C; (c) 15°C; (d) 35°C; (e) 50°C.

In Figure 4.23, values of the complex modulus determined with methods III (E^*_{BC3} and E^*_{Dyn3}) and IV (E^*_{BC4} and E^*_{Dyn4}) for the longitudinal mode of the cylinder are plotted along with values of $E^*_{Ref.}$. The same figure can be found in APPENDIX G for the longitudinal mode of the straight beam. A very good agreement is seen between the complex modulus values obtained with methods III and IV. Therefore, the simplified approach used in the first step of method IV does not introduce any bias to characterize the global LVE behaviour. Moreover, one value of the complex modulus back-calculated at each temperature seems to be sufficient to find the constants simulating the global LVE behaviour of the material. Method IV is quite interesting because the approach used in the first step is very easy to apply, it limits the number

of constants to identify at each temperature to two and it considerably reduces the computational time (a calculation for a given temperature is between five and ten times faster with method IV than with method III). However, as seen previously, method IV is only adapted for the longitudinal mode of vibration.

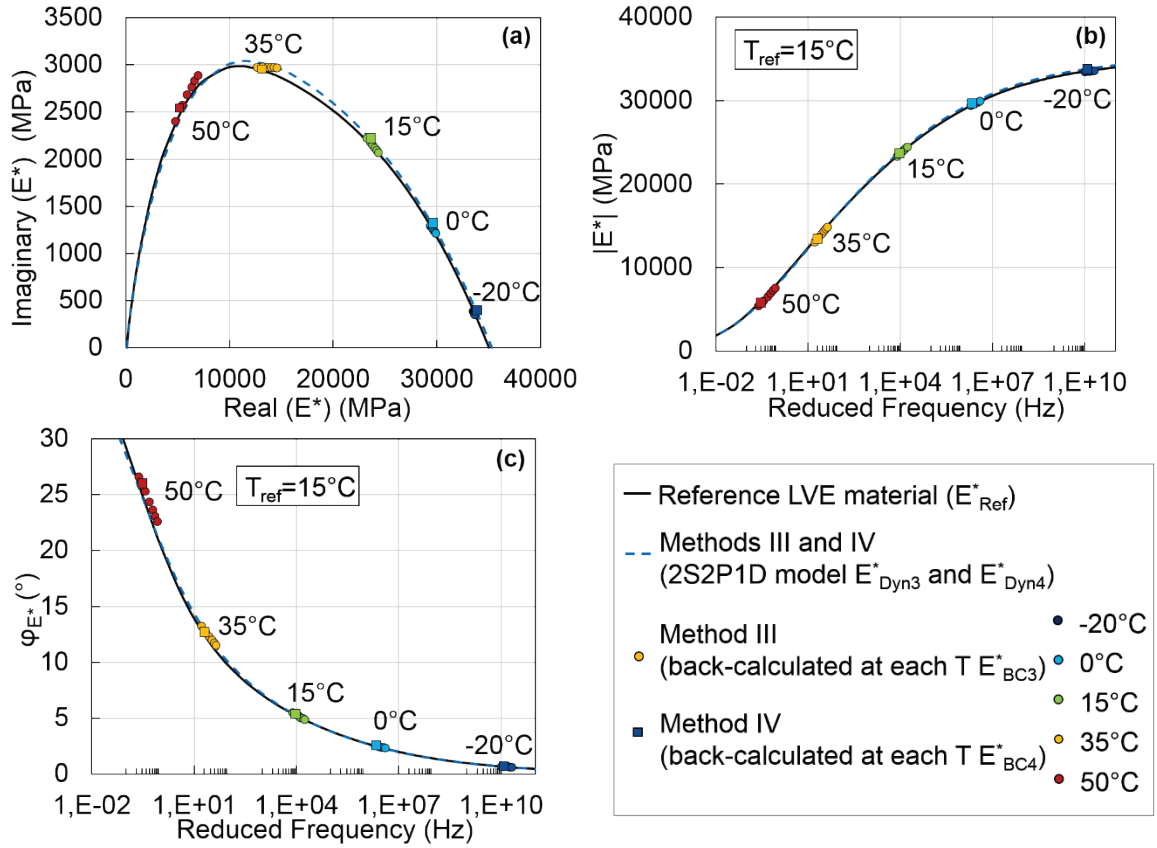

Figure 4.23. Comparison of the values of the complex modulus determined with methods III (E^*_{BC3} and E^*_{Dyn3}) and IV (E^*_{BC4} and E^*_{Dyn4}) with the values of the complex modulus of the reference LVE material (E^*_{Ref}). (a) Cole-Cole plot; (b) and (c) master curves of the norm and of the phase angle of the complex modulus at 15°C. Results for the longitudinal mode of the cylinder.

4.3.2 Method V: determination of the complex modulus and complex Poisson's ratio simulating the global LVE behaviour of the material in two steps

4.3.2.1 Principle of the method

This method is the only method that gives access to the complex Poisson's ratio. It is only applicable for the longitudinal mode of vibration. Similarly to methods III and IV, the method is divided into two steps.

In the first step of the method, the complex modulus of the material is modelled with the 2S2P1D model while the Poisson's ratio is modelled with a constant real value noted ν. At each temperature, a three-stages optimization process is used to determine the constants E_0, $\tau_{E15°C}$, k and δ of the 2S2P1D model and the real value ν of the Poisson's ratio. The two first stages aim to find realistic values of constants E_0, $\tau_{E15°C}$, k, δ and ν prior to the third stage. Constants E_{00},

h, β, C_1 and C_2 of the 2S2P1D model and WLF equation are fixed during the three stages of the process that is repeated at each temperature:

- The first step of method III is applied with two slight modifications:
  - Only the frequencies selected along the first resonance peak are used as input for the optimization.
  - The Poisson's ratio is modelled with a constant real value fixed to 0.3 instead of being modelled with the 2S2P1D model (cf. Figure 4.24).

The aim of this stage is to guarantee that final values of optimized constants E_0, $\tau_{E15°C}$, k and δ are representative of the material behaviour at the considered temperature. If it's not the case, the values of ν determined in the second stage could be completely incorrect. Only the longitudinal mode guarantees that this stage will provide values of E_0, $\tau_{E15°C}$, k and δ representative of the material behaviour at the considered temperature because it is the only mode for which the influence of the Poisson's ratio on the first resonance is negligible.

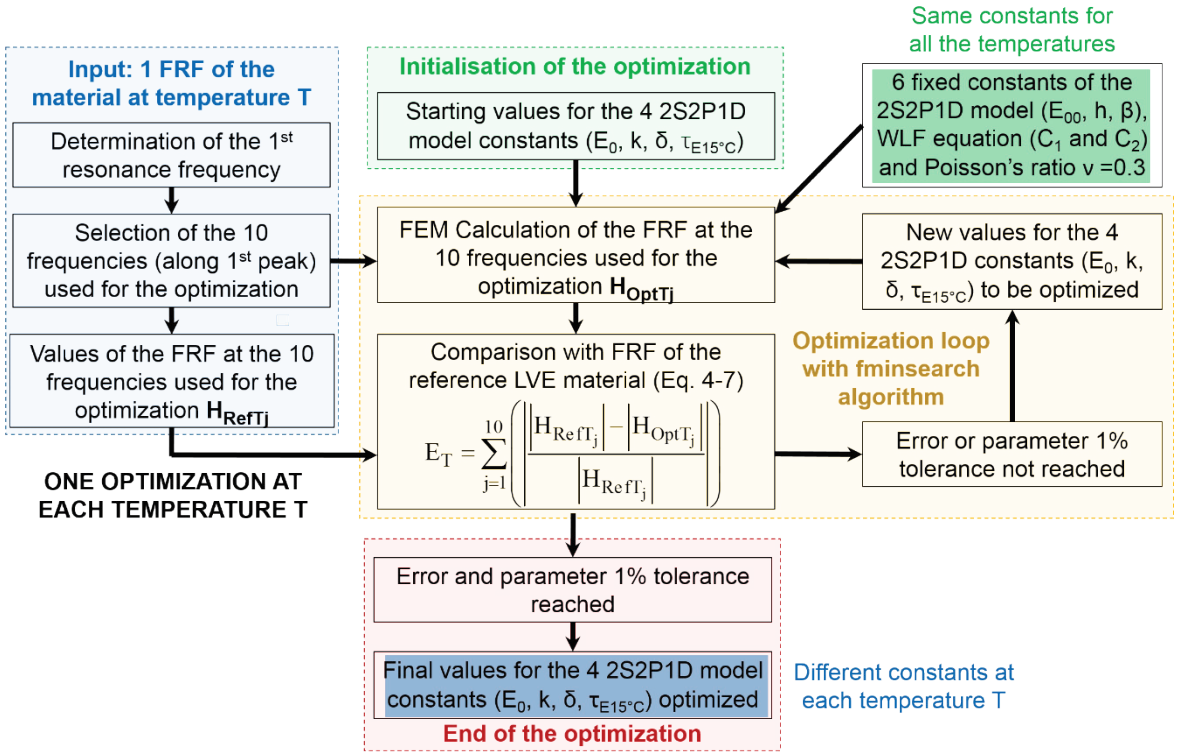

Figure 4.24. Principle of the first stage of the first step of method V.

- Then, constants E_0, $\tau_{E15°C}$, k and δ of the 2S2P1D model are fixed to the values obtained at the end of the first stage. The real value of the Poisson's ratio is adjusted by dichotomy until the second resonance frequency of the calculated FRF matches with the second resonance frequency of the input FRF. Consequently, it is not possible to use method V if only one resonance peak is available.
- Finally, the first step of method III is applied with one slight modification: the Poisson's ratio is modelled with a constant real value that is optimized along constants E_0, $\tau_{E15°C}$, k and δ of the 2S2P1D model (cf. Figure 4.25). The values of constants E_0, $\tau_{E15°C}$, k and δ of the 2S2P1D model and constant ν determined in the two first stages are used as starting values for the optimization.

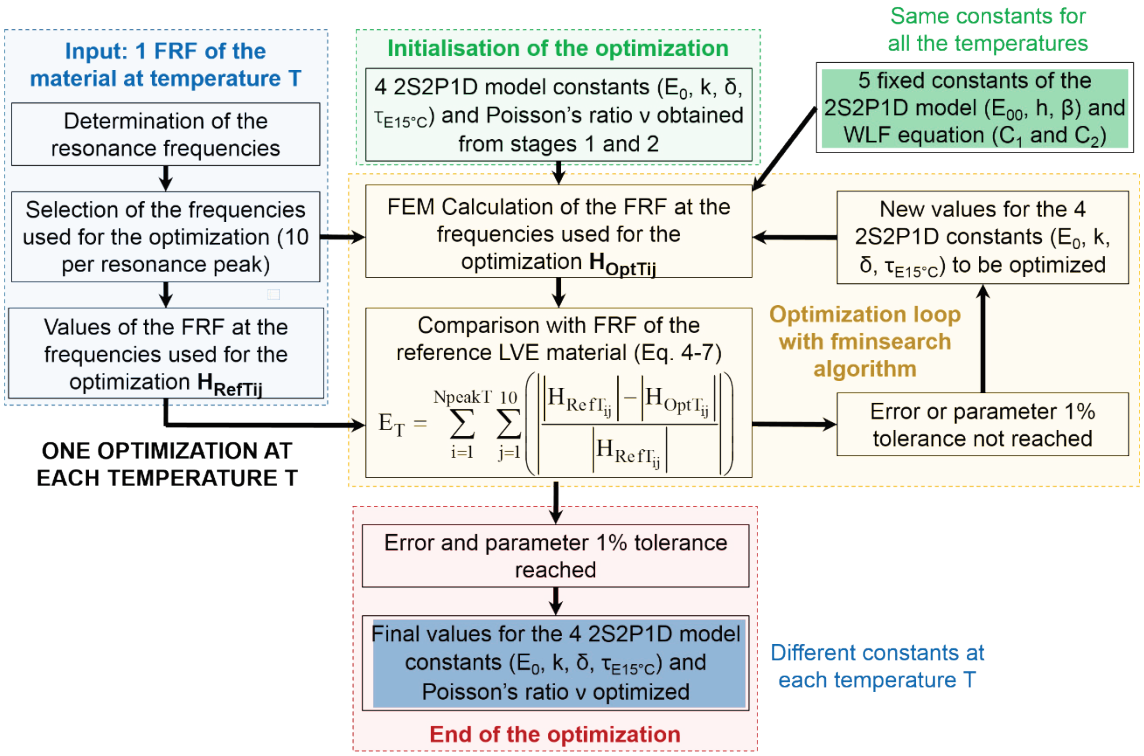

Figure 4.25. Principle of the third stage of the first step of method V.

In the second step, the same procedure than in methods I, III and IV (cf. Figure 4.6) is applied to determine the values of the seven constants of the 2S2P1D model and WLF equation (E_0, $\tau_{E15°C}$, k, δ, h, C_1 and C_2) simulating the global LVE behaviour of the material. In addition, the real values of the Poisson's ratio determined at each temperature in the first step of method V are used to fit the constants ν_{00}, ν_0 and $\tau_{\nu 15°C}$ of the 2S2P1D model assuming two hypotheses:

- The real values of the Poisson's ratio obtained at each temperature in the first step of the method are the values of the Poisson's ratio at the first resonance frequency of the corresponding temperature.
- The WLF equation determined for the complex modulus is also valid for the complex Poisson's ratio (Nguyen Q. T., Di Benedetto, Sauzéat, & Tapsoba, 2013).

The main advantage of this method is that the constants ν_{00}, ν_0 and $\tau_{\nu 15°C}$ of the 2S2P1D model can be determined in the second step of the method. It is the only inverse method proposed for which the complex Poisson's ratio can be determined.

4.3.2.2 Results for the reference LVE material

The method described in the previous section was tested on the reference LVE material. Because the method is adapted only for the longitudinal mode, the flexural mode of the disc and the longitudinal and flexural modes of the cylinder were not considered. The reference FRFs were calculated at the same temperatures and frequencies than for methods II, III and IV (cf. sections 4.3.1.2.2, 4.3.1.3.2 and 4.3.1.4.2). Due to the necessity to have at least two resonance frequencies at each temperature in this method (cf. section 4.3.1.4.1), reference FRFs were calculated for frequencies up to 30 kHz at -20°C and 0°C for the longitudinal mode of the cylinder.

The values of the five constants E_0, $\tau_{E15°C}$, k, δ and ν determined at each temperature (in the first step are given in APPENDIX H for both studied configurations. The values of E^*_{BC5} determined in the first step are very similar to the values of E^*_{BC3} determined in the first step of method III. Consequently, the constants of the 2S2P1D model and WLF equation (E_0, $\tau_{E15°C}$, k, δ, h, C_1 and C_2) simulating the global LVE behaviour determined in the second step of method V are the same than in methods III and IV (cf. Table 4.11). The values obtained for constants ν_{00}, ν_0 and $\tau_{\nu 15°C}$ of the 2S2P1D model are listed in Table 4.12. The value of constant $\gamma_{E\nu}$ (see equations (4-5) and (4-8)) is also given in Table 4.12. The values of constants ν_{00} and ν_0 are very close to those of the reference LVE material. The value of constant $\tau_{\nu 15°C}$ is a little bit different than for the reference LVE material but the ratio $\gamma_{E\nu}$ is equal to the ratio of the reference LVE material.

Table 4.12. Values of the constants ν_{00}, ν_0, $\tau_{\nu 15°C}$ and $\gamma_{E\nu}$ of the 2S2P1D model simulating the global LVE behaviour of the material that are identified in the second step of the fifth inverse method for the longitudinal mode of the cylinder and of the straight beam.

Configuration	ν_{00}	ν_0	$\tau_{\nu 15°C}$	$\gamma_{E\nu}$
C-L	0.445	0.188	2.40	0.0316
B-L	0.435	0.188	3.26	0.0316

The comparison of the FRFs is presented in Figure 4.26 for the longitudinal mode of the cylinder and can be found in APPENDIX H for the longitudinal mode of the straight beam. Both the FRFs after optimization and the global LVE FRFs are in very good agreement with the reference FRFs. The agreement for the FRFs after optimization is better than what was observed with method IV (cf. Figure 4.22), which shows the interest of optimizing the value of the Poisson's ratio in the first step of the method.

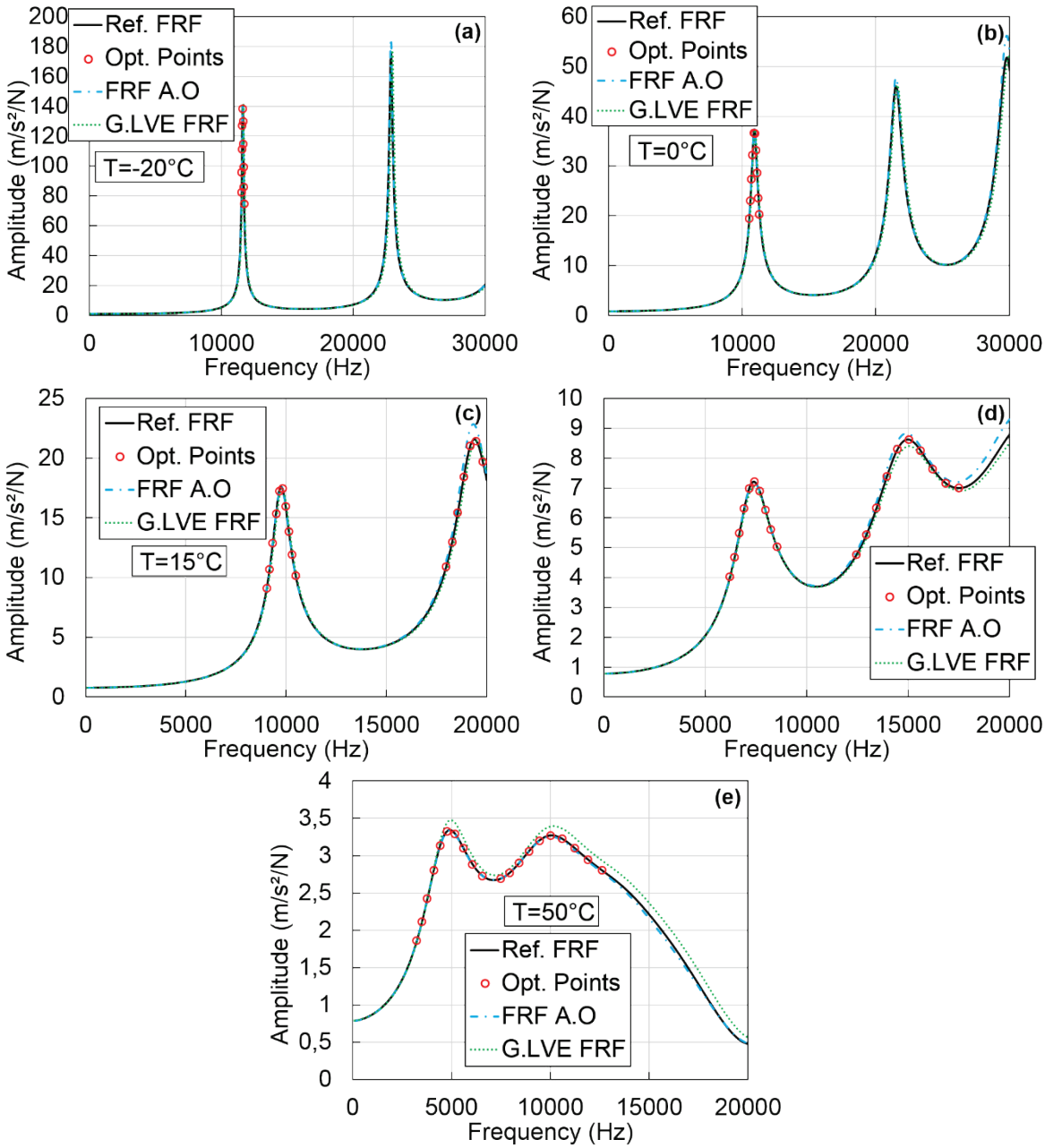

Figure 4.26. Comparison of the reference FRFs (noted Ref. FRF) with the FRFs after optimization (noted FRF A.O) and the global LVE FRFs (noted G.LVE FRF) for method V. Values of the reference FRFs at the frequencies where the optimization is performed (noted Opt. Points) are also plotted. Example for the longitudinal mode of the cylinder at: (a) -20°C; (b) 0°C; (c) 15°C; (d) 35°C; (e) 50°C.

In Figure 4.27, values of the complex modulus determined with methods III (E^*_{BC3} and E^*_{Dyn3}) and V (E^*_{BC5} and E^*_{Dyn5}) for the longitudinal mode of the cylinder are plotted along with values of $E^*_{Ref.}$. The same figure can be found in APPENDIX H for the longitudinal mode of the straight beam. A very good agreement is seen between the complex modulus values obtained with methods III and V and of the reference LVE material, which confirms the good accuracy of method V.

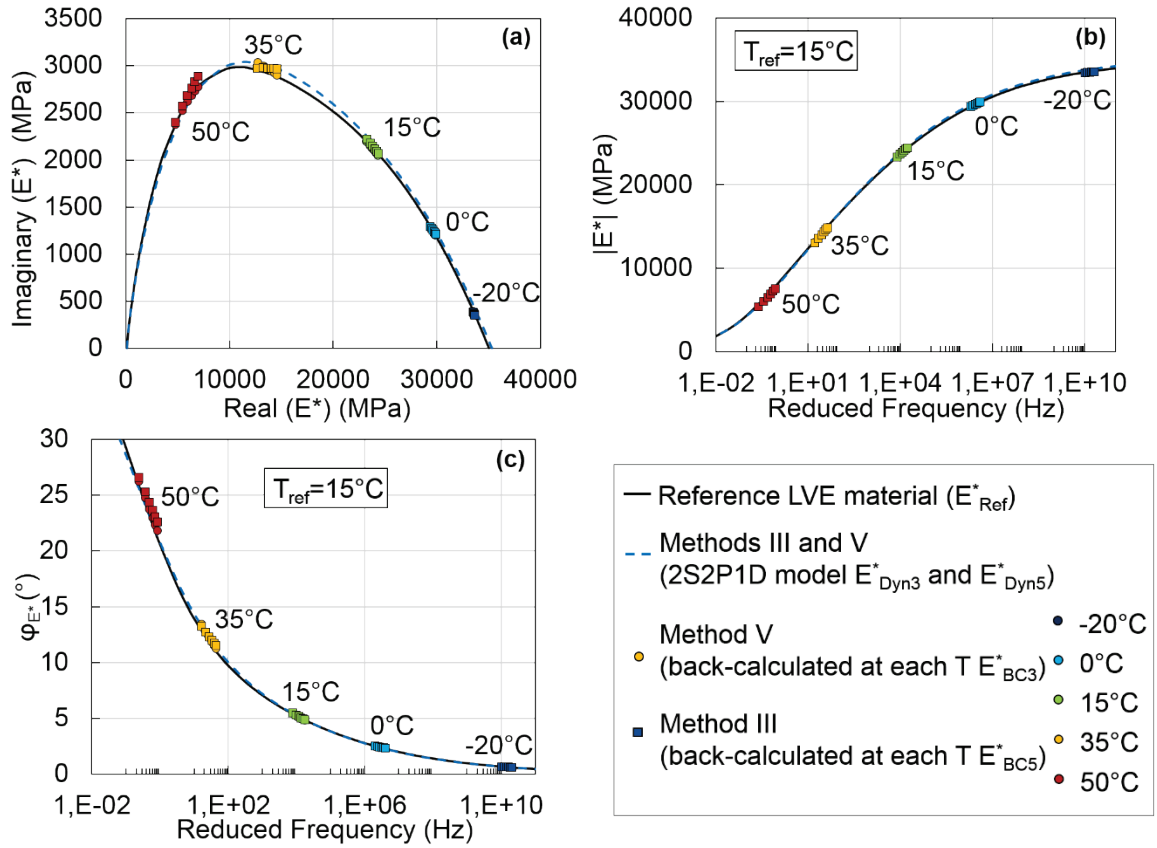

Figure 4.27. Comparison of the values of the complex modulus determined with methods III (E^*_{BC3} and E^*_{Dyn3}) and V (E^*_{BC5} and E^*_{Dyn5}) with the values of the complex modulus of the reference LVE material (E^*_{Ref}). (a) Cole-Cole plot; (b) and (c) master curves of the norm and of the phase angle of the complex modulus at 15°C. Results for the longitudinal mode of the cylinder.

The real values of the Poisson's ratio back-calculated at each temperature in the first step (noted ν_{BC5}) and the values of the complex Poisson's ratio simulating the global LVE behaviour of the material determined in the second step (noted ν^*_{Dyn5}) are compared with the values of the complex Poisson's ratio of the reference LVE material (noted ν^*_{Ref}) in Figure 4.28. The same figure can be found in APPENDIX H for the longitudinal mode of the straight beam. The values of ν_{BC5} and ν^*_{Dyn5} are in good agreement with the values of ν^*_{Ref}. It demonstrates that the complex Poisson's ratio is determined accurately with method V. This is confirmed in Figure 4.29 where master curves at 15°C of the relative difference (respectively the difference) between the norm (respectively the phase angle) of ν^*_{Dyn5} and ν^*_{Ref}. are plotted for both studied configurations. The maximum relative difference is about 3% for the norm of the complex Poisson's ratio and the maximum difference is about 0.15° for the phase angle of the complex Poisson's ratio.

Method V is the only method that enables to determine the complex Poisson's ratio, using the longitudinal mode of vibration. As demonstrated in the previous paragraphs, the characterization of the global three-dimensional LVE behaviour of the material is very accurate with method V. Therefore, method V is well-adapted when the characterization of the complex Poisson's ratio is an objective. However, it is the most complex proposed method and it is more recommended to use methods III or IV when characterizing only the complex modulus.

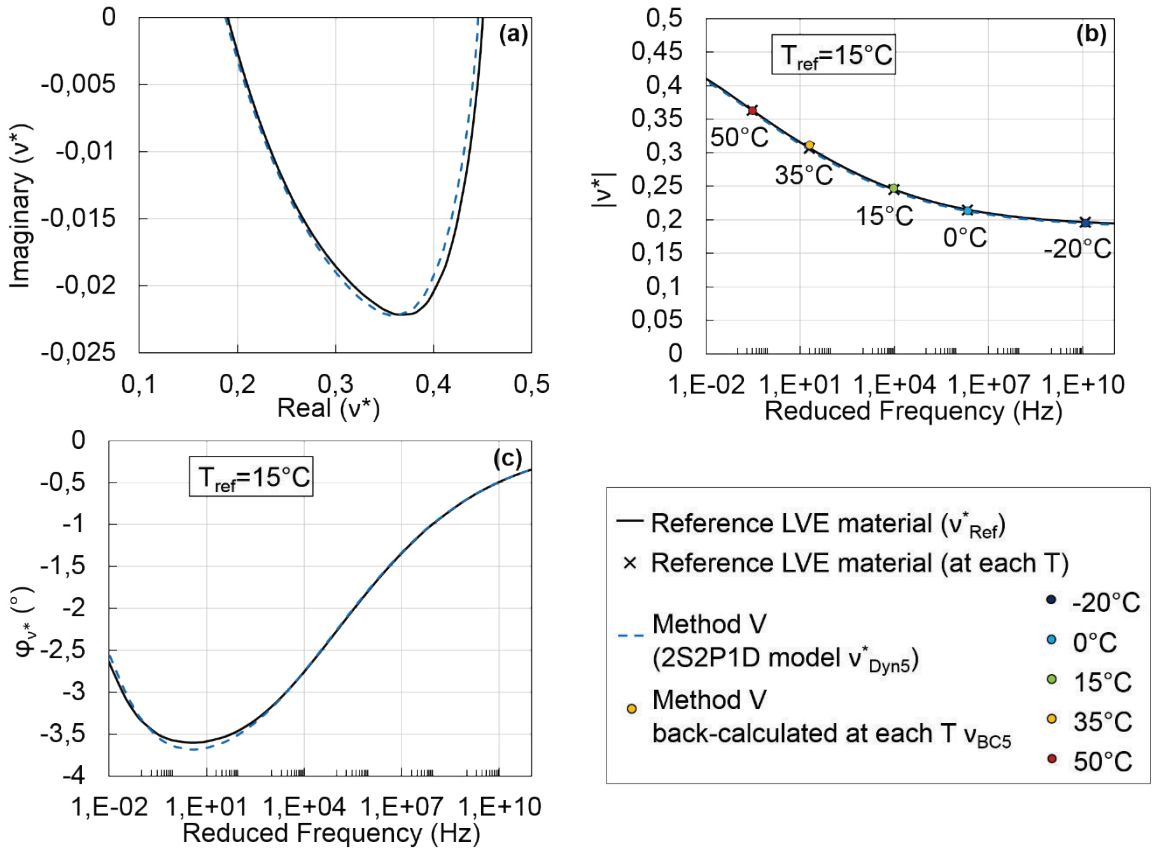

Figure 4.28. Comparison of the values of the complex Poisson's ratio determined with methods V (real values ν_{BC5} and ν^*_{Dyn5}) with the values of the complex Poisson's ratio of the reference LVE material (ν^*_{Ref}). (a) Cole-Cole plot; (b) and (c) master curves of the norm and of the phase angle of the complex modulus at 15°C. Results for the longitudinal mode of the cylinder.

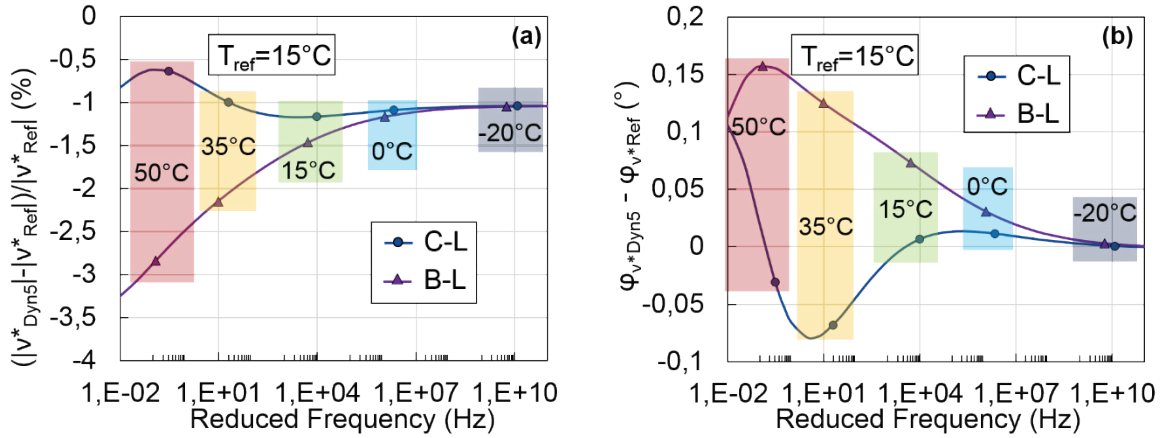

Figure 4.29. Master curve at 15°C of: (a) the relative difference between the norm of the complex Poisson's ratio determined with method V ($|\nu^*_{Dyn5}|$) and of the reference LVE material ($|\nu^*_{Ref}|$) ;(b) the difference between the phase angle of the complex Poisson's ratio determined with method V (φ_{ν^*Dyn5}) and of the reference LVE material (φ_{ν^*Ref}). Results for the two studied configurations.

4.3.3 Summary and remarks about the different methods

Method I is not adapted to characterize the LVE behaviour of bituminous mixtures on a wide frequency and temperature range because of its limits for the intermediate and high temperatures (as can be seen in section 4.3.1.1.2). In method II, the optimization proposed follows a global approach, which may not be adapted for application to experimental measurements. Therefore, these two methods are not recommended for application to bituminous mixtures specimens.

The last three methods are all very accurate and are recommended to characterize the LVE behaviour of bituminous mixtures specimens from dynamic measurements. The similarities and differences between these three methods are detailed in Figure 4.30. The three methods are based on the same approach divided in two main steps:

- In the first step, an optimization process is repeated at each tested temperature to obtain the LVE properties at the corresponding temperature.
- In the second step, the global LVE behaviour of the material is determined using the results obtained at each temperature in the first step. The same five constants of the 2S2P1D model (E_0, $\tau_{E15°C}$, k, δ and h) and two constants of the WLF equation (C_1 and C_2) constants are determined with a similar process than the one used when fitting the 2S2P1D model with experimental complex modulus data.

Though the general principle of the three methods is the same, some differences exist. The main differences are:

- The modelling of the complex modulus in the first step of the methods is different:
  - In methods III and V, the complex modulus is modelled with the 2S2P1D model.
  - In method IV, the complex modulus is simply modelled with a norm and a phase angle independents of the frequency.
- The modelling of the complex Poisson's ratio in the first step of the methods is also different:
  - In method III, the complex Poisson's ratio is modelled with the 2S2P1D model, with constants ν_{00}, ν_0 and $\gamma_{E\nu}$ fixed.
  - In method IV, the Poisson's ratio is fixed at 0.3.
  - In method V, the Poisson's ratio is modelled with a real value independent of the frequency that is identified at each temperature.
- The complex modulus is back-calculated at each temperature for several frequencies (six in this study) selected in a frequency range including all resonance frequencies in methods III and V while only one value is back-calculated at the first resonance frequency with method IV.
- Methods IV and V are only accurate for the longitudinal mode of vibration.
- Method IV has quite interesting advantages comparing to method III and V:
  - It does not require to use a rheological model taking into account the frequency and temperature dependency of the behaviour in the first step.
  - Only two constants are determined in the first step (four are determined in method III and five in method V).

  - The optimization process in the first step is very easy to apply because the two determined constants are obtained by dichotomy.
  - Thanks to the previous observations, the computational time is considerably reduced in the first step of method IV (between five and ten times faster than methods III and V).
- Method V is the only method for which the complex Poisson's ratio can be determined.

In addition, results from our back-calculations for the reference LVE material, for all studied vibration modes, showed that complex modulus obtained at each temperature in the first step are quite close for the three methods. Consequently, the values of the seven 2S2P1D model and WLF equation constants determined in the second step are also quite close or identical in our case. It is therefore recommended to use method V only if the characterization of the complex Poisson's ratio is targeted. In the other cases, methods III and IV are more recommended. Method IV is the best choice to simplify the calculations and to reduce the computational time but it is only accurate for the longitudinal mode of vibration.

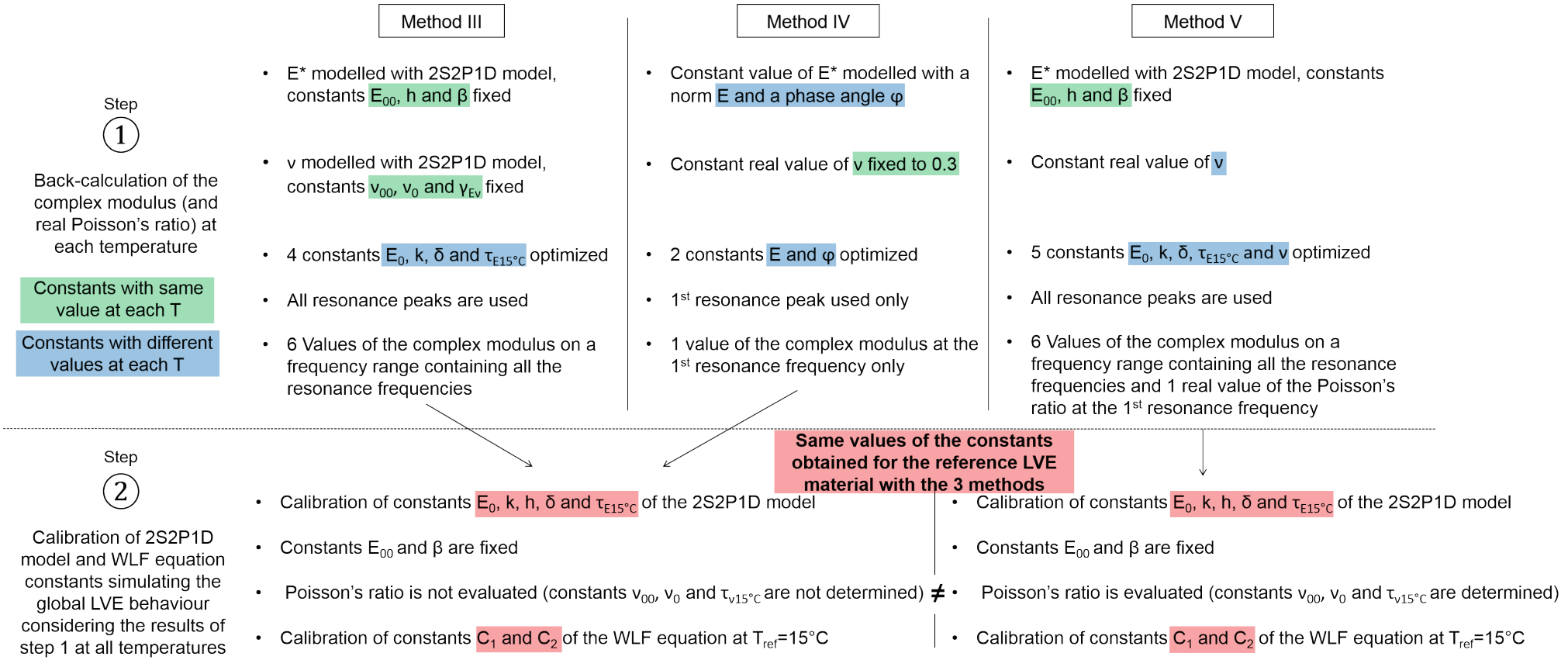

Figure 4.30. Comparison of methods III, IV and V. Values of constants noted as fixed are set to the values of the reference LVE material or to values determined from other tests.

5 EXPERIMENTAL CAMPAIGNS

Five experimental campaigns were carried out in the course of this thesis. The aim of this chapter is to present the materials tested in the different campaigns and the tests performed. A summary of the results is given for each experimental campaign while all the results can be found either in the papers attached to this thesis or in appendices. The first experimental campaign is part of an international project between French and Swedish laboratories called FSDyn. The four other experimental campaigns correspond to tests performed on different types of bituminous mixtures: a material with an optimized granular skeleton (MOGS), a Swedish mixture (SM), a material with high reclaimed asphalt pavement content (MHRAPC) and materials from airport pavement (MAP). Table 5.1 gives an overview of the samples tested in each experimental campaign and the modes of vibration used for the dynamic tests. The samples for which cyclic tension-compression tests were performed are also specified.

Table 5.1. Overview of the five experimental campaigns.

Experimental campaign	Samples	Mode of vibration	Cyclic T.C test
FSDyn	2 cylinders	Longitudinal	Yes
	2 straight beams	Longitudinal	No
	4 discs	Flexural	No
MOGS	2 cylinders	Longitudinal	Yes
SM	1 straight beam	Longitudinal	Yes
MHRAPC	3 cylinders	Longitudinal	Yes
MAP	14 cylinders	Longitudinal	On 2 cylinders

The main focuses of the experimental campaigns are to demonstrate the repeatability of the dynamic tests from one sample of a material to another and to compare the results obtained from dynamic tests with the results obtained from cyclic tension-compression tests that are commonly used to characterize bituminous mixtures LVE properties.

In the five presented experimental campaigns, different comparisons are carried out. The notations used are introduced hereafter. Regarding the FRFs that are compared:

- The FRFs calculated with the LVE properties or the constants of the 2S2P1D model determined at each temperature in the first step of the inverse methods. They are called FRFs after optimization and are noted FRF A.O.
- The FRFs calculated with the constants of the 2S2P1D model and WLF equation simulating the global LVE behaviour of the material determined in the second step of the inverse methods. They are called global LVE FRFs and are noted G.LVE.FRF.
- The FRFs measured experimentally from dynamic tests are called experimental FRFs and are note Exp. FRF.

Regarding the complex modulus values that are compared:

- The complex modulus determined from dynamic tests in the first step of the methods, noted E^*_{BCp} (norm $|E^*_{BCp}|$ and phase angle φ_{E^*BCp}) where p is the index of the considered method (p=2, 3, 4 or 5 in this section).
- The complex modulus of the 2S2P1D model simulating the global LVE behaviour of the material determined from dynamic tests in the second step of the methods, noted E^*_{Dynp} (norm $|E^*_{Dynp}|$ and phase angle φ_{E^*Dynp}) where p is the index of the considered method (p=2, 3, 4 or 5 in this section).
- The experimental complex modulus data obtained from cyclic tension-compression tests, noted E^*_{ExpTC} (norm $|E^*_{ExpTC}|$ and phase angle φ_{E^*ExpTC}).
- The complex modulus of the 2S2P1D model simulating the global LVE behaviour of the material determined from tension-compression tests experimental results, noted E^*_{TC} (norm $|E^*_{TC}|$ and phase angle φ_{E^*TC}).

Regarding the complex Poisson's ratio values that are compared:

- The real Poisson's ratio determined from dynamic tests in the first step of method V, noted ν_{BC5}.
- The complex Poisson's ratio of the 2S2P1D model simulating the global LVE behaviour of the material determined from dynamic tests in the second step of method V, noted ν^*_{Dyn5} (norm $|\nu^*_{Dyn5}|$ and phase angle φ_{ν^*Dyn5}).
- The experimental complex Poisson's ratio data obtained from cyclic tension-compression tests, noted ν^*_{ExpTC} (norm $|\nu^*_{ExpTC}|$ and phase angle φ_{ν^*ExpTC}).
- The complex Poisson's ratio of the 2S2P1D model simulating the global LVE behaviour of the material determined from tension-compression tests experimental results, noted ν^*_{TC} (norm $|\nu^*_{TC}|$ and phase angle φ_{ν^*TC}).

5.1 French-Swedish project for the evaluation of bituminous mixtures properties from dynamic tests (FSDyn)

The first experimental campaign is part of an international project called FSDyn project. This international project was funded by the Swedish transport administration. It is a collaboration between three Swedish companies (PEAB asphalt, SKANSKA and NCC), the Swedish national road and transport research institute (VTI), a French company (EIFFAGE) and our LTDS laboratory at the "Ecole nationale des travaux publics de l'état" (ENTPE). The principal objective of this project was to evaluate the reproducibility of the dynamic test developed in this thesis between different laboratories. To do that, dynamic tests were performed on the same eight specimens by each laboratory with their own experimental devices and experimental measurements were compared. Moreover, cyclic tension-compression tests were performed at ENTPE laboratory on two specimens used in the project to add a comparison between the results of dynamic tests and more conventional cyclic tests. The project is still on-going and some results such as the comparison of the LVE properties determined by the different laboratories are missing. Full results of the project will be further published in scientific journals or presented in conferences. The main findings up until now are presented in the next sections.

5.1.1 Materials

Two different materials were used in this project. The first material is a Swedish base course bituminous mixture produced by PEAB asphalt and labelled ABS. It has a continuous 0/16 grading curve and a 70/100 bitumen. Two disc specimens (ABS-D9 and ABS-D10) of this material were tested in the project. The second material is a French surface course bituminous mixture with an optimized granular skeleton produced by EIFFAGE and called GB5. This material. has a continuous 0/14 grading curve, it contains 30% of RAP and the bitumen is a 35/50 polymer modified bitumen. More details about the materials will be found in APPENDIX I. Six specimens of this materials were tested in the FSDyn campaign: two cylinders (GB5-C1 and GB5-C2), two straight beams (GB5-B2 and GB5-B4) and two discs (GB5-D1 and GB5-D3). Table 5.2 gives some details about the eight specimens considered in this experimental campaign.

Table 5.2. Specimens tested in the FSDyn experimental campaign. (D stands for discs, C for cylinders and B for straight beams).

Specimen	H (mm)	D (mm)	W (mm)	L (mm)	Density (kg/m^3)	Void ratio (%)
ABS-D9	40.6	150.0	x	x	2 450	2.6
ABS-D10	40.4	150.0	x	x	2 443	2.9
GB5-D1	32.0	99.7	x	x	2 422	2.4
GB5-D3	31.4	99.8	x	x	2 439	1.7
GB5-C1	162.4	64.2	x	x	2 403	3.1
GB5-C2	157.8	64.3	x	x	2 366	4.6
GB5-B2	50.2	x	50.3	299.6	2 399	3.3
GB5-B4	49.8	x	50.4	300.0	2 409	2.9

5.1.2 Tests performed

The dynamic tests were performed at five temperatures and a conditioning time of four hours between each temperature was respected. Therefore, the total duration of the test is twenty hours. Because of the different bitumen of the two materials, the damping properties change, especially for the high temperatures. As a result, specimens of the ABS material that are made with a softer bitumen must be tested at lower maximum temperatures than the GB5 specimens (30°C and 40°C against 35°C and 50°C as seen in Figure 5.1). The same three other temperatures are used for both materials (-20°C, 0°C and 15°C). The chronology of the tests is detailed in Figure 5.1.

The four discs were tested in flexural mode while the two cylinders and the two straight beams were tested in longitudinal mode. Our laboratory was the first to test the GB5 specimens and the last to test the ABS specimens. In addition, dynamic tests were performed a second time on the two GB5 cylinders at the end of the project. Following the second round of dynamic tests, cyclic tension-compression tests were performed on these two cylinders. The dates of the different tests and the modes of vibration used for the dynamic tests are summarized in Table 5.3

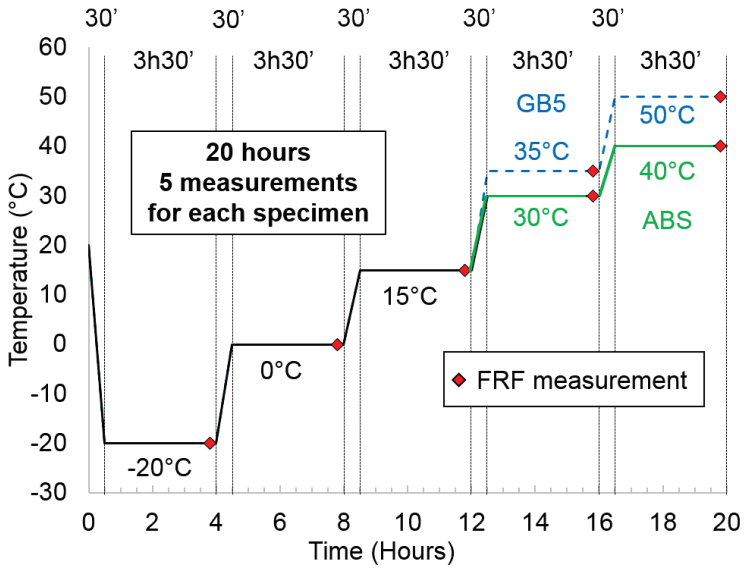

Figure 5.1 Chronology of the dynamic tests in the FSDyn experimental campaign.

Table 5.3. Summary of the tests performed in the FSDyn experimental campaign.

Specimen	Date of dynamic tests	Mode of vibration	Date of cyclic T.C tests
ABS-D9	25/10/17	Flexural	x
ABS-D10	27/10/17	Flexural	x
GB5-D1	18/09/17	Flexural	x
GB5-D3	20/09/17	Flexural	x
GB5-C1	29/09/17 08/06/18	Longitudinal	25/06/18
GB5-C2	01/10/17 10/06/18	Longitudinal	02/07/18
GB5-B2	25/09/18	Longitudinal	x
GB5-B4	27/09/18	Longitudinal	x

5.1.3 Results

5.1.3.1 Comparison of the FRFs measurements from all laboratories

One of the main interest of the FSDyn project is that the same eight specimens were tested by all laboratories. Therefore, it is possible to compare directly the FRFs measured by the five different laboratories. The relative standard deviation (RSD) was calculated for the two or three first resonance frequencies and amplitudes for each specimen tested. The results are plotted in function of the temperature in Figure 5.2. It is seen in Figure 5.2 that the amplitude variability is far more important than the frequency variability. Indeed, the average RSD is of about only 1.5% for the resonance frequencies while it is of about 25% for the amplitudes. This indicates that the measurements of the resonance frequencies are more accurate than the measurements of the amplitudes. Also, it is seen that the frequency variability increases with temperature. This is especially true for the discs (in green) which present the highest RSD values both for the resonance frequencies and amplitudes. Since the discs are the only geometry tested in flexural mode, the previous observations suggest to choose cylinders (in blue) or straight beams (in red) tested in longitudinal mode to reduce the variability of the measurements.

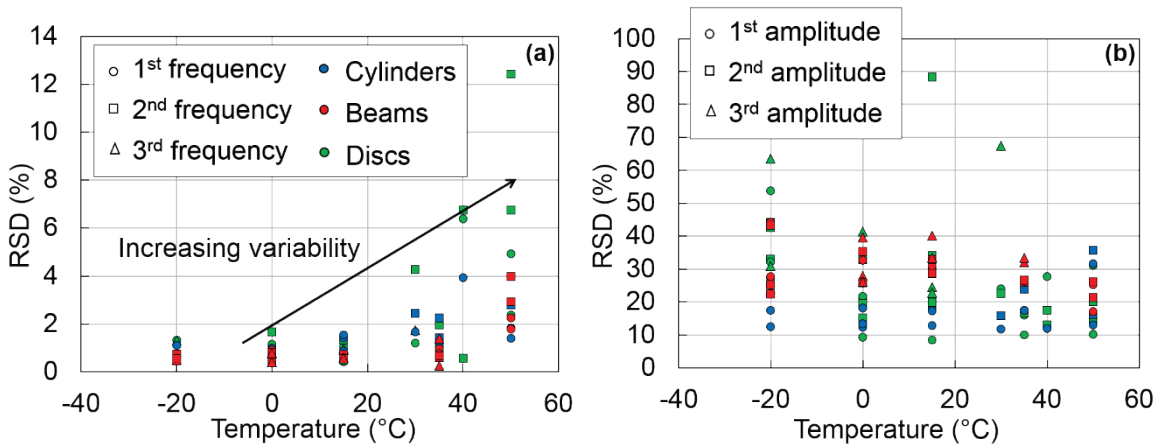

Figure 5.2 RSD in function of temperature for the eight specimens tested by five different laboratories in the FSDyn project: (a) Three first resonance frequencies; (b) Three first resonance amplitudes.

The variability of the measurements is relatively high in comparison with the results of the repeatability study of the dynamic tests (see section 3.3.1), especially for the amplitude variability. As a reminder, values of the RSD were around 0.5% for the resonance frequencies and 2% for the amplitudes at the resonance frequencies. The reproducibility of dynamic tests between different laboratories is still satisfying but it can be improved, especially for the measurements of the amplitudes.

The variability of the measurements is not due to different positions of the impact or of the accelerometer because the positions were clearly indicated on the specimens to make sure that every laboratory uses the same. The different experimental devices (impact hammer, accelerometer and signal conditioner) used by the laboratories were suspected to be a potential reason of the variability observed. A short study was carried out between the ENTPE and EIFFAGE to evaluate the influence of using experimental devices from different laboratories on the FRFs measurements. In this study, dynamic tests were performed on cylinder GB5-C1 using six different experimental configurations in which sensors and signal conditioners from ENTPE and from EIFFAGE were used. The list of experimental configurations is given in Table 5.4. At least fifteen minutes were waited between two configurations to make sure that the system is stabilized at the moment of the measurement. If the system is not stabilized, the amplitude of both the impact force and the acceleration cannot be measured accurately. The same study was performed at -20°C and at 35°C. Note that the same model of impact hammer (PCB model 086E80) and accelerometer (PCB model 353B15) are used by the ENTPE and EIFFAGE but the signal conditioner is different (PCB model 482C15 at ENTPE and PCB model 480B21 at EIFFAGE).

Table 5.4. Six experimental configurations used to evaluate the influence of using experimental devices from different laboratories on the FRFs measurements.

Experimental device	Config. 1	Config. 2	Config. 3	Config. 4	Config. 5	Config. 6
Impact hammer	ENTPE	ENTPE	EIFFAGE	ENTPE	EIFFAGE	EIFFAGE
Accelerometer	ENTPE	EIFFAGE	ENTPE	ENTPE	EIFFAGE	EIFFAGE
Signal conditioner	ENTPE	ENTPE	ENTPE	EIFFAGE	ENTPE	EIFFAGE

The RSD was calculated for the two first resonance frequencies and amplitudes and the values obtained are far lower from those observed in Figure 5.2: 0.2% for the two first resonance frequencies and 2.8% and 5.6% for the amplitudes at the first and second resonance frequencies.

Therefore, using different experimental devices cannot explain the variability of the measurements observed, at least for the ENTPE and EIFFAGE. The different experimental procedures used by the laboratories (e.g. measurements performed inside or outside the thermal chamber, time waited for the stabilization of the system, use of an automated or manual impact hammer, etc.) and the different levels of practice of each laboratory with dynamic tests are probable explanations to the variability of the measurements. The different sampling frequencies (between 50 kHz and 1 MHz) used by each laboratory may also have an impact.

5.1.3.2 LVE properties of all specimens evaluated from dynamic tests at ENTPE

The values of the constants of the 2S2P1D model and WLF equation at 15°C simulating the global LVE behaviour of each specimen are listed in Table 5.5. Note that results for the first round of dynamic tests of the GB5 cylinders are presented in this section. The values of the constants obtained after the optimizations at each temperature are given in APPENDIX J for all the specimens. The figures showing the complex modulus values determined from dynamic tests for all the specimens can also be found in APPENDIX J.

Table 5.5. Values of the constants of the 2S2P1D model and WLF equation simulating the global LVE behaviour determined from dynamic tests for all the specimens of the FSDyn experimental campaign. The results for the GB5 cylinders were obtained from the first round of dynamic tests with method V and the results for the other specimens were obtained with method III.

	2S2P1D model								**WLF equation at 15°C**	
Specimen	**E_0 (MPa)**	**$\tau_{E15°C}$ (s)**	**k**	**δ**	**h**	**ν_0**	**ν_{00}**	**$\tau_{\nu15°C}$ (s)**	**C_1**	**C_2**
GB5-C1 (1st round)	43 500	9.0E-2	0.130	1.17	0.442	0.31	0.55	2.0E-1	19.2	139.5
GB5-C2 (1st round)	40 700	7.4E-2				0.27	0.40	1.0E3		
GB5-D1	38 800	7.0E-2				x	x	x		
GB5-D3	x	x	x	x	x	x	x	x	x	x
GB5-B2	43 300	3.1E-2	0.130	0.96	0.442	x	x	x	16.0	123.0
GB5-B4	43 200	3.2E-2				x	x	x		
ABS-D9	41 100	1.3E-3	0.160	0.85	0.468	x	x	x	19.1	191.0
ABS-D10	40 800	1.4E-3				x	x	x		

The results from Table 5.5 were obtained by analyzing the dynamic measurements performed on the two GB5 cylinders with method V (cf. section 4.3.2.1) while method III (cf. section 4.3.1.3.1) was used for all the other specimen. The analysis methods used were chosen following the recommendations from section 4.3.3. The specimens GB5-C1 and GB5-C2 are the only specimens for which method V was used because they are the only specimen for which the complex Poisson's ratio was measured with tension-compression tests. It should be remembered that constants E_{00} and β are fixed to 100MPa and 250 for all methods of inverse analysis and constants $\tau_{\nu15°C}$, ν_0 and ν_{00} are only determined with method V. For specimen GB5-D3, it was impossible to determine constants simulating the global LVE behaviour of the material because of measurements problems. These problems may be due to the disc geometry that is not well-adapted for dynamic tests. Comparison of the experimental FRFs and calculated FRFs (after optimization at each temperature and the global LVE FRFs is plotted in Figure 5.3 for specimen GB5-C1. The same figures for all specimens can be found in APPENDIX J.

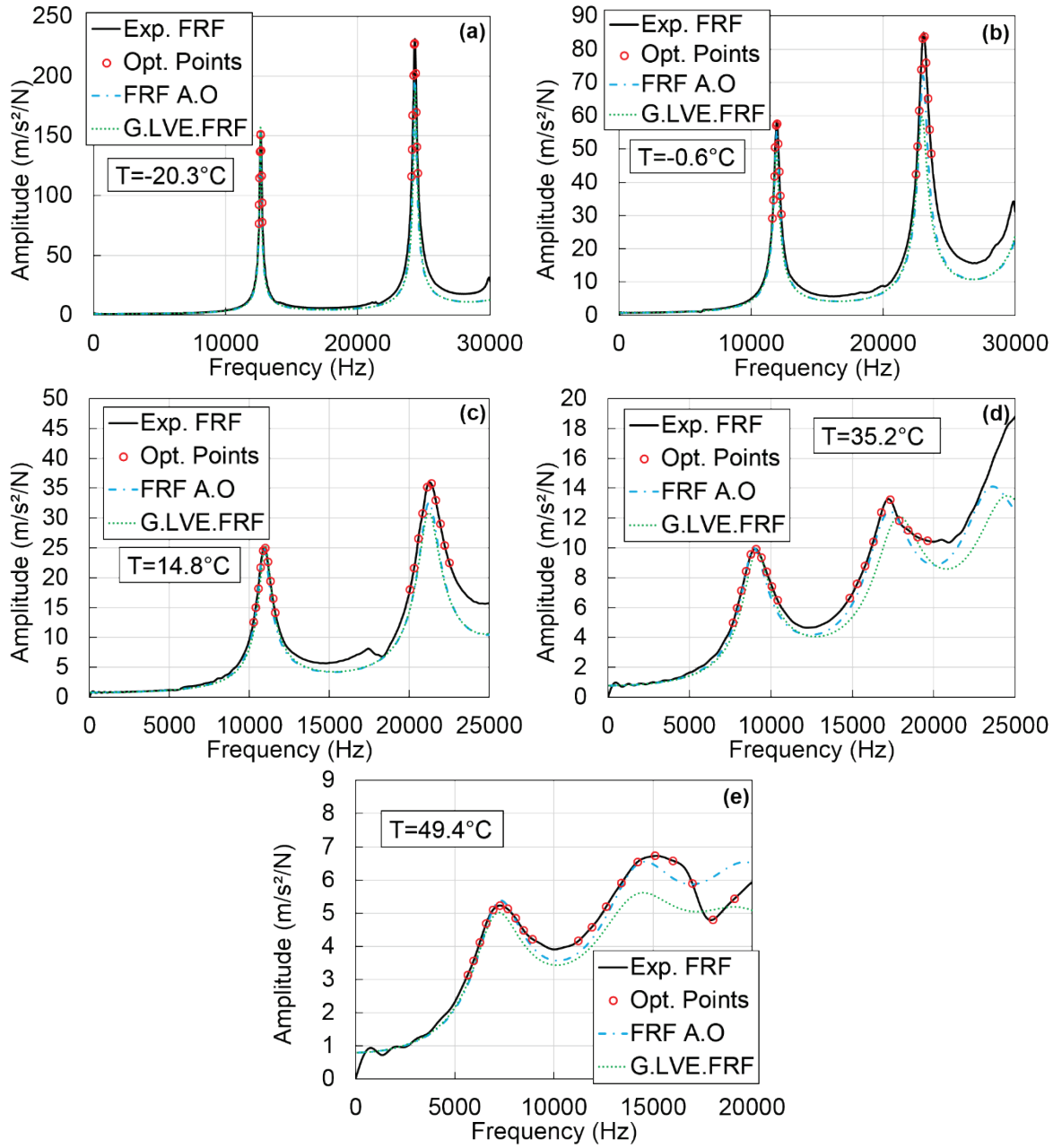

Figure 5.3 Comparison of the experimental FRFs measured at the beginning of the project (noted Exp. FRF) with the FRFs after optimization (noted FRF A.O) and the global LVE FRFs (noted G.LVE FRF) for specimen GB5-C1. Values of the experimental FRFs at the frequencies where the optimization is performed (noted Opt. Points) are also plotted. (a) T=-20.3°C; (b) -0.6°C; (c) 14.8°C; (d) 35.2°C; (e) 49.4°C.

The match between the experimental FRFs and both the FRFs after optimizations and the global LVE FRFs is good, especially for frequencies up to the first resonance frequencies. For higher frequencies, the fit is not as good especially for the amplitudes but it remains satisfying.

Interestingly, the values of constants k, δ and h of the 2S2P1D model listed in Table 5.5 are the same for the two ABS specimens. They also are the same for the GB5 cylinders and disc. This result was expected because these constants of the 2S2P1D model are only depending on the bitumen and should therefore be equal for all specimens of the same material. However, constant δ obtained for the GB5 beams is different than constant δ obtained for the rest of the GB5 specimens. The reason for this difference is not identified. Effects on the Cole-Cole plot

and the master curves at 15°C for the norm and phase angle of the normalized complex modulus are shown in Figure 5.4. The normalized complex modulus E^*_N depends only on constants $\tau_{E15°C}$, k, δ, h and β and not on constants E_0 and E_{00}:

$$E^*_N = \frac{E^* - E_{00}}{E_0 - E_{00}} \tag{5-1}$$

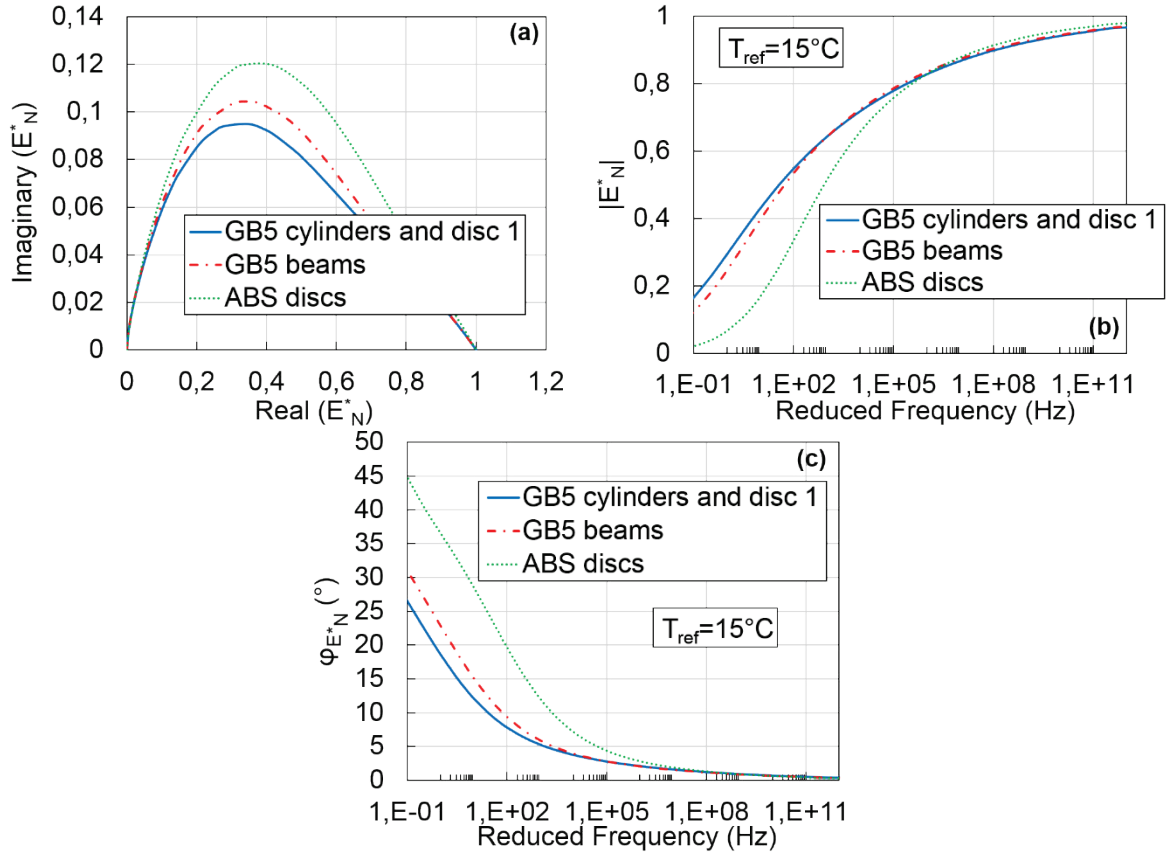

Figure 5.4 Comparison of the values of the normalized complex modulus determined from dynamic tests for the specimens tested in the FSDyn experimental campaign. (a) Cole-Cole plot; (b) and (c) master curves of the norm and of the phase angle of the normalized complex modulus at 15°C.

Figure 5.4 shows that the different values of constant δ for the GB5 cylinders and discs and the GB5 beams have few effects and curves corresponding to the three geometries are in good agreement, especially for the norm of the normalized complex modulus. It demonstrates the good repeatability of the dynamic tests for different geometries. In addition, the curves corresponding to the ABS discs are quite different than the curves of the GB5 specimens with lower values of the norm of the normalized complex modulus and higher values of the phase angle for reduced frequencies below 10^5 Hz. This difference observed is characteristic of a mixture with a softer bitumen, which is the case of the ABS specimens.

Another interesting result from Table 5.5 is that the constants C_1 and C_2 of the WLF equation at 15°C are the same for the two ABS specimens. They also are the same for the GB5 cylinders and discs but they are different for the GB5 beams. The corresponding shift factors are plotted in Figure 5.5. It is seen in Figure 5.5 that the correlation between the shift factors of the GB5 beams and the shift factors of the GB5 cylinders and discs is excellent except for

temperatures higher than 35°C. It confirms the observations raised from Figure 5.4 showing that only the high temperatures behaviour is slightly different between the GB5 beams and the rest of the GB5 specimens. It is also observed that the shift factors of the ABS discs are quite different than the shift factors of the GB5 specimens, also due to the difference in bitumen.

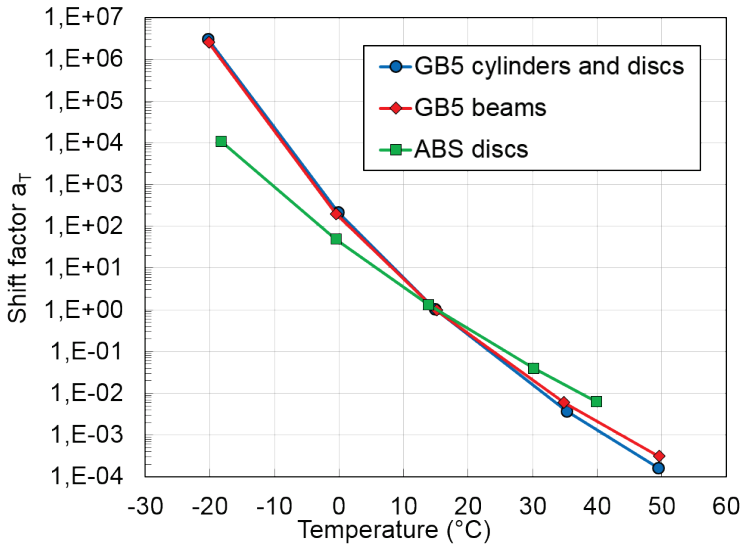

Figure 5.5 Comparison of the shift factors determined from dynamic tests for the specimens tested in the FSDyn experimental campaign.

5.1.3.3 Comparison of the LVE properties of the GB5 cylinders determined from dynamic tests and cyclic tension-compression tests

After the second dynamic tests performed on the GB5 cylinders, cyclic tension-compression tests were performed on the same specimens. The values of the constants of the 2S2P1D model and WLF equation at 15°C simulating the global LVE behaviour of the two GB5 cylinders determined from the second round of dynamic tests are listed in Table 5.6. These constants were obtained using method V, as for the first round of dynamic tests. The constants determined from the tension-compression tests are listed in Table 5.7. Constants E_{00} and β of the 2S2P1D model can be determined from cyclic tension-compression tests because experimental data are available for lower frequencies than with dynamic tests (see Figure 3.7).

Table 5.6. Values of the constants of the 2S2P1D model and WLF equation simulating the global LVE behaviour determined from the second round of dynamic tests with method V for the two GB5 cylinders.

	2S2P1D model								**WLF equation at 15°C**	
Specimen	**E_0 (MPa)**	**$\tau_{E15°C}$ (s)**	**k**	**δ**	**h**	**v_0**	**v_{00}**	**$\tau_{v15°C}$ (s)**	**C_1**	**C_2**
GB5-C1 (2nd round)	44 600	6.5E-2	0.130	1.17	0.442	0.31	0.55	2.0E-1	19.2	139.5
GB5-C2 (2nd round)	41 300	7.2E-2				0.27	0.40	1.0E3		

Table 5.7. Values of the constants of the 2S2P1D model and WLF equation simulating the global LVE behaviour determined from cyclic tension-compression tests performed at the end of the FSDyn experimental campaign for the two GB5 cylinders.

	2S2P1D model										WLF equation at 15°C	
Specimen	**E_{00} (MPa)**	**E_0 (MPa)**	**$\tau_{E15°C}$ (s)**	**k**	**δ**	**h**	**β**	**ν_0**	**ν_{00}**	**$\tau_{\nu15°C}$ (s)**	**C_1**	**C_2**
GB5-C1	20	44 000	0.24	0.172	2.15	0.56	150	0.28	0.6	100	24.7	165.9
GB5-C2	28	39 600	0.24	0.172	2.15	0.56	150	0.31	0.5	200	24.7	165.9

The Cole-Cole plot and the master curves at 15°C of the norm and phase angle of the complex modulus obtained from both tests (E^*_{BC5}, E^*_{Dyn5}, E^*_{ExpTC} and E^*_{TC}) are plotted in Figure 5.6 for the cylinder GB5-C1. The same figure for cylinder GB5-C2 can be found in APPENDIX J. A very good agreement between the values of the complex modulus obtained from both tests is seen in Figure 5.6. To confirm this observation, the master curves at 15°C of the relative difference (respectively the difference) between the norm (respectively the phase angle) of E^*_{Dyn5} and E^*_{TC} were plotted in Figure 5.7 for both cylinders. The norm of the complex modulus evaluated from dynamic tests is globally higher that the norm of the complex modulus evaluated with cyclic tension-compression tests but the maximum relative difference is less than 10%. The phase angle of the complex modulus evaluated from both tests are in very good agreement with less than 1° of difference at 50°C. These results demonstrate that for the GB5 material, dynamic tests give complex modulus values very close from those of the tension-compression tests. Moreover, due to the nonlinearity of bituminous mixtures with the applied strain (Airey & Rahimzadeh, 2004; Nguyen, Di Benedetto, & Sauzéat, 2015; Babadopoulos, 2017; Mangiafico, Babadopoulos, Sauzéat, & Di Benedetto, 2018), values of the norm of the complex modulus are expected to be a few percent higher with the dynamic tests than with the cyclic tension-compression tests. This is what is observed in Figure 5.7 and this could explain part of the differences between both tests.

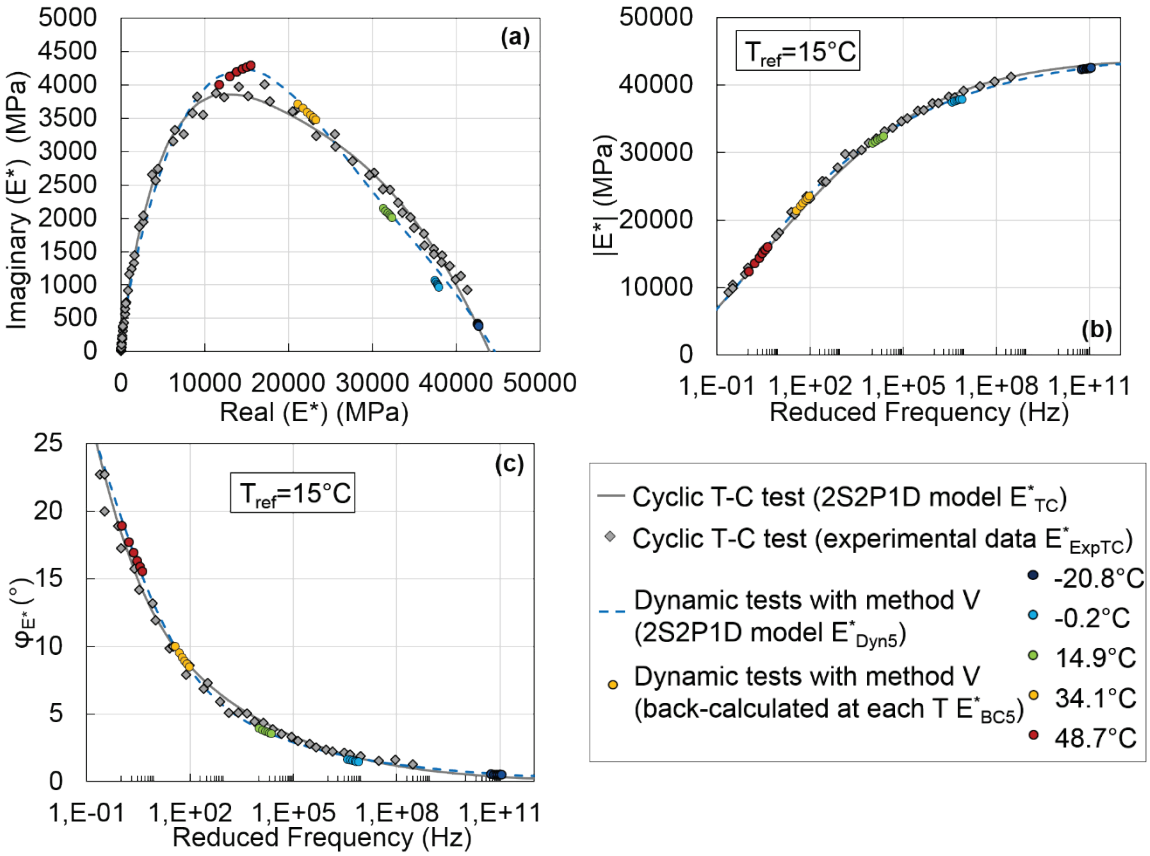

Figure 5.6 Comparison of the values of the complex modulus determined from dynamic tests with method V (E^*_{BC5} and E^*_{Dyn5}) with the values of the complex modulus determined from cyclic tests (E^*_{ExpTC} and E^*_{TC}). (a) Cole-Cole plot; (b) and (c) master curves of the norm and of the phase angle of the complex modulus at 15°C. Results for specimen GB5-C1.

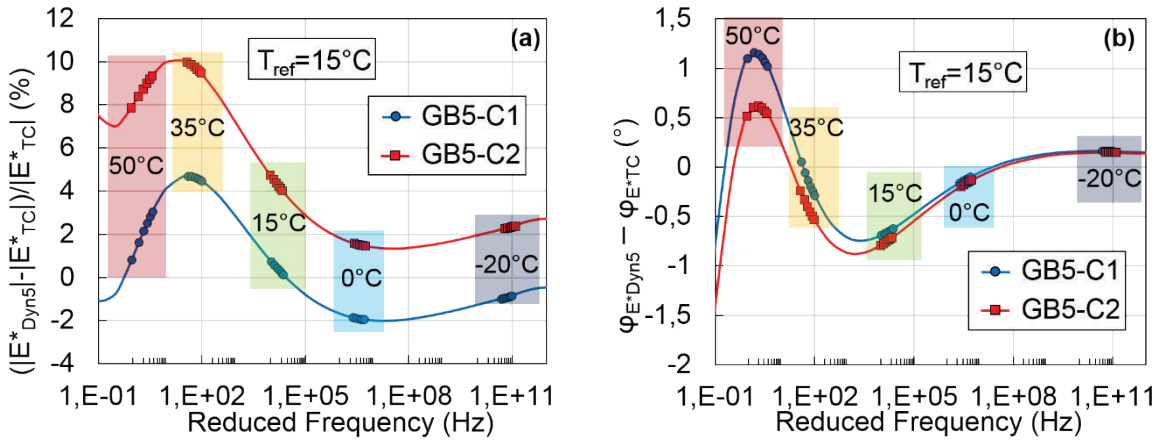

Figure 5.7 Master curve at 15°C of: (a) the relative difference between the norm of the complex modulus determined from dynamic tests with method V ($|E^*_{Dyn5}|$) and from cyclic tests ($|E^*_{TC}|$); (b) the difference between the phase angle of the complex modulus determined from dynamic tests with method V (φ_{E^*Dyn5}) and from cyclic tests (φ_{E^*TC}). Results for the GB5 cylinders tested in the FSDyn experimental campaign.

The same comparison was carried out for the values of the complex Poisson's ratio (ν_{BC5}, ν^*_{Dyn5}, ν^*_{ExpTC} and ν^*_{TC}). The values of ν^*_{Dyn5} and ν^*_{TC} are in good agreement for cylinder GB5-C1 as seen in Figure 5.8. The same figure can be found in APPENDIX J for cylinder GB5-C2. Moreover, Figure 5.9 shows that there is less than 0.08 of difference between the norm of the complex Poisson's ratio determined from both tests and less than 0.8° for the phase angle of

the complex Poisson's ratio. Considering the difficulty to determine accurately values of the complex Poisson's ratio in experimental tests, these differences are not surprising and the evaluation of the complex Poisson's ratio from dynamic tests seems to be a promising approach.

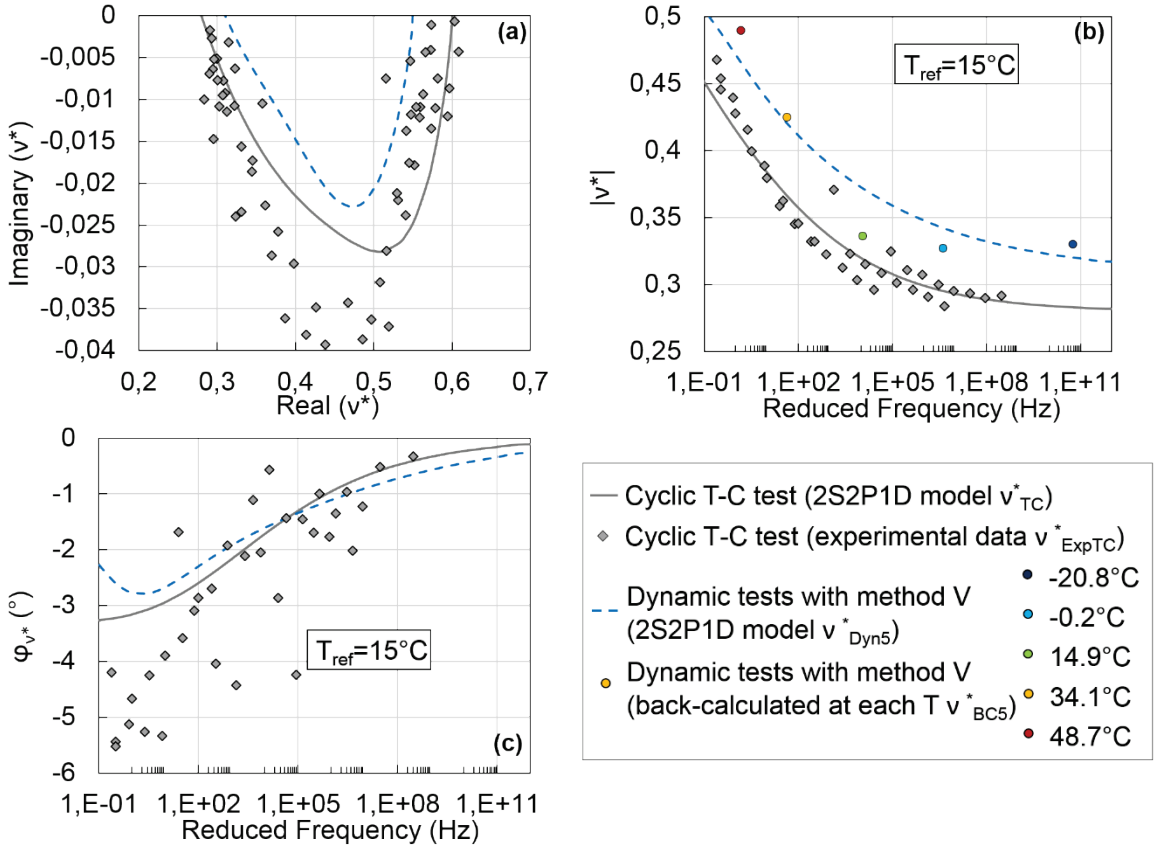

Figure 5.8 Comparison of the values of the complex Poisson's ratio determined from dynamic tests with method V (real values v_{BC5} and v^*_{Dyn5}) with the values of the complex Poisson's ratio determined from cyclic test (v^*_{ExpTC} and v^*_{TC}). (a) Cole-Cole plot; (b) and (c) master curves of the norm and of the phase angle of the complex Poisson's ratio at 15°C. Results for specimen GB5-C1.

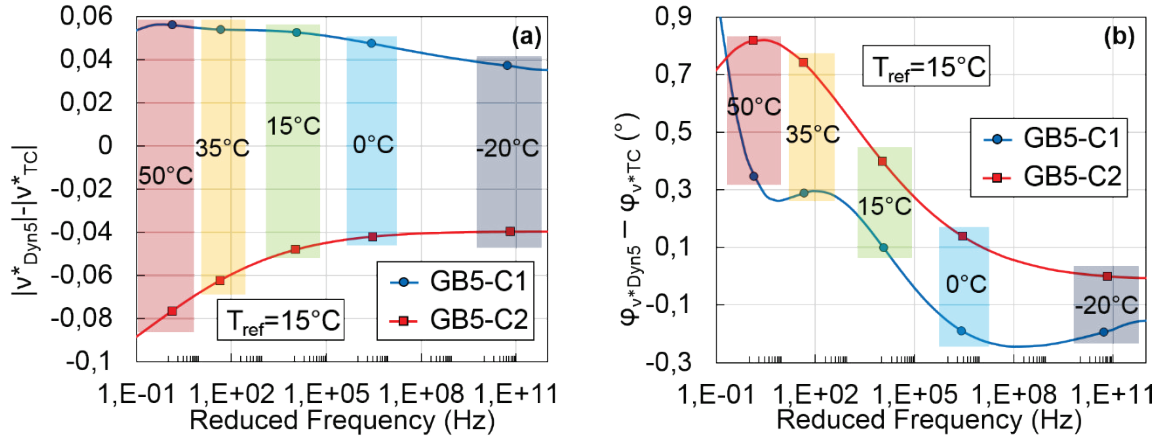

Figure 5.9 Master curve at 15°C of: (a) the relative difference between the norm of the complex Poisson's ratio determined from dynamic tests with method V ($|v^*_{Dyn5}|$) and from cyclic tests ($|v^*_{TC}|$); (b) the difference between the phase angle of the complex Poisson's ratio determined from dynamic tests with method V (φ_{v^*Dyn5}) and from cyclic tests (φ_{v^*TC}). Results for the GB5 cylinders tested in the FSDyn experimental campaign.

Finally, the shift factors obtained from dynamic tests and from tension-compression tests were compared. Results are plotted in Figure 5.10 in which a good agreement is seen between the shift factors obtained from both tests, especially for the low temperatures.

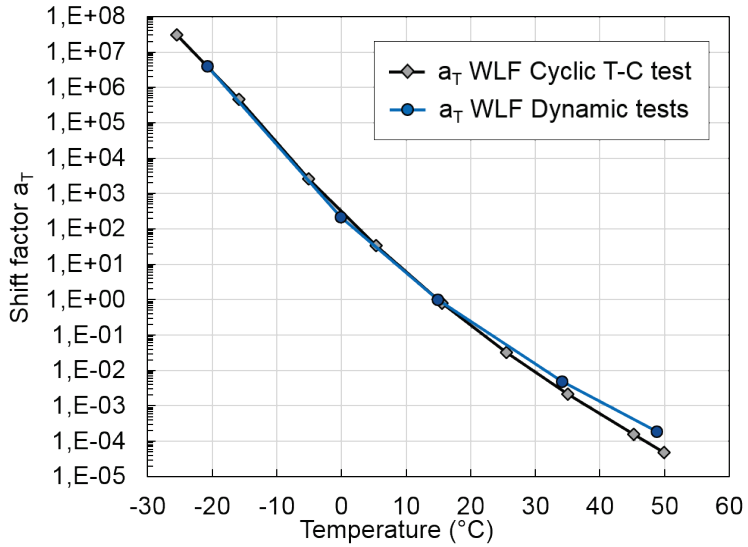

Figure 5.10 Comparison of the shift factors determined from dynamic tests and from cyclic tension-compression tests for the two GB5 cylinders tested in the FSDyn experimental campaign.

5.1.3.4 Effects of material ageing for the GB5 cylinders

The FRFs measured for specimen GB5-C2 at the beginning and at the end of the project at -20°C and 15°C are plotted in Figure 5.11 (a) and (b). The FRFs measured for specimen GB5-C1 at 35°C and 50°C at the beginning and at the end of the project are also plotted in Figure 5.11 (c) and (d). FRFs for all temperatures can be found in APPENDIX J for both cylinders. For specimen GB5-C2, the resonance frequencies and the amplitudes are higher at the end of the project than at the beginning of the project. For this specimen, the same trend is observed for all temperatures. However, for specimen GB5-C1, the same effect is observed only for temperatures up to 15°C. At 35°C, the amplitudes measured at the end of the project are lower and at 50°C, both the resonance frequencies and the amplitudes are lower.

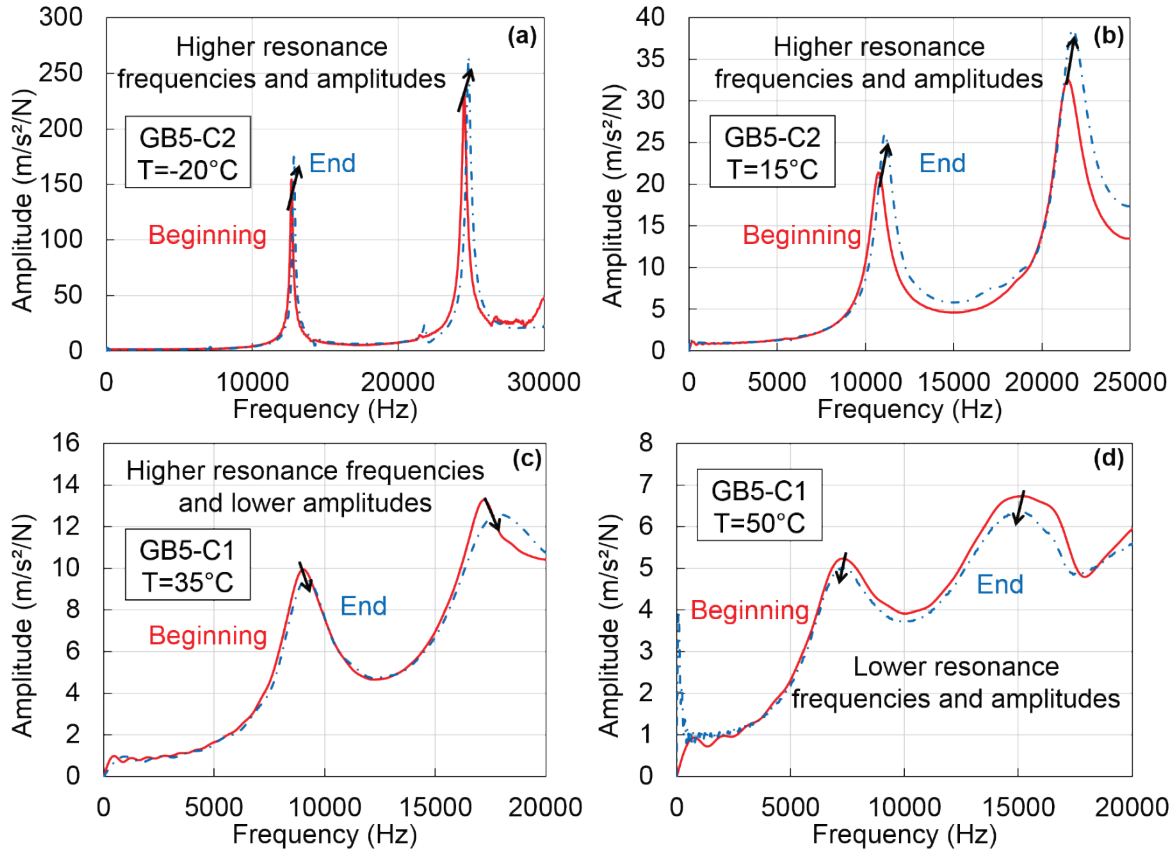

Figure 5.11 FRFs measured at the beginning and at the end of the FSDyn project for the two GB5 cylinders: (a) GB5-C2 at -20°C; (b) GB5-C2 at 15°C; (c) GB5-C1 at 35°C; (d) GB5-C1 at 50°C.

The values of the constants of the 2S2P1D model and WLF equation at 15°C simulating the global LVE behaviour of the two GB5 cylinders at the beginning and at the end of the project are listed in Table 5.5 and Table 5.6, respectively. For both specimens, the constant E_0 is slightly higher at the end of the project than at the beginning, which corresponds to a stiffer norm of the complex modulus for the low temperatures. Constant $\tau_{E15°C}$ is also a little bit lower at the end of the project for both specimens. However, the impact of these differences is very limited with a maximum relative difference of 4% for the norm of the complex modulus and a maximum phase angle difference of 1° between the beginning and the end of the project as seen in Figure 5.12. Therefore, the differences observed on the FRFs measurements between the first round and the second round of dynamic tests have very little influence on the determination of the complex modulus.

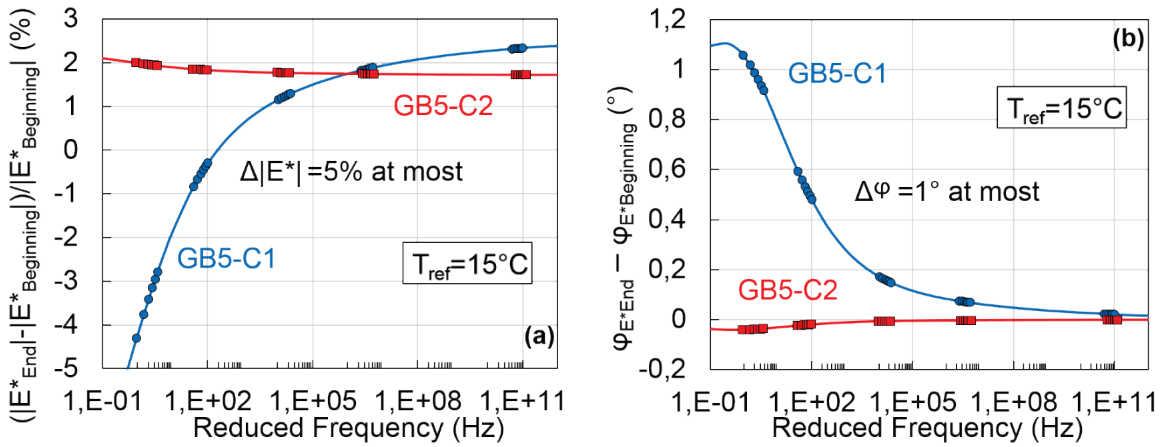

Figure 5.12 (a) Relative difference in % at 15°C between the norm of the complex modulus evaluated from dynamic tests at the end ($|E^*_{End}|$) and at the beginning ($|E^*_{Beginning}|$) of the FSDyn project for the two GB5 cylinders; (b) Difference in ° at 15°C between the phase angle of the complex modulus evaluated from dynamic tests at the end (φ_{E^*End}) and at the beginning ($\varphi_{E^*Beginning}$) of the FSDyn project for the two GB5 cylinders.

For the complex Poisson's ratio, the real values of the Poisson's ratio back-calculated at each temperature in the first step of method V (cf. section 4.3.2.1) are very similar at the beginning (noted ν_{BC5Beg}) and at the end (noted ν_{BC5End}) of the project (cf. Figure 5.13). Consequently, the same values of constants $\tau_{\nu 15°C}$, ν_0 and ν_{00} can be used at the beginning and at the end of the project to fit the values of ν_{BC5Beg} and ν_{BC5End} in the second step of method V (ν^*_{Dyn5}) as seen in Figure 5.13. Therefore, the differences observed between the FRFs measured at the beginning and at the end of the FSDyn project have very little influence on the determination of the complex Poisson's ratio.

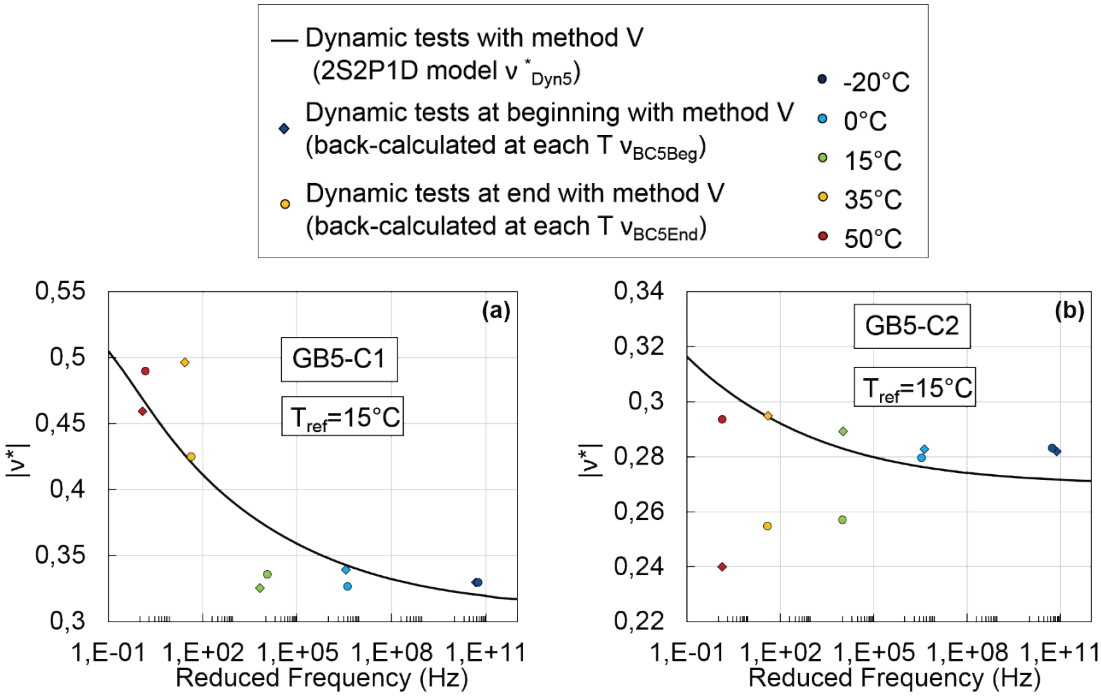

Figure 5.13 (a) Master curves at 15°C of the real values of the Poisson's ratio back-calculated at each temperature from dynamic tests with method V at the beginning (ν_{BC5Beg}) and at the end (noted ν_{BC5End}) of the FSDyn project. The master curves of the norm of the complex Poisson's ratio determined from dynamic tests with method V (ν^*_{Dyn5}) are also plotted. (a) Specimen GB5-C1; (b) Specimen GB5-C2.

5.2 Experimental campaign with the Swedish mixture (SM)

The main objectives of this experimental campaign are to compare:

- The LVE properties determined from dynamic tests for the beam tested in this section and for the discs of the same material (ABS) tested in the FSDyn experimental campaign (cf. section 5.1.3.2).
- The LVE properties determined from dynamic and cyclic tension-compression tests for the Swedish mixture.

5.2.1 Material

The material is the ABS Swedish base course bituminous mixture already introduced in the FSDyn experimental campaign (see section 5.1.1). One straight beam not used in the FSDyn campaign was tested in this campaign. Details about this beam are given in Table 5.8.

Table 5.8. Specimen tested in the SM experimental campaign.

Specimen	H (mm)	W (mm)	L (mm)	Density (kg/m^3)	Void ratio (%)
ABS-P4	49.0	49.0	147.5	2 475	2.8

5.2.2 Tests performed

Dynamic tests were performed on the beam following the same procedure than for the ABS specimen in the FSDyn campaign (see Figure 3.1). One week after the dynamic tests, the beam was tested with the cyclic tension-compression. The Poisson's ratio was not measured during the cyclic test.

5.2.3 Comparison of the LVE properties determined from dynamic tests for the beam and for the discs of the same material tested in the FSDyn experimental campaign

The values of the constants of the 2S2P1D model and WLF equation at 15°C simulating the global LVE behaviour determined from dynamic tests and from the tension-compression test are given in Table 5.9. To obtain these values, the dynamic tests were analyzed with method III (cf. section 4.3.1.3.1). As a reminder, constants E_{00} and β are not evaluated with method III and they were fixed to the values of the constants of the reference LVE material (E_{00}=100MPa and β=250). The values of the constants obtained after the optimizations at each temperature are given in APPENDIX K. Comparison of the experimental FRFs and calculated FRFs (after optimization at each temperature and the global LVE FRFs) can also be found in APPENDIX K.

Table 5.9. Values of the constants of the 2S2P1D model and WLF equation simulating the global LVE behaviour determined from dynamic tests with method III for the beam tested in the SM experimental campaign.

	2S2P1D model					WLF equation at 15°C	
Specimen	E_0 (MPa)	$\tau_{E15°C}$ (s)	k	δ	h	C_1	C_2
ABS-P4	42 200	0.0015	0.178	1.32	0.570	13.5	110.5

The values of the constants obtained are different than the values obtained for the disc specimens of the same material tested in the FSDyn campaign (cf. Table 5.5). The influence of these differences was evaluated by plotting in Figure 5.14 the Cole-Cole plot and master curves

at 15°C of the norm and phase angle of the normalized complex modulus (equation (5-1)). The curves corresponding to the beam and to the discs are in good agreement on the whole frequency range except for the phase angle, for which slight differences (less than 5°) appear for reduced frequencies under 100 Hz. However, the repeatability of dynamic tests between the beam geometry and the disc geometry remains satisfying for the ABS material.

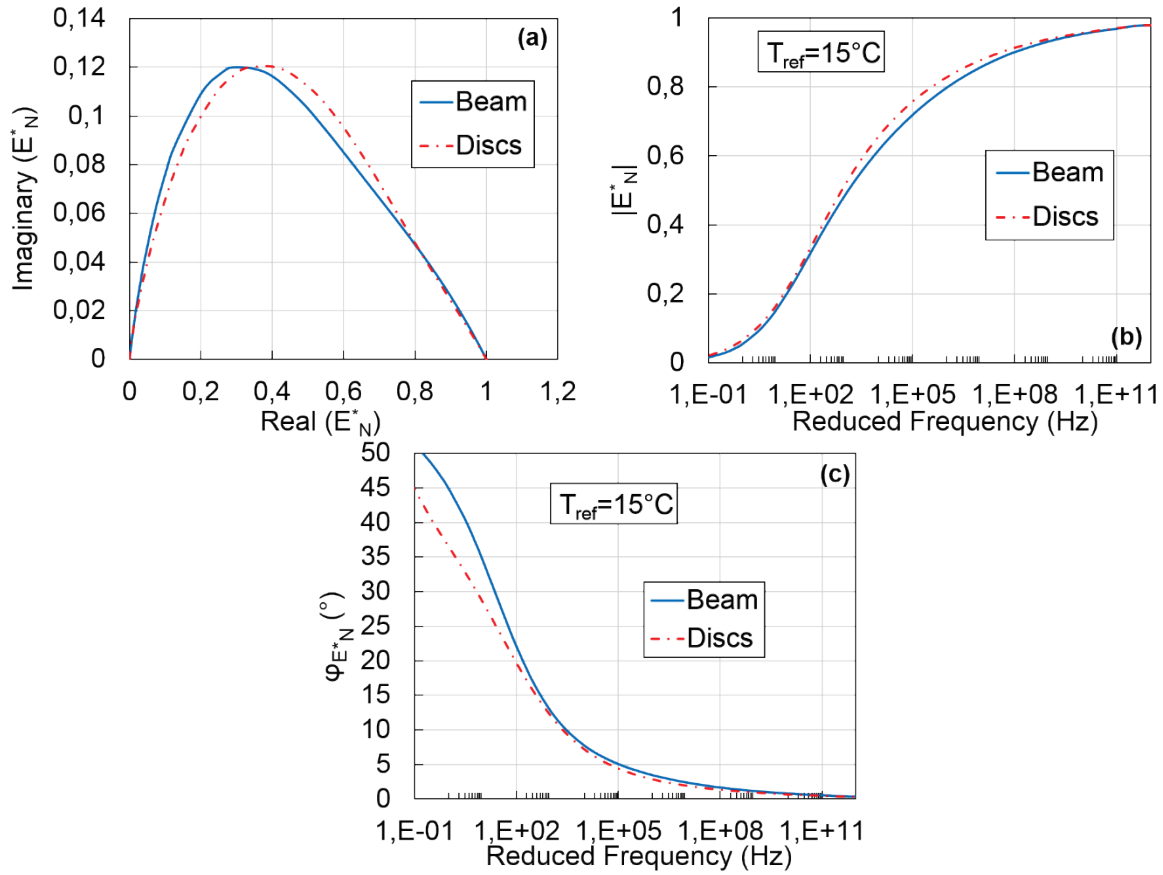

Figure 5.14 Comparison of the values of the normalized complex modulus determined from dynamic tests for the beam and for the discs of the ABS material tested in the FSDyn and SM experimental campaigns. (a) Cole-Cole plot; (b) and (c) master curves of the norm and of the phase angle of the normalized complex modulus at 15°C.

5.2.4 Comparison of the LVE properties determined from dynamic tests and from the cyclic tension-compression test

The values of the constants of the 2S2P1D model and WLF equation at 15°C simulating the global LVE behaviour of the beam determined from the tension-compression test are given in Table 5.10.

Table 5.10. Values of the constants of the 2S2P1D model and WLF equation simulating the global LVE behaviour determined from the cyclic tension-compression test performed on the beam tested in the SM experimental campaign.

	2S2P1D model							**WLF equation at 15°C**	
Specimen	**E_{00} (MPa)**	**E_0 (MPa)**	**$\tau_{E15°C}$ (s)**	**k**	**δ**	**h**	**β**	**C_1**	**C_2**
ABS-P4	15	41 500	1.8E-3	0.230	1.90	0.60	150	25.3	186.8

Values of the complex modulus obtained from both tests (E^*_{BC3}, E^*_{Dyn3}, E^*_{ExpTC} and E^*_{TC}) are plotted in Figure 5.15 for the ABS-P4 beam. A good agreement is seen between the different curves.

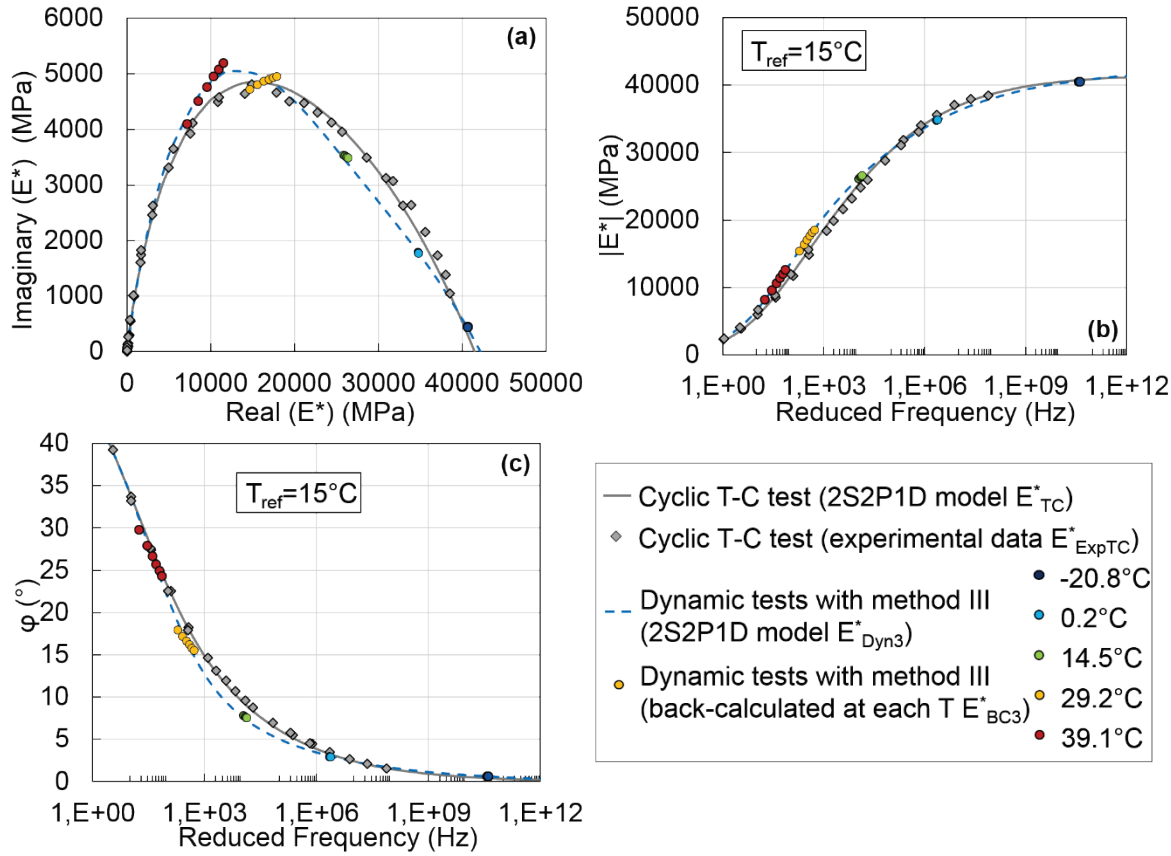

Figure 5.15 Comparison of the values of the complex modulus determined from dynamic tests with method III (E^*_{BC3} and E^*_{Dyn3}) with the values of the complex modulus determined from cyclic tests (E^*_{ExpTC} and E^*_{TC}). (a) Cole-Cole plot; (b) and (c) master curves of the norm and of the phase angle of the complex modulus at 15°C. Results for specimen ABS-P4.

In addition, the relative difference (respectively the difference) between the norm (respectively the phase angle) of E^*_{Dyn3} and E^*_{TC} was calculated and results are plotted in Figure 5.16. The norm of the complex modulus evaluated from dynamic tests is globally higher than the norm of the complex modulus evaluated with cyclic tension-compression tests. The maximum relative difference is around 20% for the norm of the complex modulus. The phase angle of the complex modulus evaluated from both tests are in very good agreement with less than 2° of difference on the whole frequency range. Nonlinearity strain (Airey & Rahimzadeh, 2004; Nguyen, Di Benedetto, & Sauzéat, 2015; Babadopoulos, 2017; Mangiafico, Babadopoulos, Sauzéat, & Di Benedetto, 2018) can explain at least a part of these differences, as already explained in section 5.1.3.3. These results demonstrate that for the ABS material, dynamic tests and cyclic tests give complex modulus values in good agreement.

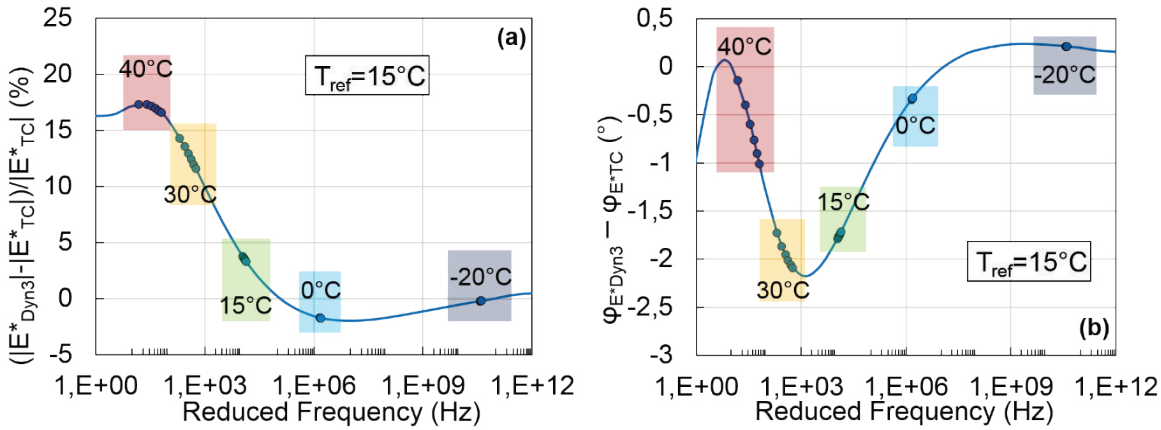

Figure 5.16 Master curve at 15°C of: (a) the relative difference between the norm of the complex modulus determined from dynamic tests with method III ($|E^*_{Dyn3}|$) and from cyclic tests ($|E^*_{TC}|$); (b) the difference between the phase angle of the complex modulus determined from dynamic tests with method III (φ_{E^*Dyn3}) and from cyclic tests (φ_{E^*TC}). Results for the ABS-P4 beam tested in the SM experimental campaign.

Finally, the shift factors obtained from dynamic tests and from tension-compression tests were compared in Figure 5.17. A good agreement is seen between the shift factors obtained from both tests.

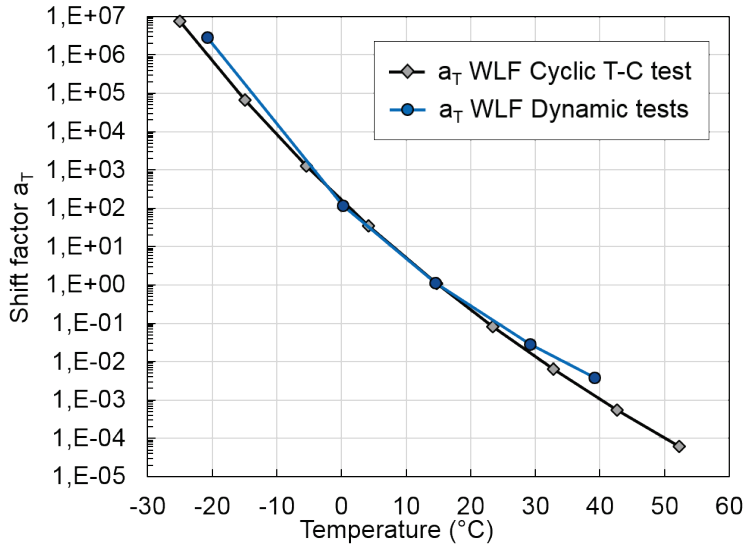

Figure 5.17 Comparison of the shift factors determined from dynamic tests and from cyclic tension-compression tests for the ABS-P4 beam tested in the SM experimental campaign.

5.3 Material with an optimized granular skeleton (MOGS)

Some results of this experimental campaign are presented in Paper V that was submitted for publication in the scientific journal Applied Science. The two main objectives of this campaign are to compare:

- The LVE properties determined from dynamic tests for the different specimens tested.
- The LVE properties determined from dynamic tests with method III (cf section 4.3.1.3.1) and with method IV and its simplified approach in the first step (cf section 4.3.1.4.1).
- The LVE properties determined from dynamic and cyclic tension-compression tests for two additional specimens of the GB5 material already introduced in section 5.1.1.

5.3.1 Material

This material corresponds to the GB5 material used in the FSDyn experimental campaign (cf. section 5.1.1). Two cylindrical specimens that were not used in the FSDyn project were tested. Details about these two specimens are given in Table 5.11.

Table 5.11. Specimens tested in the MOGS experimental campaign.

Specimen	H (mm)	D (mm)	Density (kg/m^3)	Void ratio (%)
GB5-C3	161.8	64.3	2 361	4.8
GB5-C4	161.8	64.2	2 355	5.1

5.3.2 Tests performed

Cyclic tension-compression tests were performed first on the two cylinders. During these two cyclic tests, the radial strain was not measured and the Poisson's ratio was therefore not evaluated. Then the lower and upper parts of the specimens were sawed to remove the caps glued to the specimens for the tension-compression tests. Dynamic tests were performed on the specimens with reduced lengths of 15.2cm following the same experimental procedure than for the GB5 specimens in the FSDyn campaign (see Figure 3.1). The two cylinders were tested in longitudinal mode. The dynamic tests were performed two weeks after the tension-compression tests.

5.3.3 Comparison of the LVE properties determined from dynamic tests with methods III and IV

The values of the constants of the 2S2P1D model and WLF equation at 15°C simulating the global LVE behaviour determined from dynamic tests with methods III (cf. section 4.3.1.3.1) and IV (cf. section 4.3.1.4.1) are given in Table 5.12. The values of the constants obtained after the separate optimizations at each temperature in the first step of the two inverse methods are given in APPENDIX L. Comparisons of the experimental FRFs and calculated FRFs (after optimization at each temperature and the global LVE FRFs) will be found in APPENDIX L for the two cylinders and the two inverse analysis methods.

Table 5.12. Values of the constants of the 2S2P1D model and WLF equation simulating the global LVE behaviour determined from dynamic tests with methods III and IV for the two cylinders tested in the MOGS experimental campaign.

	2S2P1D model					WLF equation at 15°C	
Specimen	**E_0 (MPa)**	**$\tau_{E15°C}$ (s)**	**k**	**δ**	**h**	**C_1**	**C_2**
GB5-C3 (Method III)	39 100	5.5E-2	0.130	1.17	0.442	19.2	139.5
GB5-C3 (Method IV)	39 800						
GB5-C4 (Method III)	40 500	7.0E-2					
GB5-C4 (Method IV)	41 100						

It is seen in Table 5.12 that except for constant E_0, the same values of the constants are obtained with both inverse methods. Moreover, values of these constants correspond to the values obtained for the GB5 cylinders in the FSDyn experimental campaign (cf. Table 5.6 and Table 5.7), which confirms the good repeatability of the dynamic tests for the GB5 material. For constant E_0, the values are slightly increasing when using inverse method IV (+700 MPa or +1.8% for GB5-C3 and +600 MPa or +1.5% for GB5-C4). However, the differences are not significant so the use of a simplified approach in the first step of inverse method IV has almost no impact on the complex modulus evaluation, at least for material GB5 (cf. Figure 5.18 and Figure 5.19).

5.3.3.1 Comparison of the LVE properties determined from dynamic tests and from cyclic tension-compression tests

The values of the constants of the 2S2P1D model and WLF equation at 15°C simulating the global LVE behaviour determined from the tension-compression tests are given in Table 5.13 for the two cylinders.

Table 5.13. Values of the constants of the 2S2P1D model and WLF equation simulating the global LVE behaviour determined from the cyclic tension-compression test performed on the two cylinders tested in the MOGS experimental campaign.

	2S2P1D model							WLF equation at 15°C	
Specimen	**E_{00} (MPa)**	**E_0 (MPa)**	**$\tau_{E15°C}$ (s)**	**k**	**δ**	**h**	**β**	**C_1**	**C_2**
GB5-C3	65	39 100	7.5E-2	0.160	1.80	0.60	350	24.7	165.9
GB5-C4	65	39 500	1.5E-1						

The complex modulus values obtained from dynamic and cyclic tests (E^*_{BC3}, E^*_{Dyn3}, E^*_{BC4}, E^*_{Dyn4}, E^*_{ExpTC} and E^*_{TC}) are plotted in Figure 5.18 for cylinder GB5-C4. The same figure can be found in APPENDIX L for cylinder GB5-C3. Figure 5.18 confirms the good agreement between results obtained from both inverse analysis methods of the dynamic tests. Results from dynamic tests are also in good agreement with the results of the tension-compression test.

The relative difference (respectively the difference) between the norm (respectively the phase angle) of E^*_{DynIII} and E^*_{TC} in the one hand, and E^*_{DynIV} and E^*_{TC} in the other hand are plotted in Figure 5.19. Results from Figure 5.19 confirm the tendency seen in Figure 5.7 and Figure 5.16: the norm of the complex modulus evaluated from dynamic tests is little higher and the relative difference remains less than 15% on the whole frequency range. The maximum difference for the phase angle is of about only 1.5°. These results confirm the results obtained

for the two GB5 cylinders tested in the FSDyn campaign showing that for the GB5 material, dynamic tests and cyclic tests give complex modulus values in good agreement. The good match between shift factors obtained from both tests was already verified in Figure 5.10

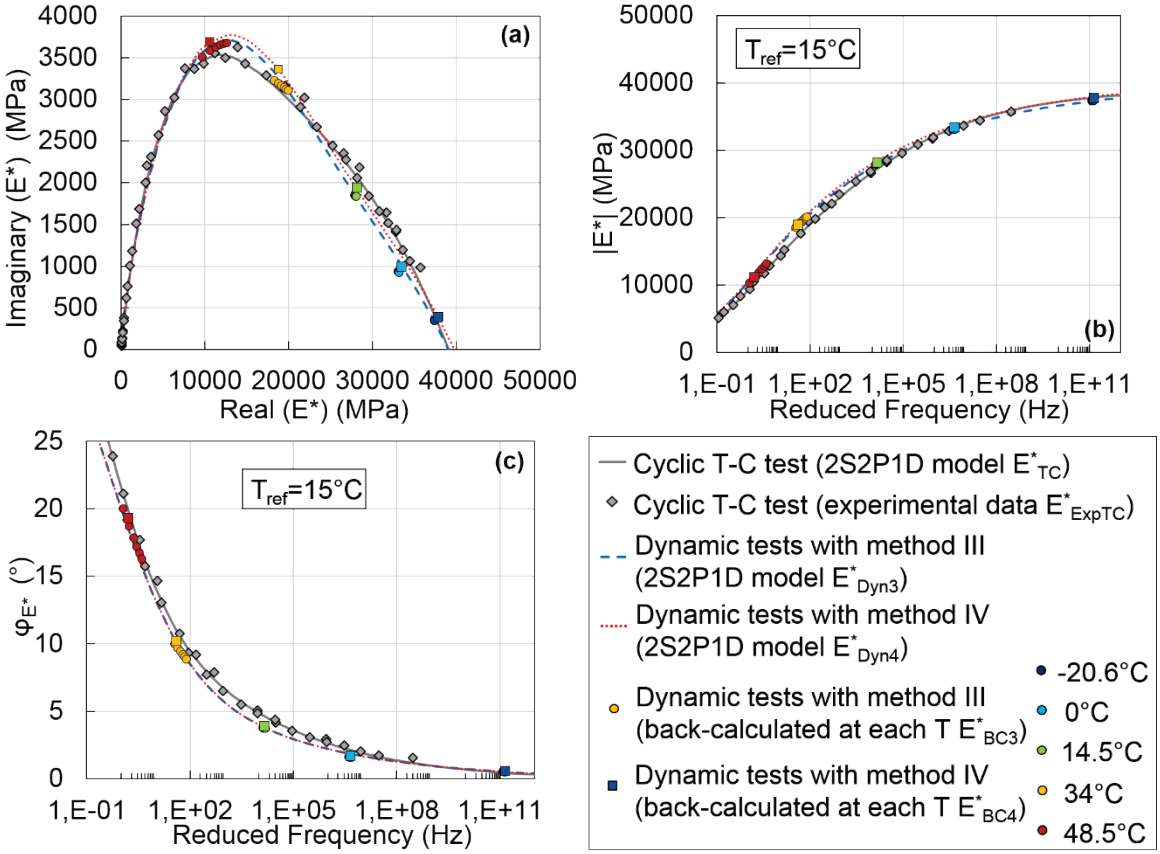

Figure 5.18 Comparison of the values of the complex modulus determined from dynamic tests with method III (E^*_{BC3} and E^*_{Dyn3}) and method IV (E^*_{BC4} and E^*_{Dyn4}) with the values of the complex modulus determined from cyclic tests (E^*_{ExpTC} and E^*_{TC}). (a) Cole-Cole plot; (b) and (c) master curves of the norm and of the phase angle of the complex modulus at 15°C. Results for specimen GB5-C3.

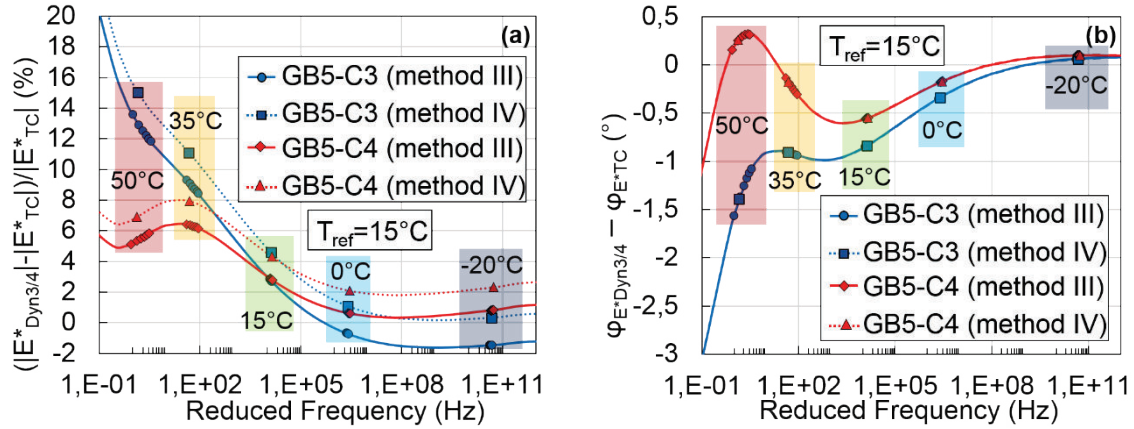

Figure 5.19 Master curve at 15°C of: (a) the relative difference between the norm of the complex modulus determined from dynamic tests with method III/IV ($|E^*_{Dyn3/4}|$) and from cyclic tests ($|E^*_{TC}|$); (b) the difference between the phase angle of the complex modulus determined from dynamic tests with method III/IV ($\varphi_{E^*Dyn3/4}$) and from cyclic tests (φ_{E^*TC}). Results for the ABS-P4 beam tested in the SM experimental campaign.

5.4 Material with high reclaimed asphalt pavement content (MHRAPC)

Some results of this experimental campaign are reported in Paper III that was published in the scientific journal Construction and Building Materials and in Paper V that was submitted for publication in the scientific journal Applied Science. The main objectives of this experimental campaign are:

- To compare the LVE properties determined from dynamic tests for the different specimens tested.
- To study the possibility of using method II (cf. section 4.3.1.2.1) to characterize the LVE behaviour of bituminous mixtures from dynamic tests.
- To compare the LVE properties determined from dynamic tests with method III (cf. section 4.3.1.3.1), method IV (cf. section 4.3.1.4.1) and method V (cf. section 4.3.2.1).
- To compare the LVE properties determined from dynamic and cyclic tests for the material with high RAP content considered in this campaign.

5.4.1 Material

The material considered in this experimental campaign is a warm mix that was fabricated in laboratory. This material has a 0/10 continuous grading curve and a 35/50 original bitumen. RAP was incorporated in the original mix to reach 70% of RAP content using a 160/220 foam bitumen. The material is labelled WF for warm foam mixture. This material was used in the Improvmure project from the French national research agency (Poirier, Pouget, Leroy, & Delaporte, 2016). More details about the material will be found in APPENDIX I. Details about the three cylinders of this material that were used in this campaign are given in Table 5.14.

Table 5.14. Specimens tested in the MHRAPC experimental campaign.

Specimen	H (mm)	D (mm)	Density (kg/m^3)	Void ratio (%)
WF-4	150.3	75.0	2 379	6.6
WF-6	150.7	75.0	2 431	4.2
WF-8	149.5	75.0	2 449	3.8

5.4.2 Tests performed

The three cylinders were first tested with cyclic tension-compression tests. Then the lower and upper parts of the specimens were sawed to remove the caps glued to the specimens for the tension-compression tests. Two rounds of dynamic tests in longitudinal mode were performed on the specimens with reduced lengths of 12.3cm:

- Seven temperatures from -20°C to 40°C in steps of 10°C were tested respecting the same chronology than in the FSDyn experimental campaign (see Figure 3.1). These tests were performed five months after the cyclic tests.
- Five temperatures (-20°C, 0°C, 15°C, 35°C, 50°C) were tested following the same procedure than for the GB5 cylinders in the FSDyn and MOGS experimental campaigns (cf. Figure 3.1). These tests were performed seven months after the cyclic tests (two months after the first round of dynamic tests).

5.4.3 Results obtained for the first round of dynamic tests analyzed with method II

The results obtained from the first round of dynamic tests and from tension-compression tests are presented and compared in Paper III. The values of the constants of the 2S2P1D model and WLF equation at 15°C simulating the global LVE behaviour determined from the tension-compression tests and from the dynamic tests are listed in Table 5.15 and Table 5.16, respectively.

Table 5.15. Values of the constants of the 2S2P1D model and WLF equation simulating the global LVE behaviour determined from cyclic tension-compression tests for the three cylinders tested in the MHRAPC experimental campaign.

	2S2P1D model										WLF equation at 15°C	
Specimen	**E_{00} (MPa)**	**E_0 (MPa)**	**$\tau_{E15°C}$ (s)**	**k**	**δ**	**h**	**β**	**ν_0**	**ν_{00}**	**$\tau_{\nu15°C}$ (s)**	**C_1**	**C_2**
WF-4	28	33 400	0.054					0.20	0.45	1.5		
WF-6	40	37 500	0.070	0.177	2.28	0.57	154	0.31	0.51	4.0	24.9	166.6
WF-8	56	36 900	0.069					0.18	0.52	3.9		

Table 5.16. Values of the constants of the 2S2P1D model and WLF equation simulating the global LVE behaviour determined from the first round of dynamic tests with method II for the three cylinders tested in the MHRAPC experimental campaign.

	2S2P1D model				WLF equation at 15°C	
Specimen	**E_0 (MPa)**	**$\tau_{E15°C}$ (s)**	**k**	**δ**	**C_1**	**C_2**
WF-4	33 584	9.5E-2	0.186	2.34	28.5	210.1
WF-6	37 748	3.4E-1	0.172	2.12	29.8	209.3
WF-8	36 554	1.1E-1	0.178	2.05	30.8	230.8

Values listed in Table 5.16 were obtained with method II (cf. section 4.3.1.2.1). The values of the constants E_{00}, h, β, γ_{Ev}, ν_0 and ν_{00} that are fixed in method II were fixed to the values of constants determined from the tension-compression tests listed in Table 5.15.

Values of constants k and δ listed in Table 5.16 are different from one specimen to another though they all are from the same material. The same observation is made for constants C_1 and C_2 of the WLF equation. These difference are due to the global approach used in method II. The influence of these differences was evaluated by plotting in Figure 5.20 the Cole-Cole plot and master curves at 15°C of the norm and phase angle of the normalized complex modulus (equation (5-1)) for the three cylinders. The curves corresponding to specimens WF-4 and WF-8 are in good agreement but they are quite different than the curves of specimen WF-6. This kind of differences between specimens of the same material having the same geometry was not seen in other experimental campaigns when using methods III, IV and V.

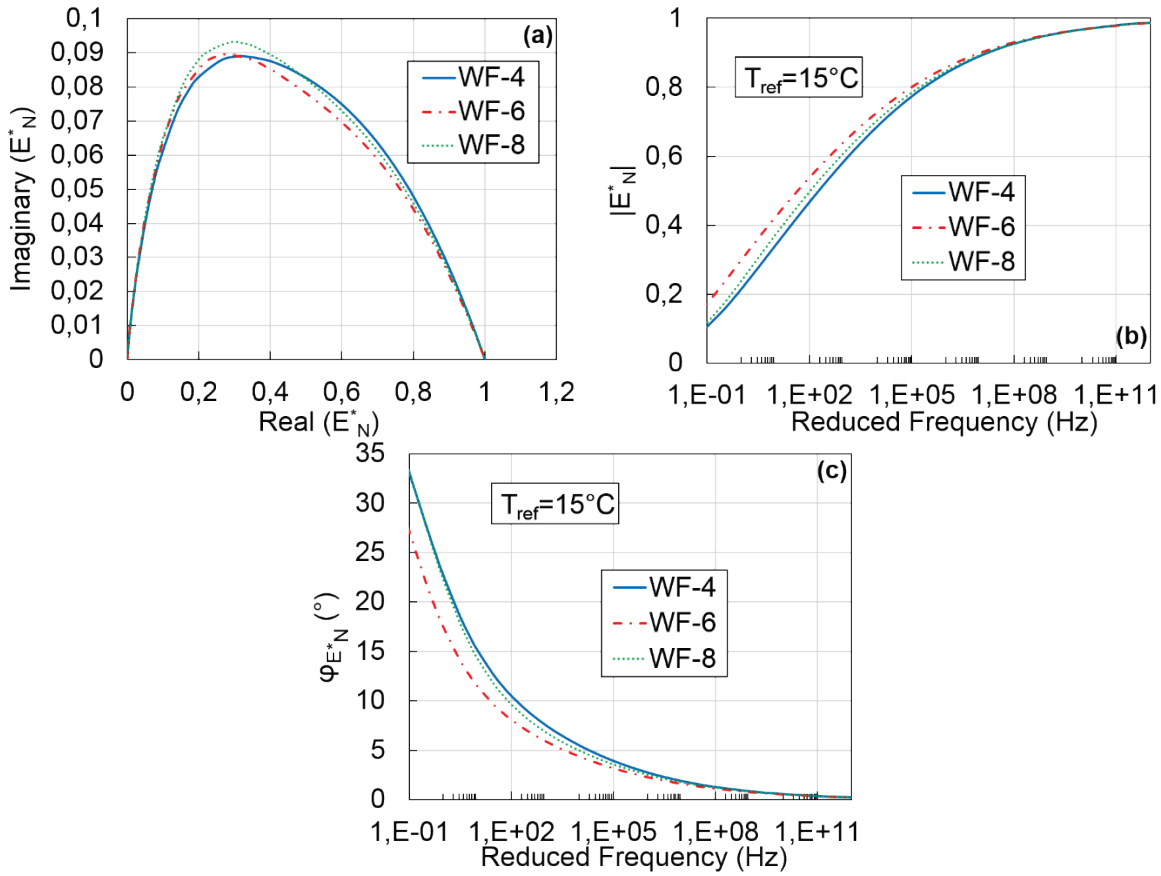

Figure 5.20 Comparison of the values of the normalized complex modulus determined from dynamic tests for the specimens tested in the MHRAPC experimental campaign. (a) Cole-Cole plot; (b) and (c) master curves of the norm and of the phase angle of the normalized complex modulus at 15°C.

The shift factors of the three cylinders obtained from dynamic tests and from tension-compression tests are compared in Figure 5.21. A good agreement is seen between all the curves and there is no significant difference between the shift factors determined from dynamic tests for the three cylinder.

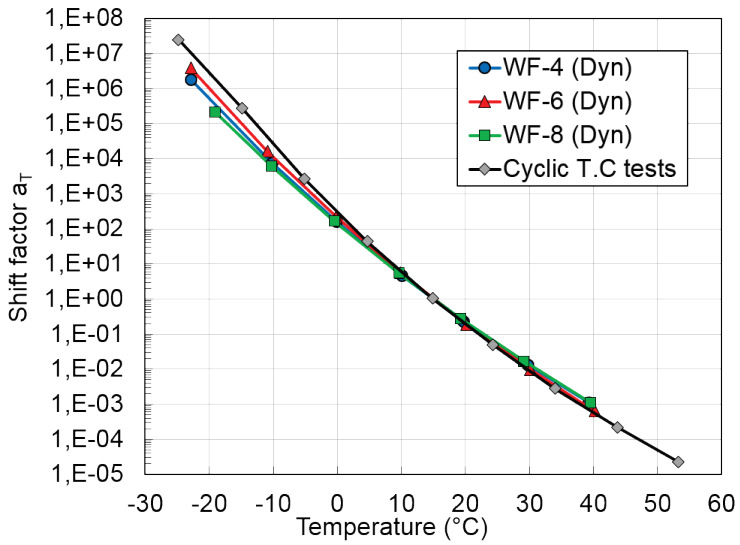

Figure 5.21 Comparison of the shift factors determined from dynamic tests with method II and from cyclic tension-compression tests for the specimens tested in the MHRAPC experimental campaign.

The relative difference (respectively the difference) between the norm (respectively the phase angle) of E^*_{DynII} and E^*_{TC} are plotted in Figure 5.22. Results from both tests are in good agreement for specimens WF-4 and WF-8 but important differences (up to 80% for the norm of the complex modulus and 7° for the phase angle) are seen for specimen WF-6. This is a direct consequence of the observations raised from Figure 5.20 and a good example that shows the risk of error when using method II. It is therefore not recommended to use this method.

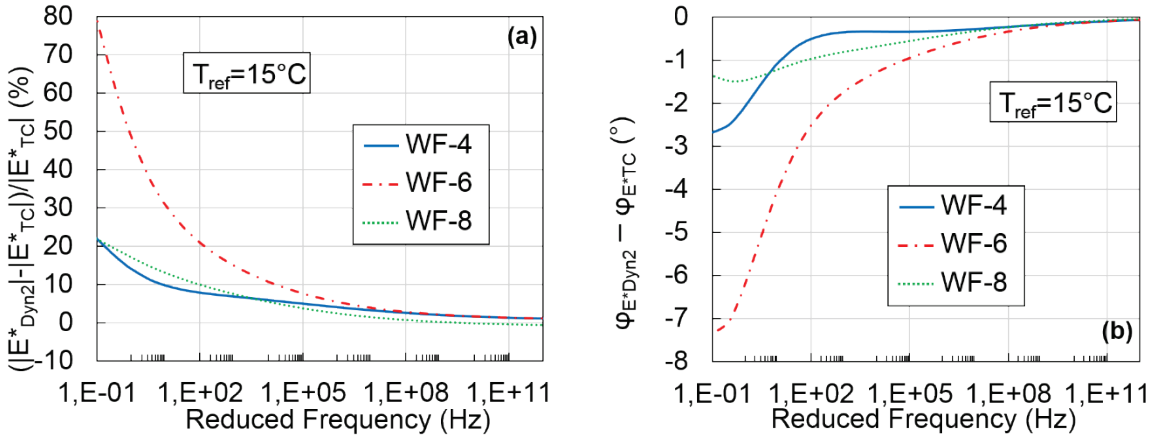

Figure 5.22 Master curve at 15°C of: (a) the relative difference between the norm of the complex modulus determined from dynamic tests with method II ($|E^*_{Dyn2}|$) and from cyclic tests ($|E^*_{TC}|$); (b) the difference between the phase angle of the complex modulus determined from dynamic tests with method II (φ_{E^*Dyn2}) and from cyclic tests (φ_{E^*TC}). Results for the WF specimens tested in the MHRAPC experimental campaign.

5.4.4 Comparison of the LVE properties determined from the second round of dynamic tests and from cyclic tension-compression tests

Some of the results obtained from the second round of dynamic tests and from the tension-compression tests are presented and compared in Paper V. The values of the constants of the 2S2P1D model and WLF equation at 15°C simulating the global LVE behaviour determined from dynamic tests are given in Table 5.17. These values were obtained using method III, IV and V to back-analyze the FRFs measurements. The values of the constants obtained after the separate optimizations at each temperature in the first step of the three methods are given in APPENDIX M. Comparisons of the experimental FRFs and calculated FRFs (after optimization at each temperature and the global LVE FRFs) will be found in APPENDIX M for methods IV and V for all specimens.

Table 5.17. Values of the constants of the 2S2P1D model and WLF equation simulating the global LVE behaviour determined from the second round of dynamic tests with methods III, IV and V for the three cylinders tested in the MHRAPC experimental campaign. Values of constants $\tau_{v15°C}$, v_0 and v_{00} were only determined with method V.

	2S2P1D model								WLF equation at 15°C	
Specimen	**E_0 (MPa)**	**$\tau_{E15°C}$ (s)**	**k**	**δ**	**h**	**v_0**	**v_{00}**	**$\tau_{v15°C}$ (s)**	**C_1**	**C_2**
WF-4 (Method III)	34 800	4.0E-2				-	-	-		
WF-6 (Method III)	38 700	7.0E-2				-	-	-		
WF-8 (Method III)	37 500	4.0E-2				-	-	-		
WF-4 (Method IV)	36 100	4.0E-2				-	-	-		
WF-6 (Method IV)	39 500	7.0E-2	0.147	1.39	0.490	-	-	-	18.9	133.2
WF-8 (Method IV)	38 500	4.0E-2				-	-	-		
WF-4 (Method V)	34 800	4.0E-2				0.110	0.55	5		
WF-6 (Method V)	38 700	7.0E-2				0.235	0.55	150		
WF-8 (Method V)	37 500	4.0E-2				0.179	0.55	1 000		

Values of the constants obtained with methods III and V are the same. It is because values of the complex modulus back-calculated at each temperature are very similar with both inverse methods as seen in Figure 5.23 for the example of specimen WF-8. The same figures can be found in APPENDIX M for the other specimens. Consequently, values of constants E_0, $\tau_{E15°C}$, k, δ, h, C_1 and C_2 determined in the second step of methods III and V are the same (cf. Table 5.17).

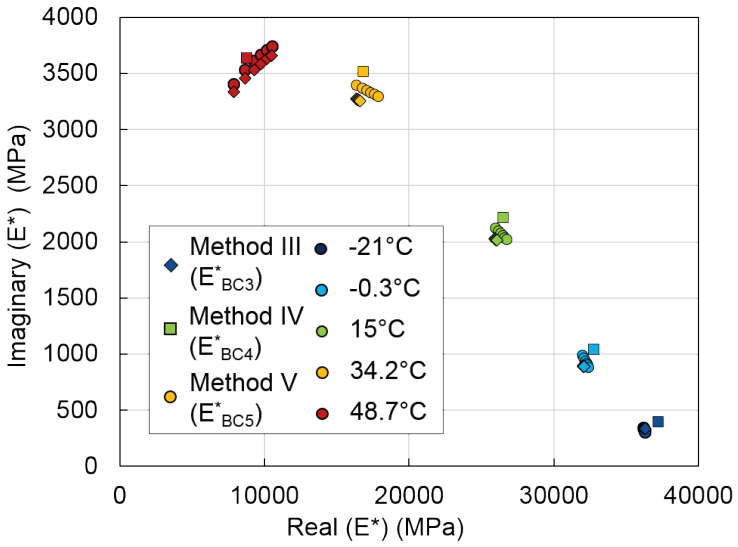

Figure 5.23 Comparison of the values of the complex modulus back-calculated from dynamic tests at each temperature with methods III (E^*_{BC3}), IV (E^*_{BC4}) and V (E^*_{BC5}). Results for specimen WF-8.

Also, similarly as in the MOGS experimental campaign (see section 5.3.3), the only differences between values of the constants determined with methods III and V and with method IV are for constant E_0 that is slightly higher with method IV. This is because the norm of the complex modulus back-calculated at each temperature with method IV are higher than with methods III and IV, especially for the low temperatures, as seen in Figure 5.23 (slight horizontal shift to the right for values obtained with method IV). However, the maximum variation of E_0 is of only 3.7% (for specimen WF-4) so the use of a simplified approach in the first step of method IV has a very limited impact on the complex modulus evaluation for material WF (cf. Figure 5.24 and Figure 5.25). Values of the complex modulus obtained from both tests (E^*_{BC4}, E^*_{Dyn4}, E^*_{BC5}, E^*_{Dyn5}, E^*_{ExpTC} and E^*_{TC}) are plotted in Figure 5.24 for specimen WF-8. The same figures will be found in APPENDIX M for the two other specimens. A good agreement is seen between the different curves plotted in Figure 5.24.

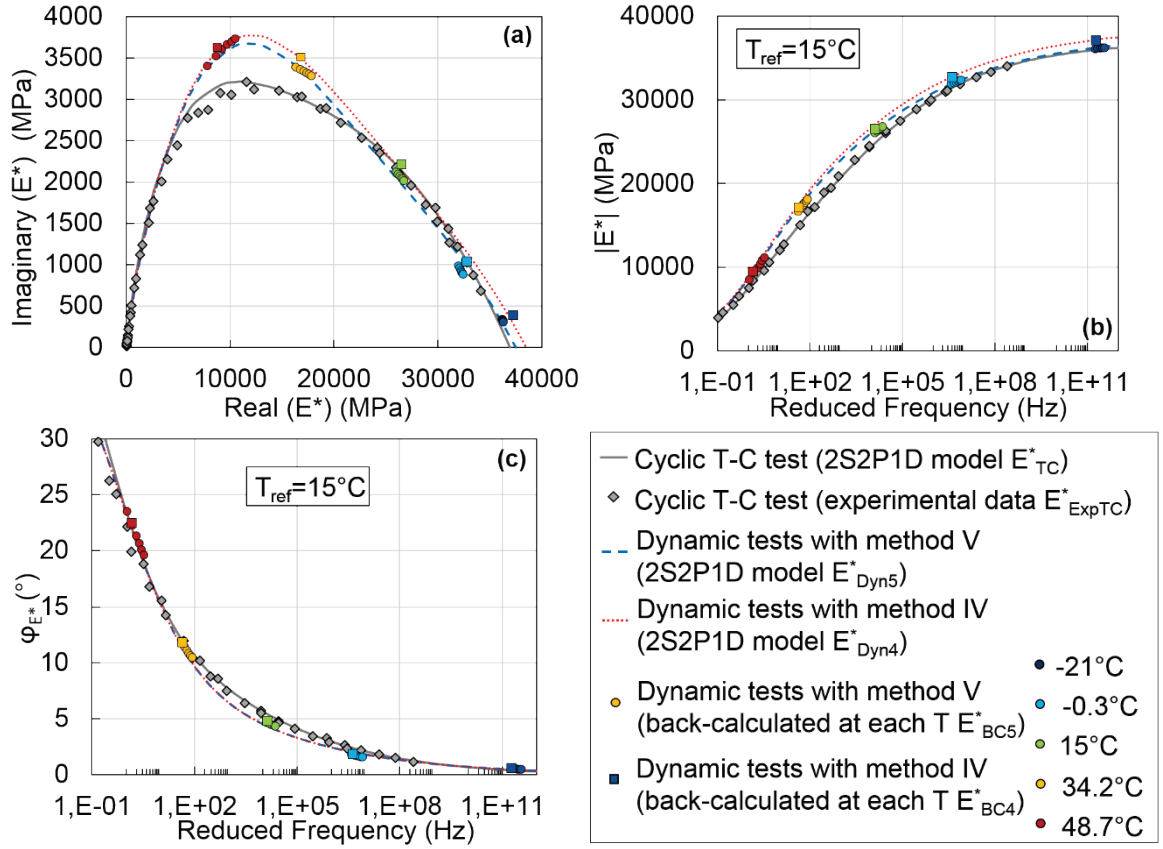

Figure 5.24 Comparison of the values of the complex modulus determined from dynamic tests with method IV (E^*_{BC4} and E^*_{Dyn4}) and method V (E^*_{BC5} and E^*_{Dyn5}) with the values of the complex modulus determined from cyclic tests (E^*_{ExpTC} and E^*_{TC}). (a) Cole-Cole plot; (b) and (c) master curves of the norm and of the phase angle of the complex modulus at 15°C. Results for specimen WF-8.

The relative difference (respectively the difference) between the norm (respectively the phase angle) of E^*_{Dyn4} and E^*_{TC} in the one hand, and E^*_{Dyn5} and E^*_{TC} in the other hand are plotted in Figure 5.25. Results from Figure 5.25 confirm the tendency of previous results: the norm of the complex modulus evaluated from dynamic tests is little higher. The relative difference remains less than 30% on the whole frequency range while the maximum difference for the phase angle is of about only 2°. For this material, the difference between results from dynamic and cyclic tests is a bit more important than for materials GB5 and ABS but the agreement between both tests remains satisfying.

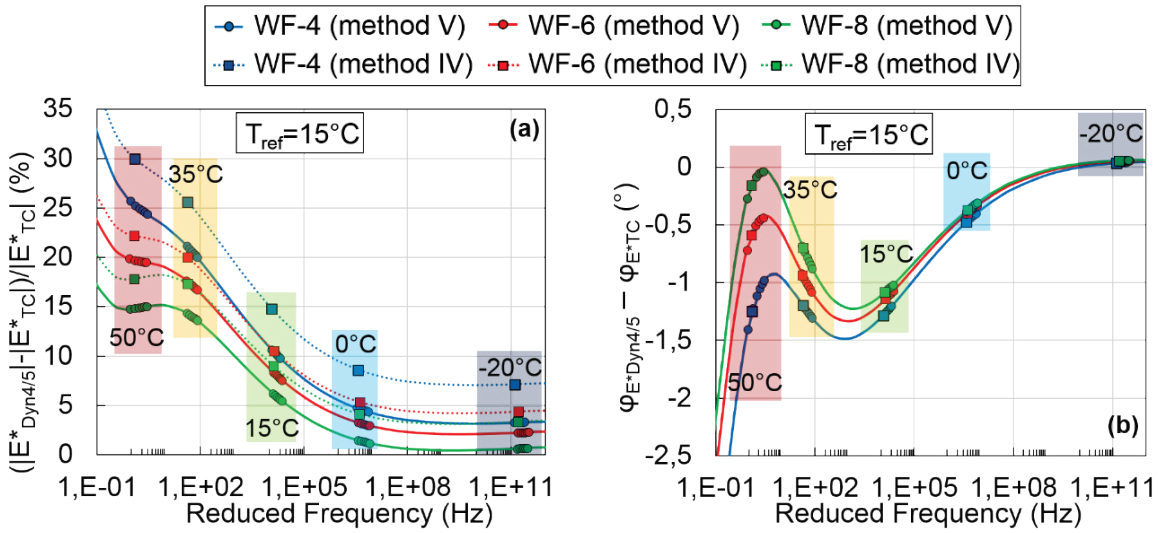

Figure 5.25 Master curve at 15°C of: (a) the relative difference between the norm of the complex modulus determined from dynamic tests with method IV/V ($|E^*_{Dyn4/5}|$) and from cyclic tests ($|E^*_{TC}|$); (b) the difference between the phase angle of the complex modulus determined from dynamic tests with method IV/V ($\varphi_{E^*Dyn4/5}$) and from cyclic tests (φ_{E^*TC}). Results for the WF specimens tested in the MHRAPC experimental campaign.

The same comparison was carried out for the values of the complex Poisson's ratio (ν_{BC}, ν^*_{Dyn}, ν^*_{ExpTC} and ν^*_{TC}). Results are plotted in Figure 5.26 and Figure 5.27. The same figure than Figure 5.26 can be found in APPENDIX M for the two other specimens. The values of the complex Poisson's ratio determined from dynamic tests are in good correlation with those determined from cyclic tests for the cylinder WF-8 as seen in Figure 5.26. Moreover, Figure 5.27 shows that there is less than 0.1 of difference between the norm of the complex Poisson's ratio determined from both tests for all specimens. However, the values of the phase angle of the complex Poisson's ratio determined with both tests are not in good agreement, especially for specimen WF-4 (up to 3° of difference). Though, considering the difficulty to determine accurately values of the complex Poisson's ratio in experimental tests, these differences are not surprising and the evaluation of the complex Poisson's ratio from dynamic tests has great potential.

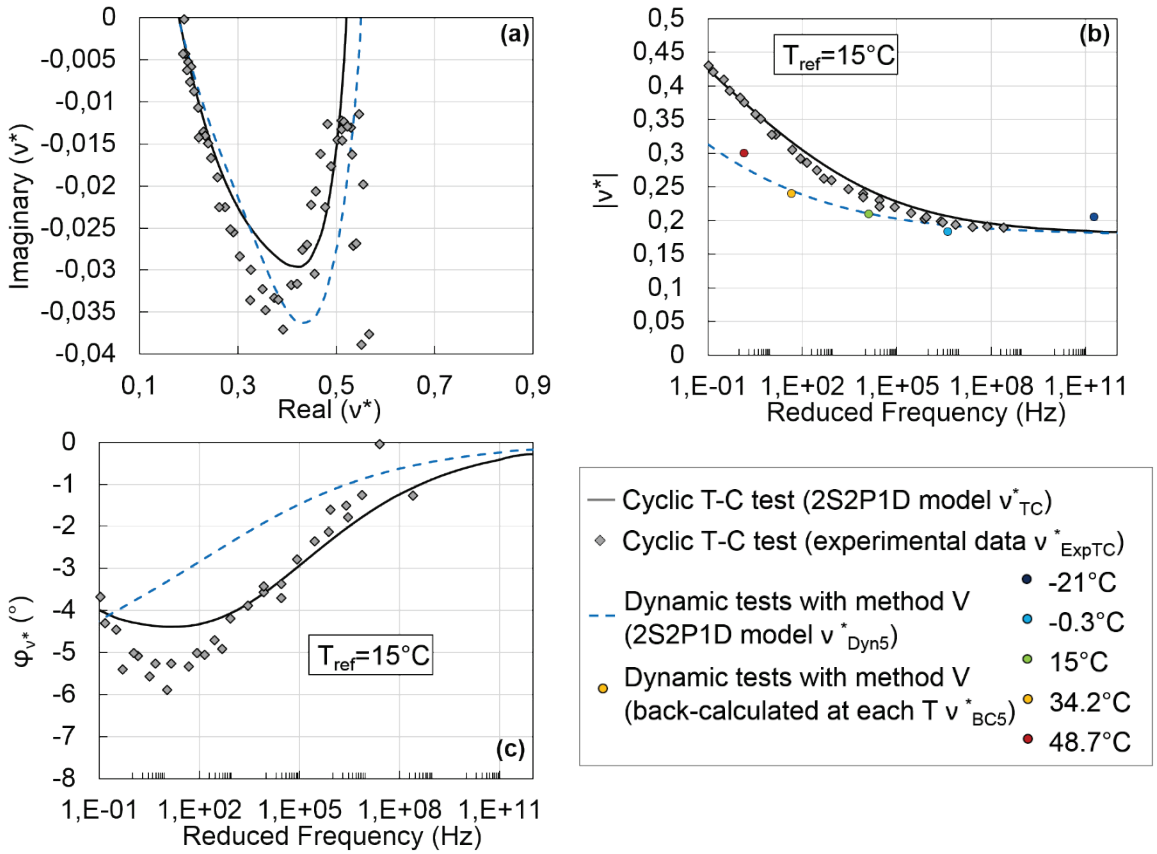

Figure 5.26 Comparison of the values of the complex Poisson's ratio determined from dynamic tests with method V (real values v_{BC5} and v^*_{Dyn5}) with the values of the complex Poisson's ratio determined from cyclic test (v^*_{ExpTC} and v^*_{TC}). (a) Cole-Cole plot; (b) and (c) master curves of the norm and of the phase angle of the complex Poisson's ratio at 15°C. Results for specimen WF-8.

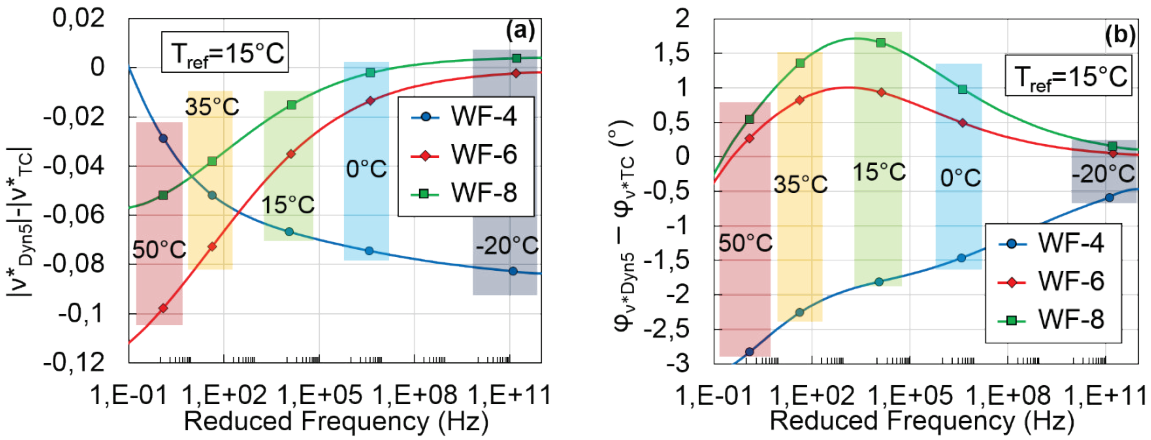

Figure 5.27 Master curve at 15°C of: (a) the relative difference between the norm of the complex Poisson's ratio determined from dynamic tests with method V ($|v^*_{Dyn5}|$) and from cyclic tests ($|v^*_{TC}|$); (b) the difference between the phase angle of the complex Poisson's ratio determined from dynamic tests with method V (φ_{v^*Dyn5}) and from cyclic tests (φ_{v^*TC}). Results for the WF cylinders tested in the MHRAPC experimental campaign.

Finally, the shift factors obtained from dynamic tests and from tension-compression tests were compared. Results are plotted in Figure 5.28 in which a good overall agreement is seen between the shift factors obtained from both tests.

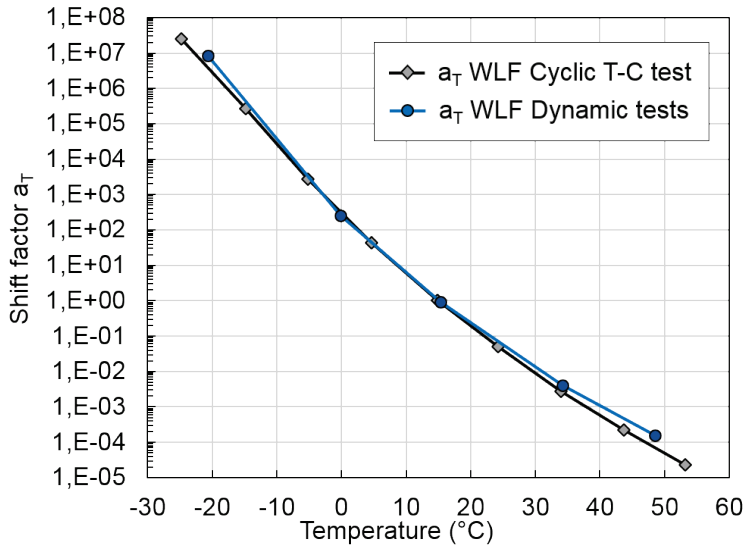

Figure 5.28 Comparison of the shift factors determined from dynamic tests with methods III, IV and V and from cyclic tension-compression tests for the three WF cylinders tested in the MHRAPC experimental campaign.

5.5 Materials from airport pavement (MAP)

The main objectives of this experimental campaign are to compare:

- To compare the LVE properties determined from dynamic tests for the specimens of the same materials.
- To compare the LVE properties determined from dynamic and cyclic tests for the materials from airport pavement considered in this campaign.

5.5.1 Materials

Two airfield pavement materials are considered in this experimental campaign. Both materials were drilled from a test track located at the test facility of the French Civil Aviation Technical Centre (Bonneuil-sur-Marne, France). This pavement was designed using the French rational design method (French civil aviation authority, 2016) with the Alizé software (Balay & Caron, 2008) for a ten years lifetime considering ten heavy weight deflectometer loads (or jumbo jets movements) per day.

The two upper layers are made of bituminous materials. The surface asphalt concrete (resp. the base asphalt concrete layer) has a continuous 0/10 (resp. 0/14) grading curve. Both materials have a 35/50 bitumen. More details about the materials will be found in APPENDIX I.

The first mixture tested in this campaign was cored from the base layer and is labelled GB. The second mixture was cored from the surface layer and is labelled BB. An unidentified layer, with a thickness of approximately 3cm was seen after the extraction of the specimens. Some specimens of this material labelled GB' were also considered in this campaign. The specimens cored from this layer were labelled GB' because it was suspected that the layer correspond to a thin layer of badly compacted material GB. Finally, note that the specimens cored in the direction of compaction are labelled GB-L, GB'-L or BB-L and the specimens cored in the transverse direction are labelled GB-T and BB-T. Details of the specimens tested in this campaign are given in Table 5.18.

Table 5.18. Specimens tested in the MAP experimental campaign.

Specimen	H (mm)	D (mm)	Density (kg/m^3)	Void ratio (%)
GB-L-1	152.1	73.5	2 410	4.1
GB-L-2	151.4	74.0	2 400	4.5
GB-L-3	150.8	33.9	2 392	4.8
GB-L-4	150.7	33.8	2 405	4.3
GB-L-5	150.6	34.0	2 375	5.5
GB'-L-1	151.3	33.9	2 275	9.4
GB'-L-2	150.1	33.9	2 291	8.8
GB'-L-3	150.8	34.0	2 260	10.0
GB-T-1	151.5	73.9	2 404	4.3
GB-T-2	151.5	73.9	2 411	4.0
BB-L-1	151.3	74.0	2 543	1.8
BB-L-2	151.0	74.1	2 541	1.9
BB-T-1	152.0	74.6	2 530	2.3
BB-T-2	151.9	74.0	2 547	1.7

5.5.2 Tests performed

The same experimental procedure than in previous campaigns was used for the dynamic tests (see Figure 3.1). The GB and GB'specimens were tested at -20°C, 0°C, 15°C, 35°C and 50°C while the BB specimens were tested at -20°C, 0°C, 15°C, 30°C and 45°C. The longitudinal mode of vibration was used for all the specimens. Two specimens (GB-L-1 and BB-L-1) were also tested with cyclic tension-compression tests performed one month after the dynamic tests.

5.5.3 LVE properties determined from dynamic tests

The values of the constants of the 2S2P1D model and WLF equation at 15°C simulating the global LVE behaviour determined from dynamic tests are listed in Table 5.19. These results were obtained with method III (cf. section 4.3.1.3.1) for all specimens except for GB-L-1 and BB-L-1 for which method V (cf. section 4.3.2.1) was used. The analysis methods used were chosen following the recommendations from section 4.3.3. The specimens GB-L-1 and BB-L1 are the only specimens for which method V was used because they are the only specimen for which the complex Poisson's ratio was measured with tension-compression tests. When using method III, the constants E_{00}, β, γ_{Ev}, ν_0 and ν_{00} were fixed in the first step of the method to the values of the constants of the reference LVE material (for E_{00} and β) and to the values of the constants determined with method V and listed in Table 5.19 (for γ_{Ev}, ν_0 and ν_{00}). For all specimens, the values of the constants obtained after the optimizations at each temperature are given in APPENDIX N. The figures showing comparisons of the experimental FRFs and calculated FRFs and the complex modulus values determined from dynamic tests will also be found in APPENDIX N.

Table 5.19. Values of the constants of the 2S2P1D model and WLF equation simulating the global LVE behaviour determined from dynamic tests with methods III and V for the specimens tested in the MAP experimental campaign.

	2S2P1D model									WLF equation at 15°C	
Specimen	**E_0 (MPa)**	**$\tau_{E15°C}$ (s)**	**k**	**δ**	**h**	**ν_0**	**ν_{00}**	**$\tau_{v15°C}$ (s)**	**γ_{Ev}**	**C_1**	**C_2**
GB-L-1 (Meth.V)	39 400	0.032	0.137	1.18	0.500	0.285	0.55	0.1	0.32	17.6	132.6
GB-L-2 (Meth.III)	38 100	0.031				-	-	-	-		
GB-L-3 (Meth.III)	36 500	0.034				-	-	-	-		
GB-L-4 (Meth.III)	36 600	0.030				-	-	-	-		
GB-L-5 (Meth.III)	37 300	0.031				-	-	-	-		
GB'-L-1 (Meth.III)	26 500	0.033	0.137	1.10	0.510	-	-	-	-		
GB'-L-2 (Meth.III)	28 400	0.035				-	-	-	-		
GB'-L-3 (Meth.III)	28 700	0.034				-	-	-	-		
GB-T-1 (Meth.III)	38 900	0.033	0.137	1.18	0.500	-	-	-	-		
GB-T-2 (Meth.III)	39 100	0.029				-	-	-	-		
BB-L-1 (Meth.V)	41 400	0.013	0.161	1.38	0.555	0.260	0.55	10	0.0013	20.0	149.3
BB-L-2 (Meth.III)	41 800	0.019				-	-	-	-		
BB-T-1 (Meth.III)	40 300	0.016				-	-	-	-		
BB-T-2 (Meth.III)	41 300	0.013				-	-	-	-		

The same values of constants C_1 and C_2 are obtained for all the specimens of each material. Values of constants k, δ and h are also the same for all specimens of each material except for the GB' cylinders for which slight differences are seen with the GB specimens. The Cole-Cole plot and the master curves at 15°C of the norm and phase angle of the normalized complex modulus (equation (5-1)) are plotted in Figure 5.29 for the GB, GB' and BB specimens. The master curves corresponding to the GB and GB' specimens are in very good agreement and they are quite different than the master curves of the BB specimens which have lower values of the norm of the normalized complex modulus and higher value of the phase angle for reduced frequencies lower than 10^5 Hz. Figure 5.29 demonstrates one more time the good repeatability of dynamic tests, even when using different dimensions for the GB and GB' cylinders. It also confirms that the material of the GB and GB' specimens is the same. The GB' specimens were probably cored from a layer not well compacted.

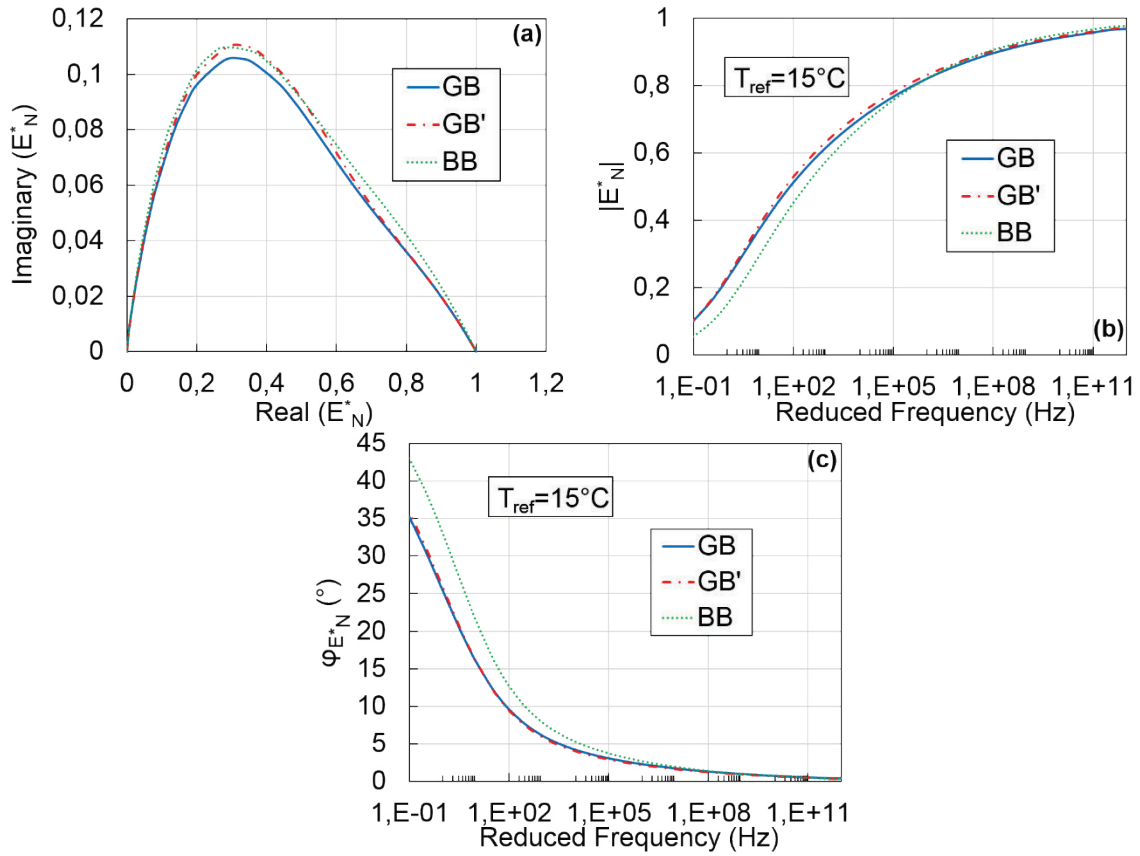

Figure 5.29 Comparison of the values of the normalized complex modulus determined from dynamic tests for the specimens tested in the MHRAPC experimental campaign. (a) Cole-Cole plot; (b) and (c) master curves of the norm and of the phase angle of the normalized complex modulus at 15°C.

5.5.4 Comparison of the LVE properties determined from dynamic tests and from cyclic tension-compression tests

The values of the constants of the 2S2P1D model and WLF equation at 15°C simulating the global LVE behaviour determined from tension compression tests are listed in Table 5.20.

Table 5.20. Values of the constants of the 2S2P1D model and WLF equation simulating the global LVE behaviour determined from cyclic tension-compression tests for specimens GB-L-1 and BB-L-1 tested in the MAP experimental campaign.

	2S2P1D model										**WLF equation at 15°C**	
Specimen	**E_{00} (MPa)**	**E_0 (MPa)**	**$\tau_{E15°C}$ (s)**	**k**	**δ**	**h**	**β**	**ν_0**	**ν_{00}**	**$\tau_{\nu15°C}$ (s)**	**C_1**	**C_2**
GB-L-1	14	37 500	0.107	0.180	2.05	0.59	130	0.21	0.30	200	27.3	184.2
BB-L-1	9	39 500	0.025	0.205	2.20	0.63	60	0.24	0.50	10	24.9	166.6

Values of the complex modulus obtained from dynamic and cyclic tests (E^*_{BC5}, E^*_{Dyn5}, E^*_{ExpTC} and E^*_{TC}) are plotted in Figure 5.30 for specimen BB-L-1. The same figure can be found in APPENDIX N for specimen GB-L-1. A good overall agreement is seen between the different curves plotted in Figure 5.30. The relative difference (respectively the difference) between the norm (respectively the phase angle) of E^*_{Dyn5} and E^*_{TC} are plotted in Figure 5.31 for both materials. Results confirm the observation from the previous campaigns: the norm of the

complex modulus evaluated from dynamic tests is little higher while no significant difference is seen for the phase angle. The relative difference remains less than 15% on the whole frequency range while the maximum difference for the phase angle is of about only 2°.

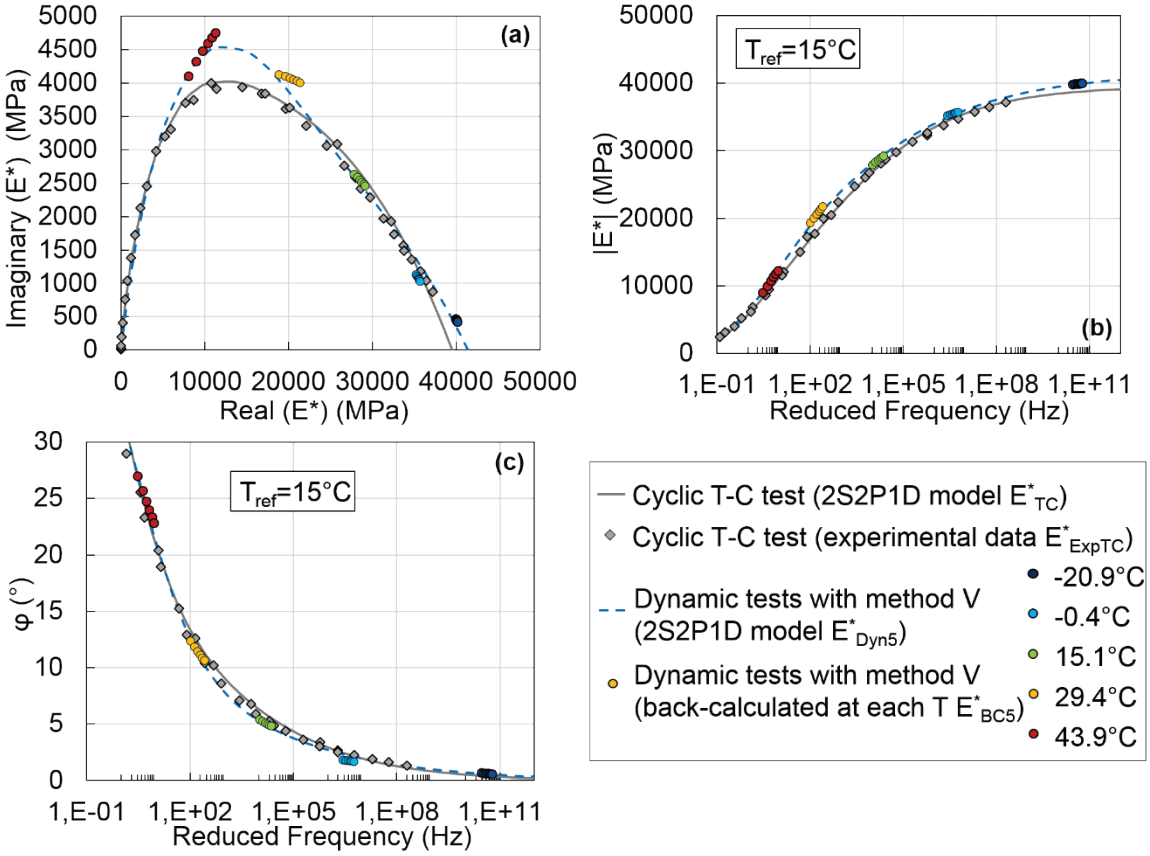

Figure 5.30 Comparison of the values of the complex modulus determined from dynamic tests with method V (E^*_{BC5} and E^*_{Dyn5}) with the values of the complex modulus determined from cyclic tests (E^*_{ExpTC} and E^*_{TC}). (a) Cole-Cole plot; (b) and (c) master curves of the norm and of the phase angle of the complex modulus at 15°C. Results for specimen BB-L-1.

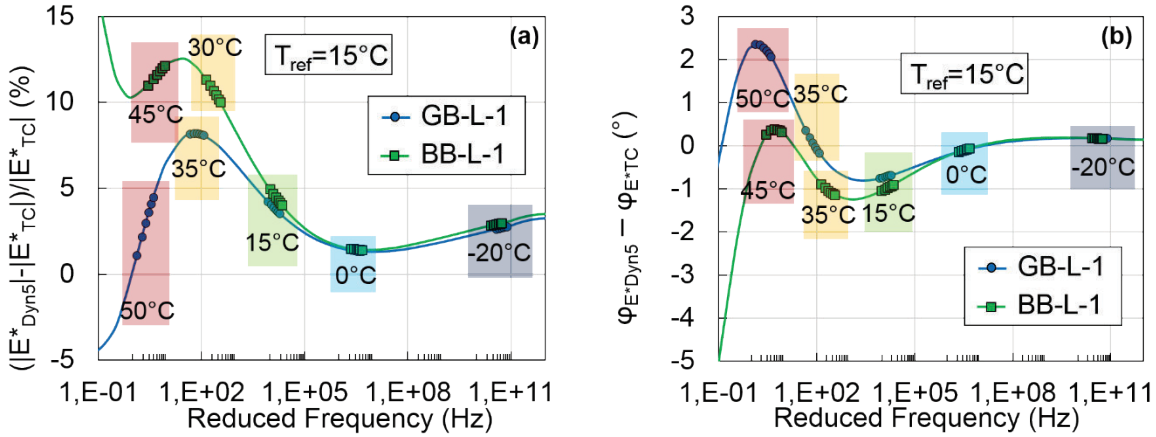

Figure 5.31 Master curve at 15°C of: (a) the relative difference between the norm of the complex modulus determined from dynamic tests with method V ($|E^*_{Dyn5}|$) and from cyclic tests ($|E^*_{TC}|$); (b) the difference between the phase angle of the complex modulus determined from dynamic tests with method V (φ_{E^*Dyn5}) and from cyclic tests (φ_{E^*TC}). Results for the GB-L-1 and BB-L-1 specimens tested in the MAP experimental campaign.

The same comparison was performed for the values of the complex Poisson's ratio (ν_{BC5}, ν^*_{Dyn5}, ν^*_{ExpTC} and ν^*_{TC}). Results are plotted in Figure 5.32 and Figure 5.33. The same figure than Figure 5.32 can be found in APPENDIX N for cylinder GB-L-1. As seen in Figure 5.32, the values of the complex Poisson's ratio determined from dynamic tests are in good agreement with those determined from cyclic tests for the cylinder BB-L-1. However, Figure 5.33 shows that more important differences exist for cylinder GB-L-1 (up to 0.25 for the norm of the complex Poisson's ratio and to 2° for the phase angle). The reason for these differences for cylinder GB-L-1 is not identified. Though, considering the difficulty to determine accurately values of the complex Poisson's ratio in experimental tests, these differences are not alarming and dynamic tests are a good possibility to obtain values of the complex Poisson's.

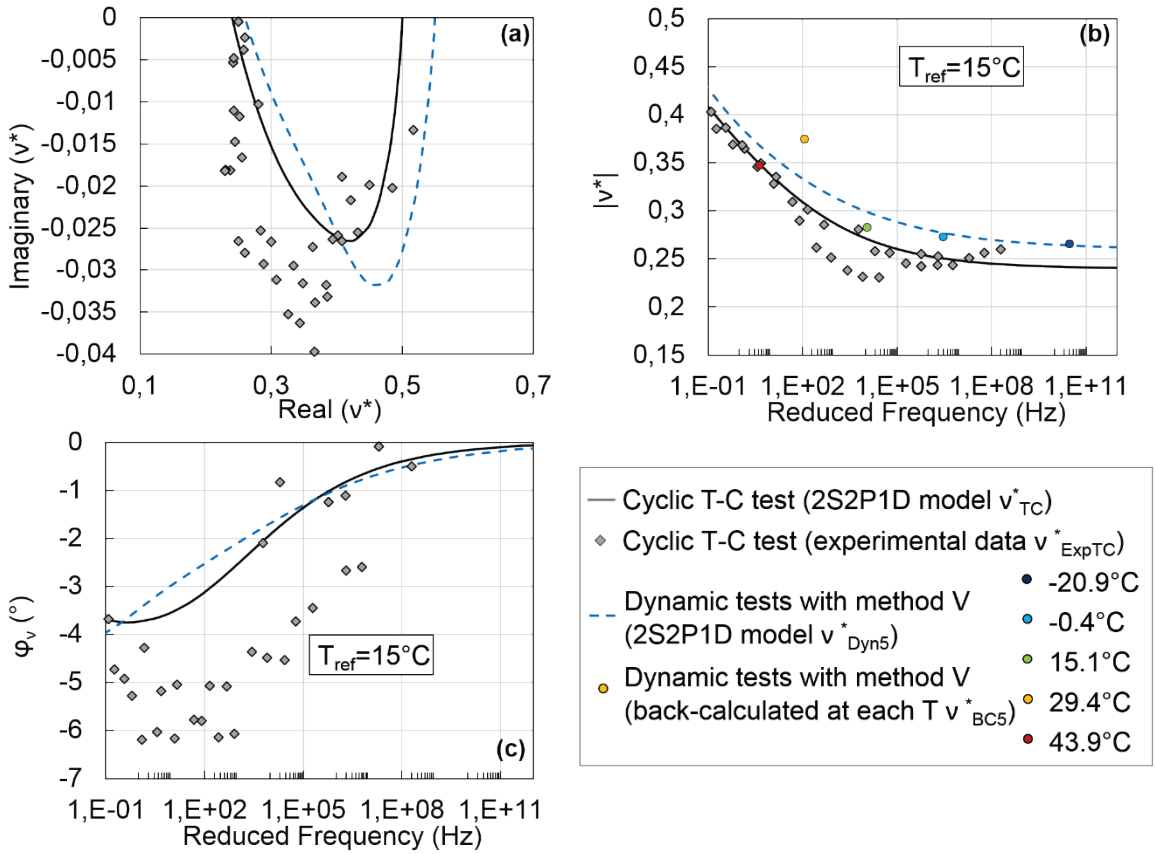

Figure 5.32 Comparison of the values of the complex Poisson's ratio determined from dynamic tests with method V (real values ν_{BC5} and ν^*_{Dyn5}) with the values of the complex Poisson's ratio determined from cyclic test (ν^*_{ExpTC} and ν^*_{TC}). (a) Cole-Cole plot; (b) and (c) master curves of the norm and of the phase angle of the complex Poisson's ratio at 15°C. Results for specimen BB-L-1.

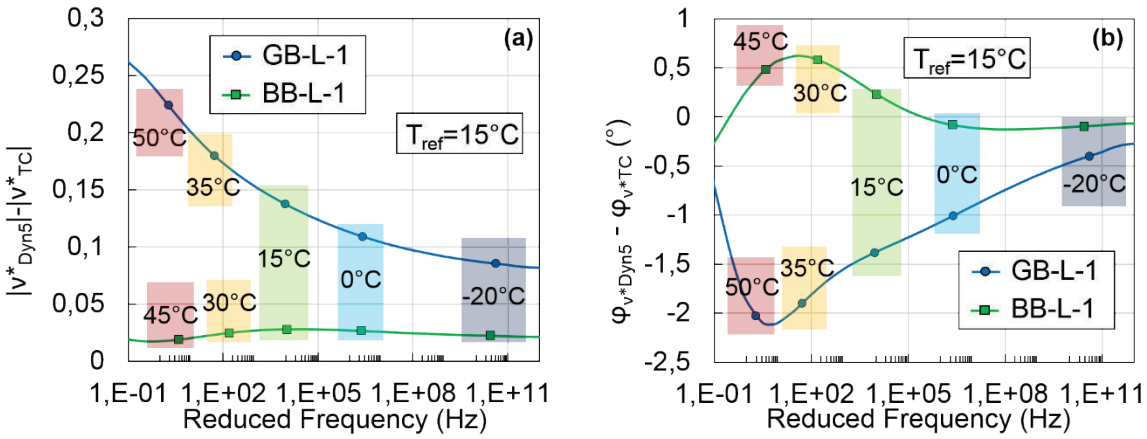

Figure 5.33 Master curve at 15°C of: (a) the relative difference between the norm of the complex Poisson's ratio determined from dynamic tests with method V ($|v^*_{Dyn5}|$) and from cyclic tests ($|v^*_{TC}|$); (b) the difference between the phase angle of the complex Poisson's ratio determined from dynamic tests with method V (φ_{v^*Dyn5}) and from cyclic tests (φ_{v^*TC}). Results for the GB-L-1 and BB-L-1 cylinders tested in the MAP experimental campaign.

Finally, the shift factors obtained from dynamic tests and from tension-compression tests are compared. in Figure 5.34 in which a good overall agreement is seen between the shift factors obtained from both tests for the two considered materials.

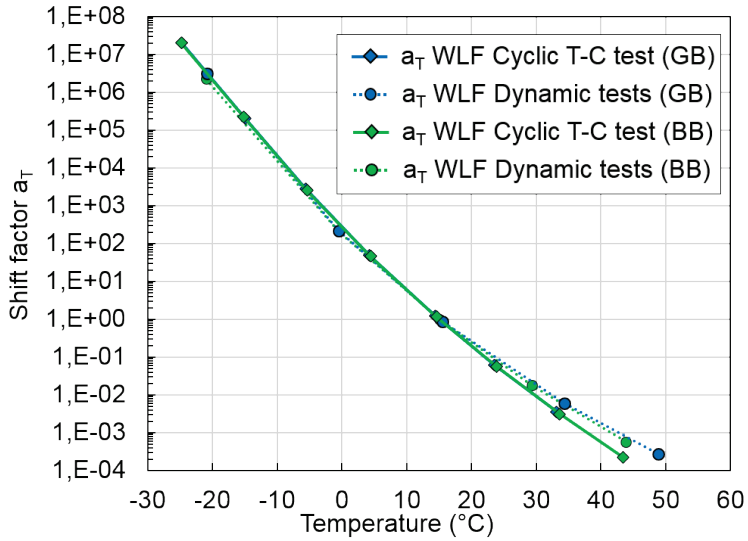

Figure 5.34 Comparison of the shift factors determined from dynamic tests with methods III, IV and V and from cyclic tension-compression tests for the GB and BB specimens tested in the MAP experimental campaign.

6 APPENDED PAPERS

Paper I : Back analysis of impact loadings on viscoelastic specimen

CARRET JEAN-CLAUDE
DI BENEDETTO HERVE
SAUZEAT Cédric

Conference Paper
10th International Conference on Road and Airfield Pavement Technology (ICPT 2017)
Honk-Kong, August 2017

BACK ANALYSIS OF IMPACT LOADINGS ON LINEAR VISCOELASTIC SPECIMEN

CARRET Jean-Claude[1], DI BENEDETTO Herve[1] and SAUZEAT Cedric[1]

[1]*LTDS (UMR CNRS 5513), University of Lyon / ENTPE, Rue M. Audin, 69518, Vaulx en Velin, France*
E-mail: jean-claude.carret@entpe.fr
E-mail: herve.dibenedetto@entpe.fr
E-mail: cedric.sauzeat@entpe.fr

ABSTRACT

In this paper, an investigation was performed to determine if the viscoelastic analysis of bituminous mixtures under dynamic loadings gives different results than the simplified elastic analysis. First, different asphalt mixes (AM) were tested with cyclic tension-compression tests and the results were analyzed using the 3 dimensional 2S2P1D linear viscoelastic (LVE) model with continuous spectrum. From a large data base considering very different types of AM, a LVE material was created considering "average" viscoelastic properties. Then, this material was used to perform finite elements method (FEM) numerical simulations of a cylinder under dynamic loadings at 8 different temperatures from -40°C to 30°C. Only longitudinal mode of vibrations is studied in this paper. The complex Young's modulus and complex Poisson's ratio were first obtained using the viscoelastic 2S2P1D model considering resonance frequencies. Then, a combined back analysis, which has the advantage of simplicity, was used to determine the elastic equivalent properties and the damping of the specimen. The complete viscoelastic analysis and the combined back analysis results regarding both parameters are discussed in the paper.

Keywords: asphalt mixes, viscoelasticity, dynamic loading, finite element calculation.

1. INTRODUCTION

Nondestructive seismic measurements such as impact loadings are economical, simple to perform and seem to be a good approach to provide accurate characterization of materials properties (Migliori et al., 1993). Wave propagation measurements (Mounier et al., 2012; Di Benedetto et al., 2009) and measurements of the fundamental resonance frequencies (Kweon G., & Kim Y. R., 2006; Whitmoyer, S.L. & Kim, Y.R., 1994) have been used to determine the complex moduli of asphalt mixtures (AM). These methods provide information for the tested VEL material only for limited number of resonant frequencies (1 to 3), which are, a priori, unknown. In these tests, simplified approximate formulations are used to determine a complex modulus for each considered temperature and mode of vibration (ASTM: C215-08, 2008). Ryden (2011) applied resonant acoustic spectroscopy (RAS) to calculate resonance frequencies for different mode types of cylindrical discs and beams. In this paper, frequency response functions (FRFs) were calculated with FEM numerical simulations of impact loadings on a cylindrical viscoelastic specimen. Only the fundamental resonance frequency of the longitudinal mode of vibration was considered for the 8 tested temperatures between -40°C and 30°C. Viscoelastic properties of the specimen were estimated at the corresponding resonance frequency with the 2S2P1D linear viscoelastic model for each temperature. Then, a combined back analysis was performed to determine the elastic equivalent properties and the damping of the specimen. Finally, results from the viscoelastic analysis and from the combined back analysis were compared.

2. MATERIALS AND TESTING

2.1 Materials and considered material model

38 specimen used in 4 different PhD thesis performed at University of Lyon / ENTPE, LTDS laboratory (Nguyen, Q. T., 2011; Mangiafico, S., 2014; Pham, N. H., 2014; Viet, P. C., 2016) were considered. From all these specimen, that represent a good range of bituminous mixture types, a material model with "averaged" viscoelastic properties were created from average values of the constants of the LVE 2S2P1D model obtained for each material. This material model was used to run the numerical simulations and analyses that are presented in the paper.

2.2 Tension-compression tests

Tension-compression tests were used to determine complex modulus of asphalt mixes. Tests were performed on cylindrical samples (150 mm high with a 75 mm diameter). Cyclic sinusoidal loadings were performed using a hydraulic press, as shown in Figure 1, in strain-controlled mode with an amplitude of 10^{-5} m/m.

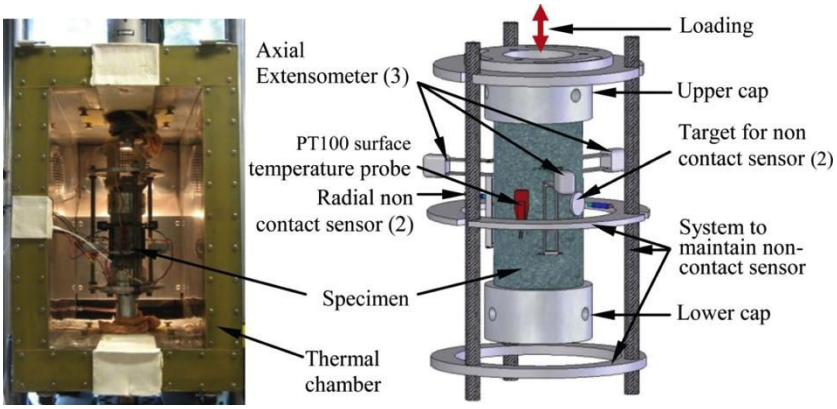

Figure 1. (left) Tension-compression test apparatus used for tests on asphalt mixes; (right) detailed scheme of measurement devices and sample).

Axial stress ($\sigma_1=\sigma_0.sin(\omega t-\phi_E)$) was measured with a load cell, while axial strain ($\varepsilon_1=\varepsilon_{01}.sin(\omega t)$) was obtained from three extensometers placed at 120° and radial strain ($\varepsilon_2=\varepsilon_{02}.sin(\omega t+\phi_v)$) was deduced from non-contact transducers (figure 1). The complex modulus and the complex Poisson's ratio at different loading frequencies and temperatures are calculated according to Eq. 1 and Eq. 2 where ϕ_E and ϕ_v is the phase of the complex modulus and of the complex Poisson's ratio, respectively.

$$E^*(\omega)=\frac{\sigma_1^*}{\varepsilon_1^*}=\left|E^*(\omega)\right|e^{i\Phi_E} \tag{1}$$

$$\nu^*(\omega)=-\frac{\varepsilon_2^*}{\varepsilon_1^*}=\left|\nu^*(\omega)\right|e^{i\Phi_\nu} \tag{2}$$

2.3 Dynamic impact tests

The test set-up of the dynamic impact tests is illustrated in Figure 2. An impact hammer equipped with a load cell (PCB model 086E80) is used to manually apply a load impulse on the specimen. An accelerometer (PCB model 353B15), attached using wax, is used to measure the standing wave modes. The specimen is placed on soft foam to achieve free boundary conditions

(Whitmoyer, S.L., & Kim, Y.R., 1994). A signal conditioner (PCB model 482C15), a data acquisition device (NI DAQ USB-6251) and a computer are connected to the hammer and to the accelerometer according to Figure 2. Only the longitudinal mode of vibration was measured in this study, by hitting the specimen in the middle of one short side while placing the accelerometer on the middle of the opposite short side (see Figure 2.).

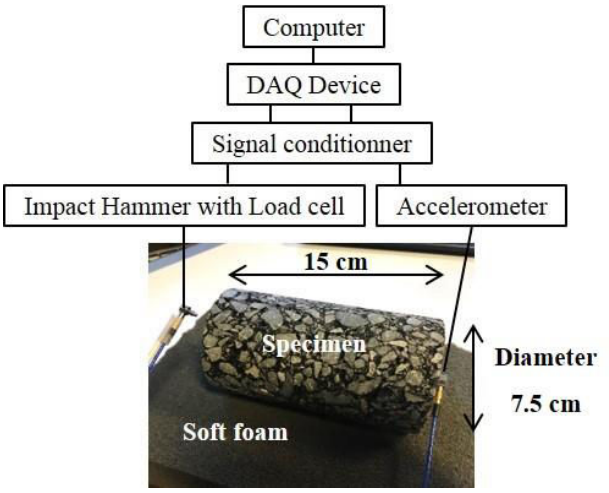

Figure 2. Dynamic impact tests set-up (ENTPE laboratory, Vaulx-en-Velin, France).

The longitudinal mode of vibration was excited by five impacts and a Frequency Response Function (FRF) has been calculated from the average of these five impacts for each measurement temperature according to Eq. 3,

$$H(f) = \left(\overline{Y(f).X^*(f)}\right) / \left(\overline{X(f).X^*(f)}\right) \tag{3}$$

where *H(f)* is the FRF, *Y(f)* is the measured acceleration, *X(f)* is the measured applied force, *X*(f)* is the complex conjugate of the applied force and the bar above represents the arithmetic mean.

3. VISCOELASTIC ANALYSIS

3.1 2S2P1D linear viscoelastic isotropic model

Experimental tension-compression tests results were analyzed using 2S2P1D model (Di Benedetto et al., 2004; Olard & Di Benedetto, 2003; Tijouani et al., 2011), developed at ENTPE. It consists of a combination of two springs, two parabolic creep elements and one dashpot. The complex modulus of the 2S2P1D model is expressed according to Eq. 4,

$$E^*_{2S2P1D}(\omega) = E_{00} + \frac{E_0 - E_{00}}{1 + \delta(j\omega\tau)^{-k} + (j\omega\tau)^{-h} + (j\omega\beta\tau)^{-1}} \tag{4}$$

Where ω is the angular frequency ($\omega=2\pi f$, where f is the frequency), E_{00} is the static modulus when ω tends towards 0, E_0 is the glassy modulus when ω tends towards $+\infty$, δ is a dimensionless constant, k and h are dimensionless constants such as $0 < k < h < 1$, β is a dimensionless constant related to Newtonian viscosity η by $\eta = (E_0-E_{00})\,\beta\tau$ and τ is the characteristic time, whose value varies only with temperature. The time-temperature superposition principle is verified for bituminous mixtures in the linear and nonlinear domains (Nguyen HM et al. 2009; Nguyen ML et al. 2013; Nguyen QT et al. 2013) using:

$$\tau(T) = a_T(T)\tau_{ref} \tag{5}$$

Where a_T is the shift factor at the temperature T given by the Williams-Landel-Ferry (WLF) equation (Ferry, 1980):

$$\log(a_T) = -\frac{C_1(T - T_{ref})}{C_2 + T - T_{ref}} \tag{6}$$

Where C_1 and C_2 are the two WLF constants and T_{ref} is the reference temperature.

Di Benedetto et al. (2007) extended the 2S2P1D model to characterize complex Poisson's ratio as given in Eq. 7,

$$\nu^*_{2S2P1D}(\omega) = \nu_{00} + \frac{\nu_0 - \nu_{00}}{1 + \delta(j\omega\tau_\nu)^{-k} + (j\omega\tau_\nu)^{-h} + (j\omega\beta\tau_\nu)^{-1}} \tag{7}$$

Where ν_{00} is the low frequency Poisson's ratio when ω tends towards 0 and ν_0 is the high frequency Poisson's ratio when ω tends towards $+\infty$. Note that the same value of the parameters δ, k, h and β are used to determine both the complex modulus and complex Poisson's ratio while τ is determined uniquely for Poisson's ratio and is therefore labeled τ_ν. The 2S2P1D parameters for the material model used in the numerical simulations (see section 2.1) are given in Table 1.

Table 1. 2S2P1D constants for the material model with "averaged" viscoelastic properties of bituminous mixtures

E_{00} (MPa)	E_0 (MPa)	ν_0	ν_{00}	δ	k	h	β	$\tau_{10°C}$ (s)	τ_ν (s)	C_1	C_2
105	35 000	0.19	0.24	2.15	0.17	0.525	505	0.1	3.165	30	210

3.2 Finite elements method numerical simulations

Finite element method (FEM) was used to calculate FRFs (Eq. 3), using the three-dimensional equation of motion in the frequency domain (Eq. 8)

$$-\rho\omega^2\mathbf{u} - \nabla.\sigma = \mathbf{F_p}e^{i\Phi} \tag{8}$$

Where ρ is the density, ω is the angular frequency, $\mathbf{u}$ is the displacement vector, ∇ is the gradient tensor operator, i is the square root of -1 and σ is the Cauchy stress tensor. $\mathbf{F_p}$ is the unity load equal to 1N and ϕ is the phase of the cyclic load.

The unity load in the model has been applied to the corresponding point of the hammer impact in the measurement of the longitudinal mode of vibration, while the response has been determined at the point corresponding to the position of the accelerometer. The simulations were performed at 8 different temperatures from -40°C to 30°C, considering steps of 20 Hz in a frequency range from 100 Hz to 20 000 Hz. More precise simulations with steps of 1 Hz were also carried out around the first resonant frequency for each temperature in order to obtain a better evaluation of the fundamental resonant frequency and of the damping of the material. The geometry used for the study was a cylinder with a 150 mm height and a 75 mm diameter. The mesh consists of tetrahedral elements with a maximum element size of 2.5 cm that was determined through a convergence study.

4. COMBINED BACK ANALYSIS

For each tested temperature, the viscoelastic FRF was calculated with FEM numerical simulations using 2S2P1D model (complex modulus and complex Poisson's ratio) of the model material (considered as isotropic) as input. From the calculated viscoelastic FRF, the fundamental resonance frequency of the longitudinal mode of vibration, f_{FL}, was determined and this frequency was used in the 2S2P1D model to calculate the corresponding longitudinal complex modulus, E^*_{FL}, and Poisson's ratio, ν^*_{FL}, according to Eq. 9 and Eq. 10.

$$E^*_{FL} = E^*_{2S2P1D}(2\pi f_{FL}) \tag{9}$$

$$\nu^*_{FL} = \nu^*_{2S2P1D}(2\pi f_{FL}) \tag{10}$$

The frequency bandwidth Δf (figure 3) was determined according to the half-power bandwidth method, and the phase angle used in the back analysis, ϕ_{BA}, was deduced using the following relationship suggested by Clough and Penzien (1993):

$$\phi_{BA} = tan^{-1}\left(\frac{\Delta f}{f_{FL}}\right) \tag{11}$$

Then, f_{FL} and three different real values of Poisson's ratio of 0.2, $|\nu^*_{FL}|$, and 0.45 were used as input in elastic FEM numerical simulations to back-calculate three elastic equivalent moduli, E_{EE1}, E_{EE2} and E_{EE3}. ϕ_{BA} was considered as the corresponding phase angle for these moduli and three complex moduli, E^*_{BA1}, E^*_{BA2} and E^*_{BA3} were determined according to Eqs. 12-14.

$$E^*_{BA1} = E_{EE1}e^{i\phi_{BA}} \tag{12}$$

$$E^*_{BA2} = E_{EE2}e^{i\phi_{BA}} \tag{13}$$

$$E^*_{BA3} = E_{EE3}e^{i\phi_{BA}} \tag{14}$$

Finally, the norm and the phase angle of the complex modulus E^*_{FL} were compared to the norm and to the phase angle of the three complex moduli E^*_{BA1}, E^*_{BA2} and E^*_{BA3} allowing to consider the effect of the Poisson's ratio value. The explanation of the combined back analysis described above is given in Figure 3.

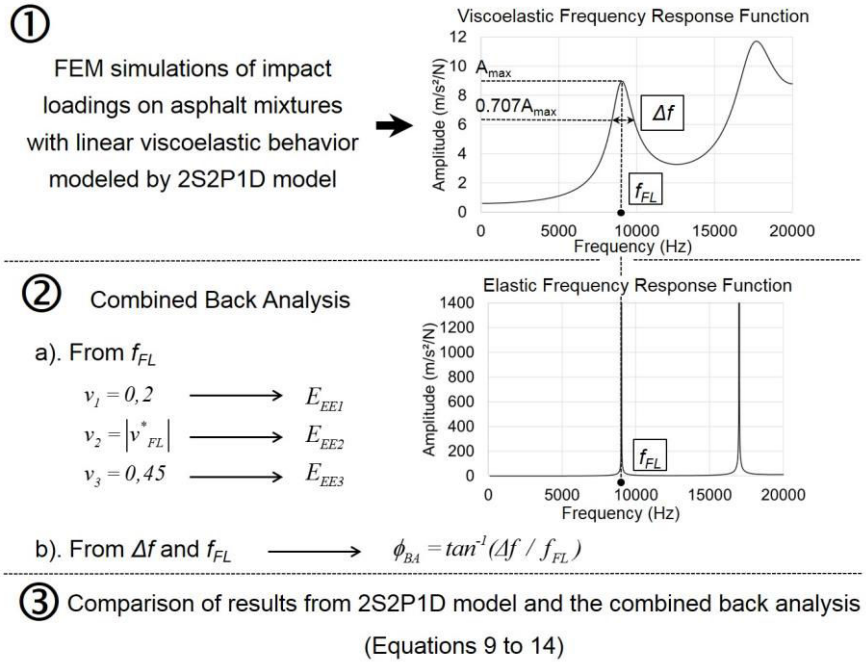

Figure 3. Explanation of the combined back analysis.

5. COMPARISON BETWEEN THE LINEAR VISCOELASTIC ANALYSIS AND THE PROPOSED COMBINED BACK ANALYSIS

The procedure described previously was used to determine the values of f_{FL}, $|E^*_{FL}|$, ϕ_{FL}, $|\nu^*_{FL}|$, ϕ_{BA}, E_{EE1}, E_{EE2} and E_{EE3} for the 8 considered temperatures. Results are given in Table 2.

Table 2. Results of the numerical simulations and the combined back analysis

	2S2P1D model			Combined Back Analysis				
T (°C)	$\|E^*_{FL}\|$ *(MPa)*	Φ_{FL} (°)	$\|\nu^*_{FL}\|$	f_{FL} *(Hz)*	Φ_{BA} (°)	E_{EE1} *(MPa)*	E_{EE2} *(MPa)*	E_{EE3} *(MPa)*
-40	34 602	0.178	0.191	12 320	0.186	34 645	34 605	34 425
-30	34 029	0.434	0.194	12 216	0.450	34 060	34 030	35 810
-20	32 890	0.943	0.198	12 006	0.969	32 900	32 890	34 585
-10	30 891	1.837	0.206	11 631	1.901	30 870	30 910	32 460
0	27 813	3.232	0.219	11 031	3.372	27 775	27 850	29 200
10	23 675	5.219	0.238	10 173	5.542	23 620	23 755	24 840
20	18 770	8.049	0.264	9 062	8.813	18 740	18 930	19 705
30	13 475	12.575	0.294	7 708	14.782	13 560	13 780	14 260

There is no temperature above 30°C in Table 2, because it was impossible to estimate the damping of the material and the phase angle with the half-power bandwidth method for such temperatures. Therefore, the relationship suggested by Clough and Penzien (Eq. 11) is not applicable for high temperatures. The solid line in Figure 4 presents the relative change of the elastic equivalent moduli E_{EE1}, E_{EE2} and E_{EE3} compared to the norm of the longitudinal complex modulus, $|E^*_{FL}|$, calculated using 2S2P1D model at the frequency f_{FL}.

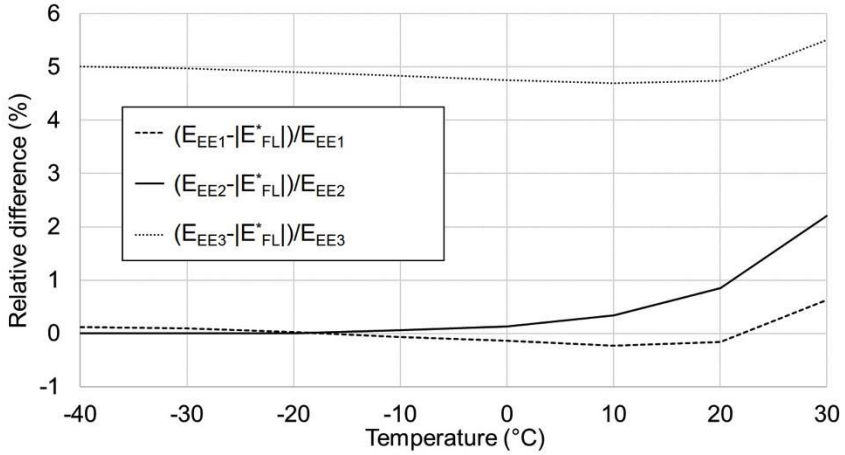

Figure 4. Relative difference between the norm of complex moduli from the combined back analysis and the norm of the 2S2P1D model complex modulus.

Figure 4. clearly shows that there is a good correlation between the elastic equivalent moduli E_{EE2} and the complex modulus from the 2S2P1D model with a maximum relative difference of less than 2.5 % at the temperature of 30°C. It can also be seen on Fig. 4 that the Poisson's ratio value has an impact on the calculation of the elastic equivalent moduli. The relative change is clearly higher for E_{EE3} that is calculated for a Poisson's ratio of 0.45. Figure 5 presents the difference in ° between the back analysis phase angle ϕ_{BA} and the phase angle ϕ_{FL} given by 2S2P1D model at the frequency f_{FL}. Figure 5 shows also a good correlation between the back analysis phase angle ϕ_{BA} and the 2S2P1D phase angle with a maximum 2.5° difference for the temperature of 30°C. It can also be observed that errors between values calculated with the combined back analysis and values given by the 2S2P1D model increase with higher temperatures, especially for the phase angle.

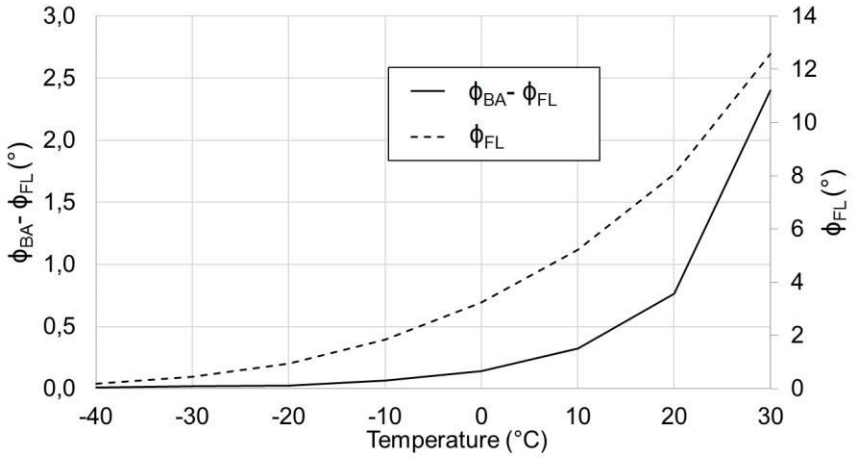

Figure 5. Difference between phase angle from the combined back analysis and the 2S2P1D model phase angle.

Figure 6 presents the different obtained complex moduli in a Cole-Cole diagram. It can be seen that the correlation between, E^*_{BA2} and complex modulus from the 2S2P1D model is very good at low temperatures which confirms the observations from Fig. 4 and 5.

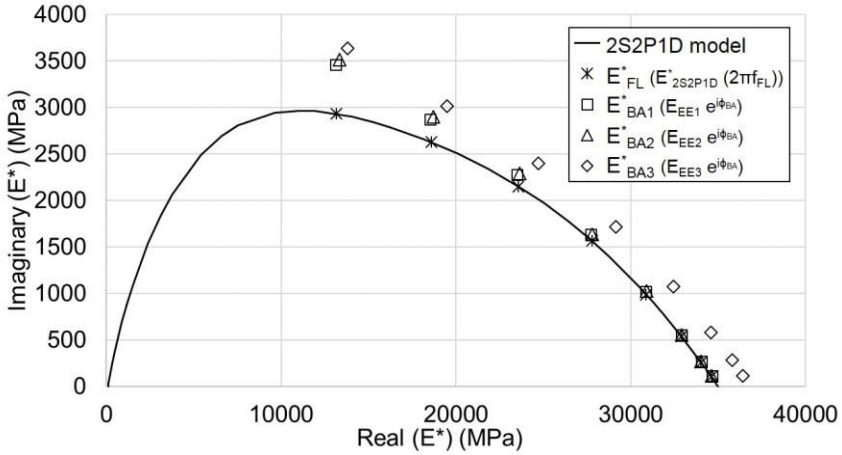

Figure 6. Complex modulus values obtained from the 2S2P1D model and the proposed combined back analysis.

6. CONCLUSION

It is shown in this paper that the proposed simplified back analysis gives good results for low and intermediate temperatures, both for the norm of the complex modulus and for the phase angle. For temperatures higher than 20°C, slight differences appear. These differences are mostly due to an overestimation of the phase angle for the higher temperatures. Therefore, the half-power bandwidth method used to determine the phase angle is not adapted for high temperatures because it overestimates the damping of the materials. Poisson's ratio effect was also studied. It was found that it has a significant impact on the calculation of the elastic equivalent modulus. The observations and findings from this study demonstrate that for temperatures under 20°C, a good evaluation of Poisson's ratio and a simplified combined back analysis are sufficient to back analyse impact loadings on asphalt mixtures. However, for higher temperatures, the method does not provide good evaluation of phase angle for values higher than about 15°. For temperatures above 30°C corresponding to phase angle of above 15° the half-power bandwidth could not be used because of too much damping in the material. These numerical results will be verified in further studies using laboratory measurements.

REFERENCES

ASTM: C215-08. (2008). *Standard Test Method for Fundamental Transverse, Longitudinal and Torsional Frequencies of Concrete Specimens*. West Conshoshocken: ASCE

Clough, R. W., & Penzien, J. (1993). *Dynamics of Structures* (2nd ed.). New-York, McGraw-Hill, Inc.

Di Benedetto, H., Olard, F., Sauzéat, C., & Delaporte, B. (2004). Linear viscoelastic behavior of bituminous materials: From binders to mixtures. *Road Materials and Pavement Design, 5*(S1), 163-202. doi: 10.1080/14680629.2004.9689992

Di Benedetto, H., Delaporte, B., & Sauzéat, C. (2007). Three dimensional linear behavior of bituminous materials: Experiments and modeling. *ASCE International Journal of Geomechanics, 7*(2), 149-157. doi: 10.1061/(ASCE)1532-3641(2007)7:2(149)

Di Benedetto, H., Sauzéat, C., & Sohm, J. (2009). Stiffness of bituminous mixtures using ultrasonic wave propagation. *Road Materials and Pavement Design, 10*(4), 789-814. doi: 10.1080/14680629.2009.9690227

Ferry, J. D. (1980). *Viscoelastic properties of polymers* (3rd ed.). New York, NY: John Wiley & Sons.

Kweon G., & Kim Y. R. (2006). Determination of the complex modulus of asphalt concrete using the impact resonance test. *Journal of Transportation Research Board, 1970*, 151-160.

Mangiafico, S. (2014). Linear viscoelastic properties and fatigue of bituminous mixtures produced with Reclaimed Asphalt Pavement and corresponding binder blends. Ph.D. Thesis, University of Lyon, ENTPE, France.

Migliori A., Sarrao J., Visscher W., Bell T., Ming L., Fisk Z., & Leisure R. (1993). Resonant ultrasound spectroscopic techniques for measurement of the elastic moduli of solids. *Physica B*, 183, 1-24.

Mounier, D., Di Benedetto, H., & Sauzéat, C. (2012). Determination of bituminous mixtures linear properties using ultrasonic wave propagation. *Construction and Building Materials, 36,* 638-647. doi: 10.1061/j.conbuildmat.2012.04.136

Nguyen, H. M., Pouget, S., Di Benedetto, H., & Sauzéat, C. (2009). Time-temperature superposition principle for bituminous mixtures. *European Journal of Environmental and Civil Engineering, 13*(9), 1095-1107. doi: 10.3166/ejece.13.1095-1107

Nguyen, M. L., Sauzéat, C., Di Benedetto, H., & Tapsoba, N. (2013). Validation of the time–temperature superposition principle for crack propagation in bituminous mixtures. *Materials and structures, 46*(7), 1075-1087. doi: 10.1617/s11527-012-9954-7

Nguyen, Q. T. (2011). Comportement thermomécanique des enrobés bitumineux sous sollicitations cycliques dans les domaines linéaire et non-linéaire. Ph.D. Thesis, University of Lyon, ENTPE, France.

Nguyen, Q. T., Di Benedetto, H., Sauzéat, C., & Tapsoba, N. (2013). Time-temperature superposition principle validation for bituminous mixes in the linear and nonlinear domain. *ASCE Journal of Materials in Civil Engineering, 25*(9), 1181-1188. doi: 10.1061/(ASCE)MT.1943-5533.0000658

Olard, F., & Di Benedetto, H. (2003). General 2S2P1D model and relation between the linear viscoelastic behaviors of bituminous binders and mixes. *Road Materials and Pavement Design, 4*(2), 185-224. doi: 10.1080/14680629.2003.9689946

Ryden, N. (2011). Resonant frequency testing of cylindrical asphalt samples. European Journal of Environmental and Civil Engineering, 15, 587-600.

Tiouajni, S., Di Benedetto, H., Sauzéat, C., & Pouget, S. (2011). Approximation of linear viscoelastic model in the 3 dimensional case with mechanical analogues of finite size – Application to bituminous materials. Road Materials and Pavement Design, 12(4), 897-930. doi: 10.1080/14680629.2011.9713899

Whitmoyer, S.L., Kim, Y.R. (1994). Determining asphalt concrete properties via the impact resonant method. *Journal of Testing Evaluation, 22*(2), 139-148.

Paper II : Multi-modal dynamic linear viscoelastic back analysis for asphalt mixes

CARRET JEAN-CLAUDE
DI BENEDETTO HERVE
SAUZEAT Cédric

Published in
Journal of Nondestructive Evaluation (2018) 37:35
https://doi.org/10.1007/s10921-018-0491-3

Journal of Nondestructive Evaluation (2018) 37:35
https://doi.org/10.1007/s10921-018-0491-3

Multi Modal Dynamic Linear Viscoelastic Back Analysis for Asphalt Mixes

Jean-Claude Carret[1] · Herve Di Benedetto[1] · Cedric Sauzeat[1]

Received: 28 August 2017 / Accepted: 28 April 2018

Abstract
In this paper, an investigation was performed to determine the accuracy of a simplified viscoelastic back analysis to interpret dynamic loading tests on asphalt mixes (AM). First, quasi-static cyclic tension–compression lab tests were performed on different AM to fit the 3 dimensional 2S2P1D linear viscoelastic (LVE) model. Considering these tests on very different types of AM, a LVE material with "averaged" viscoelastic properties was obtained. Then, these "averaged" viscoelastic properties were considered to perform finite elements method numerical simulations of dynamic loading tests on a cylinder. The simulations were performed at ten different temperatures from − 40 to 50 °C. The longitudinal, flexural and torsional modes of vibration are studied. The complex Young's modulus and complex Poisson's ratio were first obtained using the viscoelastic 2S2P1D model at the first resonance frequency for the three studied modes of vibration. Then, a combined viscoelastic back analysis, which has the advantage of simplicity, was used to determine the elastic equivalent properties and the phase angle of the material. The results obtained directly with the 2S2P1D model and the results from the combined viscoelastic back analysis results regarding both the Young's modulus and the Poisson's ratio are discussed in the paper.

Keywords Asphalt mixes · Viscoelasticity · Dynamic loading · Finite element calculation · Back analysis

1 Introduction

Seismic measurements such as impact loadings are economical, simple to perform and are nondestructive tests. These tests seem to be a good approach for providing accurate characterization of materials properties [1]. Measurement of the flying time in wave propagation tests [2–4] and measurement of the fundamental resonance frequencies through resonance testing [5,6] have been used to determine the complex modulus of asphalt mixtures. These methods give information on the tested LVE material only for a limited number of resonance frequencies (1–3), which are, a priori, unknown. The analysis of the results of these tests is based on simplified approximate formulations used to determine a complex modulus for each considered temperature and mode of vibration [7,8]. Ryden and Gudmarsson [9,10] applied resonant acoustic spectroscopy (RAS) to calculate resonance frequencies of cylindrical discs and beams for different modes of vibration. These tests require simplified method such as the half-power bandwidth method to evaluate the damping of the specimen. In this paper, a comparison between the direct viscoelastic analysis and a simplified back analysis of a specimen under impact loadings were performed. The differences between the two approaches and the limitations of the simplified back analysis were highlighted. LVE finite element method numerical simulations of impact loadings on a cylindrical specimen were carried out. These numerical tests were performed at 10 different temperatures between − 40 and 50 °C for three different modes of vibration: the longitudinal mode, the flexural mode and the torsional mode. The analysis of these computations were limited to the first resonance frequency for each mode. Viscoelastic properties of the specimen were estimated at the corresponding resonance frequency for each mode of vibration and for each temperature using the 2S2P1D linear viscoelastic model. Then, a combined back analysis—it is the type of method mostly used to analyze impact testing on asphalt materials—was used to evaluate the elastic equiva-

✉ Jean-Claude Carret
jean-claude.carret@entpe.fr

Herve Di Benedetto
herve.dibenedetto@entpe.fr

Cedric Sauzeat
cedric.sauzeat@entpe.fr

[1] LTDS (UMR CNRS 5513), University of Lyon / ENTPE, Rue M. Audin, 69518 Vaulx en Velin, France

Published online: 07 May 2018

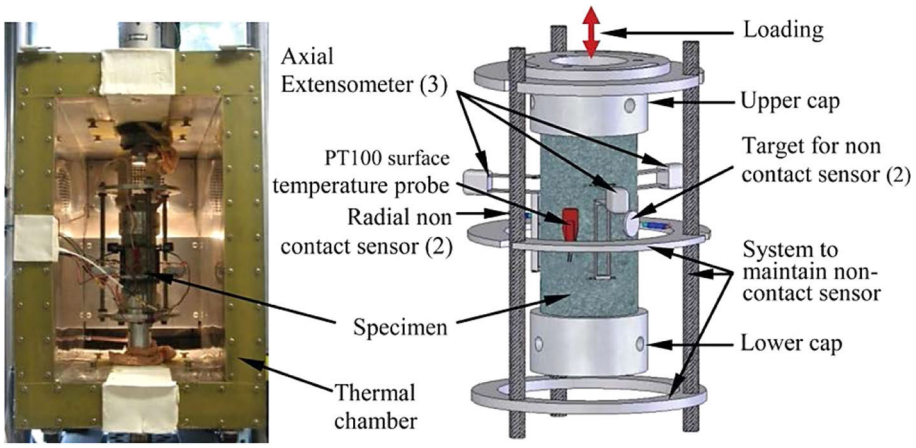

Fig. 1 (left) Tension–compression test apparatus used for tests on asphalt mixes; (right) detailed scheme of measurement devices and sample

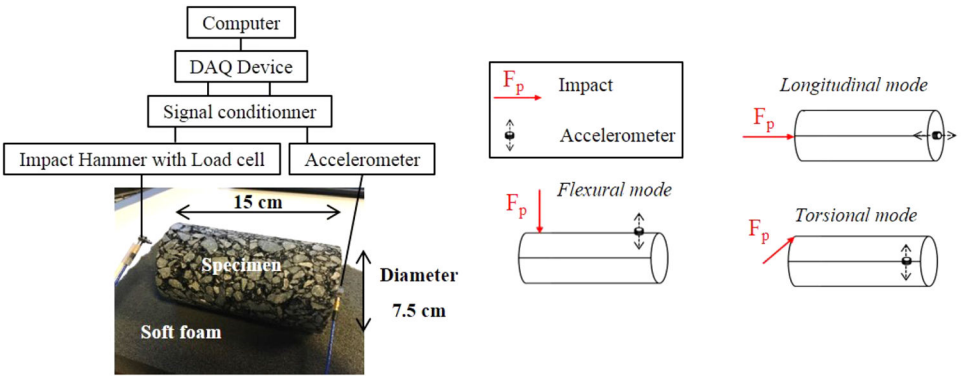

Fig. 2 (left) Dynamic impact tests set-up (ENTPE/LTDS laboratory), case of the longitudinal mode; (right) Position of the accelerometer and of the impact for the three considered modes of vibration

lent properties and the phase angle of the material. Finally, results obtained directly with the 2S2P1D model and from the combined back analysis were compared.

2 Materials and Experimental Tests

2.1 Materials and Considered Material for Modelling

38 specimens are first considered in this study. They were previously tested (cyclic tension–compression test—see following section-) during 4 different Ph.D. theses performed at the University of Lyon / ENTPE, LTDS laboratory [11–17]. The wide variety of these specimens represents a good range of asphalt mixes types and makes it possible to consider a material with averaged viscoelastic properties. This material was given the average values of the constants of the 2S2P1D LVE model obtained for the 38 specimens. All the numerical simulations and analyses that are presented in this paper were performed on this average material.

2.2 Cyclic Tension–Compression Tests

The tension–compression tests were used to determine the complex Young's modulus and the complex Poisson's ratio of asphalt mixes. The tests were performed on cylindrical samples (150 mm high with a 75 mm diameter). Cyclic sinusoidal loadings were applied using a hydraulic press, as shown in Fig. 1, in strain-controlled mode with an amplitude of around $5 * 10^{-5}$ m/m.

The axial stress ($\sigma_1 = \sigma_0.sin(\omega t - \phi_E)$) was measured with a load cell with a ± 25 kN maximum load and a 25N accuracy. The axial strain ($\varepsilon_1 = \varepsilon_{01}.sin(\omega t)$) was obtained by means of three extensometers placed at 120° from each other (Fig. 1). The radial strain ($\varepsilon_2 = \varepsilon_{02}.sin(\omega t + \phi_\nu)$) was deduced from measurements of two non-contact transducers (Fig. 1). The complex modulus and the complex Poisson's ratio at different loading frequencies (from 0.01 to 10 Hz) and different temperatures (from -30 to 50 °C) are calculated according to Eqs. 1 and 2 where ϕ_E and ϕ_ν are the phases of the complex modulus and of the complex Poisson's ratio respectively.

$$E^*(\omega) = \frac{\sigma_1^*}{\varepsilon_1^*} = \left|E^*(\omega)\right| e^{i\Phi_E} \tag{1}$$

$$\nu^*(\omega) = -\frac{\varepsilon_2^*}{\varepsilon_1^*} = \left|\nu^*(\omega)\right| e^{i\Phi_\nu} \tag{2}$$

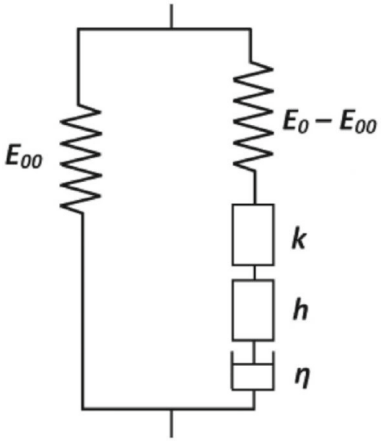

Fig. 3 Representation of the 2S2P1D LVE model in the 1-dimension case

2.3 Dynamic Impact Tests and Conditions for the Numerical Simulations

The sample geometry used for tension–compression test (7.5 cm diameter and 15 cm height) was considered for dynamic test. In this paper only numerical tests are presented but the associated lab test set-up of the dynamic impact tests is shown on the left of Fig. 2. The loading is manually applied on the specimen with an impact hammer equipped with a load cell (PCB model 086E80). The standing wave modes are measured with an accelerometer (PCB model 353B15) glued to the specimen. During the test, the specimen lays on soft foam to ensure free boundary conditions [6]. The impact hammer and the accelerometer are connected to the data acquisition system that consists of a signal conditioner (PCB model 482C15), a data acquisition device (NI DAQ USB-6251) and a computer (see Fig. 2). It is possible to excite different modes of vibration depending on the position of the impact and of the accelerometer [18,19]. The configurations for the three different modes of vibration considered in this study are described on the right of Fig. 2. These configurations were used for the FEM numerical simulations (see Sect. 3.2).

3 Linear Viscoelastic Analysis

3.1 2S2P1D LVE Isotropic Model

The tension–compression tests results were analyzed using the 2S2P1D LVE model developed at ENTPE [20–22]. It consists of a combination of two springs, two parabolic creep elements (also called fractional-derivative model [23]) and one dashpot as schematized in the 1-dimension case in Fig. 3.

The introduced model has seven parameters and the complex modulus of the 2S2P1D model is expressed according to Eq. 3,

$$E^*_{2S2P1D}(\omega) = E_{00} + \frac{E_0 - E_{00}}{1 + \delta(j\omega\tau)^{-k} + (j\omega\tau)^{-h} + (j\omega\beta\tau)^{-1}} \quad (3)$$

where j is complex number defined by $j^2 = -1$, ω is the angular frequency ($\omega = 2\pi f$, where f is the frequency), E_{00} is the static modulus when $\omega \to 0$, E_0 is the glassy modulus when $\omega \to +\infty$, δ is a dimensionless constant, k and h are dimensionless exponents such as $0 < k < h < 1$, β is a dimensionless constant related to the Newtonian viscosity η by $\eta = (E_0 - E_{00})\beta\tau$ and τ is the characteristic time, function of temperature. The time-temperature superposition principle (TTSP) is verified for asphalt mixes in the linear and nonlinear domains [16,24,25] using:

$$\tau(T) = a_T(T)\tau_{ref} \quad (4)$$

where a_T is the shift factor at the temperature T defined by the Williams–Landel–Ferry (WLF) equation [26]:

$$\log(a_T) = -\frac{C_1(T - T_{ref})}{C_2 + T - T_{ref}} \quad (5)$$

where C_1 and C_2 are the two constants of the WLF equation and T_{ref} is the reference temperature. The WLF parameters used in this study are listed in Table 1 and the corresponding shift factors are plotted in Fig. 4. Di Benedetto et al. [27] extended the 2S2P1D model to characterize the complex Poisson's ratio as given in Eq. 6,

$$\nu^*_{2S2P1D}(\omega) = \nu_{00} + \frac{\nu_0 - \nu_{00}}{1 + \delta(j\omega\tau_\nu)^{-k} + (j\omega\tau_\nu)^{-h} + (j\omega\beta\tau_\nu)^{-1}} \quad (6)$$

where ν_{00} is the low frequency Poisson's ratio when $\omega \to 0$ and ν_0 is the high frequency Poisson's ratio when $\omega \to +\infty$. The same values of the parameters δ, k, h and β are used to determine both the complex modulus and complex Poisson's ratio while τ is determined also for the Poisson's ratio and is therefore labeled τ_ν. The constants of the 2S2P1D LVE model for the material used in the numerical simulations (see Sect. 2.1) are given in Table 1. The complex modulus (E*) and the complex Poisson ratio (ν^*) of the average material are plotted in Fig. 5 (master curves) and Fig. 6 (normalized cole–cole curves).

3.2 Finite Element Method Simulations

Finite element method is widely used on pavement for different applications [28–32]. In this study, the behavior of

Table 1 2S2P1D constants at the reference temperature of 10 °C for the material with "averaged" viscoelastic properties of asphalt mixes used for the numerical simulations

$E_{00}(MPa)$	$E_0(MPa)$	ν_0	ν_{00}	δ	k	h	β	$\tau_{10°C}(s)$	$\tau_\nu(s)$	C_1	C_2
105	35,000	0.19	0.42	2.15	0.17	0.525	505	0.1	3.165	30	210

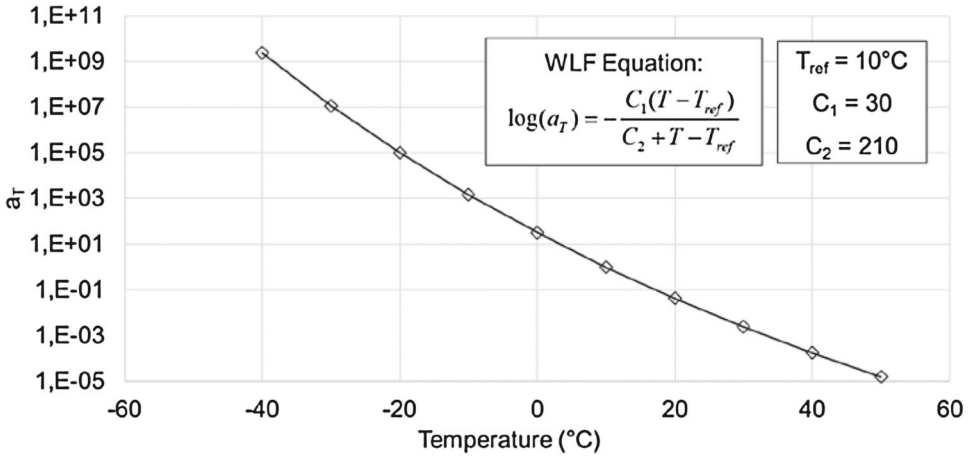

Fig. 4 Shift factor versus temperature for the considered WLF parameters

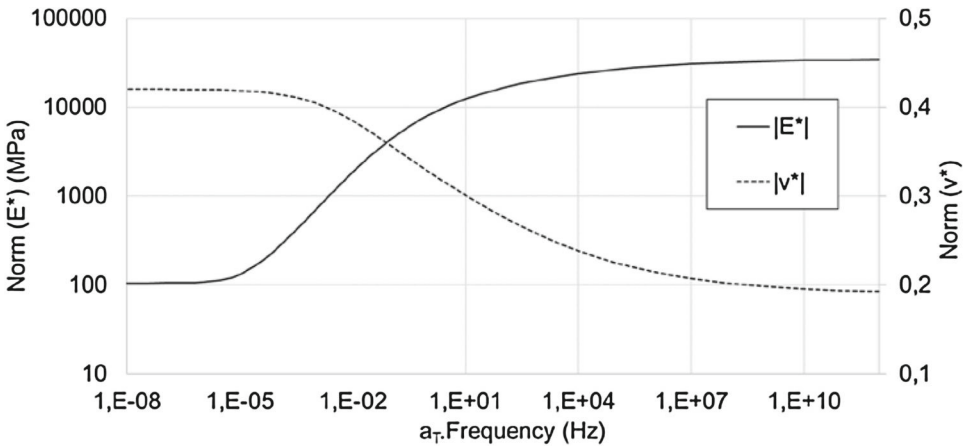

Fig. 5 Master curves at 10 °C for the norm of the complex Young's modulus (solid line) and for the norm of the complex Poisson's ratio (dot line) for the material used for the numerical simulations

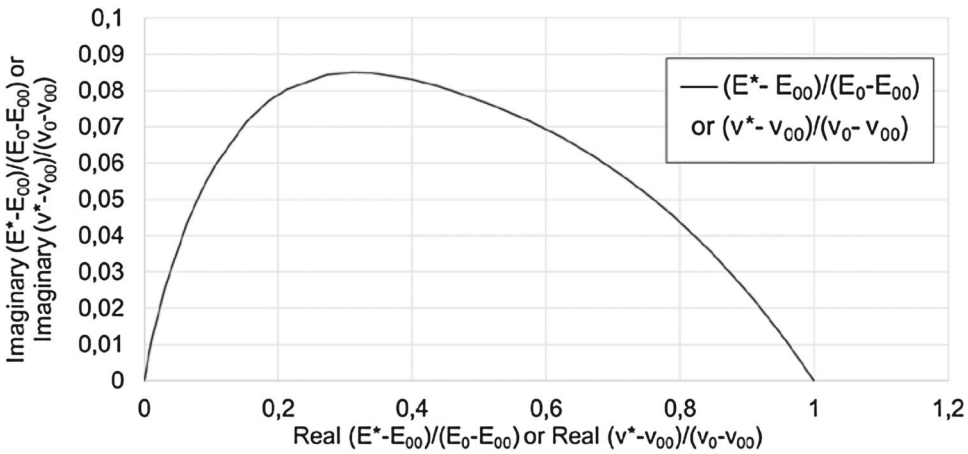

Fig. 6 Cole–Cole plot for the normalized complex Young's modulus and for the normalized complex Poisson's ratio for the material used for the numerical simulations

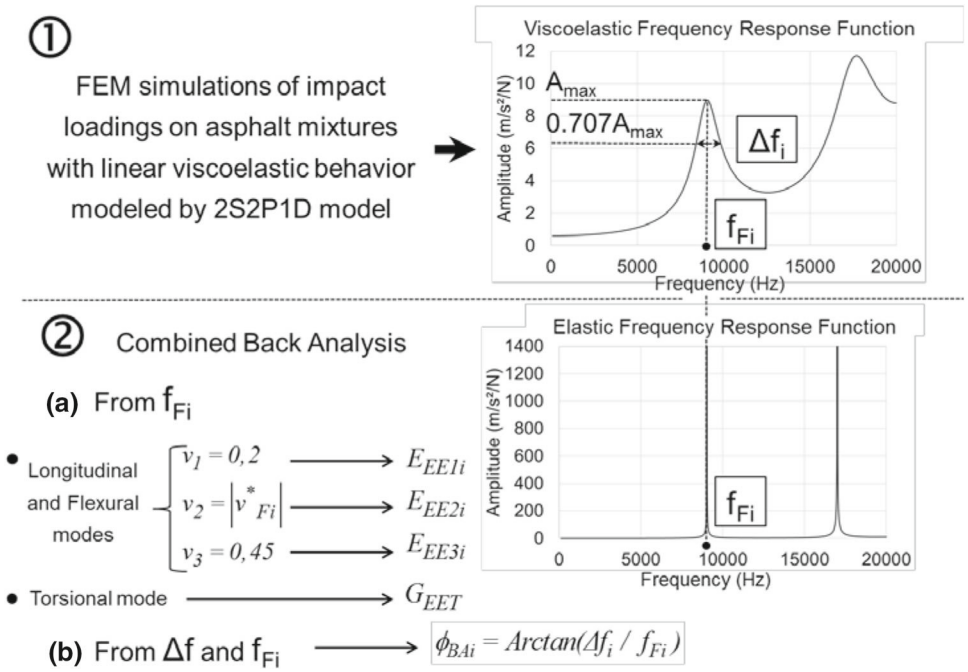

Fig. 7 FEM calculation and principle of the combined back analysis

the material under dynamic loadings was calculated with FEM numerical simulations. The 2S2P1D model complex modulus and complex Poisson's ratio (Table 1) were used as input for the material properties and the material was considered as isotropic. The Comsol software was used to solve the three-dimensional equation of motion in the frequency domain (Eq. 7):

$$-\rho\omega^2\mathbf{u} - \nabla.\sigma = \mathbf{F_p}e^{i\Phi} \tag{7}$$

where ω is the angular frequency, ρ is the density, $\mathbf{u}$ is the displacement vector, ∇ is the gradient tensor operator, i is complex number defined by $i^2 = -1$ and σ is the Cauchy stress tensor. $\mathbf{F_p}$ is the unity load and ϕ is the phase of the cyclic load.

The unity load has been applied to the corresponding point of the hammer impact while the response has been determined at the position of the accelerometer for the three considered modes of vibration (see Fig. 2). The simulations were performed at 10 different temperatures every 10 °C from − 40 to 50 °C, in a frequency range from 100 to 20,000 Hz considering steps of 20 Hz. Finer analysis with steps of 1 Hz were also carried out around the first resonant frequency for each temperature and for each mode of vibration in order to obtain a better evaluation of the first resonance frequency and of the damping of the material. The geometry used in this study was a cylinder with a 75 mm diameter and a 150 mm height. The mesh consists of tetrahedral elements with a maximum element size of 2.5 cm that was determined through a convergence study.

4 Combined Back Analysis

Back analysis methods are used for different applications on pavement [33,34]. The proposed combined back analysis is based on the analysis of the first resonance peak for each temperature and for each mode of vibration. Figure 7 explains the principle of the back analysis for one temperature. In the first step (see Fig. 7), the first resonance frequency of each mode of vibration f_{Fi} ($i = L$ for the longitudinal mode, $i = F$ for the flexural mode and $i = T$ for the torsional mode) was deduced from the FEM simulations. The frequency bandwidth Δf_i was also determined for each mode of vibration from the FEM simulations using the half-power bandwidth method (see Fig. 3). For the longitudinal and flexural modes of vibration, the frequencies f_{Fi} were used in the 2S2P1D model to calculate the corresponding complex modulus E^*_{Fi}, and Poisson's ratio, ν^*_{Fi}, according to Eqs. 8 and 9:

$$E^*_{Fi} = E^*_{2S2P1D}(2\pi f_{Fi}) \tag{8}$$
$$\nu^*_{Fi} = \nu^*_{2S2P1D}(2\pi f_{Fi}) \tag{9}$$

For the torsional mode of vibration, the frequency f_{FT} was used in the 2S2P1D model to calculate the corresponding complex shear modulus G^*_{FT} according to Eq. 10:

$$G^*_{FT} = G^*_{2S2P1D}(2\pi f_{FT}) \tag{10}$$

The phase angle used in the back analysis ϕ_{BAi} was deduced using the following relationship suggested by Clough and Penzien [35]:

$$\phi_{BAi} = Arctan\left(\frac{\Delta f_i}{f_{Fi}}\right) \tag{11}$$

In the second step of the combined back analysis (see Fig. 7), 2 different approaches were used. For the longitudinal and flexural modes of vibration, three cases corresponding to three different real values of Poisson's ratio of 0.2, $|\nu^*_{Fi}|$, and 0.45 were studied. Three elastic equivalent moduli E_{EE1i}, E_{EE2i} and E_{EE3i} associated to the three cases were back-calculated through elastic FEM numerical simulations for these two modes of vibration. For the torsional mode of vibration, the shear modulus is independent of the Poisson's ratio value. Therefore, only one elastic equivalent shear modulus G_{EET} was back-calculated through elastic FEM numerical simulations. Then ϕ_{BAi} was considered as the corresponding phase angle for the three considered modes of vibration. Three complex moduli E^*_{BA1i}, E^*_{BA2i} and E^*_{BA3i} were determined according to Eqs. 12–14 for the longitudinal and flexural mode and one complex shear modulus G^*_{BAT} was determined according to Eq. 15.

$$E^*_{BA1i} = E_{EE1i}e^{i\phi_{BAi}} \tag{12}$$
$$E^*_{BA2i} = E_{EE2i}e^{i\phi_{BAi}} \tag{13}$$
$$E^*_{BA3i} = E_{EE3i}e^{i\phi_{BAi}} \tag{14}$$
$$G^*_{BAT} = G_{EET}e^{i\phi_{BAT}} \tag{15}$$

5 Evaluation of the Proposed Combined Back Analysis

5.1 Principle of the Comparison

The procedure described in the previous section was used to determine the values of f_{Fi}, E^*_{Fi} (norm and phase angle ϕ_{Fi}), $|\nu^*_{Fi}|$, ϕ_{BAi}, E_{EE1i}, E_{EE2i} and E_{EE3i} for the longitudinal and flexural modes of vibration and the values of f_{FT}, G^*_{FT} (norm and phase angle ϕ_{FT}), ϕ_{BAT} and G_{EET}. All these values were calculated for the 10 considered temperatures. Table 2 details the name of the variables evaluated in the back analysis in the different cases studied for clarity. Results are given in Tables 3, 4 and 5 in appendix.

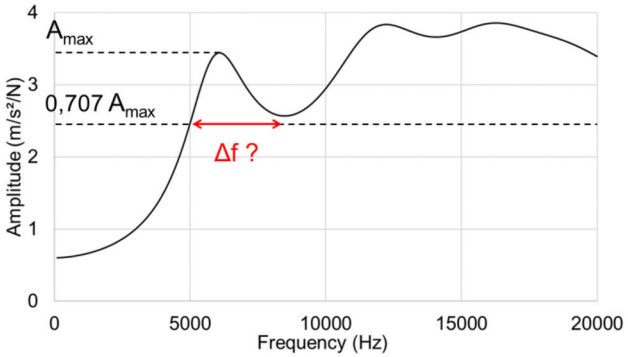

Fig. 8 Example of the half-power bandwidth method limitations at high temperatures where it was not possible to obtain Δf (numerical simulation for the longitudinal mode at 40 °C)

For temperatures higher than 30 °C, it was not possible to estimate the phase angle of the material for the longitudinal and the torsional modes of vibration. This is due to too much damping in the material for such temperatures that made the estimation of the frequency bandwidth impossible with the half-power bandwidth method (see Fig. 8).

In order to evaluate the accuracy of the proposed combined back analysis, the different values obtained were compared. For the longitudinal and flexural modes of vibration, the norm and the phase angle of the 2S2P1D model complex modulus E^*_{Fi} obtained at the frequency f_{Fi} (Eq. 8) were compared to the norm and to the phase angle of the three complex moduli E^*_{BA1i}, E^*_{BA2i} and E^*_{BA3i} (Eqs. 12–14) obtained from the simplified back analysis. The three studied cases allow to consider the effect of the Poisson's ratio value. For the torsional mode of vibration, the norm and the phase angle of the 2S2P1D model complex shear modulus G^*_{FT} obtained at the frequency f_{FT} (Eq. 10) were compared to the norm and to the phase angle of the complex shear modulus G^*_{BAT} (Eq. 15) obtained from the simplified back analysis.

Table 2 Summary of the variables evaluated in the different cases studied for the back analysis

Mode of vibration	Case studied	Elastic equivalent modulus	Phase angle	Complex modulus
Longitudinal	ν_1 =0.2	E_{EE1L}	ϕ_{BAL}	E^*_{BA1L}
	$\nu_2 = \lvert \nu^*_{2S2P1D}(f_L)\rvert$	E_{EE2L}		E^*_{BA2L}
	ν_3 =0.45	E_{EE3L}		E^*_{BA3L}
Flexural	ν_1 =0.2	E_{EE1F}	ϕ_{BAF}	E^*_{BA1F}
	$\nu_2 = \lvert \nu^*_{2S2P1D}(f_F)\rvert$	E_{EE2F}		E^*_{BA2F}
	ν_3 =0.45	E_{EE3F}		E^*_{BA3F}
Torsional	Independent of ν	G_{ET}	ϕ_{BAT}	G^*_{BAT}

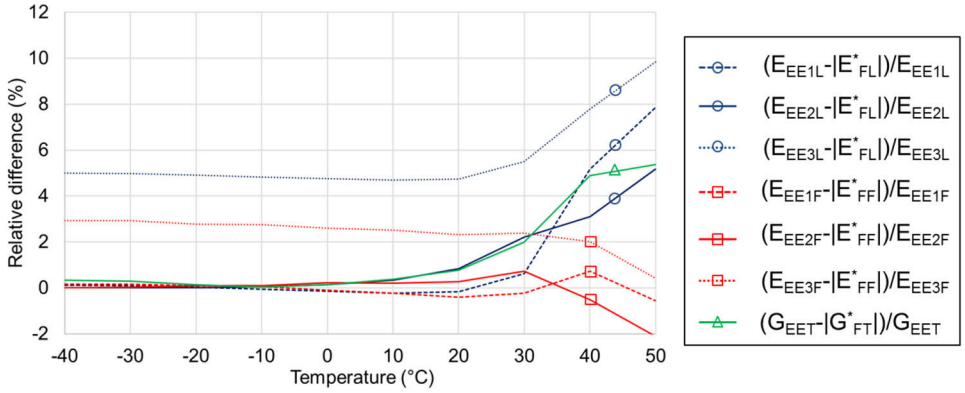

Fig. 9 Relative difference between the elastic equivalent modulus obtained from the combined back analysis (Fig. 3) and the norm of the 2S2P1D model value obtained at the first resonance frequency (Eqs. 8–10) for the three considered modes of vibration and different considered Poisson's ratio values

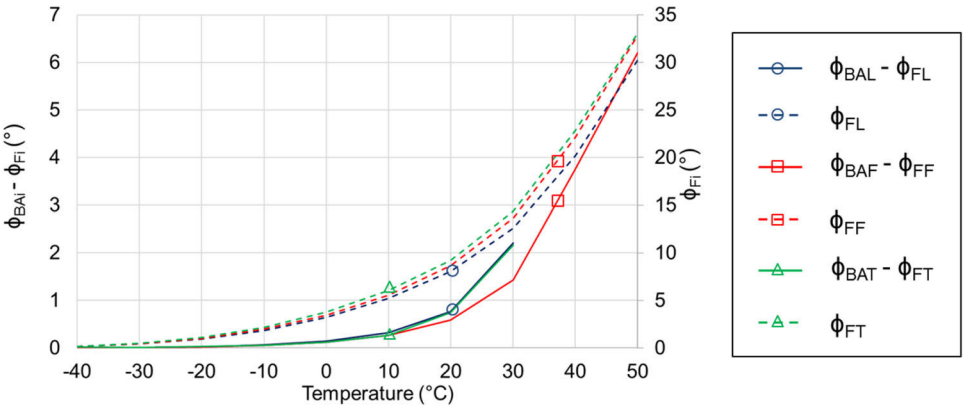

Fig. 10 2S2P1D model phase angle obtained at the first resonance frequency (Eqs. 8–10) (dot lines) and difference with the phase angle obtained from the combined back analysis (Fig. 3) (solid lines) for the three considered modes of vibration

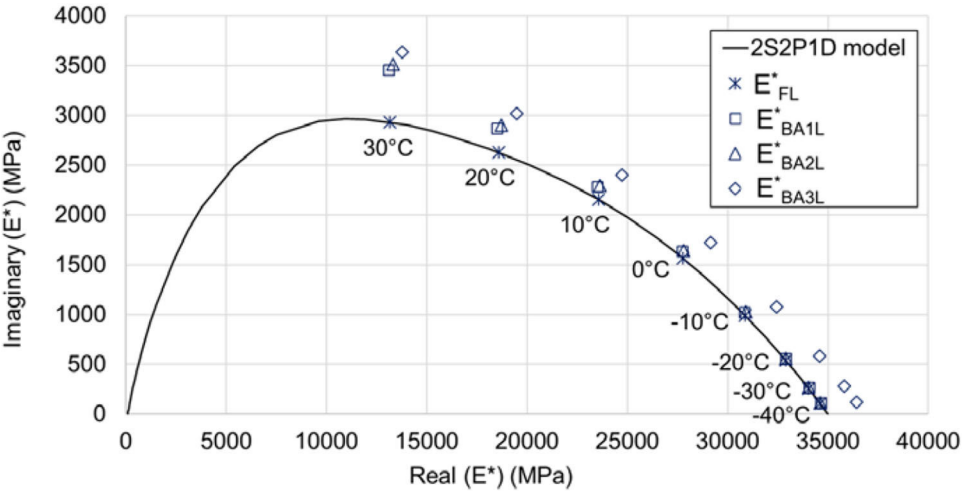

Fig. 11 Complex modulus values obtained from the 2S2P1D model at the first resonance frequency of the longitudinal mode (Eq. 8) and values obtained from the proposed combined back analysis for the three considered values of Poisson's ratio (Fig. 3) for the longitudinal mode of vibration (Eqs. 12–14)

5.2 Results and Discussion

Figure 9 presents the relative difference between the elastic equivalent moduli E_{EE1i}, E_{EE2i} and E_{EE3i} and the norm of the complex modulus $|E^*_{Fi}|$ calculated using the 2S2P1D model at the resonance frequencies f_{Fi}. Lines with a circle (in blue) are for the longitudinal mode of vibration while lines with a square (in red) are for the flexural mode of vibration. Also on Fig. 6, the relative difference between the elastic equivalent shear modulus G_{EET} and the norm of the complex shear modulus $|G^*_{FT}|$ calculated using 2S2P1D model at the frequency f_{FT} is plotted (green line with a triangle). The solid lines on Fig. 6 clearly indicate that there is a good correlation between the elastic equivalent modulus E_{EE2i} and the norm of the complex modulus from the 2S2P1D model $|E^*_{Fi}|$ and also between the elastic equivalent shear modu-

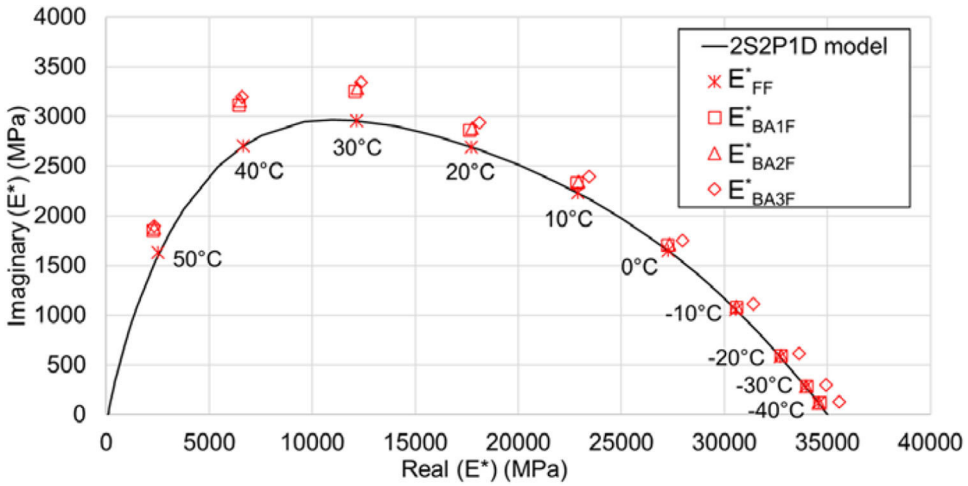

Fig. 12 Complex modulus values obtained from the 2S2P1D model at the first resonance frequency of the flexural mode (Eq. 8) and values obtained from the proposed combined back analysis for the three considered values of Poisson's ratio (Fig. 3) for the flexural mode of vibration (Eqs. 12–14)

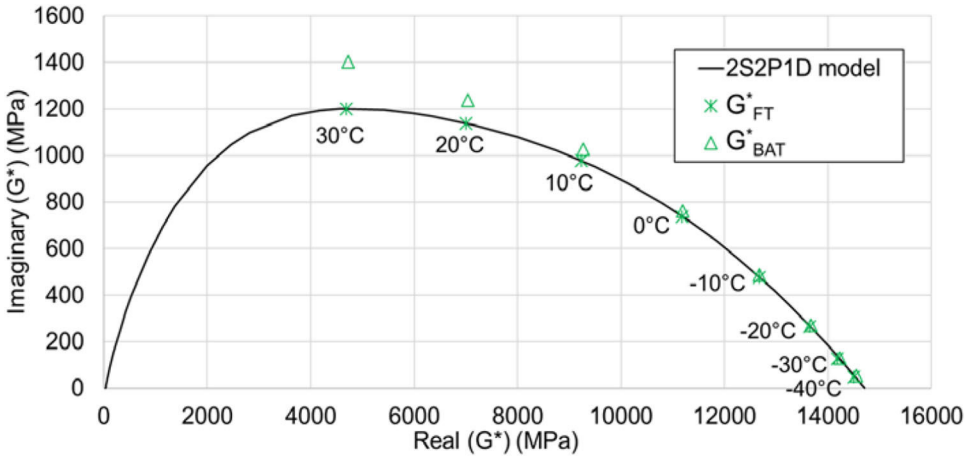

Fig. 13 Complex shear modulus values obtained from the 2S2P1D model at the first resonance frequency of the torsional mode (Eq. 10) and values obtained from the proposed combined back analysis (figure 3) for the torsional mode of vibration (Eq. 15)

lus and the norm of the complex shear modulus from the 2S2P1D model $|G^*_{FT}|$. This is particularly true for temperatures below 30 °C with a maximum relative difference of less than 2.5%. At higher temperatures, the error increases for the three modes of vibration but it remains less than 6%. It can also be seen on Fig. 6 that the Poisson's ratio value has an impact on the calculation of the elastic equivalent moduli. The relative difference is clearly higher for E_{EE3i} (around 3% for the flexural mode and around 5% for the longitudinal mode) that is calculated for a Poisson's ratio of 0.45, a value away from the two other studied cases. Nevertheless, the impact of the Poisson's ratio value remains limited.

Figure 10 presents the phase angle ϕ_{Fi} given by the 2S2P1D model at the frequency f_{Fi} (dot lines) and also the difference in degree (°) with the combined back analysis phase angle ϕ_{BAi} for the three considered modes of vibration. Figure 4 shows a good agreement between the back analysis phase angle ϕ_{BAi} and the 2S2P1D model phase angle ϕ_{Fi} with a maximum difference of around 2° at 30 °C for the longitudinal and torsional modes. For the flexural mode, it can be seen that the difference significantly increases for temperatures above 30 °C to reach 6° at 50 °C. This proves the inaccuracy of the half-power bandwidth method at high temperature: when there is too much damping in the material, the damping is overestimated and so is the phase angle.

For the complex modulus or complex shear modulus as well as for the phase angle, differences between values obtained from the 2S2P1D model at the first resonance frequency and values obtained with the combined back analysis increase with the temperature but remain limited. Figures 11, 12 and 13 present the different complex moduli in a Cole–Cole diagram for the three considered modes of vibration and the three different values of Poisson's ratio. On Figs. 7 and 8 corresponding to the longitudinal mode and to the flexural mode respectively, it can be seen that the values of E^*_{BA1i} or E^*_{BA2i} and E^*_{Fi} are rather close, especially at low temperatures. E^*_{BA3i} does not fit so well with E^*_{Fi}. It is due to the effect of the Poisson's ratio value as already noted on Fig. 6. Figure 9 corresponding to the torsional mode shows a good agreement between G^*_{BAT} and G^*_{FT}, especially for the low temperatures. All the observations from Figs. 11, 12 and 13 confirm the conclusions already raised from Figs. 9 and 10.

6 Conclusion

The proposed simplified back analysis proposed in this paper gives good results, both for the norm of the complex modulus and for the phase angle at low and intermediate temperatures. Slight differences appear for temperatures higher than 20 °C. They are mostly due to an overestimation of the phase angle. Therefore, the half-power bandwidth method used to determine the phase angle is not adapted for high temperatures because it overestimates the damping of the materials. The influence of the Poisson's ratio value was also studied. It was found that it has a limited impact on the calculation of the elastic equivalent modulus (less than 5%). The observations and findings from this study demonstrate that for temperatures below 20 °C, a simple assumption on constant real value for Poisson's ratio and the proposed simplified combined back analysis are enough to analyse accurately impact loadings in order to obtain the behaviour of asphalt mixes.. This is very interesting to obtain quickly and accurately the LVE properties at high frequencies. However, the limitation with the temperature gives only access to a small part of the master curve that can be estimated with this method. In addition, for higher temperatures corresponding to values of the phase angle higher than about 15°, the method does not provide a good evaluation of the phase angle. Therefore, for temperatures higher than 30 °C corresponding to phase angle of above 15° the half-power bandwidth could not be used because of too much damping in the material. These numerical results need to be checked and validated in further studies using laboratory measurements.

Appendix

Table 3 Results of the numerical simulations and the combined back analysis (longitudinal mode)

T(°C)	2S2P1D model			Combined back analysis				
	$\lvert E^*_{FL}\rvert(MPa)$	ϕ_{FL} (°)	$\lvert\nu^*_{FL}\rvert$	$f_{FL}(Hz)$	ϕ_{BAL} (°)	$E_{EE1L}\ (MPa)$	$E_{EE2L}\ (MPa)$	$E_{EE3L}\ (MPa)$
−40	34,602	0.178	0.191	12,320	0.186	34,645	34,605	34,425
−30	34,029	0.434	0.194	12,216	0.450	34,060	34,030	35,810
−20	32,890	0.943	0.198	12,006	0.969	32,900	32,890	34,585
−10	30,891	1.837	0.206	11,631	1.901	30,870	30,910	32,460
0	27,813	3.232	0.219	11,031	3.372	27,775	27,850	29,200
10	23,675	5.219	0.238	10,173	5.542	23,620	23,755	24,840
20	18,770	8.049	0.264	9062	8.813	18,740	18,930	19,705
30	13,475	12.575	0.294	7708	14.782	13,560	13,780	14,260
40	8179	20.188	0.327	6080	×	8440	8625	8870
50	3746	30.621	0.362	4160	×	3950	4065	4155

Table 4 Results of the numerical simulations and the combined back analysis (flexural mode)

T(°C)	2S2P1D model			Combined back analysis				
	$\lvert E^*_{FF}\rvert\ (MPa)$	ϕ_{FF} (°)	$\lvert\nu^*_{FF}\rvert$	$f_{FF}\ (Hz)$	ϕ_{BAF} (°)	$E_{EE1F}\ (MPa)$	$E_{EE2F}\ (MPa)$	$E_{EE3F}\ (MPa)$
−40	34,569	0.193	0.192	7619	0.203	34,625	34,575	35,580
−30	33,948	0.47	0.194	7549	0.486	34,000	33,960	34,940
−20	32,720	1.019	0.199	7410	1.044	32,750	32,750	33,630
−10	30,580	1.977	0.207	7161	2.031	30,595	30,610	31,420
0	27,317	3.461	0.221	6764	3.587	27,290	27,380	28,030
10	22,991	5.571	0.242	6201	5.838	22,935	23,040	23,570
20	17,933	8.63	0.268	5472	9.218	17,860	17,980	18,350
30	12,518	13.671	0.3	4573	15.101	12,490	12,610	12,815
40	7177	22.12	0.334	3460	25.880	7140	7230	7325
50	3002	32.832	0.37	2220	39.036	2940	2985	3015

Table 5 Results of the numerical simulations and the combined back analysis (torsional mode)

T (°C)	2S2P1D model		Combined back analysis		
	$\lvert G^*_{FT}\rvert\ (MPa)$	ϕ_{FT} (°)	$f_{FT}\ (Hz)$	ϕ_{BAT} (°)	$G_{EET}\ (MPa)$
−40	14,502	0.192	8033	0.214	14,550
−30	14,184	0.514	7954	0.526	14,225
−20	13,653	1.107	7795	1.139	13,670
−10	12,681	2.152	7512	2.203	12,685
0	11,205	3.769	7065	3.887	11,220
10	9284	6.051	6437	6.321	9320
20	7090	9.227	5639	9.967	7145
30	4834	14.371	4684	16.540	4930
40	2711	22.839	3560	×	2850
50	1107	33.091	2280	×	1170

References

1. Migliori, A., Sarrao, J., Visscher, W., Bell, T., Ming, L., Fisk, Z., Leisure, R.: Resonant ultrasound spectroscopic techniques for measurement of the elastic moduli of solids. Physica B **183**, 1–24 (1993)
2. Di Benedetto, H., Sauzéat, C., Sohm, J.: Stiffness of bituminous mixtures using ultrasonic wave propagation. Road Mater. Pavement Des. **10**(4), 789–814 (2009). https://doi.org/10.1080/14680629.2009.9690227
3. Mounier, D., Di Benedetto, H., Sauzéat, C.: Determination of bituminous mixtures linear properties using ultrasonic wave propagation. Constr. Build. Mater. **36**, 638–647 (2012). https://doi.org/10.1061/j.conbuildmat.2012.04.136
4. Norambuena-Contreras, J., Castro-Fresno, D., Vega-Zamanillo, A., Celay, M., Lombillo-Vozmediano, I.: Dynamic modulus of asphalt mixture by ultrasonic direct test. NDT E Int. **43**(7), 629–634 (2010)
5. Kweon, G., Kim, Y.R.: Determination of the complex modulus of asphalt concrete using the impact resonance test. J. Transp. Res. Board **1970**, 151–160 (2006)
6. Whitmoyer, S.L., Kim, Y.R.: Determining asphalt concrete properties via the impact resonant method. J. Test. Eval. **22**(2), 139–148 (1994)
7. Tavassoti-Kheiry, P., Boz, I., Solaimanian, M., Qiu, T.: Evaluation of nondestructiveness of resonant column testing for characterization of asphalt concrete properties. J. Test. Eval. **46**(2), 631–640 (2018)
8. ASTM: C215–08. Standard Test Method for Fundamental Transverse. ASCE, Longitudinal and Torsional Frequencies of Concrete Specimens, West Conshoshocken (2008)
9. Gudmarsson, A., Ryden, N., Birgisson, B.: Application of resonant acoustic spectroscopy to asphalt concrete beams for determination of the dynamic modulus. Mater. Struct. **45**, 1903–1913 (2012). https://doi.org/10.1617/s11527-012-9877-3
10. Ryden, N.: Resonant frequency testing of cylindrical asphalt samples. Eur. J. Environ. Civil Eng. **15**, 587–600 (2011)
11. Mangiafico, S., Di Benedetto, H., Sauzéat, C., et al.: Influence of reclaimed asphalt pavement content on complex modulus of asphalt binder blends and corresponding mixes: experimental results and modelling. Road Mater. Pavement Des. **14**(S1), 132–148 (2013)
12. Mangiafico, S., Di Benedetto, H., Sauzéat, C., et al.: Statistical analysis of the influence of RAP and mix composition on viscoelastic and fatigue properties of asphalt mixes. Mater. Struct. **48**(4), 1187–1205 (2015)
13. Nguyen, H.P., Di Benedetto, H., Sauzéat, C., et al.: Reclaimed asphalt pavement and additives' influence on 3D linear behavior of warm mix asphalts. Road Mater. Pavement Des. **16**(3), 569–591 (2015)
14. Nguyen, H.P., Di Benedetto, H., Sauzéat, C., et al.: Analysis and modeling of 3D complex modulus tests on hot and warm bituminous mixtures. Mech. Time-depend. Mater. **19**(2), 167–186 (2015)
15. Nguyen, Q.T.: Comportement thermomécanique des enrobés bitumineux sous sollicitations cycliques dans les domaines linéaires et non-linéaire. Ph.D. Thesis, University of Lyon, ENTPE, France (2011)
16. Nguyen, Q.T., Di Benedetto, H., Sauzéat, C., Tapsoba, N.: Time-temperature superposition principle validation for bituminous mixes in the linear and nonlinear domain. ASCE J. Mater. Civil Eng. **25**(9), 1181–1188 (2013). https://doi.org/10.1061/(ASCE)MT.1943-5533.0000658
17. Viet, P.C., Di Benedetto, H., Sauzéat, C., Lesueur, D., Pouget, S., Olard, F., Dupriet, S.: Complex modulus and fatigue resistance of bituminous mixtures containing hydrated lime. Constr. Build. Mater. **139**, 24–33 (2017). https://doi.org/10.1016/j.conbuildmat.2017.02.042
18. Gudmarsson, A., Ryden, N., Di Benedetto, H., Sauzéat, C., Tapsoba, N., Birgisson, B.: Comparing linear viscoelastic properties of asphalt concrete measured by laboratory seismic and tension-compression tests. J. Nondestr. Eval. **33**, 571–582 (2014). https://doi.org/10.1007/s10921-014-0253-9
19. Gudmarsson, A., Ryden, N., Di Benedetto, H., Sauzéat, C.: Complex modulus and complex Poisson's ratio from cyclic and dynamic modal testing of asphalt concrete. Constr. Build. Mater. **88**, 20–31 (2015). https://doi.org/10.1016/j.conbuildmat.2015.04.007
20. Di Benedetto, H., Olard, F., Sauzéat, C., Delaporte, B.: Linear viscoelastic behavior of bituminous materials: from binders to mixtures. Road Mater. Pavement Des. **5**(S1), 163–202 (2004). https://doi.org/10.1080/14680629.2004.9689992
21. Olard, F., Di Benedetto, H.: General 2S2P1D model and relation between the linear viscoelastic behaviors of bituminous binders and mixes. Road Mater. Pavement Des. **4**(2), 185–224 (2003). https://doi.org/10.1080/14680629.2003.9689946
22. Tiouajni, S., Di Benedetto, H., Sauzéat, C., Pouget, S.: Approximation of linear viscoelastic model in the 3 dimensional case with mechanical analogues of finite size—application to bituminous materials. Road Mater. Pavement Des. **12**(4), 897–930 (2011). https://doi.org/10.1080/14680629.2011.9713899
23. Gourdon, E., Sauzéat, C., Di Benedetto, H., Bilodeau, K.: Seven-parameter linear viscoelastic model applied to acoustical damping materials. J. Vib. Acoust. **137**(6), 061003 (2015). https://doi.org/10.1115/1.4030719

24. Nguyen, H.M., Pouget, S., Di Benedetto, H., Sauzéat, C.: Time-temperature superposition principle for bituminous mixtures. Eur. J. Environ. Civil Eng. **13**(9), 1095–1107 (2009). https://doi.org/10.3166/ejece.13.1095-1107
25. Nguyen, M.L., Sauzéat, C., Di Benedetto, H., Tapsoba, N.: Validation of the time-temperature superposition principle for crack propagation in bituminous mixtures. Mater. Struct. **46**(7), 1075–1087 (2013). https://doi.org/10.1617/s11527-012-9954-7
26. Ferry, J.D.: Viscoelastic Properties of Polymers, 3rd edn. Wiley, New York (1980)
27. Di Benedetto, H., Delaporte, B., Sauzéat, C.: Three dimensional linear behavior of bituminous materials: experiments and modeling. ASCE Int. J. Geomech. **7**(2), 149–157 (2007). https://doi.org/10.1061/(ASCE)1532-3641(2007)7:2(149)
28. Cannone Falchetto, A., Moon, K.-H., Lee, C.B., Wistuba, M.P.: Correlation of low temperature fracture and strength properties between SCB and IDT tests using a simple 2D FEM approach. Road Mater. Pavement Des. **18**(sup2), 329–338 (2017). https://doi.org/10.1080/14680629.2017.1304258
29. Cho, Y.S., Lin, F.B.: Spectral analysis of surface waves in single and multi-layer slabs with finite thickness using finite element modelling. NDT E Int. **38**(3), 195–202 (2005)
30. Taherkhani, H., Jalali, M.: Investigating the performance of geosynthetic-reinforced asphaltic pavement under various axle loads using finite-element method. Road Mater. Pavement Des. (2016). https://doi.org/10.1080/14680629.2016.1201525
31. Yesuf, G.Y., Hoff, I.: Finite element modelling for prediction of permanent strains in fine-grained subgrade soils. Road Mater. Pavement Des. **16**(2), 392–404 (2015). https://doi.org/10.1080/14680629.2015.1013053
32. You, L., Yan, K., Hu, Y., Liu, J., Ge, D.: Spectral element method for dynamic response of transversely isotropic asphalt pavement under impact load. Road Mater. Pavement Des. (2016). https://doi.org/10.1080/14680629.2016.1230513
33. Madsen, S.S., Levenberg, E.: Dynamic backcalculation with different load-time histories. Road Mater. Pavement Des. (2017). https://doi.org/10.1080/14680629.2017.1307263
34. Riccardi, C., Cannone Falchetto, A., Leandro, P., Losa, M., Wistuba, M.: A novel back-calculation approach for determining the rheological properties of RAP binder. Road Mater. Pavement Des. **18**(sup1), 359–381 (2016). https://doi.org/10.1080/14680629.2016.1266778
35. Clough, R.W., Penzien, J.: Dynamics of Structures, 2nd edn. McGraw-Hill Inc, New-York (1993)

Paper III : Comparison of the 3-dim linear viscoelastic behavior of asphalt mixes determined with tension-compression and dynamic tests

CARRET JEAN-CLAUDE
PEDRAZA Alvaro
DI BENEDETTO HERVE
SAUZEAT Cédric

Published in
Construction and Building Materials 174 (2018) 529–536
https://doi.org/10.1016/j.conbuildmat.2018.04.156

Construction and Building Materials 174 (2018) 529–536

Contents lists available at ScienceDirect

Construction and Building Materials

journal homepage: www.elsevier.com/locate/conbuildmat

Comparison of the 3-dim linear viscoelastic behavior of asphalt mixes determined with tension-compression and dynamic tests

Jean-Claude Carret *, Alvaro Pedraza, Hervé Di Benedetto, Cédric Sauzeat

LTDS (UMR CNRS 5513), University of Lyon/ENTPE, Rue M. Audin, 69518 Vaulx en Velin, France

HIGHLIGHTS

- Dynamic tests can be used to characterize the LVE behavior of asphalt mixes.
- Asphalt mixes with 70% of RAP were tested with dynamic tests.
- Small differences exist between results from complex modulus and dynamic tests.
- Norm of the complex modulus obtained from dynamic tests is higher.
- Phase angle of the complex modulus obtained from dynamic tests is lower.

ARTICLE INFO

Article history:
Received 11 January 2018
Received in revised form 13 April 2018
Accepted 18 April 2018
Available online 24 April 2018

Keywords:
Asphalt mixes
Linear viscoelasticity
Complex modulus
Dynamic measurements
Tension-compression tests
Frequency response functions

ABSTRACT

In this paper, conventional cyclic tension-compression tests and dynamic measurements have been applied to three cylindrical specimens of asphalt mixes. The results of the two tests have been compared. For the tension-compression tests, the complex modulus was obtained from the measurements of the axial stress and axial strain. For the dynamic testing, an instrumented impact hammer and an accelerometer have been used to obtain the frequency response functions of the specimens at different temperatures. The dynamic complex modulus was then back calculated by optimizing finite element calculated frequency response functions to match the measured frequency response functions. The 2S2P1D linear viscoelastic model was used to estimate master curves of the complex modulus for the two test methods. The two tests give similar results. However, the dynamic measurements give a higher value of the norm of the complex modulus and a lower value of the phase angle compared to the tension–compression results. This result is probably explained by the nonlinearity of asphalt mixes as dynamic tests are performed at a much smaller strain level than the tension-compression tests.

1. Introduction

The complex modulus is widely known as the fundamental parameter to characterize the linear viscoelastic (LVE) behavior of asphalt mixes (AM), which is essential in pavement design. Conventional cyclic tension-compression tests are costly, complex to perform and they are not adapted for in situ measurements. Therefore, there is a need for alternative test methods that are more economical and that could be applied on field pavement structures. Dynamic measurements such as impact loadings [1,2] are economical, simple to perform and are very well known for accurate characterization of material properties in different applications [3]. Dynamic measurements can also be used for in situ quality control of pavement [4,5]. Dynamic testing of AM to determine the complex modulus have been performed through measurements of the flying time in wave propagation tests [6–8]. Resonance testing has also been used to evaluate the complex modulus of AM through the measurements of the fundamental resonance frequencies of AM specimens [9–11]. These two methods are based on simplified approximate formula that give access to the complex modulus only for a limited number of geometries and frequencies. Therefore, the frequency dependency of AM cannot be characterized through these two tests. Resonant acoustic spectroscopy intends to increase the number of frequency for which the complex modulus can be calculated [12–15]. Although, this method still not provide enough information to estimate the global master curve for AM. Frequency response functions (FRFs) measurements have been used to characterize viscoelastic materials over a wide frequency range [16–18]. Laboratory measurements of FRFs for AM

* Corresponding author.
E-mail addresses: jean-claude.carret@entpe.fr (J.-C. Carret), alvaro.pedraza@entpe.fr (A. Pedraza), herve.dibenedetto@entpe.fr (H. Di Benedetto), cedric.sauzeat@entpe.fr (C. Sauzeat).

https://doi.org/10.1016/j.conbuildmat.2018.04.156
0950-0618/

have showed promising results [19] and enables a direct comparison between master curves obtained from tension-compression tests and from dynamic measurements. Duttine et al. in 2007 and Ezaoui et al. in 2009 [20,21] have showed that the combination of both conventional measurements and dynamic testing is useful to improve the characterization of sands. The same approach was used on AM by Gudmarsson et al. in 2014 and 2015 [22,23] and it showed small differences between the two test methods due to the known nonlinearity of asphalt concrete [24–26] and because the applied strain levels are different in the two methods. In this paper, three specimens of the same AM containing 70% of reclaimed asphalt pavement (RAP) were tested with tension-compression tests and dynamic testing. The LVE properties of the specimens obtained with the two different methodologies were compared. The results show that the two test methods give similar results.

2. Methodology

The tests presented in this paper were performed at the ENTPE laboratory (University of Lyon). The tension-compression tests were performed first. Then the upper and lower part of the sample were sawed in order to eliminate the caps glued on the specimens for these tests. Then, dynamic tests were performed on the same specimen with a reduced length. More details on the materials and on the two different experimental procedures are presented in the following sections.

2.1. Materials

Three different specimens of the same material are considered in this paper. The material was fabricated for the IMPROVMURE project [27], a project from the French national research agency studying the environmental and mechanical impact of multi-recycling on asphalt mixes. It is a laboratory designed asphalt mix containing 70% of RAP after one cycle of recycling. Details of the three studied specimens are reported in Table 1. To simplify the notation in the next tables, each specimen is identified to its abbreviation. Tension-compression tests and dynamic tests were performed on each specimen.

2.2. Conventional characterization of the LVE behavior with complex modulus test

2.2.1. Tension-compression complex modulus tests

Cyclic tension-compression tests were used to determine the complex modulus of the three considered specimens. Cylindrical samples having a height of 150 mm and a diameter of 75 mm were used for these tests. Cyclic sinusoidal axial loadings were applied using a hydraulic press in strain-controlled mode with an amplitude of around 50 μm/m. A load cell measured the axial stress ($\sigma_1 = \sigma_0.\sin(\omega t\text{-}\varphi_E)$ or $\sigma_1 = \sigma_0.e^{i(\omega t-\varphi E)}$ in complex notation) while the axial strain ($\varepsilon_1 = \varepsilon_{01}.\sin(\omega t)$ or $\varepsilon_1 = \varepsilon_{01}.e^{i\omega t}$ in complex notation) was obtained from the average of the three extensometers placed at 120°. Finally, the radial strain ($\varepsilon_2 = \varepsilon_{02}.\sin(\omega t + \varphi_v)$ or $\varepsilon_2 = \varepsilon_{02}.e^{i(\omega t+\varphi v)}$ in complex notation) was deduced from two non-contact transducers. The tension-compression tests were performed at 9 temperatures from −25 °C to 55 °C in steps of 10 °C and at 8 loading frequencies (0.003, 0.01, 0.03, 0.1, 0.3, 1, 3 and 10 Hz). Details of the experimental set up are shown in Fig. 1 and an example of experimental data for two cycles of loading at 1 Hz and 15 °C, is presented in Fig. 2.

The complex modulus and complex Poisson's ratio at the different temperatures and frequencies were calculated according to Eqs. (1) and (2) where σ_1^*, ε_1^* and ε_2^* are the complex expressions of σ_1, ε_1 and ε_2, φ_E is the phase of the complex modulus and φ_v is the phase of the complex Poisson's ratio.

$$E^*(\omega) = \frac{\sigma_1^*}{\varepsilon_1^*} = |E^*(\omega)|e^{i\varphi_E} \quad (1)$$

$$\nu^*(\omega) = -\frac{\varepsilon_2^*}{\varepsilon_1^*} = |\nu^*(\omega)|e^{i\varphi_\nu} \quad (2)$$

Table 1
Details of the specimen used in this study.

Specimen	Abbreviation	Mass (g)	Height (mm)	Diameter (mm)	Density (kg/m^3)	Void ratio (%)	Bitumen content (%)
LWF-70-1-1-4	4	1293	0.123	75	2379	6.6	5.4
LWF-70-1-1-6	6	1320	0.123	75	2431	4.2	5.4
LWF-70-1-1-8	8	1330	0.123	75	2449	3.8	5.4

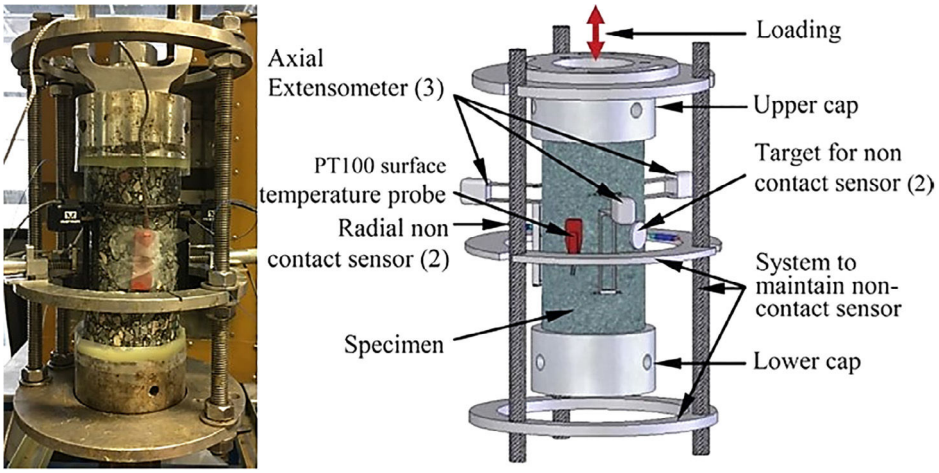

Fig. 1. (left) Tension-compression test apparatus used for tests on asphalt mixes (ENTPE laboratory, Vaulx-en-Velin, France); (right) detailed scheme of measurement devices and sample.

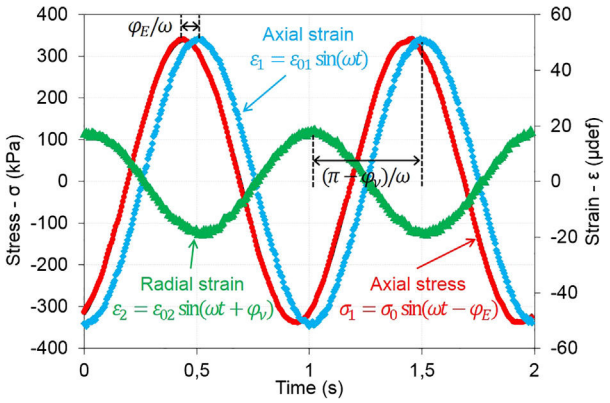

Fig. 2. Tension-compression experimental data for two loading cycles at 15 °C for specimen LWF-70-1-1-4 (axial strain, axial stress and radial strain).

2.2.2. 2S2P1D linear viscoelastic model

The 2S2P1D model [28–30], developed at ENTPE, was used to fit the tension-compression tests results. This model is a combination of two springs, two parabolic elements and one dashpot (Fig. 3). In the 3-dimensions case [31], the model has an expression for both the complex modulus and complex Poisson's ratio. These expressions are given in Eqs. (3) and (4) where ω is the angular frequency ($\omega = 2\pi f$, where f is the frequency), E_0 and ν_0 are the high frequency modulus and Poisson's ratio, E_{00} and ν_{00} are the low frequency modulus and Poisson's ratio, k and h are dimensionless constants such as $0 < k < h < 1$, δ is a dimensionless constant, β is a dimensionless constant related to Newtonian viscosity η by $\eta = (E_0 - E_{00})\,\beta\tau$ and τ_E and τ_ν are the characteristic times of the complex modulus and of the complex Poisson's ratio, whose value varies only with temperature.

$$E^*_{2S2P1D}(\omega) = E_{00} + \frac{E_0 - E_{00}}{1 + \delta(j\omega\tau_E)^{-k} + (j\omega\tau_E)^{-h} + (j\omega\beta\tau_E)^{-1}} \quad (3)$$

$$\nu^*_{2S2P1D}(\omega) = \nu_{00} + \frac{\nu_0 - \nu_{00}}{1 + \delta(j\omega\tau_\nu)^{-k} + (j\omega\tau_\nu)^{-h} + (j\omega\beta\tau_\nu)^{-1}} \quad (4)$$

The time-temperature superposition principle is verified for asphalt mixes in the linear and nonlinear domains [32–34] so it is possible to calculate a characteristic time at any given temperature using Eq. (5):

$$\tau(T) = a_T(T)\tau_{ref} \quad (5)$$

where τ_{ref} is the characteristic time at the reference temperature and a_T is the shift factor at the temperature T given by the Williams-Landel-Ferry equation [35]:

$$\log(a_T) = -\frac{C_1(T - T_{ref})}{C_2 + T - T_{ref}} \quad (6)$$

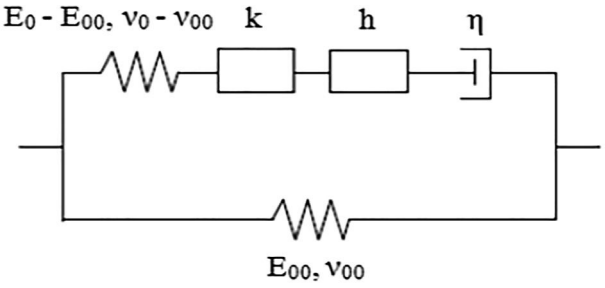

Fig. 3. Analogical representation of the 2S2P1D LVE model.

where T_{ref} is the reference temperature and C_1 and C_2 are the two WLF constants. Considering the use of shift factors, 12 parameters are required to characterize the LVE behavior of asphalt mixes at any temperature and frequency.

2.3. Dynamic tests

2.3.1. Experimental procedure

For the dynamic tests, the same specimen previously tested with tension-compression tests were used. An impact hammer (PCB model 086E80) was used as an external input to excite the specimens and to generate standing waves inside. The order of magnitude of the maximum strain in the specimen induced by the impact is of about 0.1 μm/m [19]. To improve the accuracy and the repeatability of these dynamic tests, an automated impact hammer was specifically designed (Fig. 4). This automated system was inspired by systems previously developed by Norman et al. in 2012 and Brüggemann et al. in 2015 [36,37]. The specimens were placed on soft foam during the test to achieve free boundary conditions. The response of the materials was recorded with an accelerometer (PCB model 353B15). The impact hammer and the accelerometer were connected to a signal conditioner (PCB model 482C15), itself connected to a data acquisition device (NI USB-6356) connected to a computer. The position of the impact and of the accelerometer depend on the geometry of the specimen and of the targeted mode of vibrations. In this study, only the longitudinal mode of vibrations of cylinders is considered. The corresponding experimental set up is displayed in Fig. 4. The impact is applied in the center of one short side of the cylinder while the acceleration is measured in the center of the opposite short side.

The measurements were performed at 7 temperatures from −20 °C to 40 °C in steps of 10 °C. The signals were recorded with a sampling frequency of 1 MHz by using an application dedicated to this task, which was developed with the MATLAB software. The record length of the signals was adjusted for each measurement temperature to record the entire vibratory response. This is necessary to take into account the increasing damping with increasing temperatures. 5 impacts were applied at each temperature and the applied force and the acceleration were recorded for each impact. An example of experimental data is shown in Fig. 5 for the specimen 4 at −10.2 °C.

For each measurement temperature, the experimental data in time domain was converted in frequency domain using Fast Fourier Transforms (FFT). The energy spectrum of the impacts allows to go up to 20 kHz in the frequency domain. Frequency Response Functions (FRFs) were therefore calculated from 1 Hz to 20 kHz in steps of 1 Hz by averaging the results of the 5 impacts according to Eq. (7):

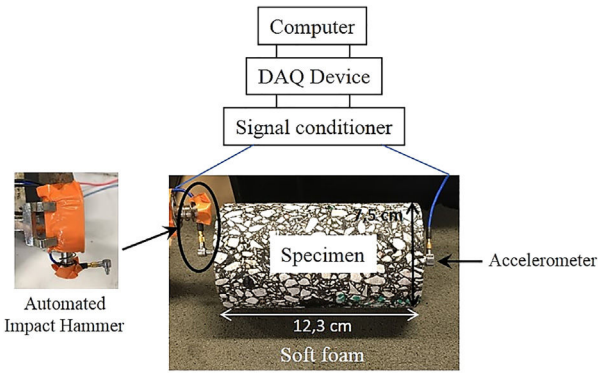

Fig. 4. Dynamic test set-up for the longitudinal mode of vibrations (ENTPE laboratory, Vaulx-en-Velin, France).

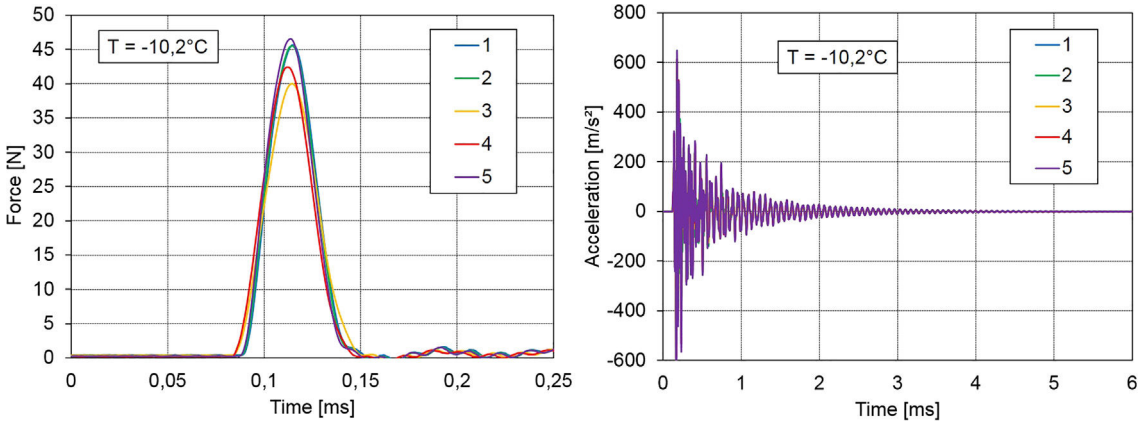

Fig. 5. Dynamic testing experimental data (five hits) in time domain for specimen 4 at −10,2 °C (left) impact force; (right) acceleration at the position of the accelerometer.

$$H(f) = (\overline{Y(f).X*(f)})/(\overline{X(f).X*(f)}) \quad (7)$$

where $H(f)$ is the FRF, $Y(f)$ is the FFT of the measured acceleration, $X(f)$ is the FFT of the applied force, $X^*(f)$ is the complex conjugate of the applied force and the bar above corresponds to the arithmetic mean. Quality of the measurements was verified using the coherence function. It gives an indicator between 0 and 1: a value of 1 means that the response is completely explained by the impact while a decreasing value means something has disrupted the test. The FRF and the coherence function for the specimen 4 at −10,2 °C is presented in Fig. 6. All tests gave an indicator very close to 1, which confirms the quality of the measurements.

2.3.2. Finite element calculations of theoretical FRFs

The finite element method (FEM) was used to calculate theoretical FRFs by resolving the following three-dimensional equation of motion in frequency domain:

$$-\rho\omega^2\mathbf{u} - \nabla.\sigma = \mathbf{F_p}e^{i\Phi} \quad (8)$$

where ρ is the density, ω is the angular frequency, $\mathbf{u}$ is the displacement vector, ∇ is the gradient tensor operator, i is a complex number such as $i^2 = -1$ and σ is the Cauchy stress tensor. $\mathbf{F_p}$ is the unity load equal to 1N and ϕ is the phase of the cyclic load. The FEM calculation was made with the COMSOL software. The material was considered perfectly homogenous and isotropic and the 2S2P1D model was used to simulate the LVE behavior of asphalt mixes. The load was applied to the corresponding point of the impact in the measurement, while the response was determined at the point corresponding to the position of the accelerometer as shown in Fig. 7. The mesh was built with tetrahedral elements with a maximum size of 2 cm which was determined through a convergence study. Results from the model were calculated in a frequency range of 100–20,000 Hz considering steps of 20 Hz. This frequency range was chosen to match the experimental frequency range.

2.3.3. Optimization of the FRFs

The complex modulus was estimated by optimizing the theoretical FRFs calculated with the finite element model (see previous section) against the experimental measured FRFs. This type of backcalculation using FEM is common for AM [38–40]. All the measurement temperatures were optimized simultaneously. The optimization was performed using the fminsearch algorithm in MATLAB. This algorithm was applied to minimize automatically and objectively the difference between the calculated and the measured FRFs. Since the resonance frequencies are directly related to the material properties, the experimental points used for the optimization were selected around these resonance frequencies at each temperature and a number of 10 points per peak was chosen. The objective function to minimize was defined according to Eq. (9):

$$Error = \sum_{i=1}^{N}\left(|H_{MNorm_i}| * \left|\frac{|H_{M_i}| - |H_{T_i}|}{|H_{M_i}|}\right|\right) \quad (9)$$

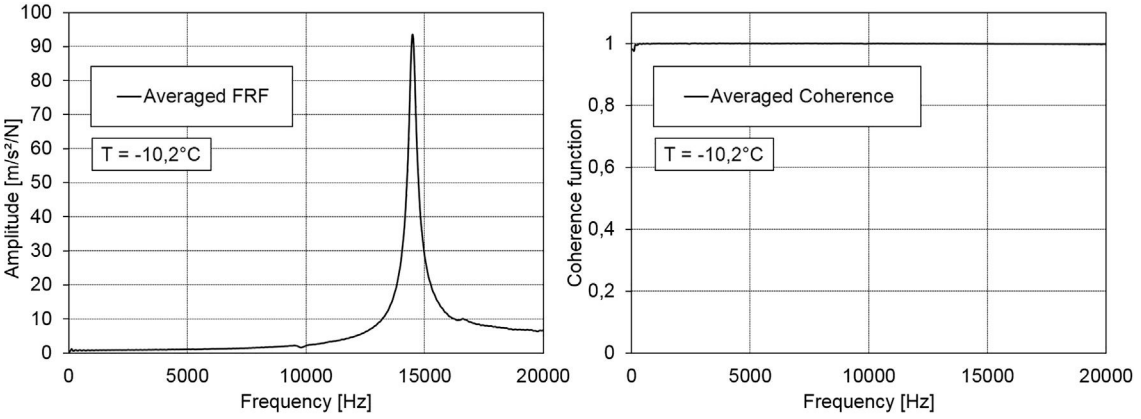

Fig. 6. Dynamic testing averaged experimental data in frequency domain for specimen 4 at −10,2 °C (left) frequency response function; (right) coherence function.

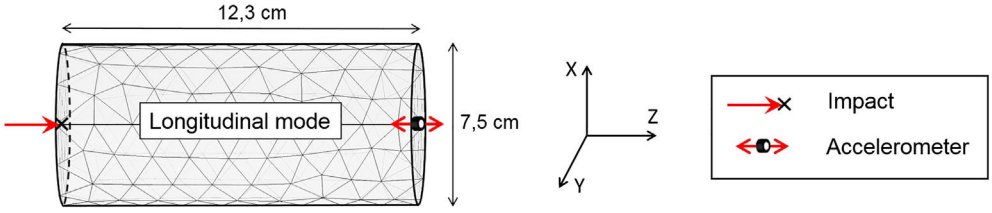

Fig. 7. Mesh and position of the impact and of the accelerometer for the finite element method numerical simulations.

where H_{MNorm} is the normalized measured FRF used to weigh the frequencies around the resonance, H_M is the measured FRF, H_T is the theoretical FRF, N is the number of optimization points and i is the index of the point. Among the 12 parameters of the 2S2P1D model, 6 have no (or very little) influence in the range of frequencies and temperatures existing for the performed dynamic tests. Then only 6 parameters (E_0, k, δ, τ_E, C_1 and C_2) were optimized. The remaining 6 parameters were fixed at the value obtained from cyclic tests. This limitation of the number of constants to be determined is of great interest because limiting the number of optimized parameters reduces considerably the computational time and the risk to obtain a wrong solution corresponding to a local minimum.

3. Results and discussion

3.1. Tension-compression test results

The complex moduli values determined through the tension-compression test for the specimen 4 are presented in Fig. 8. The cole-cole representation shows a good continuity of the measurements performed at different temperatures. It indicates that the material is rheologically simple and that the time-temperature superposition principle is valid. Therefore, a master curve was created at the reference temperature of 14.9 °C. The 2S2P1D model was fitted to the experimental data and is also plotted on Fig. 8. A very good agreement between the model and the experimental data can be observed.

The estimated values of the 2S2P1D model parameters to fit the experimental tension-compression data are given in Table 2. Note that the values of k, h, δ and β are the same for all the specimens. This is because these parameters are only depending on the bitumen which is the same for the 3 cylinders.

3.2. Dynamic test results

The measured and the optimized FRFs for the specimen 4 at −22.9 °C and at 19.7 °C are displayed on Fig. 9. The experimental data used for the optimization are also presented in this figure. The optimized FRFs was obtained following the process described in Section 2.3.3. A good agreement between the experimental FRFs and the optimized FRFs can be seen.

The optimized parameters of the 2S2P1D model to match the experimental FRFs are given in Table 3. As explained previously, only the values of E_0, k, δ, τ_E, C_1 and C_2 were determined. The values of the other parameters are equal to the ones obtained from the tension-compression tests. It can be seen that a slight difference

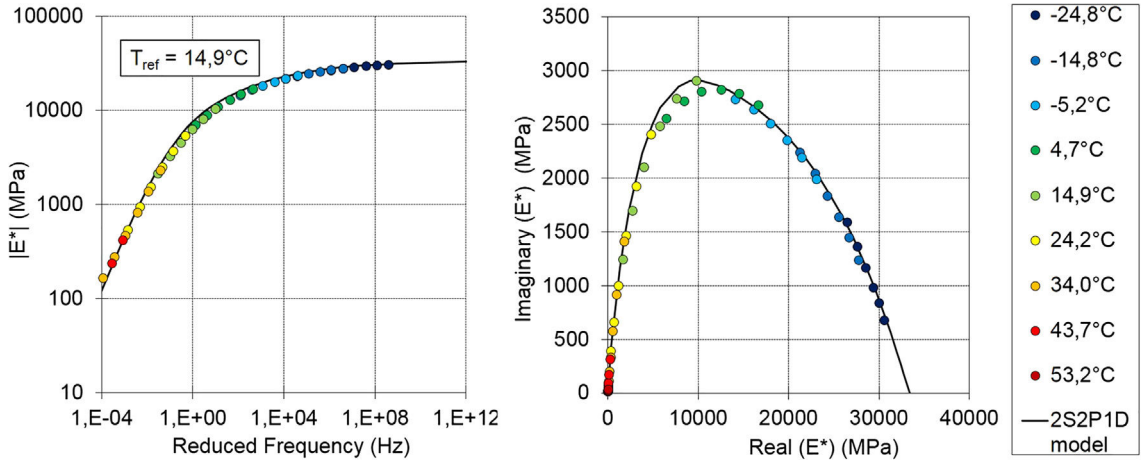

Fig. 8. Tension-compression test results for specimen 4 and 2S2P1D model simulation. (left) master curve at 14,9 °C; (right) cole-cole diagram.

Table 2
2S2P1D model constants to match the tension-compression measurements.

Specimen	E_{00} (MPa)	E_0 (MPa)	ν_0	ν_{00}	δ	k	h	β	$\tau_{E15°C}$ (s)	$\tau_{\nu15°C}$ (s)	C_1	C_2
4	28	33,400	0.198	0.426	2.28	0.177	0.571	154	0.056	1.60	25.1	167.5
6	52	37,400	0.231	0.510	2.28	0.177	0.571	154	0.074	4.20	24.1	159.7
8	56	36,900	0.179	0.550	2.28	0.177	0.571	154	0.072	12	25.1	167.5

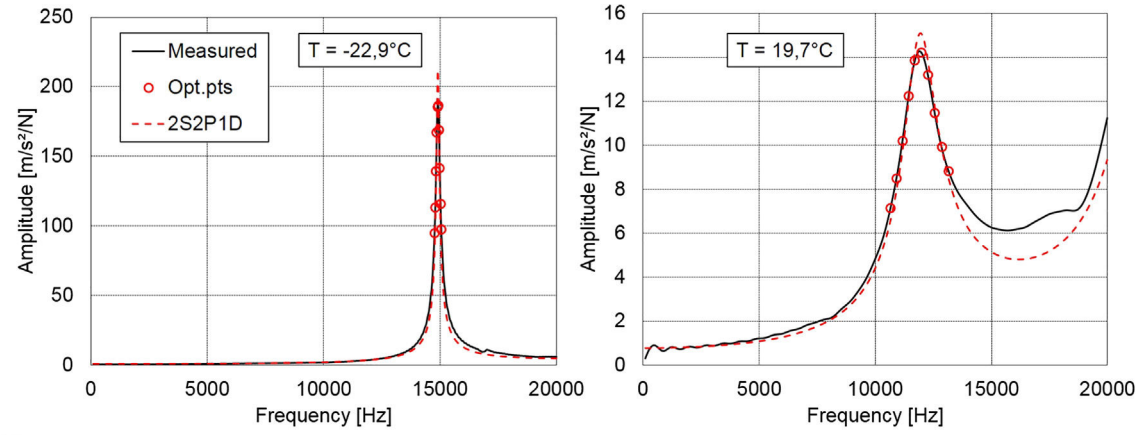

Fig. 9. Measured and optimized FRFs for specimen 4. (left) at −22,9 °C; (right) at 19,7 °C.

Table 3
Optimized 2S2P1D model parameters to match the dynamic measurements.

Specimen	E_{00} (MPa)	E_0 (MPa)	ν_0	ν_{00}	δ	k	h	β	$\tau_{E15°C}$ (s)	$\tau_{\nu15°C}$ (s)	C_1	C_2
4	28	33,584	0.198	0.426	2.34	0.186	0.571	154	0.095	1.60	28.5	210.1
6	52	37,748	0.231	0.510	2.12	0.172	0.571	154	0.34	4.20	29.8	209.3
8	56	36,554	0.179	0.550	2.05	0.178	0.571	154	0.108	12	30.8	230.8

is obtained between "dynamic" and "cyclic" constants. The impact of this difference on the material behavior description is presented in the next section.

3.3. Comparison of the dynamic and the tension-compression test results

In Fig. 10, the characteristic times obtained from the tension-compression tests and from the dynamic measurements are shown. Characteristic times from the dynamic testing tend to be lower than the characteristic times from tension-compression for the low temperatures. The trend is reversed for the high temperatures. The reason of this difference should be further investigated.

Fig. 11a and 11b presents the master curves for the norm and the phase angle of the complex modulus at a reference temperature of 15 °C for specimen 4. Experimental data from the tension-compression test are plotted with the two 2S2P1D model master curves obtained from the calibrations on the tension-compression and dynamic tests. Frequencies near the resonance frequencies were chosen at each measurement temperature of the FRFs to perform a direct comparison between the values obtained from the two plotted 2S2P1D model. It is shown that the norm of the complex modulus obtained from the dynamic tests is higher than the values obtained with the tension-compression test while it is the contrary for the phase angle. This effect observed in previous studies [22,23] was expected because different strain levels are applied in the two test methods (about 50 μm/m for the tension-compression tests against about 0.1 μm/m for the dynamic tests) and asphalt mixes have a behavior which is strongly dependent on the strain level [24–26]. Therefore, using both tension-compression measurements and dynamic tests can improve the knowledge of the nonlinear behavior of asphalt mixes. Since the norm of the complex modulus is higher and the phase angle is lower for the dynamic measurements, a smaller loss factor (loss modulus/storage modulus) is expected compared to the results of the tension-compression tests. This is confirmed in Fig. 11c, where the dynamic results are located to the right of the tension-compression results in the cole-cole representation when calculated at the same temperature and same frequencies. It is also observed that the dynamic and tension-compression master curves are in good agreement in the cole-cole space. Differences observed between the two test methods are higher for the low frequencies (or the high temperatures). This is shown in Fig. 12 in which the relative differences between the norm of the complex modulus from the dynamic tests and from the tension-compression tests are plotted in the frequency range from 0.1 Hz to 10^{10} Hz at the reference temperature of 15 °C. In the same figure, the differences between the phase angles are also presented. This observation was also expected because the nonlinear behavior of asphalt mixes regarding the strain level is dependent on the temperature and on the frequency. For the same strain level difference, the norm and the phase of the complex modulus are more affected by nonlinearities when the frequency decreases or when the temperature increases [24–26].

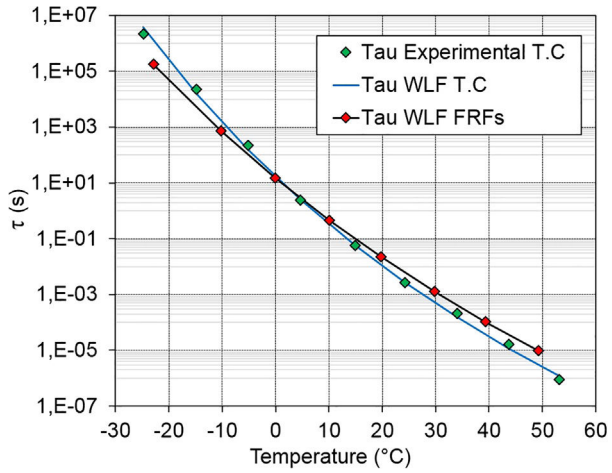

Fig. 10. Comparison of the values of tau obtained from the tension-compression tests and obtained from the dynamic measurements (experimental values and WLF fitted curves).

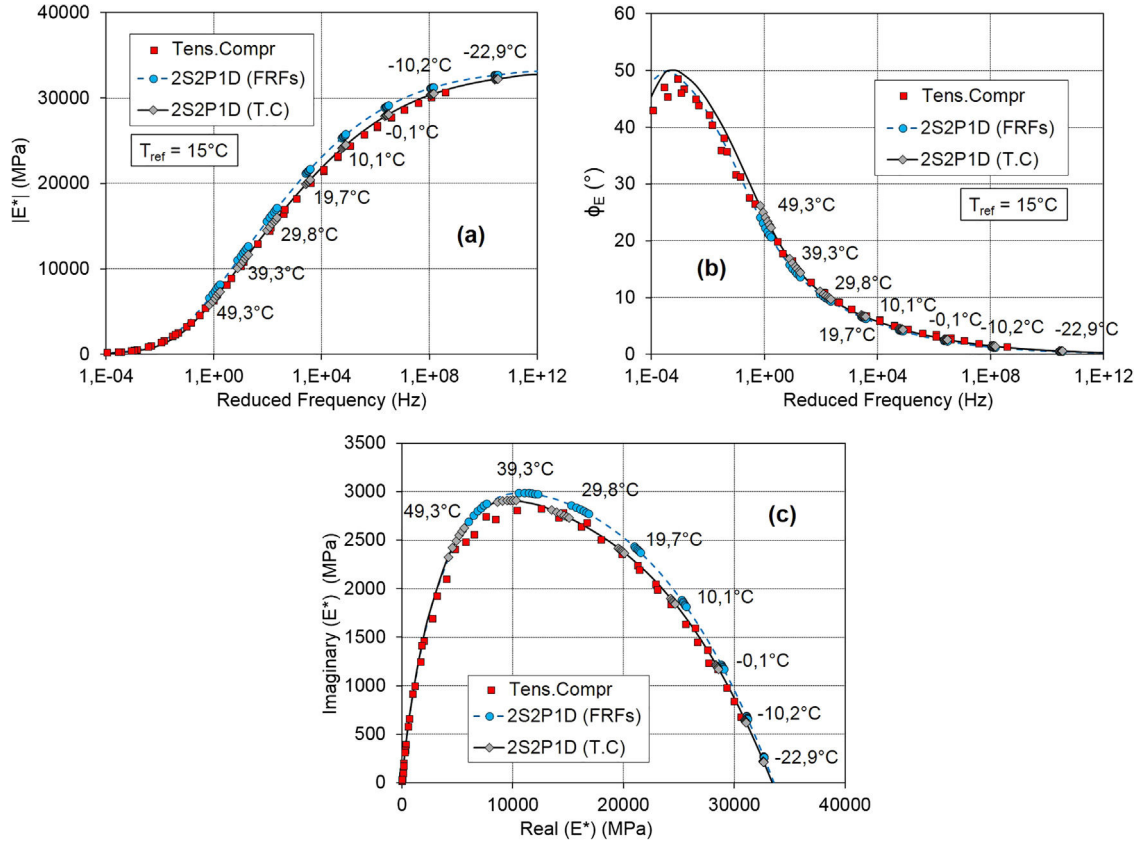

Fig. 11. Comparison of the complex modulus determined through the tension-compression and the dynamic tests for specimen 4. (a) Master curve of the norm of the complex modulus at 15 °C; (b) master curve of the phase angle at 15 °C; (c) cole-cole diagram.

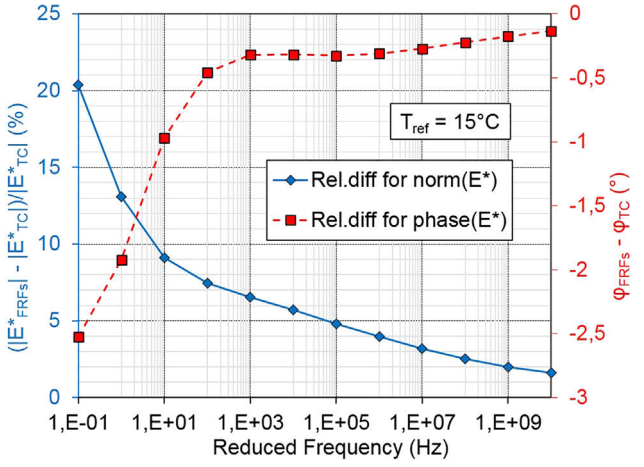

Fig. 12. Relative difference of the norm of the complex modulus obtained from the dynamic and the tension-compression tests and difference between the phase angles as a function of reduced frequency.

4. Conclusion

In this paper, two test methods to characterize the LVE behavior of asphalt mixes were used and compared. Three different specimen were tested with both methods and results were analysed. It is shown that the conventional approach using tension-compression tests gives lower values for the norm of the complex modulus and higher values for the phase angle than the dynamic measurements. The differences observed between the two methods are more important for the low frequencies and the high temperatures. Since the dynamic tests are performed at a much smaller strain level than the tension-compression tests, these results were expected and they agree previous research on the strain level dependency of asphalt mixes. The dynamic measurements are performed at very high frequencies compared to the frequency used for the tension-compression tests. Therefore, the combination of the two tests methods is useful to improve the characterization of the LVE behavior of asphalt mixes on a wider frequency range. In addition, the presented research shows that dynamic tests, which have the great advantage of being rapid, cheap and non-destructive, can provide the 3-dimensional linear viscous behavior of asphalt mixes on a wide range of frequencies and temperatures.

Conflict of interest

None.

References

[1] W.G. Halvorsen, D.L. Brown, Impulse technique for structural response frequency testing, J. Sound Vibr. 1977 (1977) 8–21.
[2] ASTM: C215-08, Standard Test Method for Fundamental Transverse, Longitudinal and Torsional Frequencies of Concrete Specimens, ASCE, West Conshoshocken, 2008.
[3] A. Migliori, J. Sarrao, Resonant ultrasound spectroscopy-applications to physics, materials measurements and nondestructive evaluation, Wiley-Interscience Publication, New-York, 1997.
[4] H. Bjurström, N. Ryden, Non-contact rolling surface wave measurements on asphalt concrete, Road Mater. Pavement Des. (2017), https://doi.org/10.1080/14680629.2017.1390491.
[5] N. Ryden, C.B. Park, Fast simulated annealing inversion of surface waves on pavement using phase-velocity spectra, Geophysics 71 (4) (2006) 49–58.

[6] H. Di Benedetto, C. Sauzéat, J. Sohm, Stiffness of bituminous mixtures using ultrasonic wave propagation, Road Mater. Pavement Des. 10 (4) (2009) 789–814.
[7] D. Mounier, H. Di Benedetto, C. Sauzéat, Determination of bituminous mixtures linear properties using ultrasonic wave propagation, Constr. Build. Mater. 36 (2012) 638–647.
[8] J. Norembuena-Contreras, D. Castro-Fresno, A. Vega-Zamanillo, M. Celaya, I. Lombillo-Vozmediano, Dynamic modulus of asphalt mixture by ultrasonic direct test, NDT&E Int. 43 (2010) 629–634.
[9] G. Kweon, Y.R. Kim, Determination of the complex modulus of asphalt concrete using the impact resonance test, J. Transp. Res. Board 1970 (2006) 151–160.
[10] A. Lacroix, Y.R. Kim, M.S.S. Far, Constructing the dynamic modulus mastercurve using impact resonance testing, Assoc. Asphalt Paving Technol. 78 (2009) 67–102.
[11] S.L. Whitmoyer, Y.R. Kim, Determining asphalt concrete properties via the impact resonant method, J. Test. Eval. 22 (2) (1994) 139–148.
[12] A. Gudmarsson, N. Ryden, B. Birgisson, Application of resonant acoustic spectroscopy to asphalt concrete beams for determination of the dynamic modulus, Mater. Struct. 45 (12) (2012) 1903–1913.
[13] R. Leisure, F. Willis, Resonant ultrasound spectroscopy, J. Phys.: Condens. Matter 9 (1997) 6001–6029.
[14] L. Ostrovsky, A. Lebedev, A. Matveyev, A. Popatov, A. Sutin, I. Soustova, P. Johnson, Application of three-dimensional resonant acoustic spectroscopy method to rock and building materials, J. Acoust. Soc. Am. 110 (4) (2001) 1770–1777.
[15] N. Ryden, Resonant frequency testing of cylindrical asphalt samples, Eur. J. Environ. Civil Eng. 15 (2011) 587–600.
[16] Z. Ren, N. Atalla, S. Ghinet, Optimization based identification of the dynamic properties of linearly viscoelastic materials using vibrating beam techniques, ASME J. Vibr. Acoust. 133 (4) (2011) 1–12.
[17] A. Renault, L. Jaouen, F. Sgard, Characterization of elastic parameters of acoustical porous materials from beam bending vibrations, J. Sound Vib. 330 (2011) 1950–1963.
[18] S.J. Rupitsch, J. Ilg, a. Sutor, R. Lerch, M. Döllinger, Simulation based estimation of dynamic mechanical properties for viscoelastic materials used for vocal fold models, J. Sound Vib. 330 (2011) 4447–4459.
[19] A. Gudmarsson, N. Ryden, B. Birgisson, Characterizing the complex modulus and Poisson's ratio of asphalt concrete specimens through modal testing, J. Acoust. Soc. Am. 132 (4) (2012) 2304–2312.
[20] A. Duttine, H. Di Benedetto, A. Ezaoui, Anisotropic small strain properties of sand and mixture of sand-clay measured by dynamic and static methods, Soils Found. 47 (3) (2007) 457–472.
[21] A. Ezaoui, H. Di Benedetto, Experimental measurements of the global anisotropic elastic behavior of dry Hostun sand during tri-axial tests, and effects of sample preparation, Géotechnique 59 (7) (2009) 621–635.
[22] A. Gudmarsson, N. Ryden, H. Di Benedetto, C. Sauzéat, N. Tapsoba, B. Birgisson, Comparing linear viscoelastic properties of asphalt concrete measured by laboratory seismic and tension-compression tests, J. Nondestr. Eval. 33 (4) (2014) 571–582.
[23] A. Gudmarsson, N. Ryden, H. Di Benedetto, Sauzéat, Complex modulus and complex Poisson's ratio from cyclic and dynamic modal testing of asphalt concrete, Constr. Build. Mater. 88 (2015) 20–31.
[24] G. Airey, B. Rahimzadeh, Combined bituminous binder and mixture linear rheological properties, Constr. Build. Mater. 18 (2004) 535–548.
[25] Q.T. Nguyen, H. Di Benedetto, C. Sauzéat, Linear and nonlinear viscoelastic behavior of bituminous mixtures, Mater. Struct. 48 (7) (2015) 2339–2351.
[26] S. Mangiafico, L. Babadopoulos, H. Di Benedetto, C. Sauzéat, Nonlinearity of bituminous mixtures, Mech. Time-Depend. Mater. (2017), https://doi.org/10.1007/s11043-017-9350-3.
[27] J.E. Poirier, S. Pouget, C. Leroy, B. Delaporte, Projets Mure et Improvmure: bilan à mi-parcours, Revue Générale des Routes et de l'Aménagement 937 (2016) 38–41.
[28] H. Di Benedetto, F. Olard, C. Sauzéat, B. Delaporte, Linear viscoelastic behavior of bituminous materials: From binders to mixtures, Road Mater. Pavement Des. 5 (S1) (2004) 163–202.
[29] F. Olard, H. Di Benedetto, General 2S2P1D model and relation between the linear viscoelastic behaviors of bituminous binders and mixes, Road Mater. Pavement Des. 4 (2) (2003) 185–224.
[30] S. Tiouajni, H. Di Benedetto, C. Sauzéat, S. Pouget, Approximation of linear viscoelastic model in the 3 dimensional case with mechanical analogues of finite size – APPLICATION to bituminous materials, Road Mater. Pavement Des. 12 (4) (2011) 897–930.
[31] H. Di Benedetto, B. Delaporte, C. Sauzéat, Three dimensional linear behavior of bituminous materials: Experiments and modeling, ASCE Int. J. Geomech. 7 (2) (2007) 149–157.
[32] H.M. Nguyen, S. Pouget, H. Di Benedetto, C. Sauzéat, Time-temperature superposition principle for bituminous mixtures, Eur. J. Environ. Civil Eng. 13 (9) (2009) 1095–1107.
[33] M.L. Nguyen, C. Sauzéat, H. Di Benedetto, N. Tapsoba, Validation of the time-temperature superposition principle for crack propagation in bituminous mixtures, Mater. Struct. 46 (7) (2013) 1075–1087.
[34] Q.T. Nguyen, H. Di Benedetto, C. Sauzéat, N. Tapsoba, Time-temperature superposition principle validation for bituminous mixes in the linear and nonlinear domain, ASCE J. Mater. Civil Eng. 25 (9) (2013) 1181–1188.
[35] J.D. Ferry, Viscoelastic Properties of Polymers, third ed., John Wiley & Sons, New York, NY, 1980.
[36] T. Brüggemann, D. Biermann, A. Zabel, Development of an automatic modal pendulum for the measurement of frequency responses for the calculation of stability charts, Proc. CIRP 33 (2015) 587–592.
[37] P.E. Norman, G. Jung, C. Ratcliffe, R. Crane, C. Davis, Development of an Automated Impact Hammer for Modal Analysis of Structures, 2012. DSTO-TN-1062.
[38] Y.S. Cho, F.B. Lin, Spectral analysis of surface waves in single and multi-layer slabs with finite thickness using finite element modelling, NDT&E Int. 38 (3) (2005) 195–202.
[39] S.S. Madsen, E. Levenberg, Dynamic backcalculation with different load-time histories, Road Mater. Pavement Des. (2017), https://doi.org/10.1080/14680629.2017.1307263.
[40] M. Mousa, M.A. Elseifi, O. Elbagalati, L.N. Mohammad, Evaluation of interface bonding conditions based on non-destructing testing deflection measurements, Road Mater. Pavement Des. (2017), https://doi.org/10.1080/14680629.2017.1400995.

Paper IV : Linear viscoelastic behavior of asphalt mixes from dynamic frequency response functions

CARRET JEAN-CLAUDE
DI BENEDETTO HERVE
SAUZEAT Cédric

Submitted to
International Journal for Numerical and Analytical Methods in Engineering

LINEAR VISCOELASTIC BEHAVIOR OF ASPHALT MIXES FROM DYNAMIC FREQUENCY RESPONSE FUNCTIONS

CARRET Jean-Claude[1], DI BENEDETTO Herve[1] and SAUZEAT Cedric[1]

[1]*LTDS (UMR CNRS 5513), University of Lyon / ENTPE, Rue M. Audin, 69518, Vaulx en Velin, France*
E-mail: jean-claude.carret@entpe.fr
E-mail: herve.dibenedetto@entpe.fr
E-mail: cedric.sauzeat@entpe.fr

ABSTRACT

In the small strain domain, asphalt mixes (AM) have a linear viscoelastic (LVE) behavior which is strongly dependent on frequency and temperature. The maximum ratio of modulus values can be up to one thousand and traditional elastic analyses are not pertinent. The possibility to characterize AM from frequency response functions (FRFs) was studied. A new optimization process using the finite element method (FEM) has been developed to back-calculate the LVE properties of AM from FRFs. The numerical optimization process was applied to a reference material with averaged LVE properties determined from tension-compression tests performed on a wide variety of AM types. The LVE properties were modeled considering the 3-Dim version of the model 2S2P1D (2 Springs, 2 Parabolic elements and 1 Dashpot). Reference FRFs for the considered reference material were obtained from FEM simulations. Three different configurations that may be of interest for practical tests were studied at 5 different temperatures. The proposed numerical optimization method consists in performing separate optimizations at each temperature to obtain the LVE properties for the considered temperature. Then values obtained at each temperature are considered to optimize 2S2P1D and Williams Landel Ferry (WLF) equation constants to simulate the global LVE behaviour of the material. The accuracy of the process was assessed regarding both the calculated FRFs and the complex modulus evaluation. Results indicate that the proposed optimization process converge almost perfectly towards the reference FRFs. The simulated complex modulus values are also in very good agreement with the values of the reference material.

Keywords: asphalt mixes, linear viscoelasticity, complex modulus, frequency response functions, optimization process, finite element method

1. INTRODUCTION

Dynamic tests such as measurements of frequency response functions (FRFs) obtained through impact loadings [1, 2] are economical, simple to perform and nondestructive. These measurements are known to provide accurate characterization of material properties in the case of elastic materials [3, 4]. Therefore, this type of measurements would be a good alternative to conventional complex modulus tests (cyclic tension-compression, flexion or others) traditionally used to determine the linear viscoelastic (LVE) characterization of asphalt mixes (AM). Different dynamic tests such as measurement of the flying time [5-7], resonance testing considering only the fundamental resonance frequency [8-10] or resonant acoustic spectroscopy (RAS) [11-14] have been applied to AM but the frequency dependency behaviour of AM cannot be evaluated properly with these tests. Recently, measurement of FRFs have been performed on LVE materials [15-16] and more specifically on AM [17, 18, 19, 20]. Gudmarsson et al. [18, 19] and Carret et al. [20] have demonstrated that FRFs measurements is a promising approach to characterize the LVE behavior. However, Carret et al. [21] have demonstrated that a simplified LVE back analysis using some results obtained from elastic approach cannot provide an accurate characterization of materials properties from FRFs. Therefore, characterizing the LVE behavior of AM from FRFs requires a more elaborate optimization approach. In this paper, a new numerical optimization process to back-calculate the LVE properties from FRFs was developed and was applied to a reference material with AM averaged LVE properties. The FRFs of this reference material were calculated with the finite element method (FEM). This procedure based on numerical experimentation eliminates any potential divergence due to physical experimentation. Therefore, only the effect of the optimization process on the characterization of the LVE properties was studied. Results of the optimization process were used to fit the 2S2P1D (2 Springs, 2 Parabolic elements and 1 Dashpot) model and the Williams Landel Ferry (WLF) constants simulating the global LVE behaviour of the material. The FRFs obtained after the optimization process were compared to the FRFs of the reference material. In addition, the simulated complex modulus obtained after the optimization process was compared to the complex modulus of the reference material. A very good agreement was observed for the FRFs as well as for the complex modulus. This demonstrates the

possibility to obtain accurately the LVE behavior of AM from FRFs and shows the good potentiality of the proposed method.

2. OBTENTION OF REFERENCE MATERAL LINEAR VISCOELATIC PROPERTIES

2.1 Procedure to obtain Reference Material properties

Cyclic tension-compression complex modulus tests were previously performed on 38 different types of AM specimens during 4 different PhD theses carried out at the University of Lyon / ENTPE, LTDS laboratory and reported in different publications [22-28]. The results from the tests of these specimens, which represent a wide range of asphalt mixes types, are used as a data base. From this data base a reference material with "averaged" linear viscoelastic properties were obtained. The LVE behavior of the reference material is described with the 2S2P1D model [29-31], whose constant values are the average of the constants obtained from each of the 38 specimens. The principle of this averaging procedure is explained in figure 1. All the numerical simulations and analyses presented in this paper were performed on this reference material.

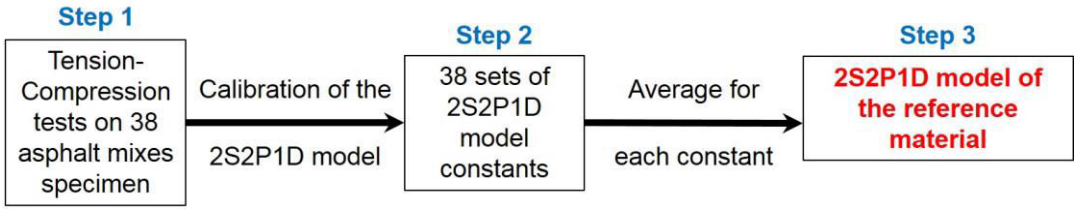

Figure 1. Principle of the process to obtain the reference material LVE properties.

2.2 Tension-Compression complex modulus tests

The complex Young's modulus and the complex Poisson's ratio for each of the 38 different types of AM were determined with tension-compression tests. These tests were performed using a hydraulic press (figure 2). Cyclic sinusoidal loadings with an axial strain amplitude of about 50 µm/m were applied on cylindrical samples with a diameter of 75 mm and a height of 150 mm. The axial stress ($\sigma_1=\sigma_0.sin(\omega t-\phi_E)$ or $\sigma_1=\sigma_0.e^{i(\omega t-\varphi_E)}$ in complex notation) was measured with a load cell. Three extensometers placed at 120° from each other were averaged to obtain the axial strain ($\varepsilon_1=\varepsilon_{01}.sin(\omega t)$ or $\varepsilon_1=\varepsilon_{01}.e^{i\omega t}$ in complex notation). The radial strain ($\varepsilon_2=\varepsilon_{02}.sin(\omega t+\phi_v)$ or $\varepsilon_2=\varepsilon_{02}.e^{j(\omega t+\varphi v)}$ in complex notation) was deduced from measurements of two non-contact transducers. The tensions-compression tests were performed at 8 different loading frequencies (from 0.003Hz to 10Hz) and 9 different temperatures from -25°C to

55°C. Equation 1 and 2 are used to calculate the complex modulus (E*) and the complex Poisson's ratio (ν*) at each temperature and frequency.

$$E^*(\omega) = \frac{\sigma_1^*}{\varepsilon_1^*} = \left|E^*(\omega)\right| e^{i\Phi_E} \quad (1)$$

$$\nu^*(\omega) = -\frac{\varepsilon_2^*}{\varepsilon_1^*} = \left|\nu^*(\omega)\right| e^{i\Phi_\nu} \quad (2)$$

Where ϕ_E and ϕ_ν are the phases of the complex modulus and of the complex Poisson's ratio respectively.

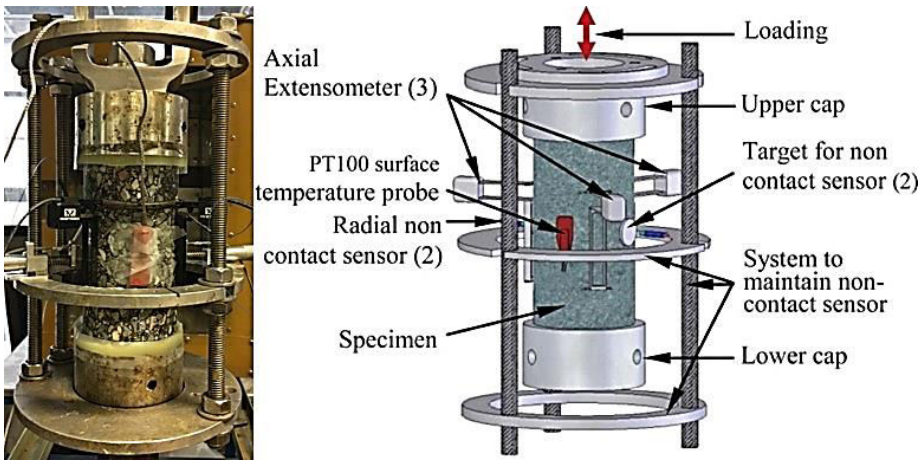

Figure 2. (left) Asphalt mix specimen during tension-compression test (Uni. of Lyon/ENTPE laboratory); (right) scheme of the sample and measurement sensors

2.3 2S2P1D linear viscoelastic model

The 2S2P1D LVE model developed at ENTPE [29-31] was used to simulate AM linear behavior. This model consists of a combination of two springs, two parabolic creep elements and one dashpot as schematized in the 1dimension case in figure 3. The complex modulus of the model is given in equation 3.

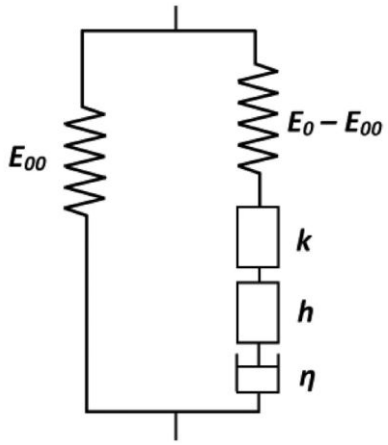

Figure 3. Representation of the 2S2P1D LVE model in the 1dimension case.

$$E^*_{2S2P1D}(\omega) = E_{00} + \frac{E_0 - E_{00}}{1 + \delta(j\omega\tau)^{-k} + (j\omega\tau)^{-h} + (j\omega\beta\tau)^{-1}} \quad (3)$$

Where ω is the angular frequency ($\omega=2\pi f$, where f is the frequency), E_0 is the high frequency modulus, E_{00} is the low frequency modulus, k and h are dimensionless constants such as $0 < k < h < 1$, δ is a dimensionless constant, β is a dimensionless constant related to Newtonian viscosity η by $\eta = (E_0\text{-}E_{00})\beta\tau$ and τ is a characteristic time of the complex modulus, whose value varies only with temperature. Previous studies [32-34] showed that the time temperature superposition principle (TTSP) is verified for asphalt mixes in the linear and nonlinear domains. This allows to calculate a characteristic time at any given temperature using equation 4.

$$\tau(T) = a_T(T)\tau_{ref} \quad (4)$$

Where τ_{ref} is the characteristic time at the reference temperature and a_T is the shift factor at the temperature T defined by the Williams-Landel-Ferry (WLF) equation [35]:

$$\log(a_T) = -\frac{C_1(T - T_{ref})}{C_2 + T - T_{ref}} \quad (5)$$

where C_1 and C_2 are the two constants of the WLF equation and T_{ref} is the reference temperature.

In the 3-dimension case [36], the model also has an expression for the complex Poisson's ratio:

$$\nu^*_{2S2P1D}(\omega) = \nu_{00} + \frac{\nu_0 - \nu_{00}}{1 + \delta(j\omega\tau_\nu)^{-k} + (j\omega\tau_\nu)^{-h} + (j\omega\beta\tau_\nu)^{-1}} \quad (6)$$

where ν_0 is the high frequency Poisson's, ν_{00} is the low frequency Poisson's ratio and τ_ν is the

characteristic time of the complex Poisson's ratio, whose value varies only with temperature. Parameters δ, k, h and β are the same the complex modulus and the complex Poisson's ratio. More details on the performed test and calibration process can be obtained in references [22 to 31].

Previous studies showed that the 2S2P1D model simulates quite correctly bituminous materials behaviour. It explains why we chose this model for our analyses. As an example, the experimental and the simulated complex modulus and complex Poisson's ratio are plotted in Cole-Cole curves for a laboratory designed warm mix containing 70% of RAP (specimen LWF-70-1-1-4 from [37]) in figure 4. The curves of the reference material are also plotted in this figure.

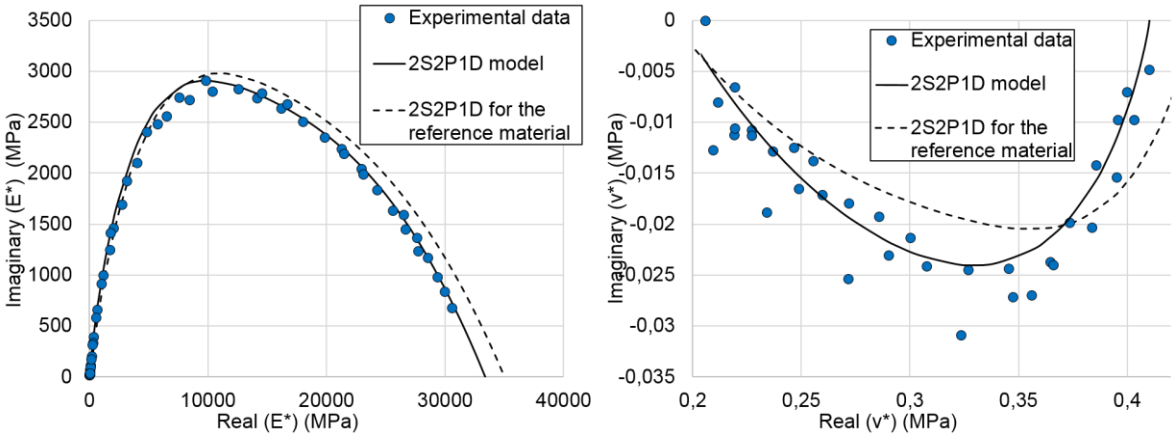

Figure 4. Example of results in Cole-Cole plot of experimental data from tension-compression test and modelling with the 2S2P1D model for specimen LWF-70-1-1-4 [37]. (left) complex modulus; (right) complex Poisson's ratio. Curves obtained for the reference material (constant given in table 1) are also plotted.

The values of the 2S2P1D model constants for the reference material (having averaged viscoelastic properties), considered in this study, are listed in table 1. Values of the relative standard deviation (RSD) for the 38 AM types are also given for each constant.

Table 1. 2S2P1D constants for reference material with "averaged" viscoelastic properties of asphalt mixes and relative standard deviation (RSD) in per cent for each constant.

	E_{00} (MPa)	E_0 (MPa)	ν_0	ν_{00}	δ	k	h	β	$\tau_{E15°C}$ (s)	$\tau_{\nu15°C}$ (s)	C_1	C_2
Average	100	35 000	0.19	0.43	2.15	0.17	0.53	250	0.1	3.165	30	210
RSD (%)	26.6	8.1	36.8	21.4	8.4	5.9	5.7	267.8	326.8	140.7	16.6	13.7

3. LINEAR VISCOELASTIC BEHAVIOR FROM FREQUENCY RESPONSE FUNCTIONS

3.1 Calculation of FRFs using finite element method numerical simulations

The frequency response functions (FRFs) for dynamic impact loadings were obtained by solving three-

dimensional equation of motion (7) in the frequency domain.

$$-\rho\omega^2\mathbf{u} - \nabla.\sigma = 0 \tag{7}$$

Free boundary conditions are assumed to solve equation 7 except at the impact point where a cyclic unity load $e^{i\omega t}$ is applied in the direction of the impact. In equation 7, ρ is the bulk density of the material set to 2 400 kg/m^3, ω is the angular frequency, $\mathbf{u}$ is the displacement vector, ∇ is the gradient tensor operator, i is a complex number such as $i^2=-1$ and σ is the Cauchy stress tensor. Equation (7) is numerically solved using finite element method (FEM) calculation made with the COMSOL software. The material was considered as isotropic and the linear viscoelastic behavior was implemented using complex modulus and complex Poisson's ratio obtained from the 2S2P1D model (Eq. 3 and Eq. 6) with the constants given in table 1. FEM calculations are commonly applied to LVE materials [38-43] and specially to solve inverse problems to determine the LVE properties [44, 45]. It should be noted though, that the implementation of a continuous spectrum LVE model in a finite element model of AM is a new and recent approach. Two different geometries were considered. The first geometry is a cylinder with a diameter of 6.5 cm and a height of 16 cm and the second geometry is a disc with a diameter of 10 cm and a height of 3 cm. The mesh was built with tetrahedral elements with a maximum size of 2 cm, which was determined following a convergence study. The longitudinal and the flexural modes of vibrations were studied for the cylinder, while only the flexural mode was considered for the disc. The positions of the impact and of the point where is calculated the acceleration (position of the accelerometer during impact tests) are indicated in figure 5. The coordinates of these positions are given in table 2 were the origin of the coordinate system corresponds to the center of gravity in each case. The FRFs considered in this study are simply defined by equation 8.

$$H(f) = \frac{A(f)}{F(f)} = \frac{(2\pi f)^2 U(f)}{1} \tag{8}$$

Where H is the FRF, A is the amplitude of the acceleration in the direction of measurement calculated at the position of the accelerometer, U is the amplitude of the displacement in the direction of measurement calculated at the position of the accelerometer, F is the impact loading corresponding to a unity load and f is the frequency. The FRFs were calculated at 5 different temperatures (-20°C, 0°C,

15°C, 35°C and 50°C) in a frequency range between 100 and 20 000 Hz by steps of 20 Hz. This range was fixed by the characteristics of the hammers and the accelerometers that can be used during physical tests (not presented in this paper).

Table 2. Coordinates of the impact and of the accelerometer in the FEM numerical simulations. Origin of the coordinate system corresponds to the center of gravity.

Case	*Point*	*X (cm)*	*Y (cm)*	*Z (cm)*
Longitudinal mode of the cylinder	Impact	0	0	-8
	Accelerometer	0	0	8
Flexural mode of the cylinder	Impact	3	0	-8
	Accelerometer	3	0	8
Flexural mode of the disc	Impact	1.5	0	-4.5
	Accelerometer	1.5	0	4.5

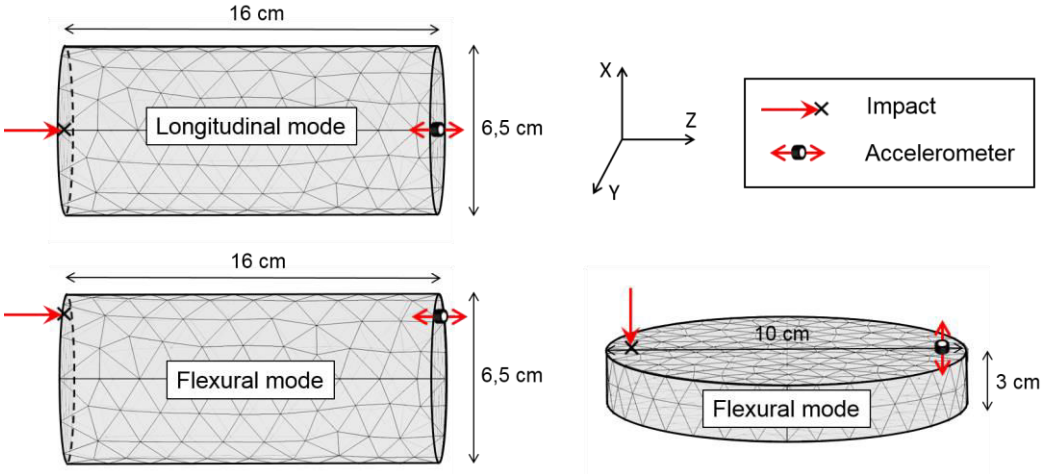

Figure 5. Position of the impact and of the accelerometer in the FEM numerical simulations for the three studied cases: the longitudinal and flexural modes for the cylinder and the flexural mode for the disc.

3.2 Optimization process

A sensitivity analysis, which is not presented in this paper, showed that only 4 constants of the 2S2P1D model (E_0, k, δ and τ_E) have a significant influence on the calculation of the FRFs. This result can be explained easily as dynamic tests mobilize “high” frequencies only. Note therefore that the complex Poisson’s ratio cannot be evaluated with this process because it also has a very small influence on the calculation of the FRFs. The optimization process consists in optimizing at each temperature separately FRFs calculated as described in 3.1 to match the reference FRF of the reference material. This is done by adjusting iteratively the values of the constants of the 2S2P1D model until the fit with the reference FRF is good enough. For these frequencies the constants of 2S2P1D not listed above have very few effect on the response. Therefore, only the constants above were considered in the optimization process. The values of the other constants were fixed to the values for the reference material as listed in table 1.

The same process described schematically in figure 6 was applied to the three considered configurations for each temperature.

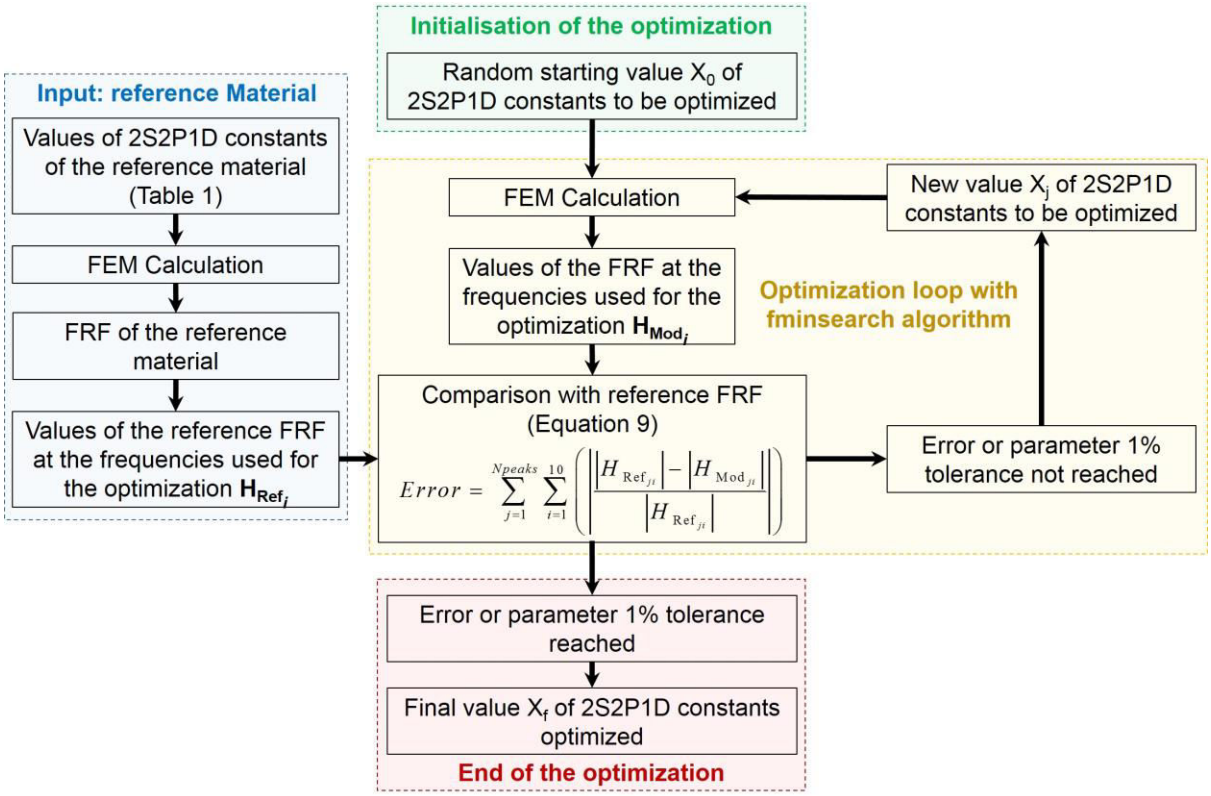

Figure 6. Scheme of the optimization process. X_f is the vector of 4 2S2P1D constants to identify.

The frequencies used for the optimization were selected around the resonance frequencies. 10 frequencies were selected along each resonance peak and the error function to minimize was defined according to equation 9.

$$Error = \sum_{j=1}^{Npeaks} \sum_{i=1}^{10} \left(\left| \frac{|H_{\mathrm{Ref}_{ji}}| - |H_{\mathrm{Mod}_{ji}}|}{|H_{\mathrm{Ref}_{ji}}|} \right| \right) \quad (9)$$

Where H_{Ref} is the reference calculated (i.e. experimental) FRF, H_{Mod} is the FRF calculated during the optimization, *Npeaks* is the number of resonance peaks, *j* is the index of the peaks and *i* is the index of the frequencies. The vector X_0 of starting values of the 2S2P1D constants to be optimized was chosen randomly by taking values in a range of +/- 15% around the average values listed in table 1. The optimization was performed in MATLAB with the "fminsearch" algorithm. This algorithm was used to minimize the error function defined by equation 9. The tolerance on the error and on the parameter

estimation was set to 1%. Therefore, the optimization process was stopped if the variation of the error and of all the values of the parameters to be optimized is less than 1% between two iterations of the optimization loop. The so called back calculated complex modulus was then estimated with the final vector X_f of 2S2P1D model constants obtained at the end of the optimization.

4. RESULTS AND DISCUSSION

4.1 Results obtained directly after the optimization process

The final values of the 2S2P1D model constants in the case of the flexural mode of vibrations of the cylinder are listed in table 3. It can be seen that these values are slightly different than the reference values given in table 1. It is also observed that the values of the optimized parameters are different from one temperature to another and from one configuration to another. These observations indicate that each set of parameter should only be used to back calculate the complex modulus at the temperature of the optimization.

Table 3. Optimized 2S2P1D constants for the 3 cases studied. "LC" corresponds to the longitudinal mode of the cylinder, "FC" to the flexural mode of the cylinder and "FD" to the flexural mode of the disc.

Constant	*E_0 (MPa)*			*δ*			*k*			*τ_{ET} (s)*		
T (°C)	*LC*	*FC*	*FD*	*LC*	*FC*	*FD*	*LC*	*FC*	*FD*	*LC*	*FC*	*FD*
-20	34 903	35 344	35 396	2.28	1.84	2.21	0.181	0.140	0.136	$8{,}4E^{4}$	$1E^{6}$	$1{,}2E^{7}$
0	35 820	36 773	36 874	1.90	2.35	2.50	0.152	0.137	0.135	$2{,}2E^{1}$	$1.8E^{2}$	$3{,}3E^{2}$
15	33 934	33 604	33 156	2.42	2.44	1.93	0.183	0.187	0.189	$1{,}8E^{-1}$	$1.6E^{-1}$	$6{,}7E^{-2}$
35	40 251	33 706	31 265	2.11	2.34	1.95	0.139	0.186	0.189	$1{,}3E^{-4}$	$3.8E^{-4}$	$3{,}8E^{-4}$
50	31 832	31 610	33 409	2.03	1.96	1.95	0.193	0.182	0.140	$9{,}1E^{-6}$	$6.4E^{-6}$	$5{,}9E^{-6}$

Figure 7 presents, i) the reference FRF, ii) the FRF calculated at the beginning of the optimization process (noted starting FRF) with the initial values of the 2S2P1D constants, and iii) the FRF calculated at the end of the optimization (noted final FRF) with the final values of 2S2P1D constants obtain from the optimization process and the values of the reference FRF at the frequencies where the distance is minimized, in the 3 cases studied at 35°C and -20°C. A very good agreement between the reference FRFs and the final FRFs obtained after optimization can be seen. It shows that the optimization process is very efficient to converge towards the reference FRFs.

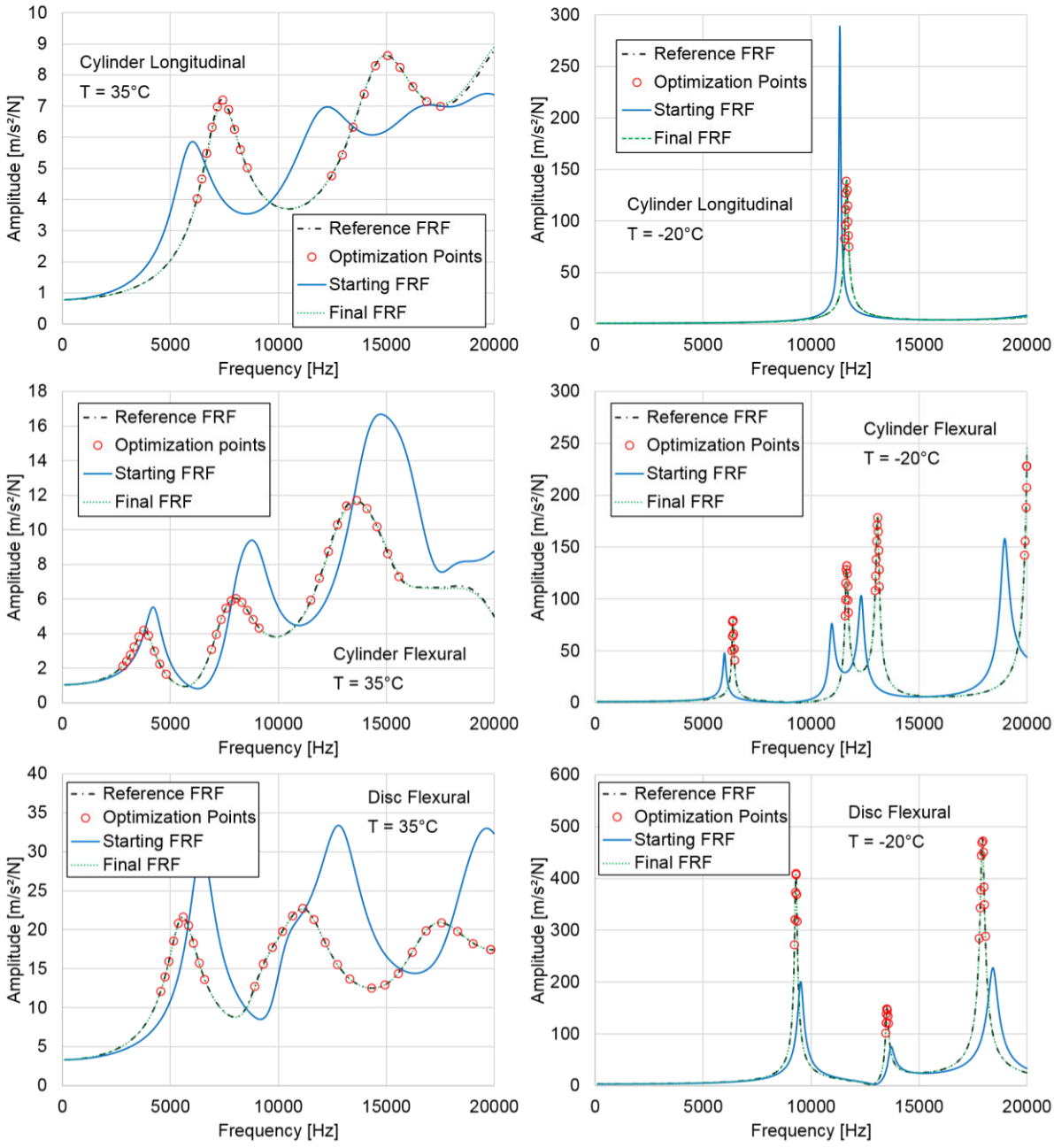

Figure 7. Reference FRF and values at the frequencies where optimization calculation is performed (noted optimization points), starting FRF at the beginning of the optimization process and final FRF after the optimization process for the 3 cases studied. (left column) T = 35°C; (right column) T = -20°C.

In addition, for each configuration and at each temperature, 6 frequencies were chosen in a narrow domain including all the resonance frequencies. The complex modulus was calculated for these 6 frequencies with the values of the 2S2P1D model constants after the optimization process using Eq. 3. The complex modulus values of the reference material were also calculated at the 6 same frequencies using Eq. 3. The principle of these calculations is detailed in figure 8 for the example of the flexural mode of the cylinder at 35°C.

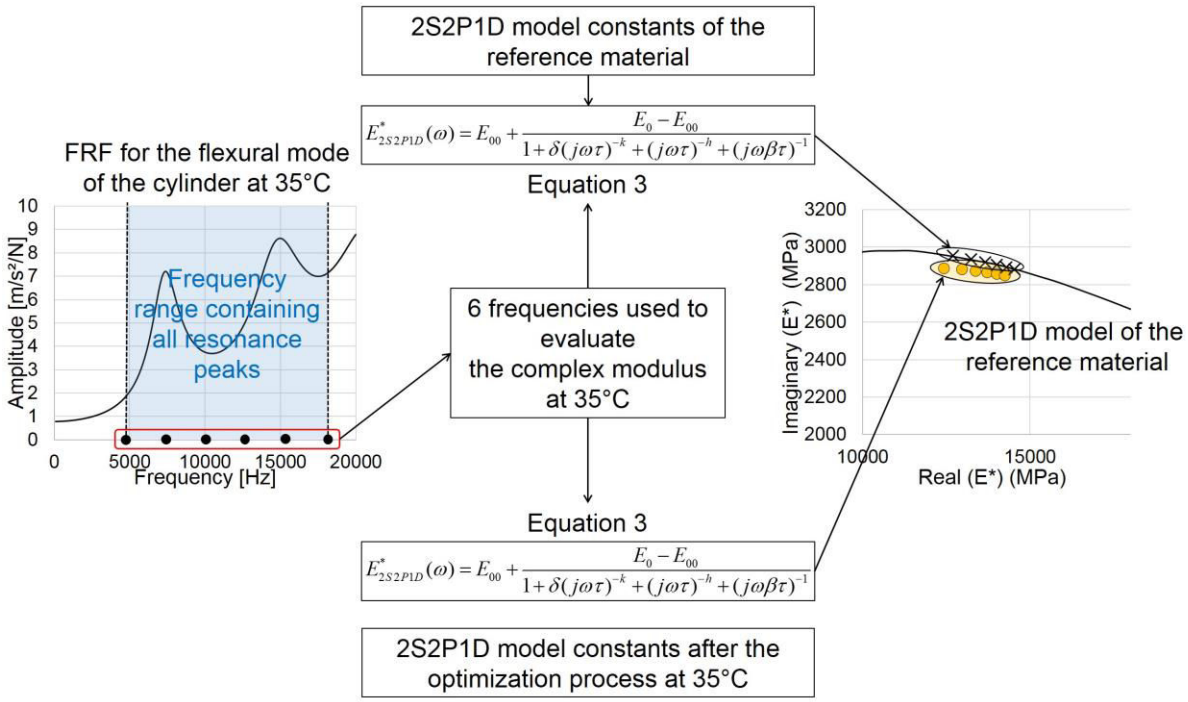

Figure 8. Principle of the calculations of the complex modulus at each temperature after the optimization process and on the reference material. Example for the flexural mode of the cylinder at 35°C.

Results are displayed in the cole-cole plan in figure 9 for the three configurations. A very good agreement between the reference values and the back calculated values can be observed for the three configurations studied.

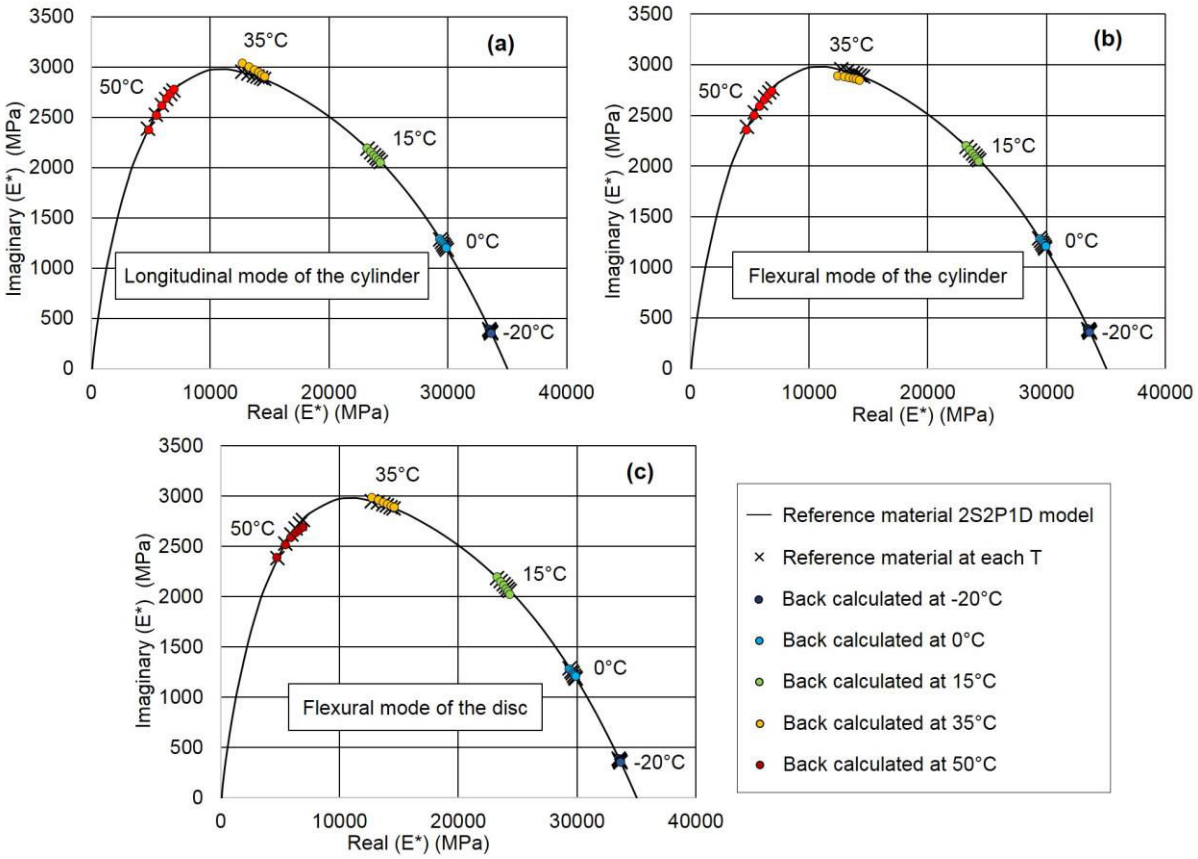

Figure 9. Comparison between the complex modulus values of the reference material and the back calculated complex modulus. (a) Longitudinal mode of the cylinder; (b) Flexural mode of the cylinder; (c) Flexural mode of the disc.

4.2 Global LVE simulation of the material

The global LVE simulation of the material is obtained from the values obtained at each temperature were the complex modulus is back calculated after optimization of the FRFs. These values are used as data points to fit a unique 2S2P1D model and to find the WLF law of the material. This is done in three steps. The first step consists in adjusting manually the values of the 2S2P1D constants until the fit in the cole-cole plan between the 2S2P1D model and the data points is satisfying. At this stage, only a visual criterion is used to assess the quality of the fit. In the second step, the experimental characteristic times τ_{exp} are determined for each temperature. To do so, the constants of the 2S2P1D model found in the first step are used to calculate the complex modulus at the same frequencies than the data points using equation 3. The experimental characteristic times τ_{exp} are optimized at each temperature separately to minimize the relative difference between the norm of the complex modulus calculated as described above and the norm of the complex modulus of the data points. Finally, the WLF law is found in the third step. A reference temperature of 15°C – the same reference temperature than the reference material

– was chosen and the 3 constants of the WLF law τ_{ref}, C_1 and C_2 were determined using the excel solver with characteristic times τ_{exp} found in the second step. This 3-steps process is illustrated in figure 10.

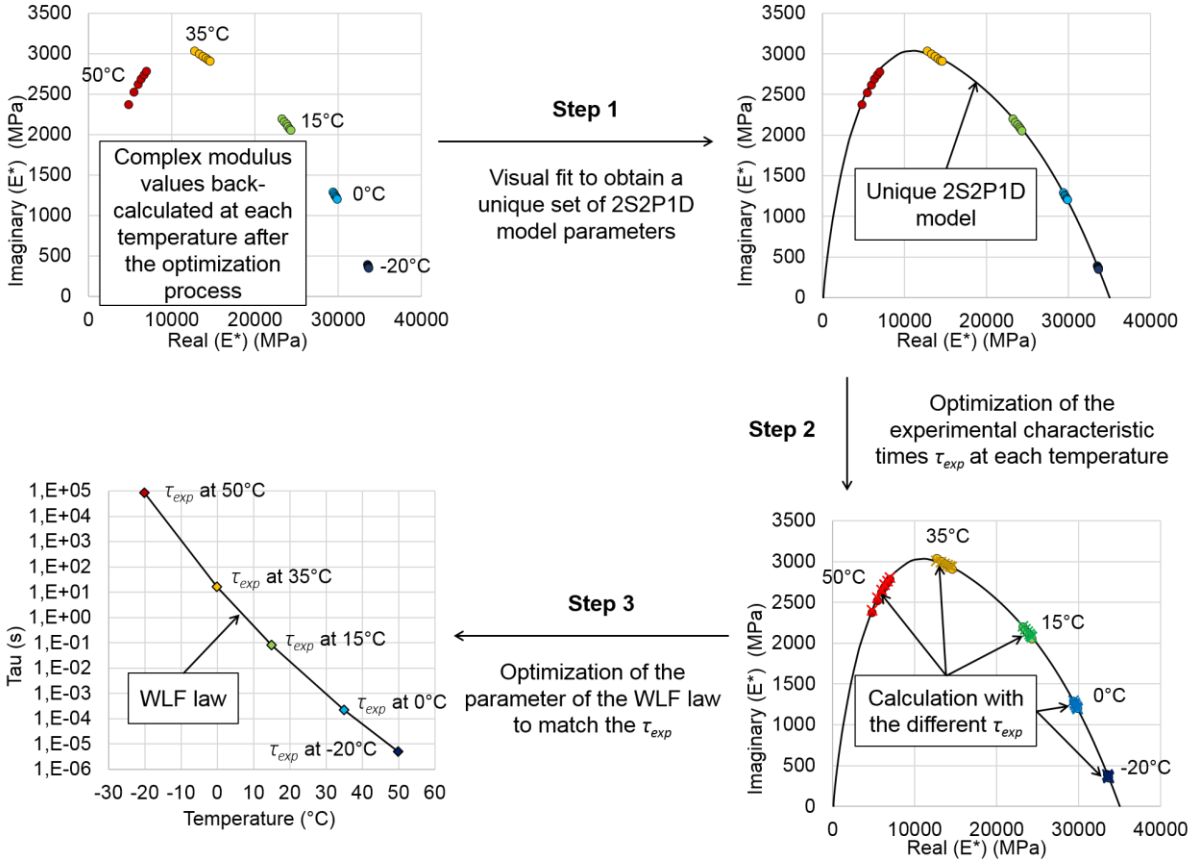

Figure 10. 3-steps process to determine the global LVE behaviour of the material from the complex modulus values back-calculated after the optimization process.

The values of the constants of the final obtained 2S2P1D models and of the WLF laws are given in table 4 for each of the three different configurations. It can be seen that the constants listed in table 4 are different but close from the constants of the reference materials listed in table 1.

Table 4. 2S2P1D and WLF constants of the global LVE behaviour for the 3 cases studied.

Configuration	E_{00} *(MPa)*	E_0 *(MPa)*	δ	k	h	β	$\tau_{E15°C}$ *(s)*	C_1	C_2
Longitudinal mode of the cylinder	100	35 300	2.01	0.169	0.500	250	0.0758	28	198.1
Flexural mode of the cylinder	100	35 000	2.27	0.172	0.543	250	0.1170	34.6	244.8
Flexural mode of the disc	100	35 000	2.10	0.170	0.510	250	0.0879	29.5	207.4

4.3 Comparison with the reference material

The complex modulus obtained from the back calculation optimization process was compared to the

complex modulus of the reference material. The master curves at 15°C for the relative difference in % (respectively in °) between the norm (respectively the phase angle) of the complex modulus of the global LVE behaviour and the norm (respectively the phase) of the complex modulus of the reference material are presented in figure 12a (respectively 12b) for the three considered configurations.

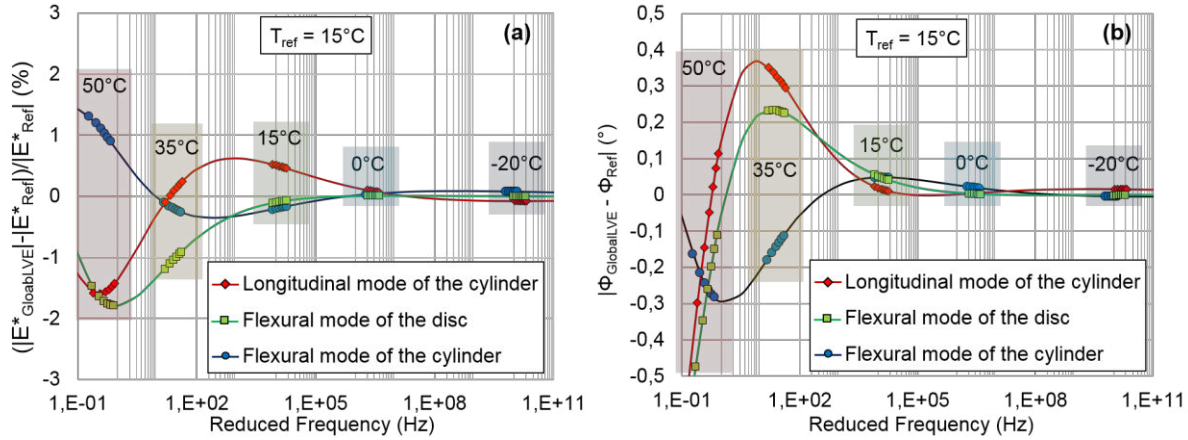

Figure 12. Master curves at 15°C for the three cases studied. (a) relative difference between the norm of the complex modulus of the back calculated LVE behaviour and the norm of the complex modulus of the reference material; (b) difference between the phase angle of the complex modulus of the back calculated LVE behaviour and the phase angle of the complex modulus of the reference material.

The maximum relative difference for the norm of the complex modulus is about 2% while it is approximately 0.5° for the phase angle. Moreover, for temperature below 15°C, corresponding to reduced frequencies higher than 1 kHz, there is almost no relative difference. These results validate the proposed back calculation procedure using the FRFs and the different steps detailed in this paper. The optimization process and the determination of global LVE behaviour introduce almost no bias effect for the material characterization. It is therefore possible to characterize completely and accurately the LVE behaviour of AM from FRFs measurements. Nevertheless, it is important to note that this study is based on FEM simulations of the FRFs and do not use experimental measurements. Other effects such as nonlinearities or experimental errors may introduce some deviations when applying this method to experimental results from complex modulus tests.

5. CONCLUSION

A process to characterize the LVE behaviour of asphalt mixes from FRFs was applied to a pure LVE reference material having averaged properties. This process includes two main steps. In the first step,

an optimization process is used to back calculate the LVE properties of the material at 5 different temperatures using the numerical FEM. In the second step, the back-calculated complex modulus values at each temperature are used to fit a unique 2S2P1D model and to obtain the two constants of the WLF law, which provides the global LVE behaviour of the material. This process was tested on three different modes (longitudinal and flexural modes for a cylinder and flexural mode for a disc) and the results were compared to the input reference material behaviour. For all the temperatures and all the configurations, the convergence toward the reference FRF is quite good. This demonstrates the efficiency of the process to optimize the FRFs. Moreover, it is also shown that the global LVE behaviour determined in the second step is in very good agreement with the LVE behaviour of the reference material. The maximum relative error is about 2% for the norm of the complex modulus and about 0.5° for the phase angle of the complex modulus. This study confirms the pertinence and the validity of the proposed optimisation back calculation method that appears as promising for application considering real experimental data. As the optimisation process is validated on the presented numerical purely LVE behaviour, possible differences obtained from tension-compression tests data should be due to other effects, such as experimental errors when measuring the FRFs or nonlinearity of AM.

REFERENCES

1. Halvorsen, W.G. & Brown, D.L. (1977). Impulse technique for structural response frequency testing. *Journal of Sound and Vibration, Nov. 1977,* 8-21.
2. ASTM: C215-08. (2008). *Standard Test Method for Fundamental Transverse, Longitudinal and Torsional Frequencies of Concrete Specimens*. West Conshoshocken: ASCE
3. Migliori A. & Sarrao, J. (1997). Resonant ultrasound spectroscopy-applications to physics, materials measurements and nondestructive evaluation. *Wiley-Interscience publication, New-York*.
4. Renault, A., Jaouen, L. & Sgard, F. (2010). Characterization of elastic parameters of acoustical porous materials from beam bending vibrations. *Journal of Sound and Vibration, 330*, 1950-1963.
5. Di Benedetto, H., Sauzéat, C., & Sohm, J. (2009). Stiffness of bituminous mixtures using ultrasonic wave propagation. *Road Materials and Pavement Design, 10*(4), 789-814.
6. Mounier, D., Di Benedetto, H., & Sauzéat, C. (2012). Determination of bituminous mixtures linear properties using ultrasonic wave propagation. *Construction and Building Materials, 36,* 638-647.
7. Norambuena-Contreras, J., Castro-Fresno, D., Vega-Zamanillo, A., Celay, M., Lombillo-Vozmediano, I. (2010). Dynamic modulus of asphalt mixture by ultrasonic direct test. *NDT and E International, 43*(7), 629-634.
8. Kweon G. & Kim Y. R. (2006). Determination of the complex modulus of asphalt concrete using the impact resonance test. *Journal of Transportation Research Board, 1970*, 151-160.
9. Lacroix, A., Kim, Y.R. & Far, M.S.S. (2009). Constructing the dynamic modulus mastercurve using impact resonance testing. *Association of asphalt paving technologists, 78*, 67-102.
10. Whitmoyer, S.L. & Kim, Y.R. (1994). Determining asphalt concrete properties via the impact resonant method. *Journal of Testing Evaluation, 22*(2), 139-148.

11. Gudmarsson, A., Ryden, N. & Birgisson, B. (2012a). Application of resonant acoustic spectroscopy to asphalt concrete beams for determination of the dynamic modulus. *Materials and Structures, 45(12),* 1903-1913.
12. Leisure, R., & Willis, F. (1997). Resonant ultrasound spectroscopy. *Journal of Physics: Condensed Matter, 9*, 6001-6029.
13. Ostrovsky, L., Lebedev, A., Matveyev, A., Popatov, A., Sutin, A., Soustova, I & Johnson, P. (2001). Application of three-dimensional resonant acoustic spectroscopy method to rock and building materials. *Journal of acoustical society of America, 110(4)*, 1770-1777.
14. Ryden, N. (2011). Resonant frequency testing of cylindrical asphalt samples. *European Journal of Environmental and Civil Engineering, 15*, 587-600.
15. Ren, Z., Atalla, N. & Ghinet, S. (2011). Optimization based identification of the dynamic properties of linearly viscoelastic materials using vibrating beam techniques. *ASME Journal of Vibration and Acoustics*, 133(4), 1-12.
16. Rupitsch, S.J., Ilg, J. Sutor, a., Lerch, R. & Döllinger, M. (2011). Simulation based estimation of dynamic mechanical properties for viscoelastic materials used for vocal fold models. *Journal of Sound and Vibration, 330*, 4447-4459.
17. Gudmarsson, A., Ryden, N. & Birgisson, B. (2012b). Characterizing the Complex Modulus and Poisson's ratio of Asphalt Concrete Specimens through Modal Testing. *Journal of acoustical society of America, 132(4)*, 2304-2312.
18. Gudmarsson, A., Ryden, N., Di Benedetto, H., Sauzéat, C., Tapsoba N. & Birgisson, B. (2014). Comparing Linear Viscoelastic Properties of Asphalt Concrete Measured by Laboratory Seismic and Tension-Compression Tests. *Journal of nondestructive evaluation, 33(4)*, 571-582.
19. Gudmarsson, A., Ryden, N., Di Benedetto, H. & Sauzéat, C. (2015). Complex modulus and complex Poisson's ratio from cyclic and dynamic modal testing of asphalt concrete. *Construction and Building Materials, 88*, 20-31.
20. Carret, J-C., Pedraza, A., Di Benedetto, H. & Sauzéat, C. (2018). Comparison of the 3-dim linear viscoelastic behavior of asphalt mixes determined with tension-compression and dynamic tests. *Construction and Building materials, 174*, 529-536.

21. Carret, J-C., Di Benedetto, H. & Sauzéat, C. (2018). Multi-modal dynamic linear viscoelastic back analysis for asphalt mixes. *Journal of Nondestructive evaluation, 37:35*.

22. Mangiafico, S., Di Benedetto, H., Sauzéat, C., et al. (2013). Influence of reclaimed asphalt pavement content on complex modulus of asphalt binder blends and corresponding mixes: experimental results and modelling. *Road Materials and Pavement Design, 14*(S1), 132-148.

23. Mangiafico, S., Di Benedetto, H., Sauzéat, C., et al. (2015). Statistical analysis of the influence of RAP and mix composition on viscoelastic and fatigue properties of asphalt mixes. *Materials and structures, 48*(4), 1187-1205.

24. Nguyen, H.P., Di Benedetto, H., Sauzéat, C., et al. (2015). Reclaimed asphalt pavement and additives' influence on 3D linear behavior of warm mix asphalts. *Road Materials and Pavement Design, 16*(3), 569-591.

25. Nguyen, H.P., Di Benedetto, H., Sauzéat, C., et al. (2015). Analysis and modeling of 3D complex modulus tests on hot and warm bituminous mixtures. *Mechanics of time-dependent materials, 19*(2), 167-186.

26. Nguyen, Q. T. (2011). Comportement thermomécanique des enrobés bitumineux sous sollicitations cycliques dans les domaines linéaires et non-linéaire. Ph.D. Thesis, University of Lyon, ENTPE, France.

27. Nguyen, Q. T., Di Benedetto, H., Sauzéat, C., & Tapsoba, N. (2013). Time-temperature superposition principle validation for bituminous mixes in the linear and nonlinear domain. *ASCE Journal of Materials in Civil Engineering, 25*(9), 1181-1188.

28. Viet, P.C., Di Benedetto, H., Sauzéat, C., Lesueur, D., Pouget, S., Olard, F., Dupriet, S. (2017). Complex modulus and fatigue resistance of bituminous mixtures containing hydrated lime. *Construction and Building Materials, 139,* 24-33.

29. Di Benedetto, H., Olard, F., Sauzéat, C., & Delaporte, B. (2004). Linear viscoelastic behavior of bituminous materials: From binders to mixtures. *Road Materials and Pavement Design, 5*(S1), 163-202.

30. Olard, F., & Di Benedetto, H. (2003). General 2S2P1D model and relation between the linear viscoelastic behaviors of bituminous binders and mixes. *Road Materials and Pavement Design, 4*(2), 185-224.

31. Tiouajni, S., Di Benedetto, H., Sauzéat, C. & Pouget, S. (2011). Approximation of linear viscoelastic model in the 3 dimensional case with mechanical analogues of finite size – Application to bituminous materials. *Road Materials and Pavement Design, 12(4)*, 897-930.

32. Nguyen, H. M., Pouget, S., Di Benedetto, H., & Sauzéat, C. (2009). Time-temperature superposition principle for bituminous mixtures. *European Journal of Environmental and Civil Engineering, 13*(9), 1095-1107.

33. Nguyen, M. L., Sauzéat, C., Di Benedetto, H., & Tapsoba, N. (2013). Validation of the time–temperature superposition principle for crack propagation in bituminous mixtures. *Materials and structures, 46*(7), 1075-1087.

34. Nguyen, Q. T., Di Benedetto, H., Sauzéat, C., & Tapsoba, N. (2013). Time-temperature superposition principle validation for bituminous mixes in the linear and nonlinear domain. *ASCE Journal of Materials in Civil Engineering, 25*(9), 1181-1188.

35. Ferry, J. D. (1980). *Viscoelastic properties of polymers* (3rd ed.). New York, NY: John Wiley & Sons.

36. Di Benedetto, H., Delaporte, B., & Sauzéat, C. (2007). Three dimensional linear behavior of bituminous materials: Experiments and modeling. *ASCE International Journal of Geomechanics, 7*(2), 149-157.

37. Pedraza, A. (2018). Propriétés thermomécaniques d'enrobés multi-recyclés. Ph.D. Thesis, University of Lyon, ENTPE, France.

38. Royis, P., Seignol, J.F. (1999) Finite element simulation of the thermoviscoplastic behaviour of bituminous concrete. *International Journal for Numerical and Analytical Methods in Geomechanics, 23*(7), 595-627.

39. Cannone Falchetto, A., Moon, K-H., Lee, C.B., Wistuba, M.P. (2017). Correlation of low temperature fracture and strength properties between SCB and IDT tests using a simple 2D FEM approach. *Road Materials and Pavement Design, 18*(sup2), 329-338.

40. Taherkhani, H., Jalali, M. (2016). Investigating the performance of geosynthetic-reinforced asphaltic pavement under various axle loads using finite-element method. *Road Materials and Pavement Design, 18*(5), 1200-1217.

41. Yesuf, G.Y., Hoff, I. (2015). Finite element modelling for prediction of permanent strains in fine-grained subgrade soils. *Road Materials and Pavement Design, 16*(2), 392-404.

42. You, L., Yan, K., Hu, Y., Liu, J., Ge, D. (2016). Spectral element method for dynamic response of transversely isotropic asphalt pavement under impact load. *Road Materials and Pavement Design, 19*(1), 223-238

43. Pouget, S., Sauzéat, C., Di Benedetto, H. & Olard, F. (2012). Modeling of viscous bituminous wearing course materials on orthotropic steel deck. *Materials and Structures, 45*(7), 1115-1125.

44. Yi, J.H., Mun, S. (2009) Backcalculating pavement structural properties using a Nelder–Mead simplex search. *International Journal for Numerical and Analytical Methods in Geomechanics, 33,* 1389-1406.

45. Levenberg E. (2012) Inverse analysis of viscoelastic pavement properties using data from embedded instrumentation. *International Journal for Numerical and Analytical Methods in Geomechanics, 37,* 1016-1033.

Paper V : Characterization of asphalt mixes behaviour from dynamic testing and comparison with conventional complex modulus tests

CARRET JEAN-CLAUDE

DI BENEDETTO HERVE

SAUZEAT Cédric

Published in

Applied Sciences 8(11) (2018) - Special Issue "Achievements and Prospects of Advanced Pavement Materials Technologies"

https://doi.org/10.3390/app8112117

applied sciences

MDPI

Article

Characterization of Asphalt Mixes Behaviour from Dynamic Tests and Comparison with Conventional Cyclic Tension–Compression Tests

Jean-Claude Carret *, Hervé Di Benedetto and Cédric Sauzéat

LTDS (UMR CNRS 5513), University of Lyon/ENTPE, Rue M. Audin, 69518 Vaulx en Velin, France; herve.dibenedetto@entpe.fr (H.D.B.); cedric.sauzeat@entpe.fr (C.S.)

* Correspondence: jean-claude.carret@entpe.fr

Received: 16 October 2018; Accepted: 29 October 2018; Published: 1 November 2018

Featured Application: Dynamic tests can be used to characterize asphalt mixes and the results obtained from dynamic tests are in good agreement with the results of conventional cyclic tests.

Abstract: In the presented research, conventional cyclic tension–compression tests and dynamic tests were performed on two types of asphalt mixes (AM). For the tension–compression tests, the complex modulus was obtained from the measurements of the axial stress and axial strain. For the dynamic tests, an automated impact hammer equipped with a load cell and an accelerometer were used to obtain the frequency response functions (FRFs) of the specimens at different temperatures. Two methods were proposed to back-calculate the complex modulus from the FRFs at each temperature: one using the 2S2P1D (two springs, two parabolic elements and one dashpot) model and the other considering a constant complex modulus. Then, a 2S2P1D linear viscoelastic model was calibrated to simulate the global linear viscoelastic behaviour back calculated from each of the proposed methods of analysis for the dynamic tests, and obtained from the tension–compression test results. The two methods of analysis of dynamic tests gave similar results. Calibrations from the tension–compression and dynamic tests also show an overall good agreement. However, the dynamic tests back analysis gave a slightly higher value of the norm of the complex modulus and a lower value of the phase angle compared to the tension–compression test data. This result may be explained by the nonlinearity of AM (strain amplitude is at least 100 times smaller for dynamic tests) and/or by ageing of the materials during the period between the tension–compression and the dynamic tests.

Keywords: asphalt mixes; linear viscoelasticity; complex modulus; dynamic measurements; tension–compression tests; frequency response function; back-analysis; finite element method

1. Introduction

Asphalt mixes (AM) have a linear viscoelastic (LVE) behaviour in the small strain domain [1] Cyclic tension–compression tests are traditionally used to determine the LVE properties of AM that are strongly dependent on frequency and temperature. However, these tests require expensive experimental devices such as hydraulic presses and are not applicable in situ. An economical alternative is to use non-destructive dynamic tests that are simple to perform and possibly adaptable for measurements on pavement structures. Impulse techniques using impact loadings [2,3] are known to provide accurate characterization of material properties in the case of elastic materials [4,5]. In the case of LVE materials, dynamic tests could be a great alternative to conventional cyclic tension–compression tests. Dynamic tests using wave propagation and measurement of the flying time [6–8] have been applied to LVE materials. Resonance testing considering only the fundamental

resonance frequency [9–11] or resonant acoustic spectroscopy (RAS) [12–15] have also been applied to AM but it is not possible to describe accurately the frequency dependency behaviour of AM with these different tests. Recently, measurement of frequency response functions (FRFs) have been performed on LVE materials [16,17] and more specifically on AM [18–21]. Gudmarsson et al. [19,20] and Carret et al. [21] showed that using FRFs measurements to derive the LVE properties of AM is a very promising approach. However, characterizing accurately the LVE behaviour of AM from FRFs is not possible through a simplified analysis [22] and it requires an elaborate approach. In this paper, two different methods using finite element calculations are proposed to obtain the LVE behaviour from FRFs. The first method consists in an optimization of the continuous spectrum 2S2P1D (two springs, two parabolic elements and one dashpot) model constants to back-calculate the complex modulus at each tested temperature while the second method is a more direct back-calculation of the complex modulus at the first resonance frequency. The two methods were applied to two different types of AM representing five specimens that were tested with cyclic tension–compression tests and with dynamic tests. Experimental complex modulus values obtained from tension–compression tests and back-calculated from FRFs with the two proposed methods were used to fit the 2S2P1D model and the Williams-Landel-Ferry (WLF) constants simulating the global LVE behaviour of the material in each case. First, the materials tested in this study are presented. Then, the LVE behaviour characterization with cyclic tests and the modelling with the 2S2P1D model are introduced. Next, dynamic tests are introduced and the two proposed back-analysis methods are explained. Finally, data from tension–compression tests are compared with results from the two methods of back-analysis of the dynamic tests.

2. Materials and Methods

Two different types of AM are considered in this paper. The first material is a warm mix that was fabricated in laboratory using bitumen foam and labelled WF for warm foam. It contains 70% of reclaimed asphalt pavement (RAP) after one cycle of recycling. This material was used in a project from the French national research agency called IMPROVMURE [23]. Three specimens of this material were tested with tension–compression and dynamic tests. The second material is a mix with an optimized granular skeleton also fabricated in laboratory and labelled GB5. It contains 30% of RAP and the bitumen used is a polymer modified bitumen (PMB). Two specimens of this material were tested with tension–compression tests and dynamic tests. Table 1 gives some indications on the five studied specimens. The tension–compression tests were performed first and the dimensions listed in Table 1 correspond to the dimensions after the specimens were cut (see Section 3.1) before performing the dynamic tests.

Table 1. Specimens used in this study.

Specimen	Mass (g)	Height (mm)	Diameter (mm)	Density (kg/m^3)	Void Ratio (%)	Bitumen Content (%)	RAP Content (%)
WF-4	1293	0.123	75	2379	6.6	5.4	70
WF-6	1320	0.123	75	2431	4.2	5.4	70
WF-8	1330	0.123	75	2449	3.8	5.4	70
GB5-3	941	0.152	64	2381	4.8	4.8	30
GB5-4	951	0.152	64	2378	5.1	4.8	30

3. Characterization of the Linear Viscoelastic (LVE) Behaviour

3.1. Cyclic Tension–Compression Tests

Cyclic tension–compression tests were first performed to determine the complex modulus and complex Poisson's ratio of the five considered cylindrical specimens. A hydraulic press was used in strain-controlled mode to apply cyclic sinusoidal axial loadings with an amplitude of around 50 µm/m. The axial stress σ_z was measured with a load cell, the axial strain ε_z was obtained from the average of

three extensometers placed at 120° from each other, and the radial strain ε_r was derived from the measurements of two non-contact sensors. The procedure developed at ENTPE/University of Lyon laboratory is detailed in other publications [24–26]. The complex notation of the axial stress, the axial strain and the radial strain are given in Equation (1):

$$\begin{aligned} \sigma_z^* &= \sigma_{0z} \cdot e^{j\omega t} \\ \varepsilon_z^* &= \varepsilon_{0z} \cdot e^{j(\omega t + \varphi_{\varepsilon z})} \\ \varepsilon_r^* &= \varepsilon_{0r} \cdot e^{j(\omega t + \varphi_{\varepsilon r})} \end{aligned} \quad (1)$$

where ω is the pulsation ($\omega = 2\pi f$, where f is the frequency), σ_{0z} is the norm of the complex axial stress and ε_{0z} and $\varphi_{\varepsilon z}$ (respectively, ε_{0r} and $\varphi_{\varepsilon r}$) are the norm and phase angle of the complex axial strain (respectively, complex radial strain). The tension–compression tests were performed at eight loading frequencies (0.003, 0.01, 0.03, 0.1, 0.3, 1, 3 and 10 Hz) and nine temperatures from −25 °C to 55 °C in steps of 10 °C. Details of the experimental set up are shown in Figure 1. The complex modulus (respectively, complex Poisson's ratio) are defined as the ratio between the axial stress and the axial strain (respectively, the opposite of the radial strain and the axial strain) and they are calculated at each temperature and frequency as follow:

$$E^* = \frac{\sigma_z^*}{\varepsilon_z^*} = |E^*| \cdot e^{j\varphi_E} \quad (2)$$

$$\nu^* = -\frac{\varepsilon_r^*}{\varepsilon_z^*} = |\nu^*| \cdot e^{j\varphi_\nu} \quad (3)$$

where E* is the complex modulus, φ_E is the phase angle of the complex modulus, ν^* is the complex Poisson's ratio and φ_ν is the phase angle of the complex Poisson's ratio.

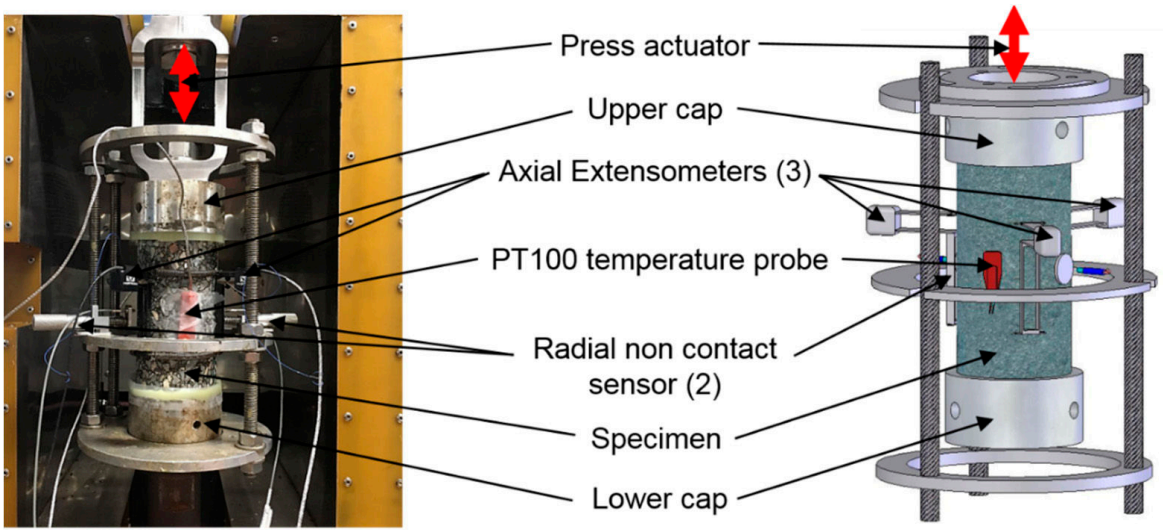

Figure 1. Tension–compression test set-up (ENTPE laboratory, University of Lyon).

3.2. Modelling of the LVE Behaviour: 2S2P1D Rheological Model

The continuous spectrum 2S2P1D model developed at ENTPE [27–29] was used to model the LVE behaviour of AM. This model is the association in series of two springs, two parabolic creep elements and one dashpot. In the three-dimension case [30], the expressions of the complex modulus and the complex Poisson's ratio, for isotropic behaviour, are given at a given reference temperature (Tref), by Equations (4) and (5), respectively.

$$E^*_{2S2P1D}(\omega) = E_{00} + \frac{E_0 - E_{00}}{1 + \delta(j\omega\tau_E)^{-k} + (j\omega\tau_E)^{-h} + (j\omega\beta\tau_E)^{-1}} \quad (4)$$

$$\nu^*_{2S2P1D}(\omega) = \nu_{00} + \frac{\nu_0 - \nu_{00}}{1 + \delta(j\omega\tau_\nu)^{-k} + (j\omega\tau_\nu)^{-h} + (j\omega\beta\tau_\nu)^{-1}} \quad (5)$$

where ω is the pulsation ($\omega = 2\pi f$, where f is the frequency), E_0 and ν_0 are the high frequency modulus and Poisson's ratio, E_{00} and ν_{00} are the low frequency modulus and Poisson's ratio, k and h are dimensionless constants such as $0 < k < h < 1$, δ is a dimensionless constant, and β is a dimensionless constant related to Newtonian viscosity η by $\eta = (E_0 - E_{00})\,\beta\tau_E$. τ_E and τ_ν are characteristic time constants of the complex modulus and Poisson's ratio linked by a constant ratio. The values of the characteristic times vary only with temperature. The time temperature superposition principle (TTSP) is verified for asphalt mixes in the linear and nonlinear domains [31–33] so it is possible to calculate the characteristic time at any given temperature using Equation (6):

$$\tau(T) = a_T(T)\tau_{ref} \quad (6)$$

where τ_{ref} is the characteristic time at the reference temperature (τ_E or τ_ν) and a_T is the shift factor at the temperature T defined by the Williams–Landel–Ferry (WLF) equation [34]:

$$\log(a_T) = -\frac{C_1(T - T_{ref})}{C_2 + T - T_{ref}} \quad (7)$$

where C_1 and C_2 are the two constants of the WLF equation and T_{ref} is the reference temperature.

4. Dynamic Tests

4.1. Measurement of the Frequency Response Functions (FRFs)

First, the specimens used for complex modulus tension–compression test were sawed to separate the glued upper and lower metallic caps before performing the dynamic measurements. An impact hammer equipped with a load cell (PCB model 086E80) was used as an external source of excitation. The order of magnitude of the maximum strain induced in the specimen by the impact is of about 0.1 µm/m [18,21]. The impact hammer was automated with a solenoid piston programmed with a microcontroller (Arduino Uno R3) to improve the repeatability of the test and to allow measurements directly inside a thermal chamber. This automated system was inspired by systems previously developed by Norman et al. in 2012 and Brüggemann et al. in 2015 [35,36]. The response of the materials was recorded with an accelerometer (PCB model 353B15). The impact hammer and the accelerometer were connected to a signal conditioner (PCB model 482C15) and the signal conditioner was connected to a data acquisition device (NI USB-6356) connected to a computer. To achieve free boundary conditions, soft foam was placed under the specimens during the tests. In this study, only the longitudinal compression mode of vibrations was considered. For this mode of vibrations, the impact is applied in the centre of one short side of the cylinder while the acceleration is measured in the centre of the opposite short side. The experimental set up for the dynamic tests corresponding to the longitudinal mode of vibrations is presented in Figure 2.

The measurements were recorded with a sampling frequency of 1 MHz by using a MATLAB application which was specifically developed for this test. Measurements were performed at five temperatures (−20, 0, 15, 35 and 50 °C) and five impacts were applied at each temperature. The applied force and the acceleration were recorded for each impact. The experimental data in time domain were then converted in frequency domain with a 1 Hz resolution using the Fast Fourier Transform (FFT). Figure 3 shows an example of the signals in time and frequency domains for specimen GB5-3 at 14.7 °C (measured temperature with a probe at the surface of the specimen).

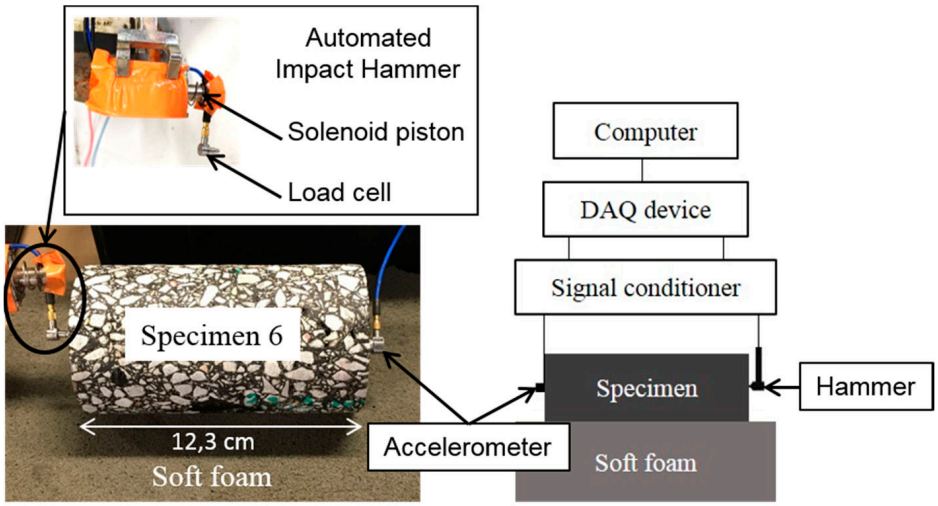

Figure 2. Test set up for the dynamic impact tests (example for specimen WF-6, ENTPE laboratory, University of Lyon).

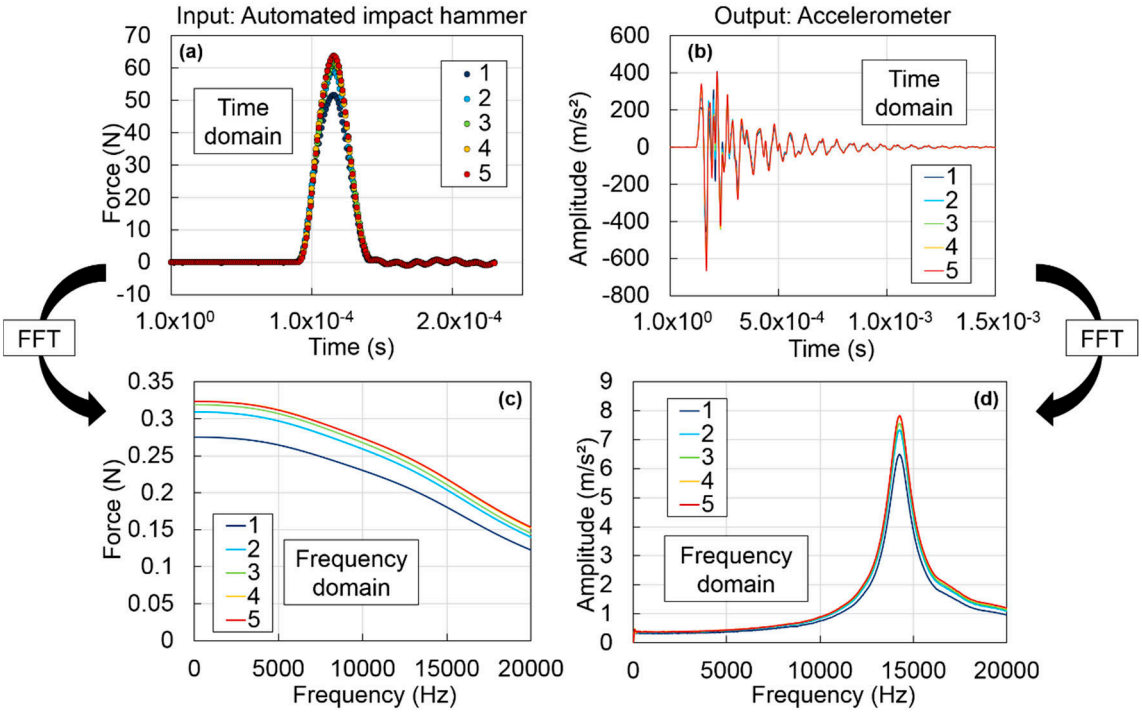

Figure 3. Dynamic test experimental data for specimen GB5-3 at 14.7 °C (5 hits): (**a**) force in time domain; (**b**) acceleration in time domain; (**c**) force in frequency domain; and (**d**) acceleration in frequency domain.

As shown in Figure 3, the frequency spectrum of the impact contains energy up to 20 kHz, which is the maximum frequency considered for the calculations of frequency response functions (FRFs) in this study. FRFs were calculated from the frequency domain signals as follow:

$$H(f) = \left(\overline{Y(f) \cdot X*(f)}\right) / \left(\overline{X(f) \cdot X*(f)}\right) \quad (8)$$

where H is the FRF, Y is the FFT of the measured acceleration, X is the FFT of the applied force, X* is the complex conjugate of the applied force and the bar above corresponds to the arithmetic

average from the five impacts. The five FRFs corresponding to each of the five impacts and the averaged FRF (Equation (8)) for specimen GB5-3 at 14.7 °C are displayed on Figure 4. Figure 4 shows that the six FRFs overlaps, which confirms the very good repeatability of the test.

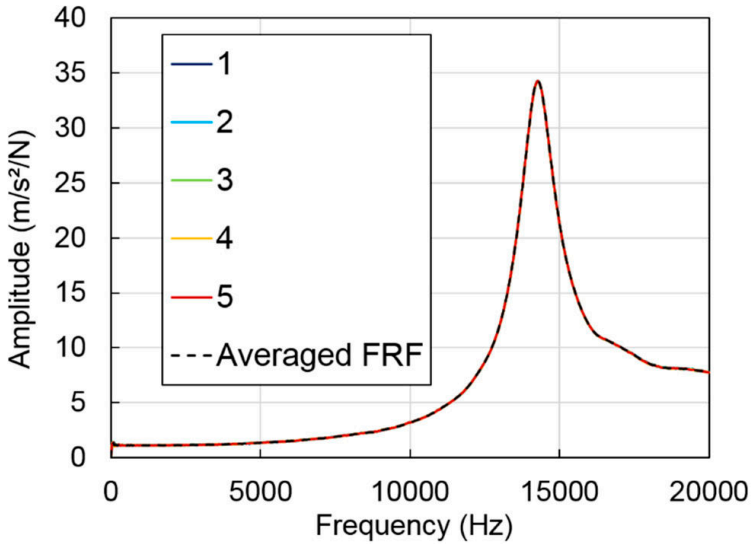

Figure 4. FRFs obtained for the 5 hits and averaged FRF (Equation (8)) of specimen GB5-3 at 14.7 °C.

Quality of the measurements was also checked with the coherence function. The coherence is a value between 0 and 1 that indicates how much of the vibratory response recorded with the accelerometer is due to the impact. For a value of 1, the response is fully explained by the impact while decreasing values indicate that something has disrupted the test. Coherence function is calculated according to Equation (9):

$$\mathrm{CF(f)} = \left(\overline{\mathrm{X*(f)\cdot Y}(f)}\right)^2 / \left(\left(\overline{\mathrm{X(f)\cdot X*(f)}}\right)\cdot\left(\overline{\mathrm{Y(f)\cdot Y*(f)}}\right)\right) \quad (9)$$

where CF is the coherence function, Y and Y* are the FFT of the measured acceleration and its complex conjugate, X and X* are the FFT of the applied force and its complex conjugate and the bar above corresponds to the arithmetic average. The coherence functions of specimen GB5-3 for the five tested temperatures are presented in Figure 5. For all temperatures, the coherence function is very good with values close to one for frequencies higher than 1000 Hz. It is therefore recommended to not use the frequencies below 1000 Hz.

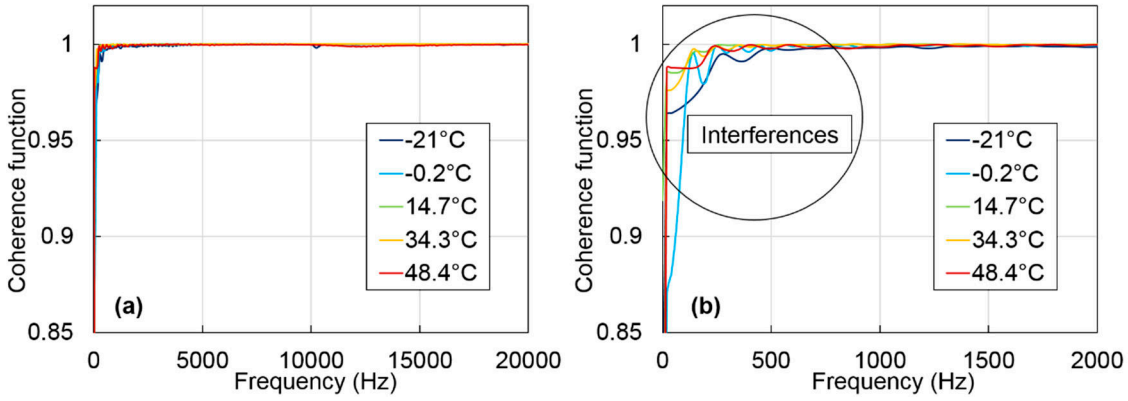

Figure 5. Coherence functions obtained for specimen GB5-3 at the five tested temperatures (**a**); and zoom on the lower frequencies (**b**).

4.2. Calculation of FRFs with the Finite Element Method (FEM)

Numerical FRFs were calculated with the finite element method (FEM) considering linear viscoelastic behaviour and the dynamic test boundary conditions. Figure 6 shows the FEM mesh and boundary conditions used for the FEM calculation of the FRFS.

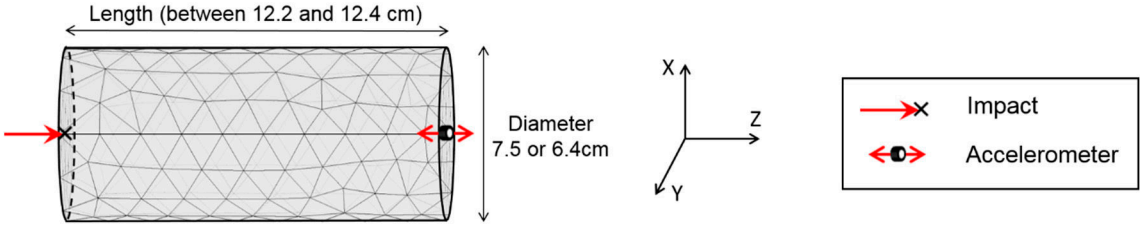

Figure 6. Finite element mesh and boundary conditions used for the FEM calculation of the FRFS.

FRFs were calculated at the desired frequencies by resolving the following three-dimensional equation of motion in frequency domain:

$$-\rho\omega^2\mathbf{u} - \nabla\cdot\sigma = 0 \tag{10}$$

where ρ is the bulk density of the material, ω is the angular frequency, $\mathbf{u}$ is the displacement vector, ∇ is the gradient tensor operator and σ is the Cauchy stress tensor. Free boundary conditions are assumed to solve Equation (10) except at the impact point where a cyclic load $e^{i\omega t}$ is applied in the direction of the impact. Since the load amplitude is unity, the calculated FRFs correspond to the calculated acceleration in direction Z (direction of vibration of the accelerometer in physical tests). Back analysis was performed considering two LVE behaviour models successively, as explained below.

4.3. Determination of the Material LVE Properties from Dynamic Tests

The LVE properties of the material were determined from the FRFs measured with the dynamic tests in two steps. The first step is a back-calculation of the complex modulus of the material at each tested temperature. Two methods, presented in the next sections, were used for this purpose. They consist in optimizing the constants of the LVE model used to calculate FRFs so that calculated FRFs match the experimental measured FRFs using dynamic tests at the considered temperature. The second step, which is the same for the two proposed methods, consists in using the complex modulus values determined in the first step at each temperature to fit a 2S2P1D model and a WLF law simulating the global LVE behaviour of the material. This operation is similar to what is done with the tension–compression test data.

4.3.1. First Method: Optimization of the 2S2P1D Model Constants to Match Experimental FRFs

Among the 10 constants of the 2S2P1D model, only four constants (E_0, k, δ and τ_E) have a significant influence for the considered range of frequencies involved during dynamic tests and need to be optimized. The complex Poisson's ratio has a very small influence on the calculation of the FRFs below 20 kHz. Poisson's ratio cannot be back-calculated with this procedure; however, it is necessary to assume values for constants ν_{00}, ν_0 and τ_ν to back-calculate the complex modulus at each temperature. For each tested temperature, the vector X of the four constants (E_0, k, δ and τ_E) to be identified was optimized iteratively so that the calculated FRFs match the experimental FRFs. The values of the six other constants were fixed to classical values for AM: E_{00} = 100 MPa, ν_0 = 0.19, ν_{00} = 0.45, h = 0.53, β = 250 and $\tau_\nu = 31.6\tau_E$. Only the values of the experimental FRFs at frequencies around the resonance frequencies are used as input in the optimization according to previous studies [19–21] that showed

their meaningful importance. Ten frequencies were selected along each resonance peak and the error function to minimize was defined as follow:

$$\text{Error} = \sum_{j=1}^{Npeaks} \sum_{i=1}^{10} \left(\left| \frac{\left|H_{Exp_{ji}}\right| - \left|H_{C_{ji}}\right|}{\left|H_{Exp_{ji}}\right|} \right| \right) \quad (11)$$

where H_{Exp} is the experimental FRF, H_C is the calculated FRF, N_{peaks} is the number of resonance peaks, j is the index of the peak and i is the index of the frequencies. The number of peaks considered for the optimization at each temperature corresponds to the number of peaks that are visible below 20 kHz (maximum considered frequency with our experimental device). This number is given in Table 2 for each temperature.

Table 2. Number of peaks considered for the optimization of the 2S2P1D model constants at each temperature.

Temperature (°C)	−20	0	15	35	50
Number of peaks	1	1	1	1	2

The optimization was performed in MATLAB with the "fminsearch" algorithm and the optimization was stopped when the error and the parameter tolerance of 1% is reached (e.g., when the variation of the error and of all the values of the four constants to be identified is less than 1% between two iterations of the algorithm). The final vector X_f of the four constants (E_0, k, δ and τ_E) was then used with the three fixed constants related to the complex modulus (E_{00}, h, and β) to back-calculate the complex modulus at the resonance frequencies of the peaks used as input for the optimization at the considered temperature. The optimization procedure to identify the four 2S2P1D model constants (E_0, k, δ and τ_E) at each temperature is explained in Figure 7.

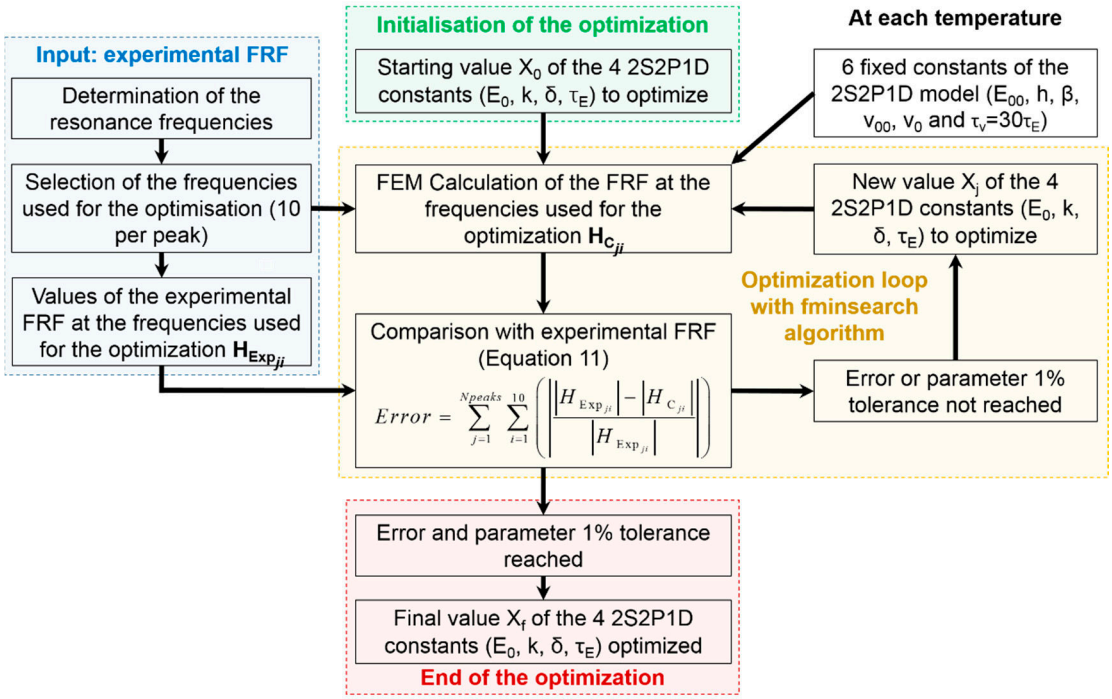

Figure 7. Method 1: Principle of the optimization procedure to identify the four 2S2P1D constants (E_0, k, δ and τ_E) at each temperature. X_f is the final vector of the four 2S2P1D constants to identify.

4.3.2. Second Method: Constant Complex Modulus Obtained from the First Resonance Peak Only

The second method is a simplified approach that does not require, in the first step, a rheological LVE model considering the frequency and temperature dependence. At each tested temperature, a constant complex modulus value and a constant real Poisson's ratio of 0.3 were considered. A numerical sensitivity analysis was performed to evaluate the influence of the norm and phase angle of the complex modulus and the real value of the Poisson's ratio on the calculation of FRFs. The influence of each LVE constant was evaluated from FRFs calculated for five values taken in the range of variation of the considered LVE constant while the two others are fixed. Table 2 lists the five values considered for each LVE constant and the corresponding fixed values of the two others. Some results are shown on Figure 8 for a cylinder with similar dimensions than those used in this study and with a density of 2400 kg/m^3. It is shown in Figure 8 that the norm of the complex modulus has an important influence on the first resonance frequency but not on the amplitude. It is the reverse for the phase of the complex modulus, while Poisson's ratio has little influence on both the frequency and the amplitude.

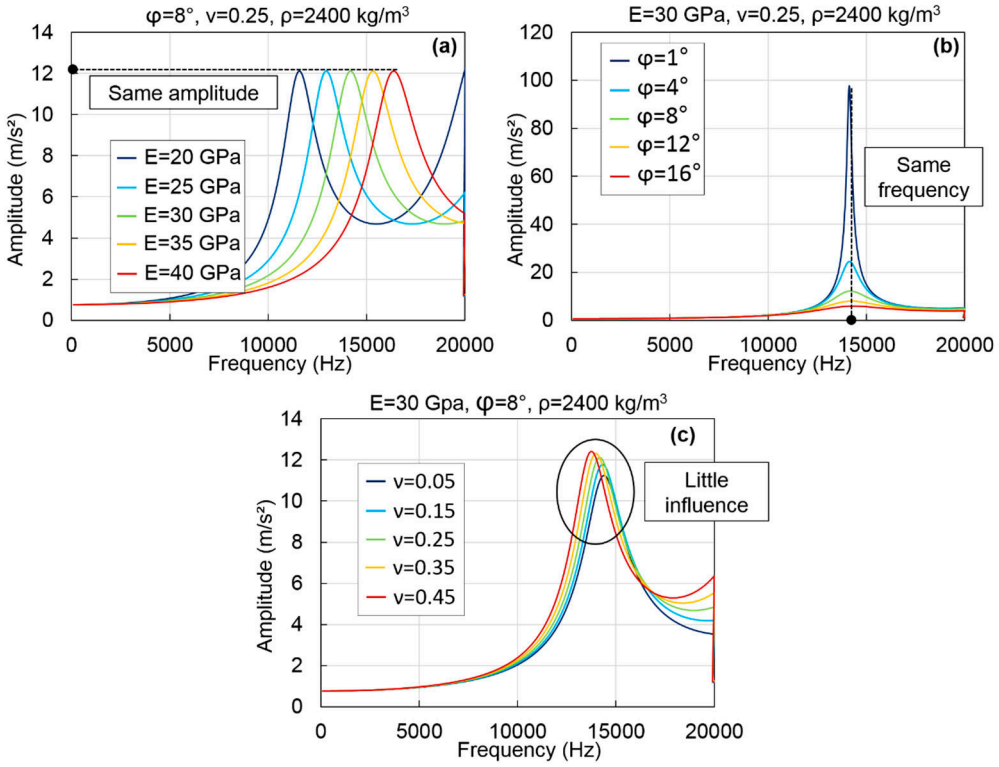

Figure 8. Influence of: E (**a**); φ (**b**); and ν (**c**) on the first peak of the FRFs corresponding to the first resonance (example of calculations for a cylinder with a 7.5 cm diameter and a 12.3 cm length).

To confirm the observation raised in Figure 8, the relative standard deviations (RSD) for the first resonance frequency and amplitude were calculated for the three studied constants. Results are given in Table 3. They confirm the previous observations and also indicate that the norm of the complex modulus has really no impact on the peak amplitude while the phase has a very little influence on the frequency. The Influence of the Poisson's ratio can be considered as negligible when compared with the influence of the two other constants. Observations presented in Figure 8 and Table 3 justify the assumption of a constant real value of 0.3 for the Poisson's ratio. In addition, the identification of the norm and phase of the complex modulus can be separated into two steps: the norm can be determined by dichotomy from the first resonance frequency and then the phase can be determined by dichotomy from the corresponding amplitude. This process was repeated iteratively until the error on

the amplitude is less than 0.1%. Figure 9 shows the principle of the back-calculation of the complex modulus using the first resonance peak of the FRFs.

Table 3. Influence of E, φ and ν on the first resonance frequency and FRF amplitude. When one of the constants varies, the two other constants are fixed at the values listed in the left column.

	E (GPa)	**20**	**25**	**30**	**35**	**40**	**RSD (%)**
φ = 8°	f (Hz)	11,580	12,940	14,180	15,320	16,380	13.5
ν = 0.25	Amplitude (m/s^2)	12.1	12.1	12.1	12.1	12.1	6×10^{-4}
	φ (°)	**1**	**4**	**8**	**12**	**16**	**RSD (%)**
E = 30 GPa	f (Hz)	14,120	14,140	14,180	14,240	14,340	0.6
ν = 0.25	Amplitude (m/s^2)	97.7	24.4	12.1	8.0	5.9	130.8
	ν	**0.05**	**0.15**	**0.25**	**0.35**	**0.45**	**RSD (%)**
E = 30 GPa	f (Hz)	14,400	14,320	14,180	13,980	13,760	1.8
φ = 8°	Amplitude (m/s^2)	11.2	11.8	12.1	12.3	12.4	4.0

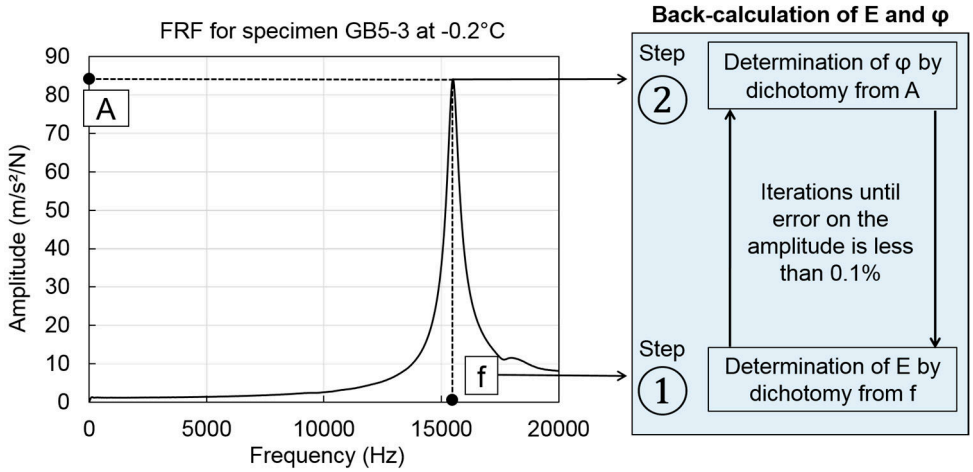

Figure 9. Method 2: Principle of the back-calculation of the complex modulus on the first resonance peak at each temperature (example for specimen GB5-3 at −0.2 °C).

4.3.3. Summary and Remarks on the Two Methods

Differences between the two proposed methods concern the first step in which the complex modulus is back-calculated at each temperature, while the second step is identical for the two methods. First, the assumptions on the Poisson's ratio value are different in the two methods. In the first method, the Poisson's ratio is a complex number, which depends on the frequency and on the temperature, and is modelled with the 2S2P1D model assuming the values of constants ν_{00}, ν_0 and τ_E/τ_ν. In the second method, a constant real value of Poisson's ratio equal to 0.3 is assumed. Another difference is that all resonance peaks under 20 kHz are considered in the first method while only the first resonance peak is used in the second method. Consequently, the second method gives only one value of the complex modulus at each temperature while the first method gives values for each resonance frequency. This difference is not essential in this study since 50 °C is the only temperature for which two peaks were observed. However, it can be interesting to evaluate more than one value of the complex modulus at each temperature. Finally, in the first method, four constants are evaluated at each temperature using a complex algorithm. In the second method, only two constants are evaluated using a simple dichotomy process. The second method is therefore very easy to apply and time-effective compared to the first method. Figure 10 highlights the main differences between the first step of the two methods and gives the principle of the second step that is identical for the two methods. Note that, even though the same constant h is fixed for the back-calculation at each temperature (in the first

step of first method), a different constant h value can be obtained during the calibration process of the second step.

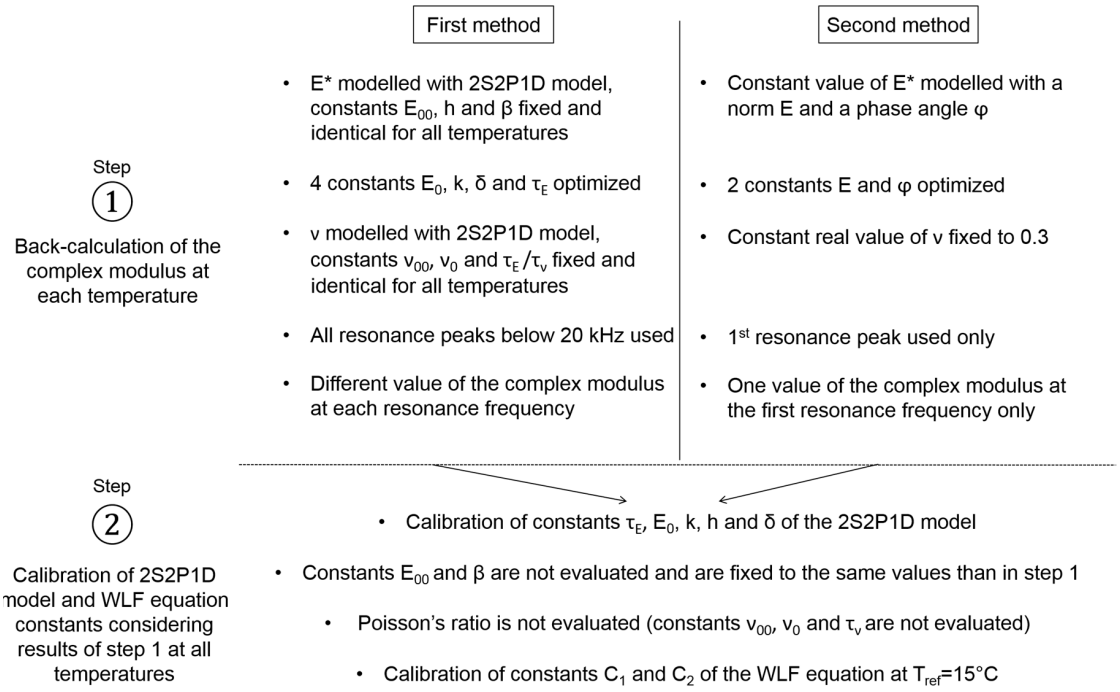

Figure 10. Summary and differences between the two proposed methods of back-analysis of the dynamic tests.

5. Results

5.1. Tension–Compression Tests Results

Results of the tension–compression tests for specimen WF-8 are plotted in Figure 11. A continuous curve can be seen on the Cole–Cole diagram, which indicates that the material is rheologically simple and that the time–temperature superposition principle (TTSP) is valid. The master curve of the norm of the complex modulus is plotted at a reference temperature (T_{ref}) of 15 °C in Figure 11. The 2S2P1D model was fitted to the experimental data and is also plotted in Figure 11. A very good agreement between the experimental data and the 2S2P1D model can be observed.

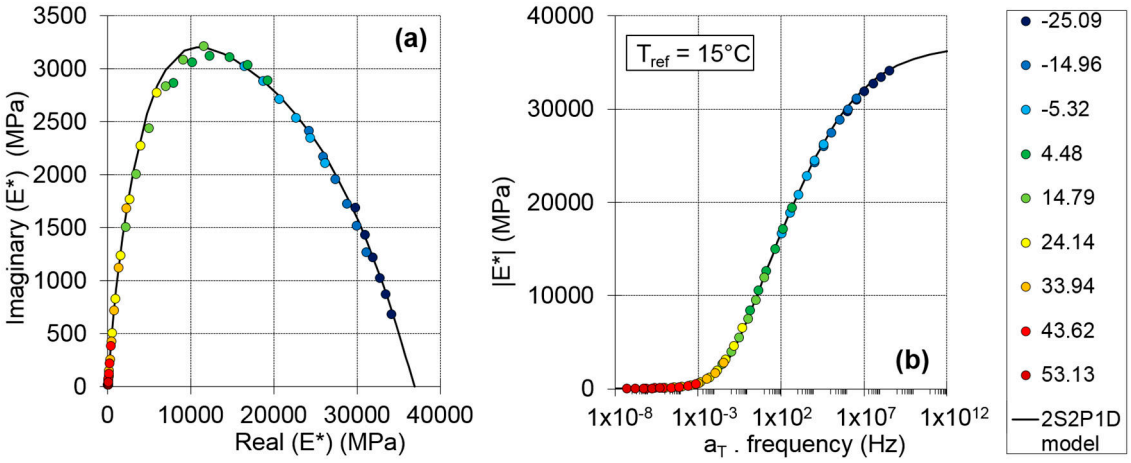

Figure 11. Tension–compression test results and fitted 2S2P1D model for specimen WF-8: (**a**) Cole–Cole diagram; and (**b**) master curve for the norm of the complex modulus at 15 °C.

The values of the 2S2P1D model and WLF equation constants obtained from the tension–compression tests are given for all specimens in Table 4. The constants k, h, δ, β, C_1 and C_2 have the same values for a given material because they are only depending on the bitumen and not on the granular skeleton as shown in previous research [27,37,38].

Table 4. Calibrated 2S2P1D constants to match tension–compression measurements.

Specimen	E_{00} (MPa)	E_0 (MPa)	δ	k	h	β	$\tau_{E15°C}$ (s)	C_1	C_2
WF-4	28	33,400	2.28	0.177	0.57	154	5.4×10^{-2}	24.9	166.6
WF-6	40	37,500	2.28	0.177	0.57	154	7.0×10^{-2}	24.9	166.6
WF-8	56	36,900	2.28	0.177	0.57	154	6.9×10^{-2}	24.9	166.6
GB5-3	65	39,100	1.80	0.180	0.60	350	7.5×10^{-2}	24.7	165.9
GB5-4	65	39,500	1.80	0.180	0.60	350	1.5×10^{-1}	24.7	165.9

The measurements were recorded with a sampling frequency of 1 MHz by using a MATLAB application which was specifically developed for this test. Measurements were performed at five temperatures (−20, 0, 15, 35 and 50 °C) and five impacts were applied at each temperature. The applied force and the acceleration were recorded for each impact. The experimental data in time domain were then converted in frequency domain with a 1 Hz resolution using the Fast Fourier Transform (FFT). Figure 3 shows an example of the signals in time and frequency domains for specimen GB5-3 at 14.7 °C (measured temperature with a probe at the surface of the specimen).

5.2. Dynamic Impact Tests Results

The complex modulus values back-calculated at each temperature from the FRFs measurements with the two proposed methods for specimen WF-8 are plotted, as an example, in Figure 12. For the first method of back-calculation, one value of the complex modulus is plotted for temperatures at which only one peak was considered for the optimization (−20, 0, 15 and 35 °C) and two values are plotted at −50 °C because two peaks exist for this temperature. Only one value of the complex modulus is presented for each temperature for Method 2 because the back-calculation is limited to the first resonance frequency, as explained previously. The master curve of the norm of the complex modulus at 15 °C was obtained considering the validity of the TTSP. The 2S2P1D model was fitted to the back-calculated modulus for both methods and the two resulting 2S2P1D model curves are also plotted in Figure 12. Good fitting of the 2S2P1D curves can be observed for both methods, which give only slightly different results.

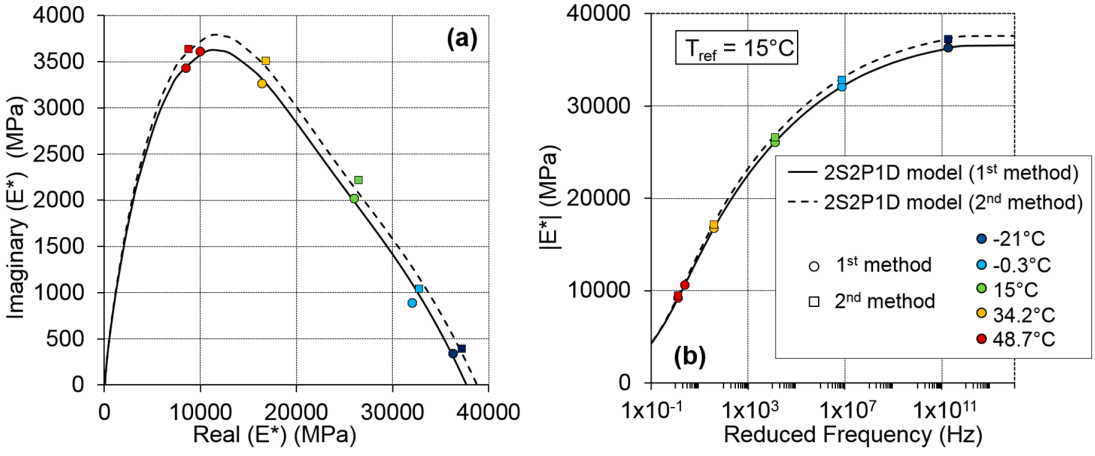

Figure 12. Dynamic test results and fitted 2S2P1D model curve for the two analysis methods for specimen WF-8: (**a**) Cole–Cole diagram; and (**b**) master curve for the norm of the complex modulus at 15 °C.

The values of the 2S2P1D model and WLF equation constants fitting the results from the two back-analysis methods are given for all specimens in Table 5 (first method) and Table 6 (second method). Note that similarly to the results of the tension–compression tests, constants k, h, δ, β, C_1 and C_2 have the same values for a given material. In addition, the same WLF equation constants can be used for the two methods and only constant E_0 differs between the first and the second method.

Table 5. Calibrated 2S2P1D constants to match complex modulus back-calculated from dynamic tests with the first method using 2S2P1D model at each temperature. Constants E_{00} and β are assumed to be 100 MPa and 250, respectively.

Specimen	E_{00} (MPa)	E_0 (MPa)	δ	k	h	β	$\tau_{E15°C}$ (s)	C_1	C_2
WF-4	100	34,800	1.39	0.142	0.49	250	4.0×10^{-2}	18.9	133.2
WF-6	100	38,700	1.39	0.142	0.49	250	7.0×10^{-2}	18.9	133.2
WF-8	100	37,500	1.39	0.142	0.49	250	4.0×10^{-2}	18.9	133.2
GB5-3	100	39,100	1.17	0.130	0.442	250	5.5×10^{-2}	19.2	139.5
GB5-4	100	40,500	1.17	0.130	0.442	250	7.0×10^{-2}	19.2	139.5

Table 6. Calibrated 2S2P1D constants to match complex modulus back-calculated from dynamic tests measurements with the second method using the first resonance peak at each temperature. Constants E_{00} and β are assumed to be 100 MPa and 250, respectively.

Specimen	E_{00} (MPa)	E_0 (MPa)	δ	k	h	β	$\tau_{E15°C}$ (s)	C_1	C_2
WF-4	100	36,100	1.39	0.142	0.49	250	4.0×10^{-2}	18.9	133.2
WF-6	100	39,500	1.39	0.142	0.49	250	7.0×10^{-2}	18.9	133.2
WF-8	100	38,500	1.39	0.142	0.49	250	4.0×10^{-2}	18.9	133.2
GB5-3	100	39,800	1.17	0.130	0.442	250	5.5×10^{-2}	19.2	139.5
GB5-4	100	41,100	1.17	0.130	0.442	250	7.0×10^{-2}	19.2	139.5
GB5-4	100	40,500	1.17	0.130	0.442	250	7.0×10^{-2}	19.2	139.5

It must be highlighted that values of constants E_{00} and β are assumed because they have no influence on the complex modulus values in the frequency range involved during the dynamic tests. The constants governing the value of the Poisson's ratio ν_{00}, ν_0 and τ_ν do not appear in Tables 5 and 6 because the Poisson's ratio was not evaluated from the dynamic tests but assumptions on the values of these constants were necessary to back-calculate the complex modulus at each temperature in the first step of the first method. A good proximity between the results obtained with the two methods is shown in Figure 12. The same observation was made for all specimens. To validate this visual impression, the relative difference between the norm (in %) and the phase (in °) of the 2S2P1D simulated complex modulus obtained from the two methods are plotted in Figure 13. In this figure, the relative difference is plotted against the reduced frequency at 15 °C for all specimens. It is seen that the second method considering a constant complex modulus at each temperature and a constant real Poisson's ratio of 0.3 gives a norm slightly higher than the first method with a maximum relative difference of about 3.7%. The phase angle determined with the two methods can be considered equivalent with less than 0.03° of difference, which was expected because only constant E_0 of the 2S2P1D model differs between the first and the second method. The slight differences between the two methods may be explained by the different assumptions on the Poisson's ratio value which is modelled with the 2S2P1D model in the first method and taken constant equal to 0.3 in the second method. However, the two proposed methods are in very good agreement. This result is interesting because the second simplified method does not require in the first step the use of an elaborate LVE model. In addition, the back-calculation process is easy to perform as the two calculated constants can be identified using dichotomy process. This new simplified approach considerably reduces the computational time and offers great potential to back-calculate the complex modulus of AM from FRFs measurements using the first resonance peak only.

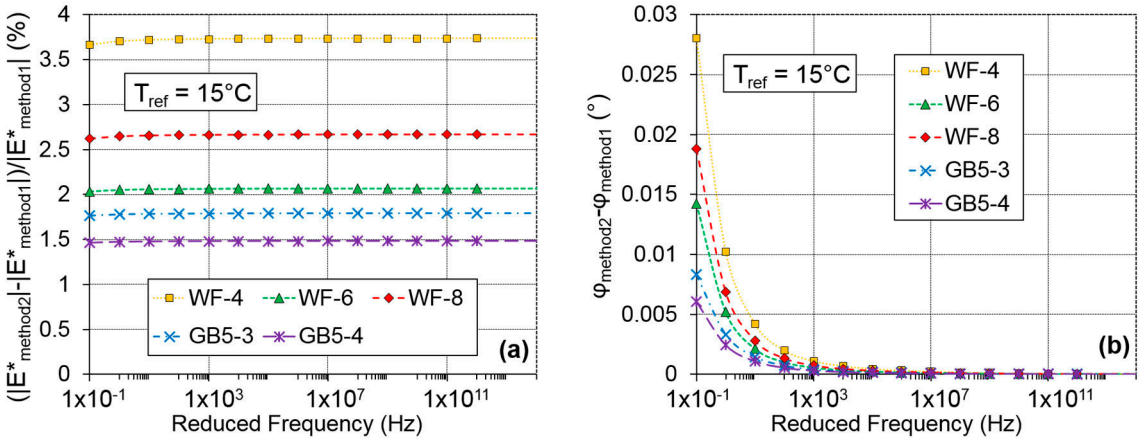

Figure 13. Difference between the complex modulus obtained from the two methods of analysis of the dynamic tests plotted at a reference temperature of 15 °C for all specimens: (**a**) relative difference for the norm of the complex modulus (in %); and (**b**) difference for the phase of the complex modulus (in °).

5.3. Comparison between Cyclic and Dynamic Tests Results

The reduced frequency range of the tension–compression and dynamic tests is different, as confirmed in Figures 10 and 11. The tension–compression tests cover a reduced frequency range between approximately 10^{-7} Hz to 10^{9} Hz at a reference temperature of 15 °C. The dynamic tests cover a reduced frequency range between approximately 1 Hz and 10^{12} Hz at the same reference temperature of 15 °C. Therefore, the best fit between the two tests is expected to be for frequencies higher than 1 Hz and lower than 10^{9} Hz for which experimental data from the two tests is available. As the two methods of back analysis of the dynamic tests give similar results, only the complex modulus obtained from the 2S2P1D model calibrated using the second method of analysis was chosen for the comparison with results of the 2S2P1D model calibrated from quasi-static tension–compression tests data. The relative difference between the norm (in %) and the phase (in °) of the complex modulus from the two calibration processes are plotted in Figure 14 where the results are plotted against the reduced frequency at 15 °C for all specimens. It is shown in Figure 14 that the complex modulus simulated from the two tests are in quite good agreement for the high reduced frequencies (>10^{7} Hz), which was expected when dealing with dynamic measurements. The norm of the dynamic complex modulus is around 3–5% higher than the norm of the complex modulus of the tension–compression tests for this frequency range and there is less than 0.2° of difference between the phase angles from both tests. For lower reduced frequencies (or higher temperatures), the relative difference increases for the norm and reach a value between 12% and 30% at 1 Hz depending on the specimen with an average value of 20.2%. The difference also increases for the phase angle but remains less than 2.5° for reduced frequencies higher than 1 Hz.

The differences observed in Figure 14 show that the dynamic complex modulus has a higher norm and a lower phase angle than the complex modulus obtained from the tension–compression tests. The differences between the two tests increase with temperature. These results are in agreement with results from previous studies using FRFs [18–21]. The differences between the two tests could be due to two phenomena. First, the level of strain applied is different in the two types of tests (about 50 μm/m for the tension–compression tests and about 0.1 μm/m for the dynamic tests). It is known that AM have a nonlinear behaviour showing a strain level dependence even at small strain amplitude [39–41]. The differences observed in this analysis are in the same direction than the observed nonlinearity: increasing of norm and decreasing of phase angle when decreasing strain amplitude. Then, nonlinearity may account for at least a part of the difference between the two tests. Another possibility is ageing of the materials. The tension–compression tests were performed several months before the dynamic tests

and this could explain why the dynamic complex modulus is stiffer. However, the overall agreement between the two tests is satisfying.

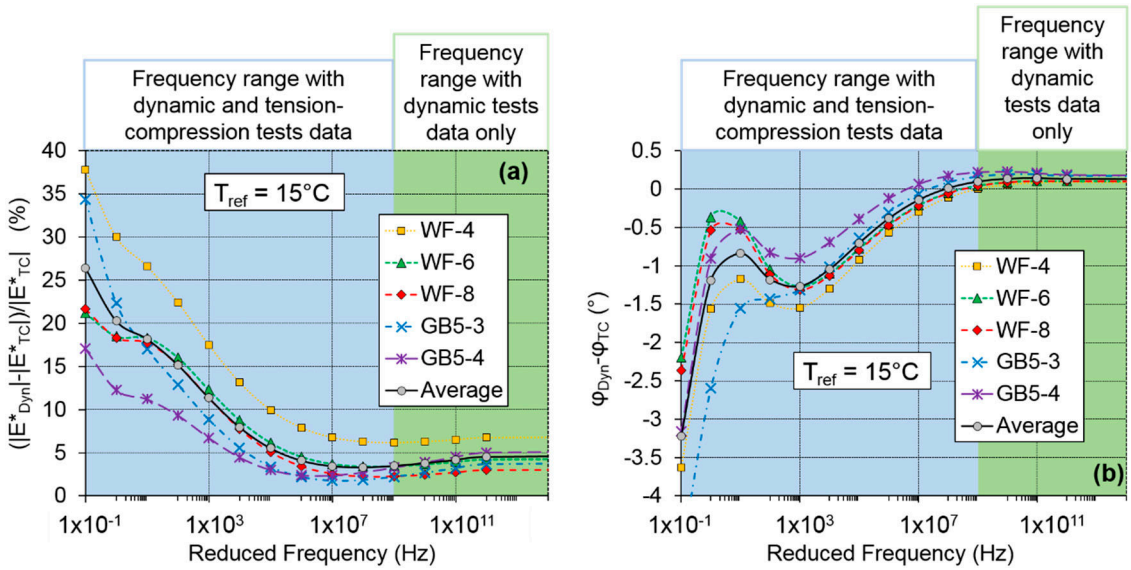

Figure 14. Relative difference between the complex modulus simulated with the 2S2P1D model calibrated from back-calculation of the dynamic tests and the complex modulus simulated with the 2S2P1D model calibrated on the data of the tension–compression tests at 15 °C for all specimens: (**a**) relative difference for the norm of the complex modulus (in %); and (**b**) relative difference for the phase of the complex modulus (in °).

The shift factors from the WLF equation obtained from the tension–compression tests and from the dynamic tests are plotted in Figure 15. It is seen that, for the low temperatures, the agreement between the shift factors from both tests is very good. For temperatures higher than 10 °C, the shift factors of the dynamic tests tend to be higher than the shift factors of the cyclic tests and the difference increases with temperature. The difference between the shift factors is more important for material labelled GB5. However, there is no apparent link between the difference observed in Figure 14 for the complex modulus and for the shift factors since the highest difference on the complex modulus evaluation correspond to a specimen of material labelled WF.

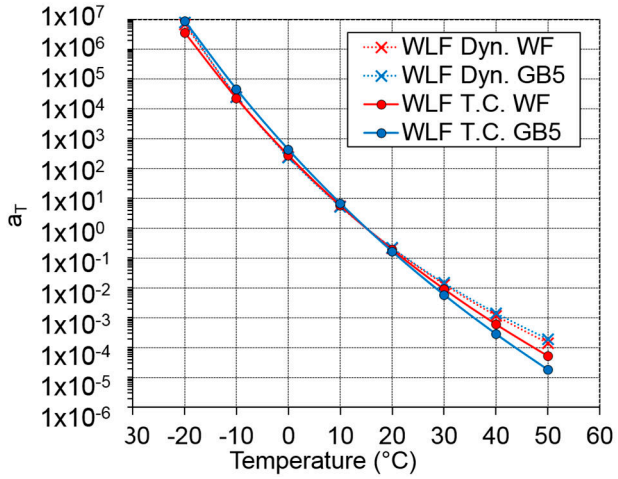

Figure 15. Shift factors of the WLF equation (Equation (7)) obtained from the tension–compression tests (WLF T.C.) and from the dynamic tests (WLF Dyn.) for the two tested materials.

6. Conclusions

In this paper, conventional cyclic tension–compression tests and dynamic tests were performed to characterize the LVE behaviour of AM on a large range of frequencies and temperatures. Two different AM and five specimens were tested with both tests and results were analysed using the 2S2P1D model.

Two methods were studied to back-calculate the complex modulus of AM from dynamic measurements at each temperature. It is shown that the same shift factors are found with the two methods. Moreover, the two methods give very similar complex modulus values (less than 4% of difference for the norm of the modulus and 0.03° for the phase angle) and the differences observes may be due to the different assumptions on the Poisson's ratio value. Therefore, the second method, which is a new and simpler approach, appears to be a good option to obtain the complex modulus of AM from FRFs.

The results of dynamic tests were also compared to the results of tension–compression tests. The shift factors from both tests are very close for the low temperatures and shift factors from dynamic tests are little higher for temperatures higher than 10 °C. The complex modulus obtained from dynamic tests have a higher norm and a lower phase angle than the ones determined with the conventional approach using cyclic tests. The differences observed between the two tests are very limited for the high frequencies or low temperatures (less than 5% for the norm and 0.2° for the phase angle) and are more important for the low frequencies or high temperatures (around 20% for the norm and 2° for the phase angle at 15 °C and 1 Hz). Since the strain level is approximately 500 times lower in the dynamic tests, the nonlinearity of AM with the level of strain amplitude may explain a part of the differences. Ageing of the materials between the tension–compression and the dynamic tests may also have an impact on the complex modulus evaluation.

The agreement between dynamic tests and the tension–compression tests is still satisfactory on the whole frequency range. The combination of the two tests methods is useful to improve the characterization of the LVE behaviour of AM on a wider frequency range because dynamic tests give access to very high frequencies. The presented research shows that dynamic tests, which have the great advantage of being cheap and rapid, can be back-analysed with a very simple model and can provide accurately the complex modulus of AM on a wide range of frequencies and temperatures.

Author Contributions: Methodology, J.-C.C., H.D.B., and C.S.; experimental tests, J.-C.C.; formal analysis, J.-C.C.; writing—original draft preparation, J.-C.C.; and writing—review and editing, H.D.B. and C.S.

Funding: This research received no external funding.

Conflicts of Interest: The authors declare no conflict of interest.

References

1. Di Benedetto, H.; Corte, J.F. *Matériaux Routiers Bitumineux 2: Constitution et Propriétés Thermomécaniques des Mélanges*; Lavoisier: Paris, France, 2005; p. 288. (In French)
2. Halvorsen, W.G.; Brown, D.L. Impulse technique for structural response frequency testing. *J. Sound Vib.* **1977**, *11*, 8–21. [CrossRef]
3. ASTM: C215-08. *Standard Test Method for Fundamental Transverse, Longitudinal and Torsional Frequencies of Concrete Specimens*; ASCE: West Conshoshocken, PA, USA, 2008.
4. Migliori, A.; Sarrao, J. *Resonant Ultrasound Spectroscopy-Applications to Physics, Materials Measurements and Nondestructive Evaluation*; Wiley-Interscience Publication: New York, NY, USA, 1997.
5. Renault, A.; Jaouen, L.; Sgard, F. Characterization of elastic parameters of acoustical porous materials from beam bending vibrations. *J. Sound Vib.* **2010**, *330*, 1950–1963. [CrossRef]
6. Di Benedetto, H.; Sauzéat, C.; Sohm, J. Stiffness of bituminous mixtures using ultrasonic wave propagation. *Road Mater. Pavement Des.* **2009**, *10*, 789–814. [CrossRef]
7. Mounier, D.; Di Benedetto, H.; Sauzéat, C. Determination of bituminous mixtures linear properties using ultrasonic wave propagation. *Constr. Build. Mater.* **2012**, *36*, 638–647. [CrossRef]

8. Norambuena-Contreras, J.; Castro-Fresno, D.; Vega-Zamanillo, A.; Celay, M.; Lombillo-Vozmediano, I. Dynamic modulus of asphalt mixture by ultrasonic direct test. *NDT E Int.* **2010**, *43*, 629–634. [CrossRef]
9. Kweon, G.; Kim, Y.R. Determination of the complex modulus of asphalt concrete using the impact resonance test. *J. Transp. Res. Board* **2006**, *1970*, 151–160. [CrossRef]
10. Lacroix, A.; Kim, Y.R.; Far, M.S.S. Constructing the dynamic modulus mastercurve using impact resonance testing. *J. Assoc. Asphalt Paving Technol.* **2009**, *78*, 67–102.
11. Whitmoyer, S.L.; Kim, Y.R. Determining asphalt concrete properties via the impact resonant method. *J. Test. Eval.* **1994**, *22*, 139–148. [CrossRef]
12. Gudmarsson, A.; Ryden, N.; Birgisson, B. Application of resonant acoustic spectroscopy to asphalt concrete beams for determination of the dynamic modulus. *Mater. Struct.* **2012**, *45*, 1903–1913. [CrossRef]
13. Leisure, R.; Willis, F. Resonant ultrasound spectroscopy. *J. Phys. Condens. Matter* **1999**, *9*, 6001–6029. [CrossRef]
14. Ostrovsky, L.; Lebedev, A.; Matveyev, A.; Popatov, A.; Sutin, A.; Soustova, I.; Johnson, P. Application of three-dimensional resonant acoustic spectroscopy method to rock and building materials. *J. Acoust. Soc. Am.* **2001**, *110*, 1770–1777. [CrossRef] [PubMed]
15. Ryden, N. Resonant frequency testing of cylindrical asphalt samples. *Eur. J. Environ. Civ. Eng.* **2011**, *15*, 587–600. [CrossRef]
16. Ren, Z.; Atalla, N.; Ghinet, S. Optimization based identification of the dynamic properties of linearly viscoelastic materials using vibrating beam techniques. *ASME J. Vib. Acoust.* **2011**, *133*, 041012. [CrossRef]
17. Rupitsch, S.J.; Ilg, J.; Sutor, A.; Lerch, R.; Döllinger, M. Simulation based estimation of dynamic mechanical properties for viscoelastic materials used for vocal fold models. *J. Sound Vib.* **2011**, *330*, 4447–4459. [CrossRef]
18. Gudmarsson, A.; Ryden, N.; Birgisson, B. Characterizing the low strain complex modulus of asphalt concrete specimens through optimization of frequency response functions. *J. Acoust. Soc. Am.* **2012**, *132*, 2304–2312. [CrossRef] [PubMed]
19. Gudmarsson, A.; Ryden, N.; Di Benedetto, H.; Sauzéat, C.; Tapsoba, N.; Birgisson, B. Comparing Linear Viscoelastic Properties of Asphalt Concrete Measured by Laboratory Seismic and Tension-Compression Tests. *J. Nondestruct. Eval.* **2014**, *33*, 571–582. [CrossRef]
20. Gudmarsson, A.; Ryden, N.; Di Benedetto, H.; Sauzéat, C. Complex modulus and complex Poisson's ratio from cyclic and dynamic modal testing of asphalt concrete. *Constr. Build. Mater.* **2015**, *88*, 20–31. [CrossRef]
21. Carret, J.-C.; Pedraza, A.; Di Benedetto, H.; Sauzéat, C. Comparison of the 3-dim linear viscoelastic behavior of asphalt mixes determined with tension-compression and dynamic tests. *Constr. Build. Mater.* **2018**, *174*, 529–536. [CrossRef]
22. Carret, J.-C.; Di Benedetto, H.; Sauzéat, C. Multi-modal dynamic linear viscoelastic back analysis for asphalt mixes. *J. Nondestruct. Eval.* **2018**, *37*, 35. [CrossRef]
23. Poirier, J.E.; Pouget, S.; Leroy, C.; Delaporte, B. Projets Mure et Improvmure: Bilan à mi-parcours. *Revue Générale des Routes et de l'Aménagement* **2016**, *937*, 38–41. (In French)
24. Gayte, P.; Di Benedetto, H.; Sauzéat, C.; Nguyen, Q. Influence of transient effects for analysis of complex modulus tests on bituminous mixtures. *Road Mater. Pavement Des.* **2015**, *17*, 271–289. [CrossRef]
25. Graziani, A.; Di Benedetto, H.; Perraton, D.; Sauzéat, C.; Hofko, B.; Poulikakos, L.; Pouget, S. Recommendation of RILEM TC 237-SIB on complex Poisson's ratio characterization of bituminous mixtures. *Mater. Struct.* **2017**, *50*, 142. [CrossRef]
26. Perraton, D.; Di Benedetto, H.; Sauzéat, C.; Hofko, N.; Graziani, A.; Nguyen, Q. 3 Dim experimental investigation of linear viscoelastic properties of bituminous mixtures. *Mater. Struct.* **2016**, *49*, 4813–4829. [CrossRef]
27. Di Benedetto, H.; Olard, F.; Sauzéat, C.; Delaporte, B. Linear viscoelastic behavior of bituminous materials: From binders to mixtures. *Road Mater. Pavement Des.* **2004**, *5*, 163–202. [CrossRef]
28. Olard, F.; Di Benedetto, H. General 2S2P1D model and relation between the linear viscoelastic behaviors of bituminous binders and mixes. *Road Mater. Pavement Des.* **2003**, *4*, 185–224. [CrossRef]
29. Tiouajni, S.; Di Benedetto, H.; Sauzéat, C.; Pouget, S. Approximation of linear viscoelastic model in the 3 dimensional case with mechanical analogues of finite size—Application to bituminous materials. *Road Mater. Pavement Des.* **2011**, *12*, 897–930. [CrossRef]
30. Di Benedetto, H.; Delaporte, B.; Sauzéat, C. Three dimensional linear behavior of bituminous materials: Experiments and modeling. *ASCE Int. J. Geomech.* **2007**, *7*, 149–157. [CrossRef]

31. Nguyen, H.M.; Pouget, S.; Di Benedetto, H.; Sauzéat, C. Time-temperature superposition principle for bituminous mixtures. *Eur. J. Environ. Civ. Eng.* **2009**, *13*, 1095–1107. [CrossRef]
32. Nguyen, M.L.; Sauzéat, C.; Di Benedetto, H.; Tapsoba, N. Validation of the time–temperature superposition principle for crack propagation in bituminous mixtures. *Mater. Struct.* **2013**, *46*, 1075–1087. [CrossRef]
33. Nguyen, Q.T.; Di Benedetto, H.; Sauzéat, C.; Tapsoba, N. Time-temperature superposition principle validation for bituminous mixes in the linear and nonlinear domain. *ASCE J. Mater. Civ. Eng.* **2013**, *25*, 1181–1188. [CrossRef]
34. Ferry, J.D. *Viscoelastic Properties of Polymers*, 3rd ed.; John Wiley & Sons: New York, NY, USA, 1980.
35. Brüggemann, T.; Biermann, D.; Zabel, A. Development of an automatic modal pendulum for the measurement of frequency responses for the calculation of stability charts. *Procedia CIRP* **2015**, *33*, 587–592. [CrossRef]
36. Norman, P.E.; Jung, G.; Ratcliffe, C.; Crane, R.; Davis, C. *Development of an Automated Impact Hammer for Modal Analysis of Structures*; DSTO-TN-1062; DSTO Defence Science and Technology Organisation: Fishermans Bend, Australia, 2012.
37. Mangiafico, S.; Di Benedetto, H.; Sauzéat, C.; Olard, F.; Pouget, S.; Planque, L. New method to obtain viscoelastic properties of bitumen blends from pure and RAP binder constituents. *Road Mater. Pavement Des.* **2014**, *15*, 312–329. [CrossRef]
38. Pouget, S.; Sauzéat, C.; Di Benedetto, H.; Olard, F. Modeling of viscous bituminous wearing course materials on orthotropic steel deck. *Mater. Struct.* **2012**, *45*, 1115–1125. [CrossRef]
39. Airey, G.; Rahimzadeh, B. Combined bituminous binder and mixture linear rheological properties. *Constr. Build. Mater.* **2004**, *18*, 535–548. [CrossRef]
40. Nguyen, Q.T.; Di Benedetto, H.; Sauzéat, C. Linear and nonlinear viscoelastic behavior of bituminous mixtures. *Mater. Struct.* **2015**, *48*, 2339–2351. [CrossRef]
41. Mangiafico, S.; Babadopoulos, L.; Di Benedetto, H.; Sauzéat, C. Nonlinearity of bituminous mixtures. *Mech. Time-Depend. Mater.* **2018**, *22*, 29–49. [CrossRef]

7 CONCLUSIONS AND PERSPECTIVES

In this thesis, a dynamic test was developed to characterize the LVE behaviour of bituminous mixtures from FRFs measurements. Numerical tools based on the FEM were developed to back analyze the experimental results of the test and to obtain the LVE properties of the materials tested. A parametric analysis was carried out to identify the LVE properties and the constants of the 2S2P1D model having the most influence on the FRFs calculation. Using the results of the parametric analysis, five methods of inverse analysis with different level of complexity were developed. The accuracy of each inverse analysis method was evaluated by applying the method to a numerical model material with averaged LVE properties (reference LVE material). Then, dynamic tests were performed on twenty-eight specimens from five different bituminous mixtures. Results of these tests are presented in five experimental campaigns. In all experimental campaigns, the repeatability of the dynamic tests was assessed. In addition, in the first experimental campaign, different laboratories tested the same specimens and the reproducibility of the dynamic tests was evaluated. Also, ten of the specimens used in this study were also tested with cyclic tension-compression complex modulus tests. For seven of these specimens, the complex Poisson's ratio was also determined from the cyclic tests and from the dynamic tests. The LVE properties (complex modulus and complex Poisson's ratio) obtained from dynamic tests and from cyclic tension-compression tests were compared. In the next paragraphs, the conclusions drawn from obtained experimental results and performed analyses are summarized.

Regarding the experimental aspects of the dynamic tests:

- It is possible to determine FRFs from dynamic tests for frequencies up to 30 kHz and for temperatures up to between 40°C and 50°C depending on the damping properties of the material tested.
- The strain amplitude corresponding to dynamic tests (≈0.1 μdef or less) is approximately 500 times lower than the strain amplitude applied during cyclic complex modulus tests (≈50 μm/m). As the behaviour of bituminous mixtures is strain amplitude dependent, this difference should be taken into account when comparing LVE properties determined from dynamic and cyclic tests.
- An automated impact hammer was developed for the dynamic tests:
  - It improves the repeatability of the measurements with RSD values about 0.5% for the resonance frequencies and 2% for the amplitudes.
  - It guarantees a very good quality of the measurements giving values of the coherence function very close to one for frequencies higher than 3 kHz.
  - It considerably simplifies the experimental procedure, reducing the variability of the measurements that can be observed when different operators perform dynamic tests.
  - It enables measurements at different temperatures without opening the door of the thermal chamber and without changing anything to the test set-up.

Regarding the results of the parametric analyses investigating the influence of the LVE properties and of the constants of the 2S2P1D model on the FRFs calculation:

- The norm of the complex modulus has a significant impact on the resonance frequencies (RSD about 120%) but no impact on the amplitudes. It is the contrary for the phase angle that has an important influence on the amplitudes (RSD about 25%) and a negligible influence on the resonance frequencies (RSD about 1%).
- Four constants of the 2S2P1D model were identified as the most influents on the FRFs calculation: constant E_0 has an important influence on the resonance frequencies while constants $\tau_{E15°C}$, k and δ have an influence on both the resonance frequencies and amplitudes. The three other constants of the 2S2P1D model governing the complex modulus value (E_{00}, β and h) have a lower influence and can be fixed when optimizing the FRFs in the first step of the proposed inverse analysis methods.
- The complex Poisson's ratio has a far lower influence than the complex modulus, and even a negligible influence for the first resonance of the longitudinal mode of vibration (RSD of 1.1% for the first resonance frequency and of 0.6% for the corresponding amplitude). The same observations are valid for constants ν_{00}, ν_0 and $\tau_{\nu 15°C}$ of the 2S2P1D model. Therefore, the effect of Poisson's ratio can be neglected in the inverse analysis to reduce the number of constants to identify, at least as a first approximation.

Regarding the results of the five inverse analysis methods applied to the reference LVE material:

- Method I is only adapted to characterize the LVE behaviour for the very high frequencies (above than 10^5 Hz at 10°C). For temperatures higher than 10°C, important errors (up to 30% for the norm of the complex modulus and 10° for the phase angle) appear showing the limitations of using a too simplified back-analysis method.
- Method II is accurate both for the norm and for the phase angle of the complex modulus with error of less than 5% and 2°, respectively. However, these results were obtained assuming that the shift factors were known which is not the case when testing a new material. In addition, the global approach used in this method may not be adapted to be used with physical measurements.
- The accuracy of methods III, IV and V is very good, with less than 2% of error for the norm of the complex modulus and 1° of difference for the phase angle. Moreover, the same constants of the 2S2P1D model (E_0, $\tau_{E15°C}$, k, δ and h) and of the WLF equation (C_1 and C_2) were found in the second step of these three inverse methods. The three methods have therefore a very comparable accuracy.
- Methods IV and V are only accurate for the longitudinal mode of vibration and should not be used with the flexural or torsional modes.
- Method IV has quite interesting advantages comparing to method III and V:
  - It does not require to use a rheological model taking into account the frequency and temperature dependency of the behaviour in the first step.
  - Only two constants are determined in the first step (four are determined in method III and five in method V).
  - The optimization process in the first step is very easy to apply because the two determined constants are obtained by dichotomy.

  - Thanks to the previous observations, the computational time is considerably reduced in the first step of method IV (between five and ten times faster than methods III and V).
- Method V is the only method for which the complex Poisson's ratio can be determined. Its evaluation with this method is very accurate (less than 4% of error for the norm of the complex Poisson's ratio and less than 0.2° for the phase angle).

Regarding the LVE properties determined from dynamic tests in the experimental campaigns:

- Measurements of FRFs at five different temperatures are sufficient to determine the global LVE behaviour of the material over a wide frequency range. For example, at 15°C, the reduced frequency range covered by the dynamic tests is approximately between 1 Hz and 10^{11} Hz.
- The characterization of the complex modulus from dynamic tests is very repeatable from one specimen of a material to another, especially when using the same geometry and mode of vibration. If different geometries or modes of vibrations are used, slight differences can appear between two specimens of the same material.
- The longitudinal mode of vibration is the easiest mode to excite and it gives the most repeatable results. Some problems appeared when using the flexural mode for the disc geometry. In addition, the longitudinal mode is the only mode for which it is possible to determine the complex modulus with a simplified analysis (in method IV) or to determine the complex Poisson's ratio (with method V). For these reasons, it is highly recommended to use the longitudinal mode of vibration in dynamic tests.
- The same global LVE behaviour is determined with methods III and V when using only the first resonance frequency of the longitudinal mode as input in method III. This result confirms the negligible influence of the Poisson's ratio on the first resonance of the longitudinal mode.
- The global LVE behaviour determined with method IV is in very good agreement with the results of methods III and V. The phase angle of the complex modulus is identical for the three methods while the norm of the complex modulus is between 1% and 3% higher with method IV. It confirms the great potential of method IV, despite its simplified approach in the first step.

Regarding the reproducibility of the dynamic tests evaluated in the FSDyn project experimental campaign:

- The reproducibility of the dynamic tests between different laboratories is satisfying but it can be improved. The variability of the measurements between different laboratories is higher than the variability observed in the repeatability study performed at ENTPE (the RSD is about 2% for the resonance frequencies and 25% for the amplitudes against approximately 0.5% and 2%, respectively).
- The influence of using different experimental devices (accelerometer, impact hammer and signal conditioner) from one laboratory to another cannot explain the variability of the measurements observed in the FSDyn project. Indeed, the RSD obtained when studying six combinations of experimental devices from ENTPE and EIFFAGE was only 0.2% for the resonance frequencies and 5.6% at most for the amplitudes (RSD about 2% for the resonance frequencies and 25% for the amplitudes between the measurements of all laboratories in the FSDyn project).

- The different experimental procedures (such as measurements performed inside or outside the thermal chamber, time waited for the stabilization of the system, use of an automated or manual impact hammer, etc.) used by each laboratory are the most evident reasons to explain the variability of the measurements.

Regarding the comparison of the LVE properties determined from dynamic tests and from cyclic tension-compression tests:

- The norm of the complex modulus determined from dynamic tests is higher than the one obtained from tension-compression tests. The difference between the two tests is only a few per cent (5% at most) for the low temperatures (or high frequencies) and it increases with temperature (or when frequency decreases). For example, considering the ten comparisons of dynamic and cyclic tests performed on specimens of five different materials, the norm of the complex modulus at 15°C and 10 Hz obtained from dynamic tests is between 4% and 25% higher than the norm of the complex modulus obtained from cyclic tests with an averaged difference of about 15%.
- The phase angle of the complex modulus determined from dynamic tests is in good agreement with the phase angle determined from cyclic tests. Almost no difference is seen for the high frequencies (or low temperatures). For higher temperatures (corresponding to frequencies below 100 Hz at 15°C.), the phase angle determined from dynamic tests tends to be slightly lower than the phase angle determined from cyclic tests. The maximum deviation between the two tests is limited to about 2°.
- These results are not surprising given that the strain amplitudes of both tests are different. The norm (respectively the phase angle) of the complex modulus tends to increase (respectively decrease) when the strain amplitude decreases, which is observed in this study. Nonlinearities effects can explain differences between 5% and 15% for the norm of the complex modulus, depending on the materials. The effects of nonlinearities for the phase angle are less important which could explain the overall good agreement between both tests
- Some differences exist between the norm of complex Poisson's ratio determined from dynamic tests and from tension-compression tests. For most of the material, there is less than 0.1 of difference for the norm of the complex Poisson's ratio. However, no clear trend is seen: the norm of the complex Poisson's ratio determined with dynamic tests can either be higher or lower than the one obtained from cyclic tests.
- The phase angle of the complex Poisson's ratio determined from dynamic tests and from cyclic tests are not in good agreement for all materials. Differences up to 3° are seen in this study. It is difficult to evaluate accurately the phase angle of the complex Poisson's ratio from dynamic tests.
- Considering the difficulty to determine accurately the complex Poisson's ratio in experimental tests, these differences are not surprising and the evaluation of the complex Poisson's ratio from dynamic tests has great potential, especially for the norm of the complex Poisson's ratio.

The aforementioned results were obtained for a wide variety of materials including polymer modified bitumen, mixtures with high RAP contents, materials drilled from an airport runway, etc. It shows that dynamic tests, which are economic and simple to perform, are very repeatable tests and can provide an accurate characterization of the LVE properties of different

types of bituminous mixtures over a wide reduced frequency range. Therefore, the results and conclusions of this work highlight the great advantages of using dynamic test to characterize bituminous materials LVE behaviour. It is hoped that the results and conclusions of this thesis will contribute to better understanding of the dynamic tests and the associated inverse analysis methods to obtain the LVE properties. In addition, it is also hoped that the results and conclusions of this thesis will encourage the scientific community working on bituminous materials to use dynamic tests for characterizing the LVE behaviour. Finally, some recommendations and perspectives for future research can be made to further develop dynamic tests and their applicability:

- It is recommended to use automated impact systems such as the one developed in this work for many reasons:
  - To standardize the experimental procedure, which will improve the reproducibility of the dynamic test.
  - To potentially couple dynamic tests with other tests such as crack or damage propagation tests. Using dynamic tests during this type of tests may give access to additional information about material properties.
  - To perform continuous measurements of FRFs, which could lead to an even better characterization of the material properties.
- The number of temperatures used for the dynamic tests could be reduced to characterize the LVE behaviour over a shorter frequency range. For example, if only one value of the complex modulus is needed (for example at 15°C and 10Hz for pavement design in the French standards), only one or two temperatures may be enough, which will reduce the duration of the test.
- The analysis of the dynamic tests should not require to use expensive finite element software. For this purpose, simplified inverse analysis methods such as method IV are very interesting. They offer great potential to calculate FRFs charts and can be more easily coded in free applications. The development of such charts or applications would probably be an important step to encourage asphalt researchers to use dynamic tests.
- Dynamic tests can be applied to real pavement structures, which enables non-destructive quality control of new and old pavements. In that case, the properties evaluated in situ and with laboratory dynamic tests can be directly compared because the strain amplitude levels are the same.

REFERENCES

Airey, G. D., & Rahimzadeh, B. (2004). Combined bituminous binder and mixture linear rheological properties. *Construction and Building Materials, 18*(7), 535-548. doi:10.1016/j.conbuildmat.2004.04.008

ASTM-C215-02. (2002). *Standard Test Method for Fundamental Transverse, Longitudinal, and Torsional Frequencies of Concrete Specimens.* ASTM International. doi:10.1520/C0215-02

Babadopoulos, L. (2017). *Phenomena occurring during cyclic loading and fatigue tests on bituminous.* Doctoral Thesis, University of Lyon, ENTPE, Lyon.

Bachmann, H. (1991). *Vibration problems in structures* (Vol. 209). Wien: Bulletin d'information.

Balay, J. M., & Caron, C. (2008). Airfiels Pavements Characteristics design and Evaluation : A Rational Design Method for Airfield Pavements : the French Alizé-Airfield Pavement Software. (RGRA, Ed.) *Europeanroads review* , 4-15.

Bedford, A., & Drumheller, D. D. (1994). *Introduction to elastic wave propagation.* John Wiley & Sons.

Biot, M. A. (1959). Dynamics of Viscoelastic Anisotropic Media. *The fourth midwestern conference on solid mechanics*, (pp. 94-108). Texas, USA.

Boltzmann, L. (1874). Zur Theorie der elastischen Nachwirkung [On the theory of the elastic aftereffect]. *Sitzungsberichte der Mathematisch-Naturwissenschaftlichen Klasse der Kaiserlichen Akademie der Wissenschaften, 70*, 275-306.

Brüggemann, T., Biermann, D., & Zabel, A. (2015). Development of an Automatic Modal Pendulum for the Measurement of Frequency Responses for the Calculation of Stability Charts. *Procedia CIRP, 33*, 587-592. doi:10.1016/j.procir.2015.06.090

Carret, J. C., Di Benedetto, H., & Sauzéat, C. (2018). Multi Modal Dynamic Linear Viscoelastic Back Analysis for Asphalt Mixes. *Journal of Nondestructive Evaluation, 37*(2), 1-11. doi:10.1007/s10921-018-0491-3

Carret, J. C., Pedraza, A., Di Benedetto, H., & Sauzéat, C. (2018). Comparison of the 3-dim linear viscoelastic behavior of asphalt mixes determined with tension-compression and dynamic tests. *Construction and Building Materials, 174*, 529-536. doi:10.1016/j.conbuildmat.2018.04.156

Clough, R. W., & Penzien, J. (1993). *Dynamics of Structures, 2nd edition.* New-York: McGraw-Hill Inc.

Commissariat général au développement durable, .. (2018). *Chiffres clés du transport.*

Corté, J. F., & Di Benedetto, H. (2005). *Matériaux routiers bitumineux 2: Constitution et propriétés thermomécaniques des mélanges.* Paris: Hermes-Lavoisier.

Delaporte, B., Di Benedetto, H., Chaverot, P., & Gauthier, G. (2007). Linear Viscoelastic Properties of Bituminous Materials: from Binders to Mastics. *Journal of the Association of Asphalt Paving Technologists, 76*, 455-494.

Di Benedetto, H., Delaporte, B., & Sauzéat, C. (2007). Three-dimensional linear behavior of bituminous materials: Experiments and modeling. *International Journal of Geomechanics, 7*(2), 149-157.

Di Benedetto, H., Olard, F., Sauzéat, C., & Delaporte, B. (2004). Linear viscoelastic behavior of bituminous materials: from binders to mixes. *Road Materials and Pavement Designs, 5*(sup1), 163-202. doi:10.1080/14680629.2004.9689992

Di Benedetto, H., Sauzéat, C., & Clec'h, P. (2016). Anisotropy of bituminous mixture in the linear viscoelastic domain. *Mechanics of Time-Dependent Materials, 20*(3), 281-297. doi:10.1007/s11043-016-9305-0

Di Benedetto, H., Sauzéat, C., & Sohm, J. (2009). Stiffness of bituminous mixtures using ultrasonic wave propagation. *Road Materials and Pavement Design, 10*(4), 789-814.

Ferry, J. D. (1980). *Viscoelastic properties of polymers.* New-York: Wiley.

French civil aviation authority. (2016). *Rational design method for flexible pavements.* Technical guide.

Gayte, P., Di Benedetto, H., Sauzéat, C., & Nguyen, Q. T. (2015). Influence of transient effects for analysis of complex modulus tests on bituminous mixtures. *Road Materials and Pavement Design, 17*(2), 271-289. doi:10.1080/14680629.2015.1067246

Graff, K. E. (1975). *Wave motion in elastic solids.* London: Oxford University Press.

Graziani, A., Di Benedetto, H., Perraton, D., Sauzéat, C., Hofko, B., Poulikakos, L., & Pouget, S. (2017). Recommendation of RILEM TC 237-SIB on complex Poisson's ratio characterization of bituminous mixtures. *Materials and Structures*. doi:10.1617/s11527-017-1008-8

Gross, B. (1968). *Mathematical Structure of the Theories of Viscoelasticity.* Paris: Hermann et Cie.

Gudmarsson, A. (2014). *Resonance testing of Asphalt Concrete.* Doctoral Thesis, KTH Royal Institute of Technology.

Gudmarsson, A., Ryden, N., & Birgisson, B. (2012). Application of resonant acoustic spectroscopy to asphalt concrete beams for determination of the dynamic modulus. *Materials and Structures, 45*(12), 1903-1913. doi:10.1617/s11527-012-9877-3

Gudmarsson, A., Ryden, N., & Birgisson, B. (2012). Characterizing the low strain complex modulus of asphalt concrete specimens through optimization of frequency response functions. *The Journal of the Acoustical Society of America, 132*(4), 2304-2312. doi:10.1121/1.4747016

Gudmarsson, A., Ryden, N., Di Benedetto, H., & Sauzéat, C. (2015). Complex modulus and complex Poisson's ratio from cyclic and dynamic modal testing of asphalt concrete. *Construction and Building Materials, 88*(30), 20-31. doi:10.1016/j.conbuildmat.2015.04.007

Gudmarsson, A., Ryden, N., Di Benedetto, H., Sauzéat, C., Tapsoba, N., & Birgisson, B. (2014). Comparing Linear Viscoelastic Properties of Asphalt Concrete Measured by Laboratory Seismic and Tension–Compression Tests. *Journal of Nondestructive Evaluation, 33*(4), 571-582.

Guo, Q. B. (2000). Determination of the dynamic elastic moduli and internal friction using thin resonant bars. *The Journal of the Acoustical Society of America, 108*(1), 167-174. doi:10.1121/1.429453

Halvorsen, W. G., & Brown, D. L. (1977). Impulse technique for structural frequency response testing. *Sound and Vibration*, 8-21.

Hartmann, B., Lee, G. F., & Lee, J. D. (1994). Loss factor height and width limits for polymer relaxations. *The Journal of the Acoustical Society of America, 95*(1), 226-233. doi:10.1121/1.408355

Havriliak, S., & Negami, S. (1966). A complex plane analysis of α-dispersions in some polymer systems. *Journal of Polymer Science Part C: Polymer Symposia, 14*(1), 99-117. doi:10.1002/polc.5070140111

Havriliak, S., & Negami, S. (1967). A complex plane representation of dielectric and mechanical relaxation processes in some polymers. *Polymer, 8*, 161-210. doi:10.1016/0032-3861(67)90021-3

Huet, C. (1963). *Étude par une méthode d'impédance du comportement viscoélastique des matériaux hydrocarbonés.* Doctoral thesis, Université de Paris.

Ingard, K. U. (1988). *Fundamental of waves and oscillations.* Cambridge University Press.

Kweon, K., & Kim, Y. R. (2006). Determination of the complex modulus of asphalt concrete using the impact resonance test. *Journal of the Transportation Research Board, 1970*, 151-160.

Lacroix, A., Kim, Y. R., Sadat, M., & Far, S. (2009). Constructing the dynamic modulus mastercurve using impact resonance testing. *Asphalt Paving Technology 2009*, *78*, pp. 67-95. Minneapolis.

Leisure, R. G., & Willis, F. A. (1997). Resonant Ultrasound Spectroscopy. *Journal of Physics: Condensed Matter, 9*(28), 6001-6029.

Madigosky, W. M., Lee, G. F., & Niemiec, J. M. (2006). A method for modeling polymer viscoelastic data and the temperature shift function. *Journal of Acoustical Society of America, 119*, 3760-3765. doi:10.1121/1.2195292

Mandel, J. (1966). *Cours de mecanique des milieux continus, Tome II: mécanique des solides.* Gauthier-Villars.

Mangiafico, S. (2014). *Linear viscoelastic properties and fatigue of bituminous mixtures produced with Reclaimed Asphalt Pavement and corresponding binder blends.* Doctoral thesis, Université of Lyon, ENTPE, Lyon.

Mangiafico, S., Babadopoulos, L., Sauzéat, C., & Di Benedetto, H. (2018). Nonlinearity of bituminous mixtures. *Mechanics of Time-Dependent Materials, 22*(1), 29-49. doi:10.1007/s11043-017-9350-3

Mangiafico, S., Di Benedetto, H., Sauzéat, C., Olard, F., Pouget, S., & Planque, L. (2013). Influence of reclaimed asphalt pavement content on complex modulus of asphalt binder blends and corresponding mixes: experimental results and modelling. *Road Materials and Pavement Design, 14*(sup1), 132-148. doi:10.1080/14680629.2013.774751

Mangiafico, S., Di Benedetto, H., Sauzéat, C., Olard, F., Pouget, S., Dupriet, L., . . . Van Rooijen, R. (2015). Statistical analysis of the influence of RAP and mix composition on viscoelastic and fatigue properties of asphalt mixes. *Materials and Structures, 48*(4), 1187-1205. doi:10.1617/s11527-013-0225-z

Maynard, J. (1996). Resonant Ultrasound Spectroscopy. *Physics today, 49*, 26-31.

Migliori, A., & Sarrao, J. L. (1997). *Resonant Ultrasound Spectroscopy - Applications to Physics, Materials Measurements and Nondestructive Evaluation.* New-York: Wiley - Interscience Publication.

Motola, Y., & Uzan, J. (2007). Anisotropy of Field-Compacted Asphalt Concrete Material. *Journal of Testing and Evaluation, 35*(1), 103-105. doi:10.1520/JTE100151

Mounier, D., Di Benedetto, H., & Sauzéat, C. (2012). Determination of bituminous mixtures linear properties using ultrasonic wave propagation. *Construction and Building Materials, 36*, 638-647.

Nazarian, S., Tandon, V., & Yuan, D. (2005). Mechanistic Quality Management of Hot Mix Asphalt Layers with Seismic Methods. *Journal of ASTM International, 2*(9), 1-12. doi:10.1520/JAI12256

Nguyen, Q. T., Di Benedetto, H., & Sauzéat, C. (2015). Linear and nonlinear viscoelastic behaviour of bituminous mixtures. *Materials and Structures, 48*(7), 2339-2351. doi:10.1617/s11527-014-0316-5

Nguyen, Q. T., Di Benedetto, H., & Sauzéat, C. (2015). Linear and nonlinear viscoelastic behaviour of bituminous mixtures. *Materials and Structures, 48*(7), 2339-2351. doi:10.1617/s11527-014-0316-5

Nguyen, Q. T., Di Benedetto, H., Sauzéat, C., & Tapsoba, N. (2013). Time Temperature Superposition Principle Validation for Bituminous Mixes in the Linear and Nonlinear Domains. *Journal of Materials in Civil Engineering, 25*(9), 1181-1188. doi:10.1061/(ASCE)MT.1943-5533.0000658

Nguyen, Q. T., Di Benedetto, H., Sauzéat, C., & Tapsoba, N. (2013). Time Temperature Superposition Principle Validation for Bituminous Mixes in the Linear and Nonlinear Domains. *Journal of Materials in Civil Engineering, 25*(9), 1181-1188. doi:10.1061/(ASCE)MT.1943-5533.0000658

Norembuena-Contreras, J., Castro-Fresno, D., Vega-Zamanillo, M., Celaya, M., & Lombillo-Vozmediano, I. (2010). Dynamic modulus of asphalt mixture by ultrasonic direct test. *NDT&E International, 43*, 629-634.

Norman, P. E., Jung, G., Ratcliffe, C., Crane, R., & Davis, C. (2012). *Development of an Automated Impact Hammer for Modal Analysis of Structures.* Australian government, Defence Science and Technology Organisation.

Nyquist, H. (1928). Certain Topics in Telegraph Transmission Theory. *Transactions of the American Institute of Electrical Engineers, 47*(2), 617-644. doi:10.1109/T-AIEE.1928.5055024

Olard, F., & Di Benedetto, H. (2003). General "2S2P1D" Model and Relation Between the Linear Viscoelastic Behaviours of Bituminous Binders and Mixes. *Road Materials and Pavement Design, 4*(2), 185-224. doi:10.1080/14680629.2003.9689946

Ostrovsky, L., Lebedev, A., Matveyev, A., Potapov, A., Sutin, A., Soustova, I., & Johnson, P. (2001). Application of three-dimensionnal resonant acoustic spectroscopy method to rock and building materials. *The Journal of the Acoustical Society of America, 110*(4), 1770-1777.

Pasqualini, D. (2006). Intrinsic nonlinearity in geomaterials: Elastic properties of rocks at low strain. In P. Delsanto (Ed.), *Universality of Noncalssical Nonlinearity Applications to Non-Destructive Evaluations and Ultrasonic* (pp. 417-423). New-York: Springer Science and Business Media.

Pedraza, A. (2018). *Propriétés thermomécaniques d'enrobés multi-recyclés.* Thèse de doctorat, Univeristé de Lyon, ENTPE, Lyon.

Perraton, D., Di Benedetto, H., Sauzéat, C., Hofko, N., Graziani, A., & Nguyen, Q. (2016). 3 Dim experimental investigation of linear viscoelastic properties of bituminous mixtures. *Materials and Structures, 49*(11), 4813-4829. doi:10.1617/s11527-016-0827-3

Pham, N. H. (2014). *Etude thermomécanique avancée de différents types d'enrobés recyclés tièdes avec additif.* Thèse de doctorat, Université de Lyon, ENTPE, Lyon.

Pham, N. H., Sauzéat, C., Di Benedetto, H., Gonzalez-Leon, J. A., Barreto, G., Nicolaï, A., & Jakubowski, M. (2015). Analysis and modeling of 3D complex modulus tests on hot and warm bituminous mixtures. *Mechanics of Time-Dependent Materials, 19*(2), 167-186. doi:10.1007/s11043-015-9258-8

Pham, N. H., Sauzéat, C., Di Benedetto, H., Gonzalez-Leon, J. A., Barreto, G., Nicolaï, A., & Jakubowski, M. (2015). Reclaimed asphalt pavement and additives' influence on 3D linear behaviour of warm mix asphalts. *Road Materials and Pavement Design, 16*(3), 569-591. doi:10.1080/14680629.2015.1021108

Phan, C. V. (2016). *Comportement thermomécanique des matériaux bitumineux traités à la chaux.* Thèse de doctorat, Université de Lyon, ENTPE, Lyon.

Phan, C. V., Di Benedetto, H., Sauzéat, C., Lesueur, D., Pouget, S., Olard, F., & Dupriet, S. (2017). Complex modulus and fatigue resistance of bituminous mixtures containing hydrated lime. *Construction and Building Materials, 139*, 24-33. doi:10.1016/j.conbuildmat.2017.02.042

Poirier, J. E., Pouget, S., Leroy, C., & Delaporte, B. (2016). Projets Mure et Improvmure: bilan à mi-parcours. *Revue Générale des Routes et de l'Aménagement, 937*, pp. 38-41.

Pouget, S., Sauzéat, C., Di Benedetto, H., & Olard, F. (2010). From the behaviour of constituent materials to the calculation and design of orthotropic steel bridge structures. *Road Materials and Pavement Design, 11*(Special Issue), 111-144.

Ren, Z., Atalla, N., & Ghinet, S. (2011). Optimization based identification of the dynamic properties of linearly viscoelastic materials using vibrating beam techniques. *Journal of Vibration and Acoustics, 133*(4), 1-12. doi:10.1115/1.4003594

Renault, A., Jaouen, L., & Sgard, F. (2011). Characterization of elastic parameters of acoustical porous materials from beam bending vibrations. *Journal of Sound and Vibration, 330*(9), 1950-1963. doi:10.1016/j.jsv.2010.11.013

Rupitsch, S. J., Ilg, J., Sutor, A., Lerch, R., & Döllinger, M. (2011). Simulation based estimation of dynamic mechanical properties for viscoelastic materials used for vocal fold models. *Journal of Sound and Vibration, 330*(18-19), 4447-4459. doi:10.1016/j.jsv.2011.05.008

Ryden, N. (2011). Resonant frequency testing of cylindrical asphalt samples. *European Journal of Environmental and Civil Engineering, 15*(4), 587-600. doi:10.1080/19648189.2011.9693349

Salençon, J. (2009). *Viscoélasticité pour le calcul des structures.* Paris: Editions de l'école Polytechnique.

Sayegh, G. (1965). *Variations des modules de quelques bitumes purs et enrobés bitumineux.* Doctoral Thesis, Université de Paris.

Shearer, P. (1999). *Introduction to seismology.* Cambridge University Press.

TenCate, J. A., Pasqualini, D., Habib, S., Heitmann, K., Higdon, D., & Johnson, P. A. (2004). Nonlinear and Nonequilibrium Dynamics in Geomaterials. *Physical Review Letters, 93*(6). doi:10.1103/PhysRevLett.93.065501

Whitmoyer, S. L., & Kim, Y. R. (1994). Determining asphalt concrete properties via the impact resonant method. *Journal of Testing and Evaluation, 22*(2), 139-148.

Williams, M. L., Landel, R., & Ferry, J. D. (1955). The Temperature Dependance of Relaxation Mechanisms in Amorphous Polymers and Other Glass-forming liquids. *Journal of the American Chemical Society, 77*(14), 3701-3707. doi:10.1021/ja01619a008

Young's Modulus of Elasticity for Metals and Alloys. (2004). Retrieved from Engineering ToolBox: https://www.engineeringtoolbox.com/young-modulus-d_773.html

Zhao, Y., Liu, H., Bai, L., & Tan, Y. (2013). Characterization of linear viscoelastic behavior of asphalt concrete using complex modulus model. *Journal of Materials in Civil Engineering, 25*(10), 1543-1548. doi:10.1061/(ASCE)MT.1943-5533.0000688